

The Influence of Peroxy Radicals
on Ozone Production



Dissertation
zur Erlangung des Doktorgrades
der Naturwissenschaften

vorgelegt beim
Fachbereich Geowissenschaften/Geographie
der Johann Wolfgang Goethe-Universität
in Frankfurt am Main

von

Graeme M. Handisides M. Sc. (Hons)
aus Mangakino, Neuseeland

Frankfurt am Main, 2001
(DF1)

vom Fachbereich Geowissenschaften / Geographie der
Johann Wolfgang Goethe-Universität als Dissertation angenommen.

Dekan: Prof. Oschmann

Gutachter: Prof. Ulrich Schmidt, Uni. Frankfurt
PD Dr. Harald Berresheim, DWD, Met. Obs. Hohenpeißenberg

Datum der Disputation: 20. Dezember 2001

*“The heavens declare the glory of God;
the skies proclaim the work of his hands.
Day after day they pour forth speech;
night after night they display knowledge.
There is no speech or language
where their voice is not heard.
Their voice goes out into all the earth,
their words to the ends of the world.”*

Psalm 19: 1-4
New International Version

To
Ana, Samuel and Rebekah

Thanks

Table of Contents

Table of Contents	x
Abstract	1
1 Introduction	3
I Photochemical Oxidation Processes in the Troposphere	9
2 Ozone Production in the Troposphere	13
2.1 Ozone production in the clean troposphere	15
2.1.1 Reservoir species and chemical loss processes	17
2.1.2 Daytime chemistry	17
2.1.3 Night-time chemistry	19
2.1.4 Hydroperoxy radicals	20
2.2 Ozone production in the presence of organic compounds	21
2.2.1 Reactions competing with ozone production	23
2.2.2 Overall influence of peroxy radicals on ozone production	24
2.3 Conclusions	25
3 Peroxy radicals in the atmosphere	27
3.1 Production of peroxy radicals	27
3.1.1 Oxidation of VOCs via the OH radical	29
3.1.2 Ozonolysis of VOCs	30
3.1.3 Night-time RO ₂ production via the nitrate radical	30
3.1.4 Photolysis of carbonyl compounds	32
3.2 Reactions involving peroxy radicals	32
3.2.1 Reaction with NO	33
3.2.2 Reaction with NO ₂	36
3.2.3 Reaction with OH	36
3.2.4 Reactions between peroxy radicals	37
3.3 Non-chemical sinks for peroxy radicals	37

3.4	Conclusion	38
4	Factors affecting the observed ozone concentration	39
4.1	Loss processes	40
4.2	Heterogeneous processes	41
4.3	Transport processes	42
4.4	Conclusions	44
II	Experimental Techniques	45
5	Measurement techniques for peroxy radicals	49
5.1	MIESR	49
5.2	Chemical amplifier (CA)	50
5.3	IMR-MS/CIMS	51
5.4	LIF-FAGE	52
5.5	Deviation from photostationary steady state (PSSD)	52
5.6	Atmospheric measurements	53
5.7	Conclusions	54
6	The chemical amplifier technique	55
6.1	Measurement principle	56
6.2	Signal modulation	58
6.3	The amplification factor	62
6.4	Organic peroxy radicals	64
6.5	The effect of water vapour on the amplification factor	67
6.6	The interpretation of RO _x measurements using the CA	70
7	The IMG chemical amplifier	71
7.1	Description of the IMG Peroxy Radical Chemical Amplifier	71
7.1.1	Inlet	74
7.1.2	NO ₂ detector	76
7.1.3	Data acquisition and control system	78
7.1.4	Data analysis software	79
7.2	Calibration of the NO ₂ detector	81
7.2.1	Automatic calibration procedure	82
7.2.2	Calibration of detector linearity	84
7.2.3	Correlation of background signal with measured oxidant levels	85
7.3	Calibration of the inlet	85
7.3.1	HO ₂ radical source	85
7.3.2	Calculation of the amplification factor	88
7.4	Error analysis	90

7.4.1	Uncertainty due to calibration	91
7.4.2	Uncertainty in ambient measurements	93
7.4.3	Total uncertainty in the measurements	94
8	Instrumentation and Site Descriptions	95
8.1	Site description: Kleiner Feldberg	95
8.2	Site description: Hohenpeissenberg	99
8.3	Measurements of atmospheric trace gases	101
8.3.1	Ozone	102
8.3.2	NO _x	104
8.3.3	PAN	105
8.3.4	SO ₂	105
8.3.5	OH/H ₂ SO ₄ (MOHp)	105
8.3.6	VOCs (MOHp)	106
8.4	Radiation measurements	107
8.4.1	Global radiation	107
8.4.2	Photolysis rates	107
8.5	Meteorological parameters	108
8.6	Data Collection	109
III	RO_x measurements: Results and Interpretation	111
9	Field measurements at Kleiner Feldberg	115
9.1	Diurnal profiles	120
9.1.1	Relationship between RO _x and solar radiation	123
9.1.2	Summary	126
9.2	Weekend Effect	127
9.3	Statistical relationships between components	130
9.3.1	Ozone	130
9.3.2	RO _x	137
9.4	Effect of wind direction	140
9.5	Conclusions	144
10	Predicting ozone	147
10.1	Calculation of ozone production	148
10.2	Observed change in ozone vs modelled production	149
10.3	Diurnal profile of ozone production	151
10.4	Statistical model for predicting ozone	154
10.5	Conclusions	155

11 Steady state OH and RO_x model	157
11.1 Measurements at Hohenpeissenberg	158
11.2 Steady-state radical balance model	163
11.3 OH balance	165
11.4 RO _x balance	168
11.5 Conclusions	171
12 The climatology of ozone on Kleiner Feldberg	173
12.1 The annual ozone profile	174
12.2 Average diurnal profiles during ozone events	177
12.3 The background ozone concentration	179
12.4 Spatial representativity of ozone measurements	183
12.5 Conclusion	195
13 Conclusion	197
Zusammenfassung	201
Appendix	209
A Description of system software	211
A.1 Control and data collection programme: rox.exe	211
A.2 Signal demodulation programme: modsig.exe	214
B Data for 1998	221
C Data for 1999	231
D Steady State Model	241
D.1 OH Radical Balance	241
D.2 RO _x radical balance	243
List of Figures	247
List of Tables	251
List of Abbreviations	253
Bibliography	255
Acknowledgements	273

Abstract

This study is a contribution towards understanding the photochemical production of ozone on the basis of the reaction between peroxy radicals (RO_x) and NO. The main aims of the study are to investigate the possibility of improving the short-term daily ozone forecast on the basis of measurements of the RO_x concentration; to investigate the relationships between the various trace gases, in particular, those between RO_x , OH and VOCs; and to investigate the extent to which the photochemical production of ozone is representative on wider temporal and spatial scales.

In order to carry out measurements of RO_x radicals for the purpose of these investigations, a chemical amplifier (CA) was built for the continuous measurement of the RO_x mixing ratio. A chain reaction takes place in the inlet of the CA involving ambient RO_x and added CO and NO, resulting in the conversion of n molecules of NO to NO_2 per RO_x radical (where n is the chain length of the reaction). The resulting NO_2 is detected by a luminol detector, which is calibrated using a purpose-built automated calibration unit. Calibration with peroxy radicals was carried out using HO_2 radicals produced by the photolysis of water vapour. The amplification factor has been corrected for the sensitivity of the CA to water vapour on the basis of published data.

Measurements made at Kleiner Feldberg during the summer months in 1998 and 1999 are presented. The average daytime mixing ratio of ozone (O_3) is well correlated with the RO_x mixing ratio. The correlations between the O_3 mixing ratio and the mixing ratios of PAN, NO or NO_2 are all much weaker. The mixing ratio of RO_x is well correlated with the mixing ratio of PAN, but exhibits a much weaker negative correlation with the mixing ratios of NO and NO_2 . However, the most significant correlation for the concentrations of both O_3 and RO_x is the correlation with ambient temperature. Consequently, the daily maximum air temperature is identified as the most important parameter for predicting afternoon O_3 concentrations. A simple statistical model for forecasting the maximum ozone concentration using temperature and the maximum ozone concentration from the previous day is capable of explaining 80% of the variance in the observed ozone concentration. Including measurements of the RO_x mixing ratio from the morning results in only a very small improvement in the explained variance.

The ozone production rate is calculated on the basis of the reaction between RO_x and NO for 52 days on which the global radiation reached 600 W m^{-2} or more. The

average production rate reached a maximum of 5 ppbv h⁻¹ at noon. The calculated production rate was then compared with the observed rate of change of the ozone concentration. The observed rate of change was about 25% of the calculated production rate. Loss processes resulted in an evening loss rate for ozone of about 2 ppbv h⁻¹.

Average diurnal profiles of O₃, RO_x and NO_x concentrations for each day of the week show a decrease in the NO_x concentration at the weekend due to reduced anthropogenic emissions, but a rise in the O₃ concentration. This cannot be explained by a rise in the RO_x concentration. In order to interpret these results, it is proposed that photochemical conditions at Kleiner Feldberg are VOC limited.

Measurements of RO_x, OH and other trace gases at Hohenpeissenberg in June 2000 are presented. These are interpreted using a steady state photochemical model. The measured OH and RO_x concentrations are reproduced well by the model results. Recycling of HO₂ by NO is found to be responsible for the high OH concentrations observed during late morning. The reaction of RO_x with NO also delays the build up of RO_x, resulting in the maximum of the RO_x mixing ratio being observed during the early afternoon. The oxidation of isoprene and terpenes was found to be the major source of RO_x and sink of OH at Hohenpeissenberg. Oxidation rates of NMHCs reached around 33×10⁶ molecule cm⁻³ s⁻¹ on one morning during the measurement campaign.

The impact of photochemical production on ozone concentrations is investigated using ozone measurements for the whole of Germany provided by UBA. The net rate of change of the ozone concentration during daylight hours is found to be similar for three stations which lie close to each other. The night-time concentrations show much greater divergence due to changes in the structure of the boundary layer. The correlation between ozone measurements at Königstein and 277 other German stations were calculated and the relationship of the correlation coefficient with the distance from Königstein was investigated. During the day, the correlation coefficient drops linearly with increasing distance of the station from Königstein. At night, no relationship is found, which is attributed to changes in the structure of the boundary layer and the dominance of local conditions. During summer, the ozone measurements at Königstein explain 50% of the variance in ozone concentration for stations lying up to about 250 km from Königstein between 11:00 and 16:00 CET. It is suggested that this is due to a well mixed boundary layer and relatively homogeneous conditions over a relatively large area.

Chapter 1

Introduction

Since its discovery by Schönbein in 1875, it has become apparent that ozone plays a major role in the atmosphere. The highest concentrations of ozone are found in the stratosphere, where it absorbs nearly all shorter wavelengths of UV radiation, thereby providing an essential shield against biologically active UV. Thus, the presence of ozone in the stratosphere protects living organisms from UV damage, allowing life to exist as we know it on land. In contrast, ozone is only present in the troposphere in trace quantities, but as an important photooxidant it plays an essential role in the self cleansing mechanism of the atmosphere.

In recent decades, ozone has received increased scientific and public attention due to the realisation that ozone levels in both the stratosphere and the troposphere are being influenced by compounds of man-made origin. Anthropogenic emissions¹ of halogen containing compounds have led to an increase in the springtime destruction of ozone in the polar stratosphere, a process which has led to regular formation of the so-called ozone hole over the Antarctic, and its Northern Hemisphere equivalent. In contrast, levels of ozone have increased in the troposphere due to increasing levels of hydrocarbons and nitrogen oxides. This situation is nicely summed up in a slogan used by the Environmental Agency for the State of Hesse in a booklet dealing with the ozone problem [*HMUEB/HMJFG*, 1993]:

“Oben zu wenig, unten zu viel” (Too little above, too much below)

Although the impression is sometimes created that tropospheric ozone is the result of human influences, the production of ozone in the troposphere is not a new phenomenon. Even in the absence of human influence, it occurs in all regions with

¹Anthropogenic emissions are those which result from human activities, e.g. due to industry, transport, fossil-fuel combustion, etc. In contrast, biogenic emissions result from biological activities, e.g. emissions of volatile compounds from plants, emissions from bacterial activity in soils, from oceans, etc. Such emissions are often natural, but can also be influenced by human activities, e.g., agriculture.

adequate levels of UV radiation and precursors. The precursors include organic compounds and nitrogen oxides, both of which are also emitted naturally. However, anthropogenic emissions can have a significant effect on the production of ozone, particularly on a regional level. Public realisation of this has led to a heightened interest in this problem, especially in light of the damage which high tropospheric ozone levels can cause.

Ozone's oxidative nature means, that in addition to oxidising organic compounds in the atmosphere, it can react with a wide range of substances on surfaces. This can cause significant damage to buildings and other materials, and can also have serious deleterious effects on biological organisms. Its effects on vegetation include damage to trees [*Krause and Köllner, 2000*], injury to leaves, and reduction of crop yield [e.g., *Weigel and Bender, 2000; European Commission, 1999*]. Humans are also susceptible to ozone, with sensitive individuals showing initial reactions at concentrations as low as $100 \mu\text{g m}^{-3}$ (50 ppbv²), although other components probably also play a role. Symptoms include reduction of respiratory functions, irritation of bronchial tract and increased sensitivity to allergens [*Höppe et al., 2000*].

The anthropogenically influenced production of tropospheric ozone has led to relatively high levels of ozone being observed in central Europe during summer periods with stable high pressure systems. Such weather patterns are typically associated with high levels of UV radiation, higher temperatures and light winds. Emission rates increase with the higher temperatures, and precursors can accumulate under the stable conditions. In the presence of elevated UV levels this leads to increased ozone production. Over a period of a few days the level of ozone can build up to levels exceeding thresholds at which damage can occur, before a change in weather conditions causes a return to normal levels.

As ozone can cause health problems for sensitive individuals at concentrations well below the peak levels measured, the reduction of these high ozone levels has become an issue of political and public interest, especially during long, hot periods in summer. This has resulted in a large number of studies worldwide, which have been carried out with a view to further understanding the production of ozone, and also to establishing procedures for minimising health risks. At the public level, it has led to the regular publication of ozone forecasts, in an attempt to assist the public themselves to take appropriate measures to avoid excessive ozone exposure.

Legislation has also been introduced in an attempt to reduce ozone levels by restricting anthropogenic emissions of ozone precursors, i.e. volatile organic compounds (VOC) and nitrogen oxides, during periods with high ozone levels. Examples of this were the ozone ordinance promulgated in the State of Hesse prior to 1995, and the federal "Ozone Law" during the period from June 1995 to the end of 1999, both of

²ppbv is the unit commonly used for the mixing ratio (parts per billion by volume) and corresponds to one litre of trace gas per 10^9 litres of air [e.g., *Seinfeld and Pandis, 1998, p. 19*]. Also used are ppmv (1 part in 10^6) and pptv (1 part in 10^{12}). The SI equivalents are nmol.mol^{-1} , $\mu\text{mol.mol}^{-1}$ and pmol.mol^{-1} , respectively. 1 ppbv of ozone corresponds to $2 \mu\text{g m}^{-3}$

which enabled the introduction of speed limits during periods of widespread, persistent high ozone concentrations. After the federal law expired at the end of 1999, the legal basis for measurement and reporting of ozone reverted to the Federal Immission Control Act of 1993 (Ordinance regarding immission levels). This requires the public to be informed of possible dangers to health in the case of one hour exposure levels reaching $180 \mu\text{g m}^{-3}$, and a warning to be issued when one hour levels exceed $360 \mu\text{g m}^{-3}$.

On a European level, the European Union has provided a common basis for monitoring and reducing ozone in both the current ozone directive 92/72/EEC and the Air Quality Framework Directive of 1996 (96/62/EEC). A daughter directive has been proposed (COM(2000) 613 final - 1999/0068 (COD)) on the basis of this Framework directive which foresees an information threshold of $180 \mu\text{g m}^{-3}$ and an alert threshold of $240 \mu\text{g m}^{-3}$. Furthermore, a target for maximum human exposure to ozone has been set, which should be reached by 2010. This foresees eight hour exposure limits for humans of $120 \mu\text{g m}^{-3}$, which should only be exceeded on fewer than 20 days per year. The directive also sets targets for long term exposure to ozone, as recommended by the WHO, in order to protect vegetation. This exposure target is expressed as accumulated exposure above a threshold mixing ratio of 40 ppbv during daylight hours, expressed in either ppbv h or $\mu\text{g m}^{-3}$ h and referred to as the AOT40 level. The proposed target for vegetation is $17\,000 \mu\text{g m}^{-3}$ h per year. This is likely to require further measures for reduction of precursors, and also requires extensive monitoring. Long term targets of not exceeding an average eight hour exposure of $120 \mu\text{g m}^{-3}$ for humans and AOT40 of $6\,000 \mu\text{g m}^{-3}$ h for vegetation also express the goal towards which the EU states are required to work. However, these long term targets will be extremely difficult to reach, as natural ozone production already accounts for a significant amount of ozone levels. This allows only limited room for further reductions.

In Germany the responsibility for monitoring ozone levels and for issuing ozone warnings and forecasts lies with the various environmental agencies, both at the federal and at the state level. Various approaches to predicting ozone levels have been applied, ranging from semi-empirical methods, such as those used by the Bureau for the Environment and Geology of the State of Hesse (Hessisches Landesamt für Umwelt und Geologie, HLUG), to the statistical methods developed for the Federal Environmental Agency (Umweltbundesamt, UBA) [Grosch and Schmitt, 1994]. Chemical models based on the chemical mechanisms and meteorological processes can also be used to simulate ozone production. Due to operating constraints, they are typically used more for diagnostic purposes than for operational prognoses. Depending on the type of model used and the number of reactions considered, these models can require relatively long computer runs and detailed information about initial concentrations and meteorological parameters.

Despite the limitations on the chemical models, they contribute to our understanding of ozone production and also indicate the impact of various ozone mitigation

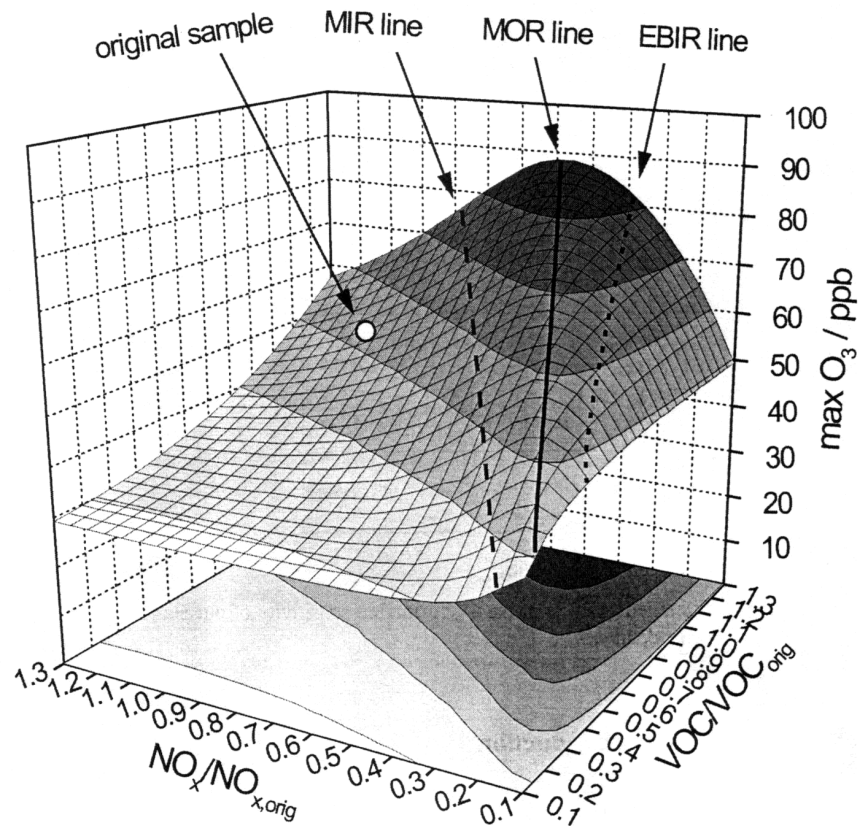


Figure 1.1: Results of a box model for the maximum amount of ozone for various initial NO_x and VOC concentrations, relative to those measured in the Halle plume in eastern Germany. MIR denotes the maximum incremental VOC reactivity; MOR is the maximum ozone reactivity scenario; and EBIR is the equal benefit incremental reactivity. Taken from *Klemm et al.* [2000].

strategies. For example, models are often used to simulate the amount of ozone produced under certain conditions and to investigate the sensitivity of the atmospheric system to changes in the initial NO_x and VOC concentrations. This is often plotted as an isopleth diagram, which shows the maximum amount of ozone produced for various NO_x and VOC levels. Figure 1.1 is an example of such a plot for the city plume for Halle in eastern Germany and shows a three dimensional plot of the maximum ozone mixing ratios modelled using the Regional Atmospheric Chemistry Model (RACM) *Klemm et al.* [2000]. This isopleth representation shows that when NO_x levels are above the level defined by the line denoted MOR in Figure 1.1, a decrease in NO_x levels leads initially to an increase in the ozone maximum. For the conditions at Halle, a reduction of NO_x to 0.46 of the initial concentration was modelled to result in an increase in the maximum ozone concentration from 52.9 ppbv to 77.7 ppbv. In contrast, a reduction in VOCs would always lead to a reduction in the ozone maximum. The situation here is referred to as being VOC sensitive. During a series of measurements

in eastern Germany, *Klemm et al.* [2000] found that all the areas had high enough NO_x levels that the ozone production was VOC-limited, so that large reductions in NO_x would be required before the ozone maximum dropped below observed levels. Evidence is presented in the current study that a similar situation is to be found at Kleiner Feldberg (see Section 9.2). Such results indicate the difficulty of attaining the targets set out in the EU directives, as reductions in both NO_x and VOC would be required.

While the general principles leading to ozone production and build up in the troposphere are relatively well known, much can still be learnt by process studies involving measurements of ozone precursors and meteorological parameters. Ozone is produced in the troposphere solely as the result of the photolysis of NO_2 . However, its concentration is determined by the complex interactions between a large number of compounds and parameters which affect the equilibrium between NO_2 , NO and ozone. Peroxy radicals (RO_x) play an important role in this process as they react with NO to produce NO_2 , and thus ozone, without destroying ozone in the process. These peroxy radicals are themselves products of the oxidation of volatile organic compounds (VOCs) by the OH radical. As such, they represent an important step in the self cleansing of the troposphere, as well as playing this crucial role in ozone production. With the development of measurement techniques for peroxy radicals over the last 20 years, it has become possible to study their relationship to ozone production under field conditions.

The current study was conceived as a contribution to this field of research by carrying out measurements of as comprehensive a range of components as possible, including the total mixing ratio of peroxy radicals. Relationships between the measured trace gases were investigated on a statistical basis as well as using a simple steady state photochemistry model. The main aims of the study were

- to investigate the possibility of improving the short-term daily ozone forecast on the basis of measurements of the RO_x concentration;
- to investigate the relationships between the various trace gases, in particular, those between RO_x , OH and VOCs; and
- to investigate the extent to which the photochemical production of ozone is representative of conditions over a wider area.

This was carried out by making measurements of the concentrations of ozone, peroxy radicals and a range of other trace gases at Kleiner Feldberg, a hill on the rim of the Rhine-Main basin, and at Hohenpeissenberg, a hill in rural Bavaria. The measurements of peroxy radical concentrations were made using a peroxy radical chemical amplifier (CA) which was built for this purpose.

The resulting measurements were analysed for relationships between the trace gases. These relationships were then used as a basis for making a statistical ozone forecast. This was extended by including the morning measurements of the peroxy

radical concentration with the hope of improving the forecast. The measurement of additional components at Hohenpeissenberg allowed the concentrations of OH and RO_x to be modelled using a simple steady state photochemistry model. This also allowed the most important sources and sinks for these radicals to be identified, and enabled the major features of the diurnal profile of the peroxy radical concentration to be interpreted. Finally, measurements of the ozone concentration from 277 German stations were analysed to determine the spatial representativity of the ozone measurements at Königstein, which is close to Kleiner Feldberg.

Part I presents an overview of the photochemical processes in the troposphere which lead to ozone production. The production of tropospheric ozone is summarised in Chapter 2 for both a clean and a polluted atmosphere. The chemistry of peroxy radicals is considered in more detail in Chapter 3, particularly with regard to their production and loss processes. Their reactions with NO are considered, as is the conversion of the resulting oxy radicals to HO₂, as this is of importance to the CA. Chapter 4 considers the various other factors which influence the observed ozone concentration.

Part II concentrates on the measurement techniques used to make the current measurements. Peroxy radicals are inherently difficult to measure due to their relatively high reactivity and low concentrations, and different approaches to their measurement and the major results from previous measurements are summarised in Chapter 5. The RO_x measurements for the current study were made using the chemical amplifier technique. The technique and its potential problems are outlined in Chapter 6. The chemical amplifier used in the current study, its calibration and the uncertainty associated with its use are described in Chapter 7. Chapter 8 describes the two measurement sites and the other instrumentation used during the study.

Part III presents the measurements themselves and their interpretation. The measurements at Kleiner Feldberg are presented in Chapter 9 along with the results of investigations into the relationship between the various trace gases and meteorological parameters. This data was then used to calculate ozone production rates, which were used as a starting point for a consideration of the possibility of improving ozone forecasts using measurements of the RO_x concentration. These results are discussed in Chapter 10. The measurements at Hohenpeissenberg and their interpretation using a steady state photochemical model are presented in Chapter 11. This part concludes with an analysis of the measured ozone concentrations from a series of measurement stations in Chapter 12.

Chapter 13 presents the main conclusions of the study.

Part I

Photochemical Oxidation Processes in the Troposphere

Overview

The photochemical production of ozone in the troposphere has a major impact on the ozone levels. Part I provides a summary of these processes, as well as an overview of other processes affecting the ozone levels observed in middle Hesse. The basic photochemistry of the troposphere is presented with an emphasis on those reactions of peroxy radicals which lead to ozone production.

As an introduction to photochemistry in the troposphere, Chapter 2 summarises the tropospheric chemistry of ozone production. Firstly, the photochemistry in an ideal atmosphere devoid of organic compounds (the so-called clean atmosphere) is considered. This is followed by a summary of the photochemistry in the presence of volatile organic compounds (i.e. in the polluted atmosphere), which are the precursors of organic peroxy radicals. In both sections the primary reactions affecting ozone and NO_x ³ levels are considered first, followed by a summary of chemical processes which can lead to the loss of these main reactive components, or to their temporary entrapment in reservoir species.

Due to the important part played by peroxy radicals in the production of ozone in the polluted atmosphere, Chapter 3 considers their origin and chemistry in more detail. Oxidation processes leading to the production of peroxy radicals are considered first. The processes relevant to the troposphere are the oxidation of volatile organic compounds by the hydroxyl radical, ozone, and the nitrate radical, and the direct photolysis of some organic compounds. The reactions of peroxy radicals with NO are then considered in some detail, as the progress of these reactions has an important influence on the accuracy of atmospheric measurements of peroxy radicals made using the chemical amplification technique. The major sinks of peroxy radicals are then presented. Measurements made by other groups are also summarised.

Further factors influencing ozone levels are considered in Chapter 4. The balance between production, loss and transport processes is then discussed, as the observed ozone concentration is effectively the sum of all these factors.

³NO_x refers to the group of nitrogen oxides involved directly in ozone chemistry: NO and NO₂.

Chapter 2

Ozone Production in the Troposphere

Despite its relatively low concentration in the atmosphere, ozone (O_3) is an important atmospheric constituent. It is not emitted naturally into the atmosphere, but is produced by photochemical processes in both the stratosphere and the troposphere. The highest concentrations of ozone are found in the stratosphere, with a maximum mixing ratio at a height of around 20-25 km, where it is formed as a result of the photolysis of molecular oxygen by UV light at wavelengths less than about 310 nm.

Ozone produced in the stratosphere makes an important contribution to ozone levels in the troposphere. It can undergo transport through the tropopause into the troposphere, especially during periods of tropospheric folding and cut-off lows, at which times extreme tropospheric ozone values may be observed in the upper free troposphere. Such events can lead to the intrusion of stratospheric ozone quite deep into the troposphere, resulting in ozone of stratospheric origin even reaching ground level at higher altitudes [e.g., *Beekman et al.*, 1997; *Kunz and Speth*, 1997]. Ozone from such events is, however, rapidly mixed with tropospheric air, so that direct observation at ground level is normally only possible at mountain stations. Nevertheless, the transport of ozone of stratospheric origin into the troposphere makes a significant contribution to the background¹ level of ozone in the troposphere. This effect was of greater importance in pre-industrial times when ozone levels were around 10 ppbv, considerably lower than they are today [*Volz and Kley*, 1988].

Photochemical production of ozone also occurs directly in the troposphere, although by a different process than in the stratosphere, as the high energy UV radiation required to photolyse molecular oxygen, O_2 , is completely absorbed in the stratosphere. It involves a complex suite of chemical interactions involving nitrogen

¹The background concentration of ozone can be considered to be the average concentration of ozone in the absence of local processes. See Section 12.3.

oxides ($\text{NO}_x = \text{NO} + \text{NO}_2$) and volatile organic compounds (VOC)² as precursor compounds³ and UV radiation as initiator of the photooxidative processes. Net production of ozone occurs in all but the cleanest air masses. Under appropriate weather conditions and when adequate levels of precursor substances are present, tropospheric ozone production can also lead to extreme ozone levels on a local or regional scale. In summer, with its higher insolation, this can result in ozone levels which are significantly higher than the European background of about 32-37 ppbv, which was measured at coastal and North European sites during the Tropospheric Ozone Research (TOR) programme [Beck and Grennfelt, 1993, 1994; Scheel *et al.*, 1997]. Episodes with very high ozone concentrations generally occur during summer time periods with stable high pressure systems and associated high levels of radiation.

Extreme peak values of ozone are most often observed in polluted regions during episodes of high temperatures and strong radiation, such as Southern Europe and the US. For example, values of around 800 ppbv were observed in California in the mid 1960s. High levels of natural ozone precursors also contribute under such conditions, because the level of biogenic emissions from vegetation increases significantly at high temperatures. Meteorological conditions also play a special role by maintaining suitable air masses in a region of intense photochemical activity for a period of a few days. This allows the concentration of photochemical oxidants, including ozone, to rise to the extreme values that are sometimes observed in such areas. Examples of this are the stable high pressure system over the Iberian peninsula [Millàn *et al.*, 1996] and the land/sea wind system in Athens [Moussiopoulos, 1994]. Both situations can cause precursor rich air to be trapped in an area with high levels of radiation, resulting in the very high photooxidant levels observed in these regions areas during ozone episodes.

While the extreme levels seen in Southern Europe and in California have not been observed in Central Europe, ozone levels of more than 200 ppbv were observed in Germany in the 1970s and 1980s [Becker *et al.*, 1985], and ozone levels of over 80 ppbv are regularly observed during warm summer periods in central Europe. In recent years, however, a series of ozone mitigation measures and general measures to reduce levels of air pollution have contributed to a decrease in the frequency of the highest ozone concentrations [Beilke, 2000; Lin *et al.*, 2000].

In contrast, the average level of the ozone background has increased slightly [e.g., Beilke, 2000; Lin *et al.*, 2000] over the same time period. The increase in the ozone

²VOC denotes the entire set of gas phase organic compounds in the atmosphere [Seinfeld and Pandis, 1998, p. 80]. The term Non-Methane Hydrocarbons (NMHC) is sometimes used to refer to all hydrocarbons, with the exception of methane. However, substituted hydrocarbons, such as aldehydes, ketones, etc., taken are also important for ozone production processes, which has led some authors to use the terms Non-Methane Organic Compounds (NMOC) or Non-Methane VOCs (NMVOC) to refer to all organic compounds except methane. These terms are used interchangeably by some authors [e.g., Finlayson-Pitts and Pitts, 1986, p. 603].

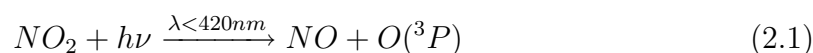
³Although both NO_x and VOCs are required as precursors for ozone production, they play different roles in the production process. VOCs provides fuel for the photochemistry, while NO_x essentially takes the role of a catalyst [c.f., Geiß and Volz-Thomas, 1992].

background is possibly partially caused by an overall reduction in ozone loss rates due to regional reductions in NO_x emissions. Depending on the level of NO_x , it can function as both an ozone precursor and as a sink due to the reaction of O_3 with NO (i.e. by NO titration.) This leads to the somewhat ironical situation, as seen in Chapter 1, that a reduction in the level of certain precursors can lead to an overall increase in ozone levels. In a statistical study of ozone data in the United States for the period 1980 - 1998, *Lin et al.* [2000] proposed that long range transport of ozone, particularly of Asian origin, was a major cause of the observed increase in the ozone level at the low end of the ozone concentration distribution. The observed increase seemed to be large scale in origin, rather than a local or regional effect. This suggests that the average level of photochemical production in the Northern Hemisphere is increasing. Thus, the general increase in precursor levels in the Northern Hemisphere due to anthropogenic activity probably contributes to the observed rise in the level of the ozone background, which has a much greater impact on average ozone levels than on the peak values.

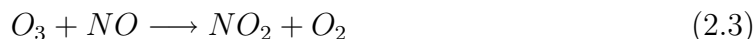
The current chapter summarises the chemical processes responsible for tropospheric ozone production. Firstly, the photochemistry affecting ozone production will be outlined for the simplified case of a hypothetical atmosphere free of organic compounds. This will be followed by a discussion of the impact of organic compounds.

2.1 Ozone production in the clean troposphere

In contrast to the situation in the stratosphere, the only known process whereby ozone is produced in the troposphere is the photolysis of NO_2 followed by the reaction of the resulting oxygen atom with molecular oxygen:



where M (as in all following reactions) is a collision partner ($M = \text{N}_2$ or O_2). Ozone may itself react with NO , regenerating NO_2 :



This last reaction is very rapid and is referred to as NO titration, as it leads to near complete destruction of NO or O_3 , depending on which of these compounds is more abundant. In an atmosphere free of organic compounds and with a constant radiation intensity, the interaction of these three species would soon establish an equilibrium state. The time required to reach equilibrium depends on the intensity of the photolysing radiation. The photolysis rate for NO_2 (j_{NO_2}) typically takes values of up to 10^{-2} s^{-1} , so that the time required to establish a photostationary steady state is of the order of a few minutes around midday during summer.

Thus, in such an atmosphere, the ozone concentration would essentially be determined by the relative rates of these reactions and the initial levels of the precursors NO and NO₂. After establishment of a photostationary steady state, the relationship of the concentrations of the three components to each other is given by the following equation [Leighton, 1961]:

$$\frac{j_{NO_2}[NO_2]}{k_{2,3}[NO][O_3]} = 1 \quad (2.4)$$

where $k_{2,3}$ ⁴ is the rate constant for Reaction (2.3).

NO and NO₂ are typically present in the atmosphere in concentrations of up to a few ppbv, although, in the free troposphere and in clean air, the concentration is normally much lower. NO concentrations are essentially zero at night as a result of the near complete titration with ozone (Reaction (2.3)), which is mostly present in high enough concentrations to ensure complete conversion of NO to NO₂. An exception to this is to be found in areas close to NO sources, e.g., near motorways, where the titration reaction can reduce ozone levels to nearly nil. Both NO and NO₂ are emitted to the atmosphere as a result of combustion processes (approximately 40% of emissions are due to the combustion of fossil fuels) and biological activity (soil emissions), and are produced directly in the atmosphere as a result of lightning [e.g., Höller *et al.*, 1999]. Direct emission of NO₂ is much less ($\leq 10\%$) than that of NO [PORG, 1997], but it is generally present in higher concentrations in the atmosphere due to the conversion of NO to NO₂. This does not only occur by reaction with ozone, but also by the termolecular reaction of NO and O₂ in regions with high NO concentrations.



The rate of this reaction is highly sensitive to the concentration of NO and drops rapidly as NO is diluted as it is transported away from its source.

Due to the close relationship between NO and NO₂ and the importance of the interconversion reactions between them, it is common to refer to the sum of these two species as NO_x ($NO_x \equiv NO_2 + NO$). A similar relationship between O₃ and its direct predecessor NO₂ means that the sum of these two species is a convenient measure of the oxidant content of an air mass [Guicherit, 1988]⁵. Fluctuations in the ozone concentration which are due to NO titration and NO₂ photolysis can thus be accounted for by considering the sum of these two oxidants, rather than O₃ alone.

⁴ $k_{2,3} = 1.9 \times 10^{-14} \text{ cm}^3 \text{ molecule}^{-1} \text{ s}^{-1}$ [Sander *et al.*, 2000]

⁵Guicherit [1988] and some other authors refer to this as “oxidant” and denote it by $O_x \equiv O_3 + NO_2$. However, as O_x is normally defined as $O_x \equiv O_3 + O$, to avoid confusion the term O_x is not used in this work.

2.1.1 Reservoir species and chemical loss processes

Even in a clean atmosphere, NO_x undergoes further reactions with other radicals⁶. The products of such radical-radical interactions are mostly stable species, so that such reactions normally lead to the loss of radicals from the system. This may be a permanent loss, through the formation of species which irreversibly remove radicals from the atmosphere, or a temporary loss, by the formation of a reservoir species that can later regenerate the parent species. While the formation of reservoir species does not directly lead to a long term reduction in ozone levels, it can lead to a spatial or temporal shift in the production pattern. Such reactions can lead directly to a decrease in the ozone concentration, or they can cause a reduction in the production rate of ozone. In the clean atmosphere, a reduction in the ozone production rate occurs whenever the immediate ozone source, NO_2 , is removed from the atmosphere, or whenever NO is removed from the atmosphere without NO_2 being produced. A further, indirect reduction of the ozone production rate occurs in the polluted atmosphere whenever organic radicals and their precursors are removed. This reduces the potential for the conversion of NO to NO_2 .

The importance of these various reactions for the ozone chemistry varies greatly, especially as some species only reach significant concentrations at night. As photochemical ozone production is a daytime process, the production of such reservoir species has no direct effect on ozone production in the clean atmosphere. They can, however, play a significant role in the polluted atmosphere due to their reactions with organic compounds.

This wider web of interactions involving nitrogen oxides is summarised schematically in Figure 2.1 for a clean atmosphere in which the extended chemistry associated with the presence of HO_2 radicals is neglected. The equilibrium between NO_x and O_3 is portrayed by the cycle involving the shaded boxes in the centre of the diagram. The boxes surrounding these central components represent species which affect this equilibrium. Arrows represent major reactions which result in the conversion of one species into another. Additional reaction partners are shown alongside the arrows. Photolysis is involved in a number of steps and is portrayed by a dashed line, with $h\nu$ representing the contribution of radiation. Species which only occur at night are represented by dark shaded boxes. The following two subsections consider these reactions and species which are important during the daytime and at night, respectively.

2.1.2 Daytime chemistry

During the day, the most important loss process is the oxidation of NO_2 to produce nitric acid (HNO_3).



⁶A radical, also referred to as a free radical, is a neutral molecule or molecule fragment possessing one or more unpaired electrons.

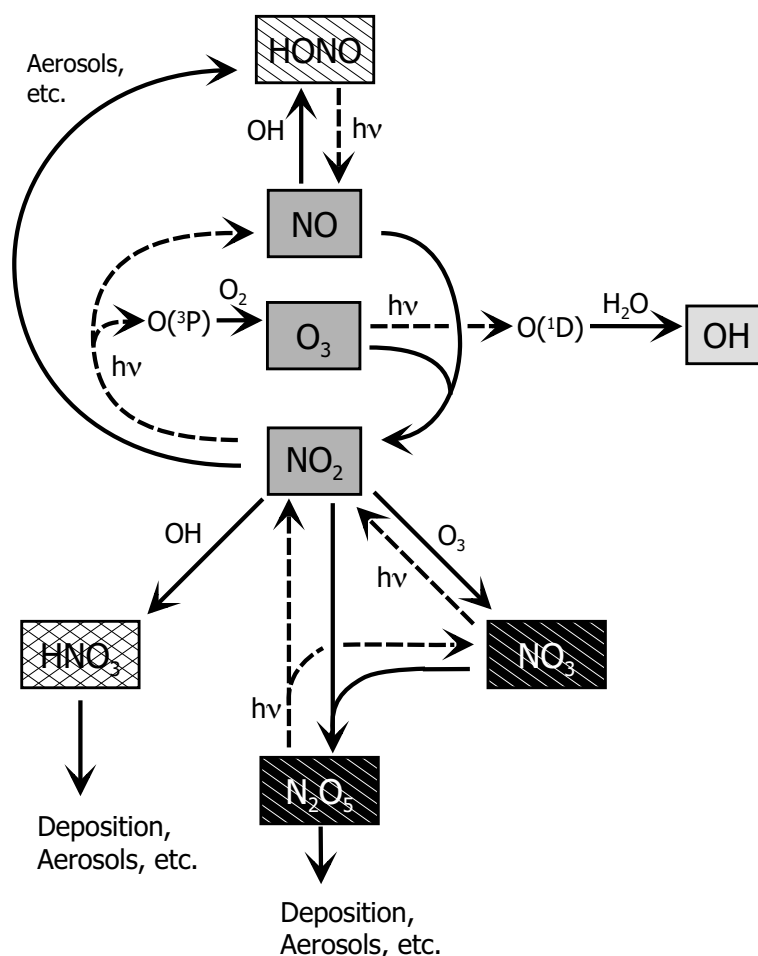


Figure 2.1: Simplified schematic representation of the chemistry leading to ozone production in the clean troposphere. The shaded boxes represent the principal components of the photostationary steady state, NO_x and O_3 . Striped boxes represent reservoir species, and the hatched box a species frequently lost from the system. Dashed lines represent photolysis paths.

Nitric acid is mainly removed from the atmosphere by heterogeneous processes⁷, so this step frequently leads to the irreversible loss of reactive nitrogen⁸ from the troposphere.

If it remains in the atmosphere long enough, nitric acid can be recycled to NO_x by photolysis, or can be oxidised by OH to produce the nitrate radical (NO_3). NO_3 is

⁷Heterogeneous reactions are those which involve more than one phase of matter. In the atmosphere this generally involves reactions between gas phase components with those on liquid or solid surfaces, and include reactions on aerosol particles, water droplets, and surfaces on the ground, including plants, etc.

⁸Reactive nitrogen includes those nitrogen species which are involved in the chemical photochemical cycles, NO_x and all their oxidation products. These include HNO_3 , HONO , NO_3 , N_2O_5 , HNO_4 , RONO_2 and RO_2NO_2 , etc. [Seinfeld and Pandis, 1998, p. 71].

rapidly photolysed to regenerate NO_2 and O_3 , so that this also results in the regeneration of NO_x . Although these processes lead to a slow regeneration of NO_2 during the daytime, they are sufficiently slow that the major sink for HNO_3 is deposition [c.f. *Jacob, 2000*].

The oxidative agent involved in converting NO_2 to HNO_3 and in many other oxidation steps is the hydroxyl radical, OH. OH is the most important oxidant of atmospheric constituents, which makes it crucial for the self cleansing process of the atmosphere. It is primarily produced as a result of the photolysis of ozone and the subsequent reaction of the resulting excited oxygen atom, $\text{O}(^1\text{D})$, with atmospheric water vapour.

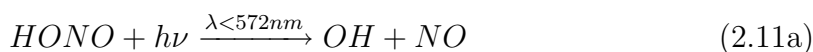


Reaction (2.9) competes with the production of OH in Reaction (2.8) and leads to ozone being regenerated via Reaction (2.2). This results in a null cycle, as ozone is neither created nor destroyed in the cycle.

OH can also oxidise NO, and this leads to the temporary removal of NO and the production of the reservoir gas nitrous acid (HONO):



HONO is of little importance for ozone chemistry as it is rapidly photolysed by near UV radiation during the daytime:



It typically has a lifetime of less than 1 hour in the boundary layer, so that it is generally unable to accumulate during the day. However there may be heterogeneous sources which lead to its accumulation at night [*Jenkin and Clmitshaw, 2000; Jacob, 2000*], despite low OH and NO concentrations. This can provide an additional source of OH radicals shortly after sunrise, but before O_3 photolysis becomes important, as HONO is photolysed at longer wavelengths than O_3 .

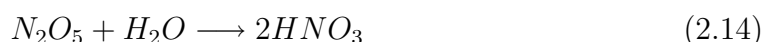
2.1.3 Night-time chemistry

At night, the OH radical is essentially absent, due to the absence of photolytic processes. Its role as the most important oxidant is taken by the NO_3 radical, which plays a significant role in removing NO_x from the clean atmosphere. It is produced

by the reaction of O_3 and NO_2 and typically reacts further in an equilibrium reaction with NO_2 to form dinitrogen pentoxide (N_2O_5):

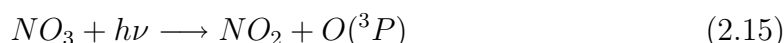


As this is an equilibrium reaction, it need not lead to long term removal of NO_x from the system. However, N_2O_5 can react to form nitric acid in the presence of water, which generally leads to removal of NO_x from the system (see section 2.1.2):



Although this occurs very slowly in the gas phase, it is probably a major loss process on water droplets and on particles [*Jenkin and Clemmitshaw, 2000*].

NO_3 is rapidly destroyed photolytically after sunrise and is not present in significant concentrations:



Following regeneration of ozone via Reaction (2.2), the equilibrium reaction (2.13) is forced towards the reactants on the left hand side, resulting in a nearly complete restoration of original precursor levels.

The nitrate radical also undergoes a rapid reaction with NO , which also regenerates NO_2 .



Thus, the nitrate radical is only active when NO concentrations are very low. This is generally true at night, due to the titration of NO by ozone. An exception is found in the immediate vicinity of NO sources.

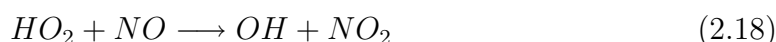
With the exception of some HNO_3 production, the only effect of NO_3 radical chemistry in the clean atmosphere is the reduction of night-time NO_x concentrations. Thus, it has little effect on O_3 formation. However, it is of greater importance in the polluted atmosphere, and will be encountered further in Chapter 3.

2.1.4 Hydroperoxy radicals

Ozone also reacts with OH , resulting in the formation of the hydroperoxy radical, HO_2 :



Ozone and OH are regenerated by the reaction of HO_2 with NO to produce NO_2 , and hence ozone via Reactions (2.1) and (2.2).



Thus, the reaction with NO results in a null cycle. The reaction of HO_2 with ozone, however, does lead to a net reduction in the amount of oxidants in the atmosphere.

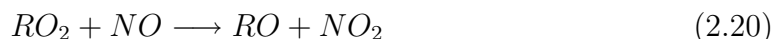
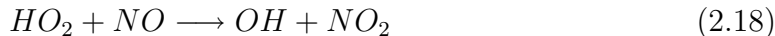


The production of hydroperoxy radicals (HO_2) opens the door to a whole new spectrum of photochemistry. This will be discussed in more detail in the following section, which deals with the effect of atmospheric organic compounds on ozone production.

2.2 Ozone production in the presence of organic compounds

In the real atmosphere, the presence of volatile organic compounds (VOC) shifts the equilibrium between NO_x and O_3 , which was discussed above, towards higher NO_2 concentrations. This occurs due to a further pathway for the conversion of NO to NO_2 which becomes available in the presence of peroxy radicals, which are intermediate oxidation products of the VOCs. This additional pathway leads directly to an increase in the rate of ozone production. The additional chemistry leading to ozone production which occurs in the presence of organic compounds is shown schematically in Figure 2.2. The elements present in the clean atmosphere are lighter in colour, while those elements which are added in the polluted atmosphere are added in black on the right of the diagram.

The ozone production rate increases as a result of the aforementioned reaction of NO with the hydroperoxy radical (HO_2) or with organic peroxy radicals:



This results in the production of NO_2 without ozone being destroyed. Reaction (2.20) represents the reaction for a generalised organic peroxy radical, RO_2 , where R is an organic rest⁹. The reaction also results in the production of an organic oxy radical, RO , which undergoes further reactions to produce other radical species. Some of these are also involved in O_3 production.

The organic peroxy radicals are products of the atmospheric oxidation of VOCs. This oxidation process is frequently initiated by the OH radical, which is partially recycled in subsequent reactions (e.g., Reaction (2.18)) and during further oxidation of the organic radical products. Ozonolysis of alkenes and oxidation by the nitrate radical also play a role in the production of peroxy radicals, which will be discussed in Chapter 3.

Under such conditions, Equation 2.4 for the simple equilibrium between O_3 and NO_x is no longer valid, as NO_2 is produced without the simultaneous destruction of O_3 . The effect of peroxy radicals and other factors disturb this equilibrium, so that the concentration of O_3 is best defined as the integral of all factors causing a change in the ozone concentration:

$$[\text{O}_3] = \int_0^t \frac{d[\text{O}_3]}{dt} dt \quad (2.21)$$

⁹R is used in the current work to refer to a general organic rest (or in some cases, to a hydrogen atom). Different organic structures are differentiated when necessary by R' , R'' , etc.

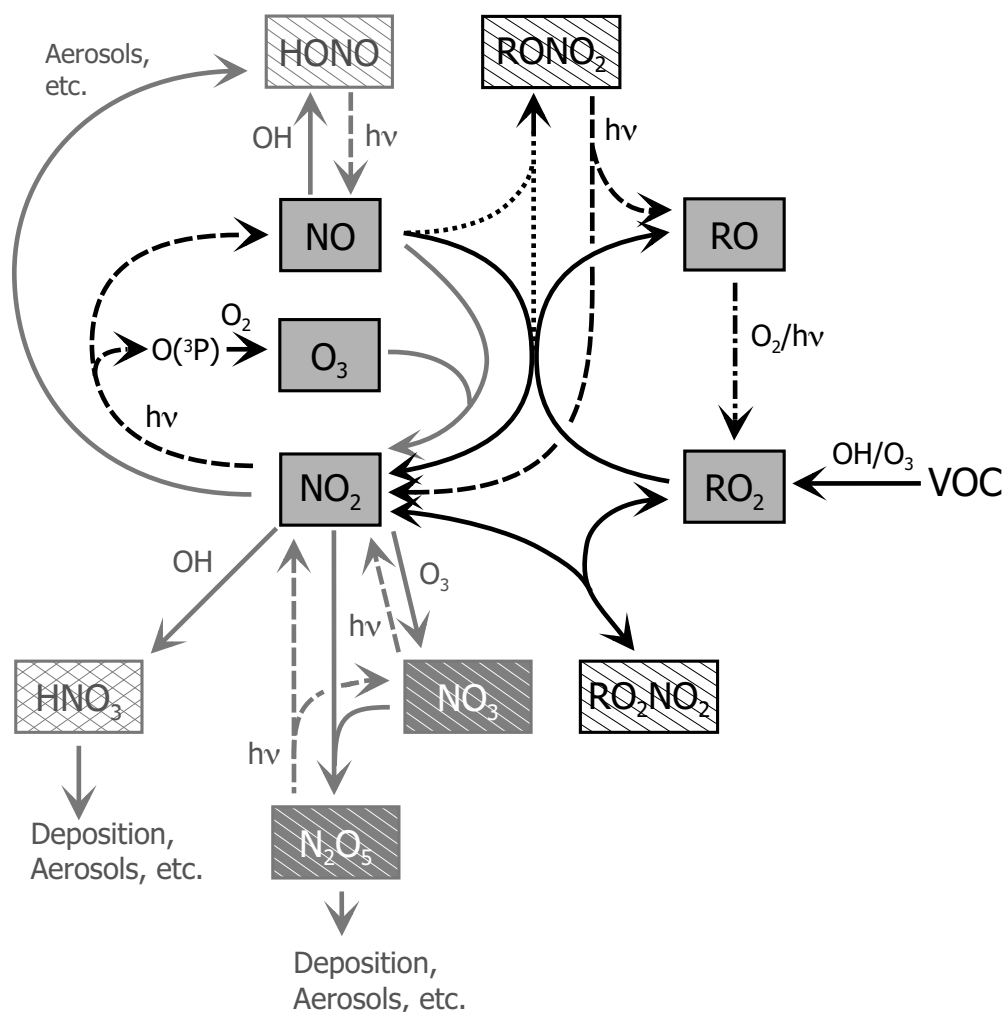


Figure 2.2: Simplified schematic representation of the impact of organic compounds on ozone production in the real troposphere. Reactions present in an idealised atmosphere are lighter in colour (c.f. Figure 2.1). The dotted line in the upper half of the diagram indicates an alternative path for the reaction of RO₂ and NO. The dashed/dotted line leading from RO to RO₂ represents a family of reactions (see Chapter 3 for details). R represents either H or an organic rest. For further details of the schematic representation, see Figure 2.1.

Such factors include photochemical production, as well as loss processes and transport. The contribution of the loss processes and transport will be discussed further in Chapter 4. The contribution of photochemical production through peroxy radicals (denoted by the subscript pc) to the net rate of change of the O₃ concentration is defined approximately by the rate of the reaction between NO and the peroxy radicals:

$$\left(\frac{d[O_3]}{dt}\right)_{pc} = [NO](k_{2.18}[HO_2] + \sum_i k_i[RO_2]_i) \quad (2.22)$$

where $[RO_2]_i$ is the concentration of each individual peroxy radical and k_i is the relevant reaction rate.

Under typical tropospheric conditions, HO_2 and the simplest organic peroxy radical (CH_3O_2) are probably the most common peroxy radicals present. However, the mix of organic radicals is potentially very complex, particularly when the radicals result from the oxidation of biogenic compounds, such as isoprene and mono-terpenes. Current measurement techniques, which will be discussed in Chapter 6, do not allow the organic species to be differentiated so that the concentration of most of the radicals individually is unknown.

Although many different peroxy radicals are involved in ozone production, for many peroxy radicals the reaction coefficient k_i can be approximated by the reaction coefficient for HO_2 , $k_{HO_2} \approx 8 \times 10^{-12} \text{ cm}^3 \text{ molecule}^{-1} \text{ s}^{-1}$, as the reaction rates for a variety of peroxy radicals lie relatively close together ($4 - 20 \times 10^{-12} \text{ cm}^3 \text{ molecule}^{-1} \text{ s}^{-1}$ [*Lightfoot et al.*, 1992]). The error introduced by this approximation depends on the structure of the organic peroxy radical¹⁰. This simplification allows the peroxy radicals to be treated as a group. The ozone production rate is then approximated by:

$$\frac{d[O_3]}{dt} \approx k^*[NO][RO_2]_{total} \quad (2.23)$$

where $k^* = k_{HO_2} \approx 8 \times 10^{-12} \text{ cm}^3 \text{ molecule}^{-1} \text{ s}^{-1}$ and $[RO_2]_{tot}$ is the total concentration of all peroxy radical species. Measurements of the total concentration of peroxy radicals and of NO thus allow the ozone production rate to be estimated.

2.2.1 Reactions competing with ozone production

Analogous to the situation in the clean atmosphere, which was discussed in Section 2.1.1, reactions between the various species involved in photochemical oxidation can interfere with ozone production, resulting in a net reduction of the ozone production rate. In addition to the reactions already discussed, the most important reactions which affect the ozone production rate are those which affect the concentration and distribution of the peroxy radicals. The most important of these reactions involving peroxy radicals are those with

- NO,
- NO_2 ,
- OH (relevant for HO_2), and
- reactions with other peroxy radicals.

These reactions will be considered in more detail in the following chapter.

¹⁰While the error is relatively small for $R = CH_3$ ($\sim 10\%$), it can be much higher when R represents a large chain or a non-alkyl chain, e.g., for $CH_3C(O)O_2$, $k = (20 \pm 3) \times 10^{-12} \text{ cm}^3 \text{ molecule}^{-1} \text{ s}^{-1}$, for $t\text{-C}_4\text{H}_9\text{O}_2$, $k = (4.0 \pm 1.1) \times 10^{-12} \text{ cm}^3 \text{ molecule}^{-1} \text{ s}^{-1}$ [*Lightfoot et al.*, 1992].

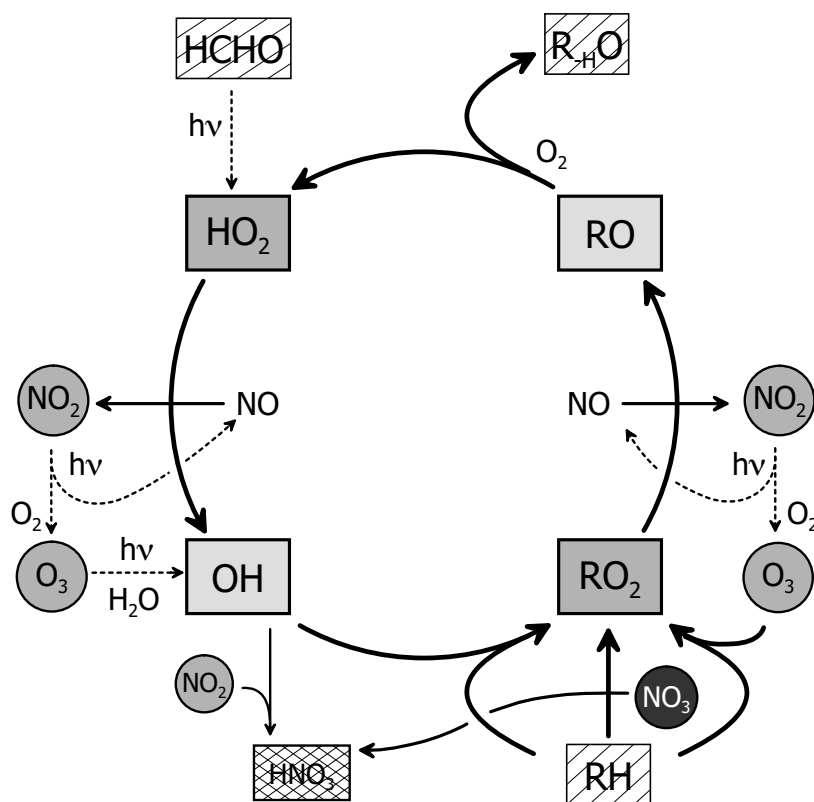


Figure 2.3: Simplified schematic representation of the oxidation cycle leading to ozone production. Shaded boxes denote the principal components of the catalytic cycle; circles denote the principal oxidised components produced as a result of the cycle; striped boxes represent organic precursors; the hatched box is an important sink; dotted lines represent photolysis.

2.2.2 Overall influence of peroxy radicals on ozone production

The overall role played by peroxy radicals in ozone production can be understood in terms of a catalytic cycle leading to oxidation of VOCs and the production of ozone as a byproduct. Figure 2.3 illustrates the role played by HO_2 and RO_2 (the shaded boxes) in this cycle. The fuel for the cycle is provided by organic compounds, which are represented by striped boxes. The HO_x radicals (OH and HO_2) play the role of the catalyst which drives the oxidation process and are recycled during the cycle. Each completed cycle results in the oxidation of one VOC molecule and in the conversion of NO to NO_2 , which is the immediate precursor to O_3 .

The presence of this cycle results in a non linear relationship between ozone and other photochemical oxidants. An example of this is the reaction of HO_2 with NO_x and ozone. While at higher NO levels the presence of HO_2 leads to ozone formation by Reactions (2.18), (2.1) and (2.2), at low levels of NO the reaction of RO_x with

ozone can lead to ozone destruction via Reaction (2.19).

Thus, competition between the reaction of HO_2 with NO and its reaction with ozone determines whether the presence of RO_x leads to ozone production or destruction. However, model calculations indicate that for an ozone level of 30 ppbv, NO concentrations of as low as 7 pptv are all that are required for production to balance destruction [Jenkin and Clemitshaw, 2000]. At higher concentrations of NO , VOC oxidation leads to net ozone production. As a result, photochemical ozone production can be expected to outweigh photochemical removal for most continental areas during daytime.

2.3 Conclusions

Peroxy radicals play a major role in the photochemical production of ozone and shift the equilibrium which would be expected in clean air conditions between ozone and NO_x towards higher concentrations of oxidised species. Thus, they make an important contribution to the high concentrations of ozone and other photochemical oxidants experienced in Central Europe under the appropriate meteorological conditions. This makes it essential that the oxidation processes involving peroxy radicals be further understood and that our current understanding be tested by field measurements, particularly in the context of ozone studies.

The following chapter provides a summary of peroxy radical chemistry. Peroxy radical production via VOC oxidation, their chemistry and sinks are summarised, with a special emphasis on the chemistry most relevant to measurements using the chemical amplifier technique.

Chapter 3

Peroxy radicals in the atmosphere

Peroxy radicals are free radicals produced as intermediates during the oxidation of organic compounds or as part of radical propagation reactions. They are relatively reactive, although less reactive than some other free radicals, e.g., OH, and take part in a number of important oxidation and radical-radical reactions in the troposphere. Their reactivity makes them relatively short lived in the atmosphere and their concentration is quite sensitive to levels of other trace gases and of radiation. As with most other highly reactive compounds, a balance is rapidly attained between the total production, loss and interconversion of free radicals so that the individual species exist in near steady state concentrations.

As a result of the important role played by peroxy radicals in the atmosphere, peroxy radical chemistry has been the subject of considerable study in recent years and has been reviewed in a number of papers [*Lightfoot et al.*, 1992; *Wallington et al.*, 1992; *Lesclaux*, 1997; *Wallington et al.*, 1997; *Tyndall et al.*, 2001]. The most important features of this radical chemistry are represented in schematic form in Figure 3.1, which shows the sources and sinks and interactions of the RO_x and HO_x radicals. The complexity of such interactions quickly becomes apparent when it is remembered that ‘R’ represents an entire class of organic rests. The current chapter discusses peroxy radical production and those aspects of their chemistry which apply to tropospheric processes and to their detection in the chemical amplifier (CA).

3.1 Production of peroxy radicals: Photooxidation of volatile organic compounds

Organic peroxy radicals originate as intermediates produced during the oxidation of VOCs and subsequent reactions. VOCs are released into the atmosphere from a large number of sources, both biogenic and anthropogenic, and as a result they embrace a wide range of organic species with a correspondingly wide range of chemical properties. The chain of reactions involved in VOC oxidation can be quite complex and depends on the structure of the initial VOC. As a result, the oxidation of more

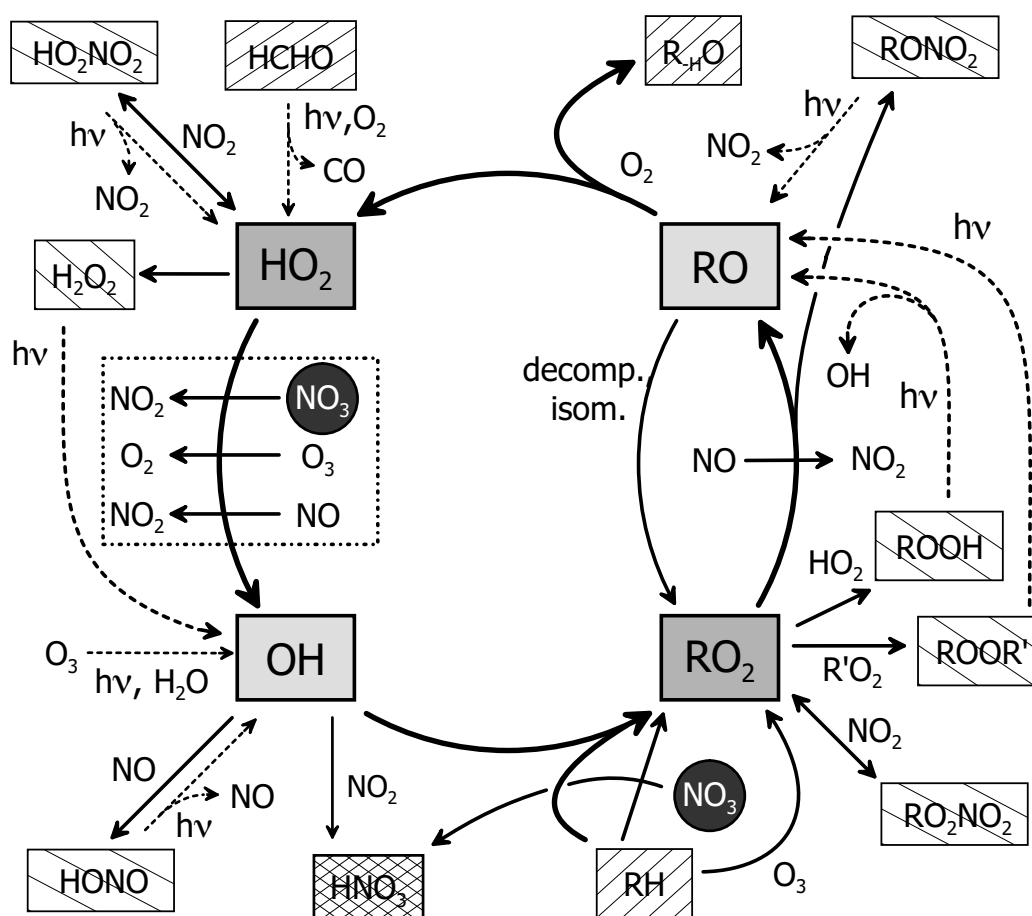


Figure 3.1: Simplified schematic representation of the tropospheric chemistry involving peroxy radicals. Shaded boxes represent the principal components of the RO_x/HO_x family; boxes with diagonal lines represent organic precursors and reservoir species; and dotted lines represent photolysis. The dotted box enclosing three reactions leading from HO_2 to OH indicates a family of competing reactions.

complex VOCs can result in a variety of peroxy radicals occurring at different stages during the process. The oxidation chemistry of a large number of VOCs has been reviewed in considerable detail in articles by *Atkinson* [1990, 1997b, 1998, 2000] and *Atkinson et al.* [1999]. Ultimately, they are oxidised to the end products CO_2 and H_2O .

The oxidation process can be initiated in several different ways:

- reaction with the hydroxyl radical, OH ,
- ozone, or
- the nitrate radical, NO_3 , or by
- photolysis of carbonyl compounds.

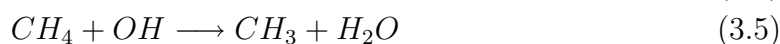
The relative importance of these different initiation steps depends on the VOC involved. In general, the reaction of VOCs with OH is the main daytime source of atmospheric peroxy radicals. However, ozone and the nitrate radical react quickly with certain classes of VOCs and can be the source of significant radical concentrations, particularly at night or during winter when the concentration of the hydroxyl radical is relatively low. The photolysis of carbonyl compounds is a further albeit minor source of peroxy radicals during daytime.

3.1.1 Oxidation of VOCs via the OH radical

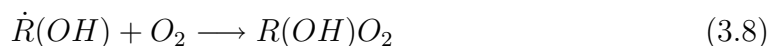
The OH radical reacts with many atmospheric organic compounds to produce HO₂ and RO₂, or with CO to produce HO₂. The initial oxidation reaction proceeds for alkanes and many other classes of compounds by means of hydrogen extraction:



In the background atmosphere, CO and CH₄ are the most important reaction partners for OH [*Lightfoot et al.*, 1992]. Other VOCs become more important closer to source regions, but generally react more quickly with OH. As a result the concentrations of these other VOCs are mostly much lower in the background troposphere than those of CO and CH₄. The oxidation of CO and CH₄ by OH results in the production of HO₂ and the methyl peroxy radical (CH₃O₂):



In contrast to this mechanism involving single bonds, for alkenes and alkynes the mechanism appears to involve an addition reaction. For alkenes this leads to various isomeric hydroxy substituted radicals¹, and ultimately to hydroxy substituted peroxy radicals, e.g. for an arbitrary R:



The reaction with alkynes results in a number of different products, including peroxy radicals. Isomerisation reactions rapidly lead to complicated reaction schemes for

¹The dot above one of the C atoms in some of the following reactions indicates the location of the unpaired electron. Although in many chemistry texts the convention is to denote all free radicals by such a dot, it is only used here when it is necessary for clarity, or to distinguish between alternatives.

VOCs with multiple bonds. Significant numbers of radicals, including peroxy radicals, are produced from the oxidation of even the simplest alkyne.

Reaction rates with OH vary considerably for different VOCs, which, together with the large variation in atmospheric concentrations, results in a wide range of atmospheric lifetimes. The atmospheric lifetimes with respect to OH are relatively long under normal conditions for alkanes, benzene and toluene, whereas for alkenes and other substituted compounds the lifetimes can be of the order of a few hours or less [Atkinson, 2000; Jenkin and Clemitshaw, 2000]. Nevertheless, even long lived species, such as methane, can make a major contribution via this pathway if they are present in high concentrations.

3.1.2 Ozonolysis of VOCs

Ozone can also initiate the oxidation of organic compounds containing a double bond (alkenes, dienes and monoterpenes) via addition across the double bond. For some species, this reaction proceeds faster than the reaction with OH. The resulting ozonide is highly energetic, and the products of its breakdown frequently include further radicals. Thus the initial loss of an ozone molecule may be at least partially compensated by further breakdown products. The initial ozonide decomposes rapidly via one of two channels to form a Criegee biradical with excess energy (denoted by \ddagger), e.g., for 2-methyl-2-butene:



The energy rich Criegee biradicals are then either collisionally stabilised, or they decompose. The products of this process include carboxylic acids, hydrogen peroxide (H_2O_2) and organic hydroperoxides (ROOH), but also peroxy radicals and other radicals, particularly if they undergo decomposition.

As a result, ozonolysis can lead directly or indirectly (e.g., via the photolysis of H_2O_2) to radical production. This can be substantial, depending on the ambient conditions and the initial VOC involved. Hence, ozonolysis can result eventually in regeneration of ozone or in net ozone production.

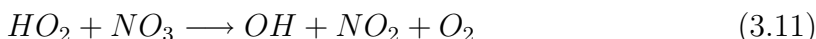
3.1.3 Night-time RO_2 production via the nitrate radical

The nitrate radical, which is produced by the reaction of ozone with NO_2 (see page 19), also oxidises some organic compounds. Although the rate of this reaction is slow for alkanes and primary alkenes, it is much faster for other alkenes and for sulphur containing compounds. As a result, the chemical lifetime of some compounds with respect to NO_3 is similar to their lifetime with OH [Jenkin and Clemitshaw, 2000]. This means that NO_3 oxidation plays an important role in the oxidation of some compounds, as well as being the most important alternative to OH oxidation at night.

As was the case for OH, the reaction proceeds for most organic compounds by H abstraction, and results in the production of an organic peroxy radical:



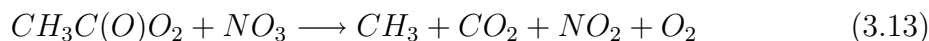
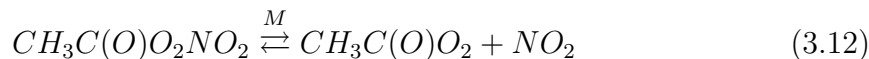
For alkenes the reaction proceeds by means of an addition reaction and initiates a complex series of reactions resulting in the production of either the oxirane and NO_2 , or of nitro-oxy substituted peroxy radicals. Further reactions involving nitro-oxy peroxy radicals lead to the production of HO_2 and a variety of nitro-oxy substituted species. This HO_2 can react with NO_3 to provide a night-time source of OH radicals:



This can lead to further VOC oxidation and to peroxy radical production at night via OH oxidation.

While the removal of potential fuel for ozone production during night-time chemistry ultimately leads to a reduction of ozone levels, night-time oxidation of VOC and NO_x does result in the formation of a number of secondary photochemical oxidants. These can promote ozone production as soon as UV radiation is present. It can also result in the presence of peroxy radicals at night and in the winter months, when photolysis is not particularly active.

Peroxy radicals have been detected at night during a number of measurement campaigns [e.g., *Behmann et al.*, 1994; *Mihelcic et al.*, 1993; *Monks et al.*, 2000], including the current work (see Part III). A correlation between NO_3 and RO_x has been observed at night during some studies, with an increase in observed RO_x concentrations during the night hours [e.g., *Carslaw et al.*, 1997]. This suggests that the nitrate radical may play a significant role in producing RO_x radicals both by VOC oxidation and via its involvement in radical propagation reactions [*Jenkin and Clemitshaw*, 2000]. One example is the reaction of NO_3 with peroxy acyl radicals, which disturbs the equilibrium leading to the formation peroxy acyl nitrates and could result in the conversion of organic nitrates, e.g. PAN, to peroxy radicals:



The oxidation of some VOCs by both NO_3 and ozone proceeds sufficiently fast that it can result in measurable concentrations of RO_x at night. Although these pathways are not nearly as important as the daytime processes for most compounds, they are nevertheless significant for some VOCs and at least partially explain the nighttime RO_x concentrations observed by many groups.

3.1.4 Photolysis of carbonyl compounds

A further source of peroxy radicals is the photolysis of aldehydes and ketones. The photolysis of formaldehyde (HCHO) in particular can be a significant source of peroxy radicals at concentrations observed in both rural and urban settings [*Jenkin and Clmitshaw*, 2000], potentially outweighing the production via OH radicals under some conditions:



The H and R radicals then form peroxy radicals via Reactions (3.4) and (3.2). This can be a significant initiator of summer pollution, especially during conditions in which the initial concentration of ozone (and hence OH) is low.

Similarly, the photolysis of nitrous acid (HONO) can lead to OH production during the early morning, following overnight accumulation of HONO.



This could lead to an early morning pulse of radical formation before the photolysis of ozone and aldehydes becomes significant. Evidence for such a pulse was observed during the current study and will be discussed in Section 9.1.1.

3.2 Reactions involving peroxy radicals

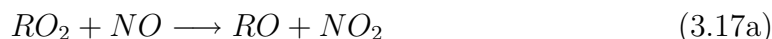
As discussed in Chapter 2, reactions involving peroxy radicals alter the concentration and distribution of the radical species, thus affecting the ozone production rate. The most important of these reactions are those with

- NO,
- NO₂,
- O₃ (see subsection 2.1.4),
- OH (relevant for HO₂), and
- other peroxy radicals.

The reaction with NO is of particular importance for the current study, as it is the critical step in peroxy radical mediated ozone production and is also crucial to the operation of the chemical amplifier (CA). Organic oxy radicals, which are potential products of this reaction, are also involved in both the CA and the cyclic production of ozone. This proceeds via their conversion to HO₂, which will also be discussed in this chapter.

3.2.1 Reaction with NO

As discussed in Section 2.2, peroxy radicals react with NO to produce primarily an organic oxy radical and NO₂ (Reaction (2.20)):



Competing with this reaction is an alternative reaction channel, leading to the production of organic nitrates (RONO₂).



This alternative branch is of importance for ozone production, as it temporarily removes peroxy radicals from the system, and also for the CA, as it reduces its sensitivity to some peroxy radicals. This branch is insignificant for short chain organic radicals ($C < 4$), but becomes increasingly important for radicals with longer chain lengths. For example, approximately 35% of secondary C₈H₁₇O₂ isomers react via pathway (3.17b) under boundary layer conditions [Lightfoot *et al.*, 1992]. Kinetics data suggest that the proportion of primary and tertiary radicals reacting via pathway (3.17a) is lower than that of secondary radicals by a factor of 2.5 or 3.3, respectively, [Atkinson, 1997b], however this is still not certain for tertiary radicals [Jenkin and Clemmitshaw, 2000]. The presence of other functional groups also has an effect on the branching ratio. For example, oxygenated functional groups may result in less efficient organic nitrate formation than for simple alkyl organic nitrates [Lightfoot *et al.*, 1992].

Alkyl nitrates are relatively stable and have been measured in the atmosphere during a number of campaigns [e.g., Shepson *et al.*, 1992; O'Brien *et al.*, 1997; Biesenthal *et al.*, 1997; Roberts *et al.*, 1998]. They generally undergo photolysis or reaction with OH, thereby releasing radicals to take part in photochemical processes. However, due to their low concentrations they are probably not a significant source of photochemical oxidants [Shepson *et al.*, 1992].

The presence of the second reaction pathway with NO has consequences for the CA used in this study, as it relies on the production of NO₂ during this reaction to measure the concentration of peroxy radicals. This will be discussed further in Chapter 6.

The organic oxy radicals produced in Reaction (3.17a) react further to produce other radical products. Under tropospheric conditions, this proceeds via

- reactions with molecular O₂,
- decomposition, and
- isomerisation [Atkinson, 1997b].

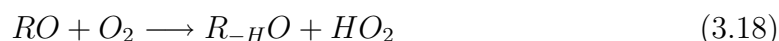
At extremely high NO_x concentrations a fourth pathway can become important, namely,

- reaction with NO_2 .

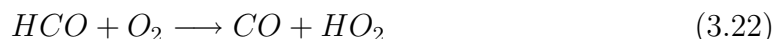
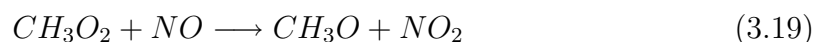
The recycling of organic oxy radicals plays a crucial role in the operation of the chemical amplifier technique, as the chain reaction which amplifies the otherwise very small signal due to peroxy radicals relies on the conversion of organic oxy radicals to HO_2 (see Chapter 6). Indeed, the efficiency of the conversion of organic oxy radicals to HO_2 determines the detection efficiency of the CA for some organic peroxy radicals.

Reaction of organic oxy radicals with O_2

The reaction with O_2 occurs preferentially for smaller radicals and involves an H-extraction reaction to produce HO_2 and an aldehyde or ketone, R_{-H}O :



It is this production of the HO_2 radical which enables the CA to detect organic peroxy radicals. In the atmosphere, the resulting aldehyde/ketone typically reacts further to produce additional radical products, so that the oxidation chain for higher organic molecules can generate a large number of free radical products. In the case of the methyl peroxy radical, the chain proceeds as follows:



The H radical produced in Reaction (3.21) subsequently reacts with molecular oxygen to form HO_2 according to Reaction (3.4). The final product of the oxidation chain is typically CO, which reacts with OH to produce HO_2 (Reactions (3.3) and (3.4)). Thus, the number of radicals resulting from VOC oxidation and which contribute to ozone production can be significant.

Conversion to HO_2 cannot occur via this pathway for tertiary peroxy radicals, which do not have an H next to the central C atom available for extraction. Consequently, the only options for such organic oxy radicals under normal conditions are decomposition or isomerisation. This is particularly significant for indirect measurement techniques such as the chemical amplifier, which rely on the conversion of the organic oxy radical to a chain propagating species such as HO_2 . In such cases, the tertiary radicals will not be detected qualitatively unless the products of other reaction pathways propagate the reaction.

Oxy radical decomposition

For larger radicals, the decomposition of the organic oxy radical becomes more important and typically results in the production of an alkyl radical and a carbonyl

compound. This results in the generation of further peroxy radicals from the alkyl radical products via Reaction (3.2), so that the radical propagation reactions can be set forth. As mentioned above, the carbonyl products can also be oxidised further or photolysed to produce further radical products.

Oxy radical isomerisation

Isomerisation becomes important for organic oxy radicals with a longer organic chain and appears to occur via a cyclic transition state, resulting in H-extraction from a $-\text{CH}_2-$ or $-\text{CH}_3$ group [Atkinson, 1997b]. This results in a hydroxy alkyl radical which can react with O_2 to produce the hydroxy alkyl peroxy radical. This is then able to react further with NO as discussed above. Thus, the isomerisation reaction typically allows the propagation of the radical reaction, although this may take place more slowly than by direct reaction with O_2 .

Reactions of oxy radicals with NO_x

Although oxy radicals can react with NO_x under atmospheric conditions, due to the slow rate of this reaction relative to the reaction with O_2 it is normally only important for tertiary radicals, for which the decomposition reaction is the other main path [Atkinson, 1997b]. The reaction can proceed via either an addition or an H-extraction pathway, although the extraction pathway is relatively minor:



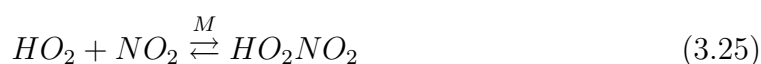
These reactions become important at high NO_x concentrations for some tertiary peroxy radicals, e.g., at 100 ppbv for the tertiary butoxy radical [Atkinson, 1997b], for which reaction with O_2 is impossible. This may occur in the CA intake, where NO_x concentrations are artificially high. In the atmosphere, the reaction products could subsequently regenerate radicals via photolysis, for example, but under the conditions in the CA intake, this pathway would generally mean that tertiary radicals took no further part in the amplification reaction.

The organic oxy products of the reaction between peroxy radicals and NO typically undergo further reactions to produce further free radicals. This may be a slow process, as in the case of the alkyl nitrates or tertiary oxy radicals, resulting in a reduction in the number of radicals available for the ozone cycle. Although in the atmosphere the radicals may eventually become involved in photochemical cycles, some of these reaction steps are so slow that more complex peroxy radicals may not be quantitatively involved in the chain reaction used in the CA, which relies on the

conversion of RO_x to NO_2 to measure the total peroxy radical concentration. Along with the alternative pathway leading to the production of alkyl nitrates, this places a limit on the degree to which a given peroxy radical is detected in the chemical amplifier.

3.2.2 Reaction with NO_2

The reaction of peroxy radicals with NO_2 results in the formation of organic peroxy nitrates (RO_2NO_2) and peroxy nitric acid (PNA, HO_2NO_2):



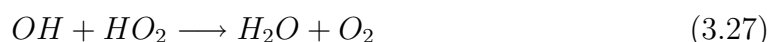
The reaction of NO_2 with peroxy radicals is only an order of magnitude slower than NO_2 photolysis, so that formation of peroxy nitrates can be significant. The rate of the reverse reaction, which regenerates RO_2 , is temperature dependent and varies greatly among the various peroxy nitrates [Atkinson *et al.*, 1999]. Some of these species have lifetimes on the order of hours to months at atmospheric temperatures. Those with simple organic groups and PNA are unstable, and have very short lifetimes, e.g., less than 1 s for $CH_3O_2NO_2$ or 30 s for PNA. In contrast, species with an electron withdrawing functional group, such as a carbonyl group, have much longer lifetimes. Long-lived peroxy nitrates and peroxy acyl nitrates (in the case of a carbonyl group) can act as significant reservoirs of NO_x and can allow the transport of NO_x to other regions. Peroxy acetyl nitrate (PAN), $CH_3C(O)O_2NO_2$, is the most important member of the family, and has mixing ratios of several ppbv during summer (c.f. Chapter 9):



PAN has a lifetime of ~ 30 minutes at $25^\circ C$, so that it decomposes quite rapidly during summer. Its lifetime at lower temperatures is much lower, allowing it to transport both NO_2 and peroxy radicals over long distances. Measurements of PAN in the Arctic have shown the presence of quite high concentrations in winter, potentially leading to spring time ozone production as temperatures rise [Beine *et al.*, 1997]. Peroxy propionyl nitrate (PPN) has also been detected in significant concentrations.

3.2.3 Reaction with OH

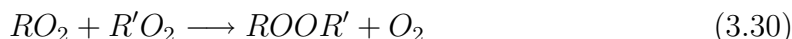
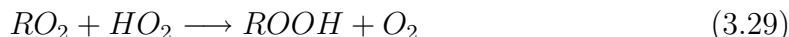
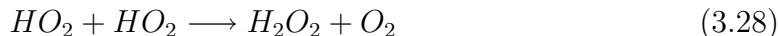
The reaction of HO_2 with OH leads to a net loss of radicals from the system:



The tropospheric concentration of OH is typically a factor 100 lower than that of HO_2 . Consequently, radical loss via this reaction is much less significant than the competing loss due to the self-reaction of HO_2 to form hydrogen peroxide.

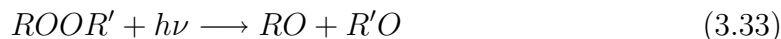
3.2.4 Reactions between peroxy radicals

When the concentration of NO_x is below about 40 pptv², the major sink for peroxy radicals is the reaction with HO_2 or with other peroxy radicals to produce peroxides:

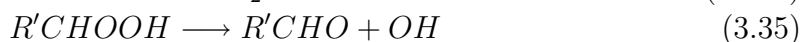
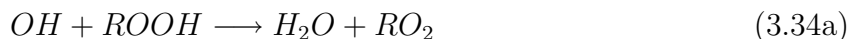


As HO_2 is frequently the most common single peroxy radical present, and the reaction rates for reactions involving HO_2 are significantly faster than those with other RO_2 species, Reactions (3.28) and (3.29) are the most likely to occur. This results in the formation of hydrogen peroxide (H_2O_2) and organic hydrogen peroxides (ROOH), rather than organic peroxides (ROOR').

The peroxides can undergo photolysis, leading to a regeneration of the hydroxyl radical [Atkinson, 1990; Gilge *et al.*, 1994] and/or an organic oxy radical:



They also react with OH , which can attack either end of the molecule. This means that the reaction can proceed via two alternative channels, both of which lead to the regeneration of radicals:



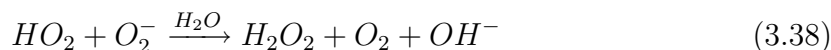
While the formation of the peroxide need not lead to a net removal of radicals from the system if it undergoes photolysis, it does lead to a local loss of free radicals. In contrast, subsequent reaction with OH reduces the total number of radicals available, as only one radical remains instead of the initial three. Peroxides can also be physically removed from the atmosphere via dry deposition, scavenging or washout, which obviously also results in the loss of radicals.

3.3 Non-chemical sinks for peroxy radicals

A further sink for peroxy radicals is the interaction with aerosol or the aqueous phase. The HO_2 radical is readily scavenged in cloud via acid-base dissociation, followed by

²The NO_x concentration at which peroxy-peroxy radical reactions begin to dominate depends on the rate coefficients for the relevant reactions and the local steady state concentration of HO_2 and other peroxy radicals.

production of H_2O_2 [*Jacob*, 2000]:



Organic RO_2 radicals are likely to be much less soluble in cloud, so that their concentration is probably affected much less by the presence of clouds, or may even be enhanced as a result of a decrease in the amount lost through reactions with HO_2 . However, the exact effect of clouds on RO_2 is still unclear. It has been speculated that net production of HO_x could take place via transition metal chemistry or organic chromophores, although *Jacob* [2000] considers this of little significance. Aqueous HO_2 has also been proposed as a catalyst for the destruction of ozone, but this is probably a very inefficient process [*Jacob*, 2000].

Model calculations indicate that HO_2 should be significantly depleted in cloud [*Jacob*, 2000]. Measurements made in cloud as part of the current work found that peroxy radical concentrations in cloud were below the detection limit, which was very high at the high relative humidities involved (see Chapter 9). This may be due to HO_2 going into solution in the aqueous phase, or it may reflect reduced production levels due to lower radiation intensities. However, the reduced sensitivity of the chemical amplifier at high relative humidities do not allow accurate measurements under such conditions (see Section 6.5). The ambient organic RO_2 concentration should not be affected much by the presence of water vapour as it has a much lower solubility than HO_2 . However, measurements of organic RO_2 using the CA also rely on reactions involving HO_2 (see Chapters 6 and 7), so that they too are affected by any sensitivity of HO_2 to liquid water.

3.4 Conclusion

Due to the large number of organic compounds present in the atmosphere, the web of chemical interactions involving peroxy radicals is huge and has only been touched on briefly in this study. For example, although the extended chemistry involving carbonyl groups and aromatic compounds has been the centre of considerable study, it has essentially been ignored here. Similarly, halogenated compounds and the associated peroxy radicals have been the subject of considerable investigation, not least because of their relevance to stratospheric processes. Fortunately, the chemistry of most classes of peroxy radicals exhibits sufficient similarities to allow them to be treated as a single class.

The importance of peroxy radicals for oxidation processes makes them an interesting candidate for further study. In particular, field measurements of peroxy radicals allow our understanding of atmospheric oxidation to be tested outside the laboratory. Measurement techniques for peroxy radicals will be discussed in more detail in Part II.

Chapter 4

Factors affecting the observed ozone concentration

Although the ozone production rate in the polluted atmosphere depends on the conversion of NO to NO₂ via peroxy radicals, the ozone concentration which is actually observed in the atmosphere depends on the balance between production, loss and transport processes. As was shown in Equation 2.21, the observed concentration is given by the integral of its rate of change due to all the various factors which affect the ozone concentration. The rate of change in the ozone concentration can be described by the following equation:

$$\frac{d[O_3]}{dt} = P_{O_3} - L([O_3]) + \tilde{\mathbf{v}} \cdot \nabla[O_3] \quad (4.1)$$

where P_{O_3} is the rate of ozone production, $L([O_3])$ is the loss rate of ozone, and $\tilde{\mathbf{v}} \cdot \nabla[O_3]$ is the rate of change in the ozone concentration due to transport processes. The first two terms contain contributions from gas phase reactions, along with contributions from heterogeneous processes and the loss of ozone due to dry deposition. Transport processes include vertical entrainment and horizontal dispersion.

Depending on the prevailing conditions, these three terms vary in their relative sizes, and it is the sum of these individual effects which determines the observed rate of change of the ozone concentration. Current measurements do not allow a complete understanding of all these factors simultaneously, and most studies seek to investigate one or more of the factors individually. The current study focuses on the photochemical production of ozone, which has already been discussed in Chapter 2. The photochemical production rate $P_{O_3,pc}$ can be calculated using Equation 2.22:

$$P_{O_3,pc} = \left(\frac{d[O_3]}{dt}\right)_{pc} = [NO](k_{2.18}[HO_2] + \sum_i k_i[RO_2]_i) \quad (2.22a)$$

The effect of the other terms in Equation 4.1 will be discussed in this chapter. Heterogeneous processes are considered separately, as they can lead to both production and loss of ozone.

4.1 Loss processes

Gas phase reactions leading to ozone destruction or a reduction in the production rate have been discussed in chapter 2, but physical processes, in particular dry deposition, also contribute to the loss of ozone from the troposphere.

Dry deposition is commonly quantified using the deposition velocity, v_d , to describe the speed with which a component is removed from the atmosphere. Measurements of deposition velocity rates for ozone lie in the range 0.002 - 2.0 cm s⁻¹ [Seinfeld, 1980]. The wide range of deposition velocities is due to the effect of a large number of factors. These factors are commonly parameterised by resistance terms, which describe those bulk factors of the atmosphere or surface which influence deposition [Seinfeld and Pandis, 1998; Wesely and Hicks, 2000]. These resistances are combined using equations which are analogous to the Kirchoff laws for electrical circuits. The reciprocal of the total resistance is equal to the deposition velocity. Each of these resistances can vary considerably, so that the calculation of dry deposition rates is quite complicated. The resulting deposition rates are highly dependent on ambient conditions and are subject to a large uncertainty [Wesely and Hicks, 2000]. Of particular importance for ozone deposition are the resistances due to stomata and soils.

Different types of vegetation can have very different deposition velocities, even for vegetation types that are grouped together in some parameterisation schemes. For example, the category containing agricultural crops covers such diverse crops as soya beans, maize, cotton and vineyards, even though the deposition velocities for these plant species differ considerably [Wesely and Hicks, 2000]. This is partially due to the large variation in leaf area and in the stomatal and cuticular resistances of various plants. Plants are affected significantly by the degree of stress they are under, so that the same plant can exhibit different properties depending on factors such as availability of water and sunlight, etc. Ozone enters the open stomata and is destroyed by rapid reactions with enzymes at inner surfaces. Stomata are typically open widest around the middle of the day, depending on the temperature and evaporation rate, and this results in a strong diurnal variation in v_d . This is consistent with measurements, which show that v_d has a maximum during the day and decreases towards night-time.

The effect of surface wetness on the deposition velocity can also vary over the whole range from mild inhibition to significant enhancement, further complicating the calculation of deposition velocity. Ozone has a low degree of solubility in water¹, so that increasing surface wetness reduces the deposition rate greatly. Similarly, the deposition rate to soils also varies significantly, depending on the degree of wetness of and the amount of organic matter present in the soils. Dry soils have much lower resistances than wetter soils [Wesely, 1983] and can make a major contribution to ozone deposition rates.

Vegetative canopies are generally quite effective at removing ozone, especially when senescent leaves are present. Deciduous forests generally have smaller stomatal

¹The Henry's law constant for ozone is $K_{298} = 1.1 \times 10^{-2}$ M atm⁻¹.

resistances than coniferous forests and hence exhibit higher deposition rates during summer. The effectiveness of ozone removal in canopies also depends on the atmospheric resistance, which determines the supply of ozone to the canopy region [Wesely, 1983; Wesely and Hicks, 2000]. The atmospheric resistance, which is a function of turbulent mixing, exhibits a pronounced diurnal variation and reaches its minimum value during the hours of maximum solar radiation. This coincides with the maximal stomatal opening and contributes to the observed maximum for v_d around midday. Model results for deciduous forest during midsummer show that typical values for the deposition velocity of ozone are in the range 0.1 - 0.8 cm s⁻¹ [Wesely, 1989] for incident radiation between 0 - 800 W m⁻², dry surfaces and moderate wind speeds.

4.2 Heterogeneous processes

In recent years it has been recognised that heterogeneous chemistry is an important process in the atmosphere and that it also influences tropospheric ozone. As a result, it has recently become the object of renewed interest and its effect on tropospheric ozone is the subject of a recent review article by Jacob [2000].

Heterogeneous processes can potentially act as both a source and a sink for ozone, although in most cases they are probably a sink. Both clouds and aerosols can take up free radicals, reservoir gases and precursors (e.g. HO₂, OH and H₂O₂), as well as affecting the amount of NO_x. It influences thereby the gas phase production of ozone. These processes may also play a direct role in the destruction of ozone, although this is still unproven [Jacob, 2000]. Ozone's low solubility means that it is not taken up significantly in cloud water. It could potentially undergo fast aqueous phase loss by reactions in the droplet, but this is probably of limited efficiency for a pH below 6 [Liang and Jacob, 1997]. This proceeds by reaction with the O₂⁻ ion, which results from the dissociation of aqueous HO₂ discussed in section 3.3, and which is recycled by oxidation of organic molecules [Arakaki and Faust, 1998]. The reaction with ozone competes with other HO₂ reactions in the aqueous phase and transition metal chemistry, so that it is probably quite inefficient.

There is some evidence for destruction of both O₃ and NO_x on soot, however this is likely to be insignificant in the atmosphere. More likely to be of significance is the reaction of ozone with unsaturated organic compounds in organic carbon aerosol, which may be a significant sink in the atmospheric boundary layer [Jacob, 2000]. Mineral dust may also be a significant local sink [Dentener *et al.*, 1996].

The presence of bromine and chlorine in activated form in the boundary layer may also lead to the catalytic destruction of ozone. These catalytic cycles are similar to those established for the stratosphere and may play a role in the marine boundary layer, for which a number of possible mechanisms have been proposed [Jacob, 2000]. This may also be important under certain circumstances, e.g. in the Dead Sea region, where high concentrations of bromine compounds have been detected [Luria, 1999; Hebestreit *et al.*, 1999], as well as in the Arctic, where sea salt Br⁻ may be accumulated

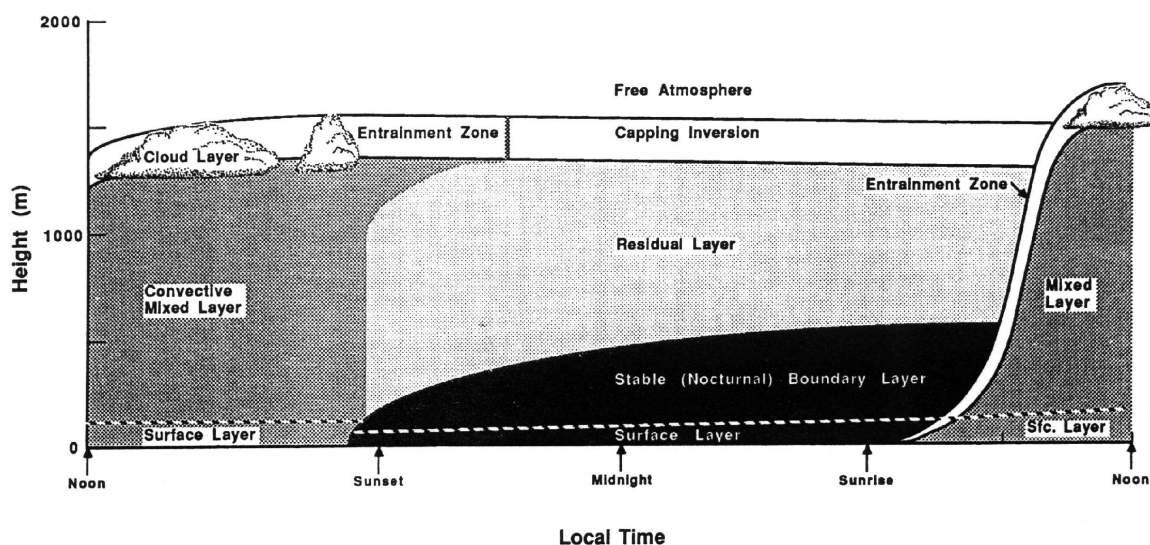


Figure 4.1: Schematic representation of the planetary boundary layer showing the various sub-layers during high pressure systems over land: a very turbulent mixed layer; a less turbulent residual layer and a nocturnal stable boundary layer of sporadic turbulence. Taken from *Stull* [1988].

on sea ice. At the concentrations normally found in the troposphere, they are unlikely to play any role in the continental boundary layer.

Although these heterogeneous processes appear to be significant in the troposphere, they are nevertheless difficult to quantify and will not be considered further in this study.

4.3 Transport processes

In a homogeneous, stationary atmosphere, the concentration of ozone would be solely defined by the balance between the production and loss of ozone. However, as neither of these conditions apply to the real atmosphere, it is necessary to consider the effect of transport processes on the ozone concentration field. These processes include both vertical entrainment of air from other levels, as well as the horizontal transport of air. Episodes of high ozone production are normally associated with stationary high pressure regions and stagnant air masses during summer, so that horizontal advection plays less of a role in determining ozone concentrations than at other times. Vertical transport, on the other hand, does play an important role in determining the shape of the diurnal profile, in combination with the daily cycle of photochemical activity.

Vertical transport of ozone is influenced by the vertical structure of the ozone distribution and of the troposphere as a whole, as well as by the dynamics of mixing processes. For high pressure systems over land, the troposphere can be considered to consist of three layers during daytime, with transition zones between them. The

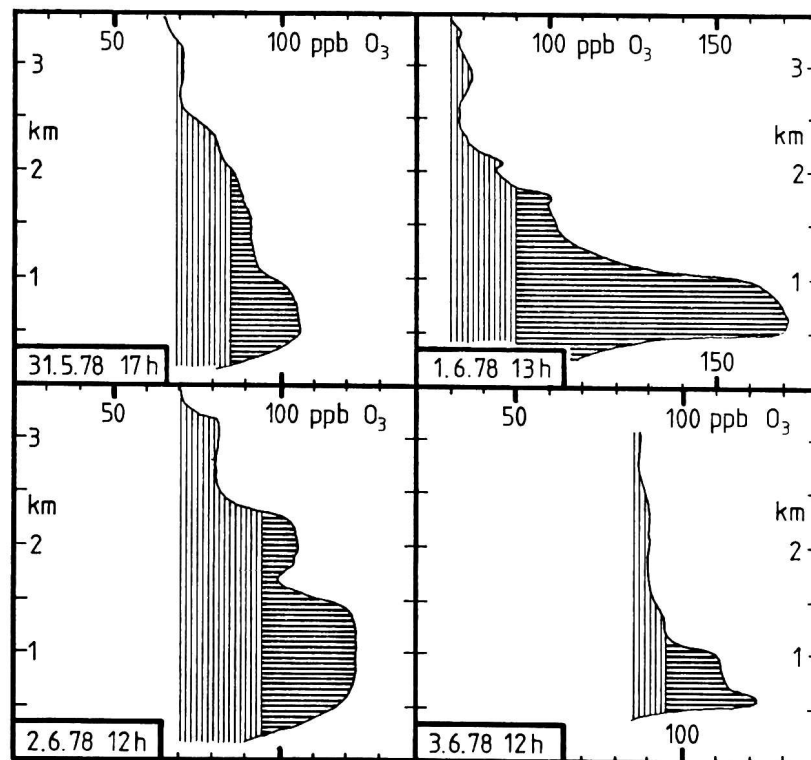


Figure 4.2: Vertical ozone profiles for the period 31 May to 3 June, 1978. The profiles were obtained during flights in the Cologne/Bonn region. The vertically shaded region is the excess ozone in the mixing layer; the horizontal shading indicates the local excess in the Cologne/Bonn region. Taken from *Fricke* [1980].

general structure is shown in Figure 4.1. The free troposphere is characterised by fairly constant mixing ratios of ozone, which increase with height. Below that is the planetary boundary layer (PBL), which can be further subdivided into the convective mixed layer and the surface layer. These are generally well mixed, although a decrease in concentration towards ground level is often observed due to deposition and reaction with NO near to ground sources.

While the PBL is well mixed during the daytime, at night the layer nearest the ground can become decoupled from higher layers. This leads to ozone depletion in the stable nocturnal boundary layer due to dry deposition and reaction with NO_x whenever NO_x sources are present. As a result, diurnal profiles of the concentration measured at low lying sites typically show a greater diurnal amplitude than those measured higher up. This decoupling of the nocturnal boundary layer from higher layers leads to the establishment of a residual layer containing high ozone concentrations produced during photochemical activity on the previous day. This can be seen in Figure 4.2, which shows a series of vertical ozone profiles measured by *Fricke* [1980]. These were obtained from measurements made during a series of flight in the

Cologne/Bonn region and shows the presence of a well defined residual layer above about 500 m even during daytime. Mixing ratios reached 170 ppbv above 500 m on 1 June. It is also apparent that the residual layer can be quite persistent.

Turbulence leads to a mixing of the layers in the morning. This can lead to an initial drop in ozone concentration as ozone-poor air from lower altitudes rises and is mixed with the ambient air. This can be followed by a rapid increase in the ozone concentration in the ozone-poor boundary layer due to vertical transport of ozone from the residual layer. Evidence for this has been found in an analysis of ozone measurements for several stations in the Rhine-Main region and will be discussed in chapter 12. The ozone concentration levels off in mid morning after the mixing process is completed². This nocturnal reservoir of ozone establishes the base level of ozone in the late morning. Photochemical production during the day is then responsible for any further rise in the ozone concentration in the absence of advection.

Advection can also lead to a change in ozone concentration which is independent of production and loss. This is of particular importance during periods when meteorological conditions lead to a change of air mass, with the associated advection of air with a different ozone concentration to the measurement site. It is most obvious at the end of a photochemical episode. The arrival of a frontal system can cause a significant drop in the ozone level within a few minutes. However, even during more stable conditions, advection in association with a gradient in the ozone field leads to changes in the ozone field.

4.4 Conclusions

The observed ozone concentration is the integral of these different processes, so that it is impossible to isolate the effect of the individual factors entirely. Nevertheless, it is possible to test our understanding of individual processes by making measurements under suitable conditions for which the other factors are nearly constant, or by averaging out the contributions of these other factors. The current study concentrates on investigating the effect of photochemical production on the ozone concentration, whereby the influence of transport and meteorological factors is found to be significant.

The photochemical production can be calculated using measured peroxy radical and NO concentrations. Such measurements were carried out at Kleiner Feldberg and Hohenpeissenberg during this study, and the instrumentation used is described in Part II. The measurements themselves are presented in Part III.

²The exact details vary from site to site due to local conditions, e.g. see Figure 12.3.

Part II
Experimental Techniques

Overview

The importance of peroxy radicals for the photochemical production of ozone has been emphasised in the discussion of tropospheric chemistry in Part I. Other factors which influence the observed ozone concentration were also discussed. Part II concentrates on the instrumentation used during the current study to investigate the relationship between peroxy radicals and ozone production, and focuses on the chemical amplifier used to measure peroxy radicals.

Following an introduction to measurement techniques for peroxy radicals in Chapter 5, Chapter 6 presents a more detailed description of the chemical amplifier technique itself. The basic chemistry and measurement principle behind the technique is presented first, followed by a discussion of the modulation technique. The CA technique relies on the conversion of the peroxy radicals to NO_2 in a chain reaction, which also results in an amplification of the signal due to peroxy radicals. The amplification factor is discussed in some detail, especially with regard to the most important factors which influence the performance of the amplifier. In particular, differences in detector response to the hydroperoxy radical, HO_2 , and to organic peroxy radicals is considered, as is the dependence of the amplification factor on relative humidity. The chapter concludes that, as long as the amplification factor used to calculate the mixing ratio concentration is corrected for the effect of water vapour, the chemical amplifier is capable of measuring upwards of 80% of the actual total RO_x mixing ratio under daytime conditions.

Building on this, Chapter 7 describes the chemical amplifier used for the measurements presented in this study. This is followed by a description of the calibration procedures and an estimate of the error associated with the instrument.

Chapter 8 concludes Part II with a description of the two sites at which measurements were made during the study: Taunus Observatory on Kleiner Feldberg and the Meteorological Observatory, Hohenpeissenberg. The other instruments and data sources used during the study are also outlined.

Chapter 5

Measurement techniques for peroxy radicals

Although the importance of free radicals to tropospheric oxidation processes has been realised since the 1970's, the measurement of peroxy radicals has only become feasible in the last two decades. Since then, several different techniques have been applied to the determination of peroxy radical concentrations in the atmosphere.

As with all free radicals, their relatively high reactivity and the resulting short lifetimes and low concentrations make direct measurement in the atmosphere difficult. This is complicated for peroxy radicals by the similarity of the absorption spectra of different peroxy radicals, so that a differentiation between the different species has not been possible using optical techniques. Nevertheless, at least one direct method and a number of indirect methods have been reported in the literature. The indirect methods typically rely on the conversion of peroxy radicals to other chemical species, which are more easily detected using existing techniques. These techniques are briefly presented below, and is followed by a summary of the most important results of published atmospheric measurements.

5.1 MIESR

The only technique allowing the direct measurement of free radicals which has been successfully applied to the measurement of both peroxy radicals and other radicals in the atmosphere¹ is the combination of Matrix Isolation and Electron Spin Resonance spectroscopy (MIESR) described by *Mihelcic et al.* [1982] and *Mihelcic et al.* [1985], and in a modified form by *Mihelcic et al.* [1990]. An air sample is sprayed, together with D₂O, onto a gold coated cold finger cooled to 77K in a vacuum (< 0.1 mbar).

¹Despite initially promising results using the Cavity Ring Down technique, which raised hopes of making speciated RO₂ measurements in the atmosphere, further evaluation of the technique has led to doubts as to whether it will be useful outside the laboratory [*D. Atkinson, personal communication*].

At these temperatures the radicals are essentially immobilised in a matrix of heavy water. The sample is subsequently analysed in the laboratory using the Electron Spin Resonance (ESR) technique to obtain a spectrum due to the interaction of the unpaired electron in the radicals with a strong magnetic field. Data is extracted from the resulting spectrum by fitting reference spectra for various radicals of interest to the observed spectrum using a numerical fitting procedure [Mihelcic *et al.*, 1990]. Measurements of NO_2 , NO_3 , HO_2 , $\text{CH}_3\text{C}(\text{O})\text{O}_2$, and the sum of the organic peroxy radicals can be obtained by this technique. The organic peroxy radicals cannot be measured separately, as their spectra overlap and are so well correlated that differentiation is unrealistic. Nevertheless, a major advantage of the method is its ability to distinguish HO_2 from organic peroxy radicals.

Samples are collected for approximately 30 minutes (8 l STP of ambient air) so that the time resolution of the method is restricted. The sampling efficiency is about 95%. The detection limit is approximately 5 pptv for HO_2 , RO_2 and NO_2 and 3 pptv for NO_3 , with an estimated accuracy of $\pm 5\%$ [Mihelcic *et al.*, 1993]. This method has been used during a number of measurement campaigns [e.g. Mihelcic *et al.*, 1993; Zenker *et al.*, 1998; Geyer *et al.*, 1999] and has also been used as a reference standard during intercomparison experiments with the chemical amplifier [e.g. Volz-Thomas *et al.*, 1999; Heitlinger *et al.*, 1997].

The main disadvantages of this method are its cost and the difficulty of maintaining the sample in a vacuum at 77 K until it can be measured in the laboratory [Schultz *et al.*, 1995]. Large amounts of liquid nitrogen are required to keep the sample temperature at 77 K, which makes the technique impractical for remote measurements and too costly for continuous operation.

5.2 Chemical amplifier (CA)

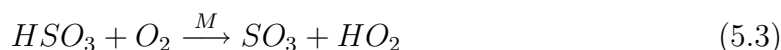
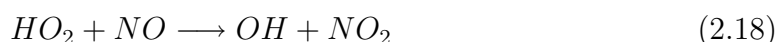
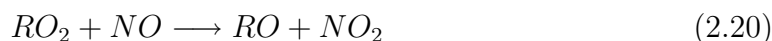
An indirect method for the quasi-continuous measurement of peroxy radicals was first proposed by Cantrell and Stedman [1982] and subsequently realised by Cantrell *et al.* [1984] as an application of the luminol based NO_2 detector described by Wendel *et al.* [1983]. Further modifications have been described by a number of groups [e.g., Hastie *et al.*, 1991; Cantrell *et al.*, 1992, 1996b]. The technique involves the conversion of peroxy radicals to NO_2 via a chain reaction with NO and CO. The NO_2 is subsequently detected using a luminol detector. The technique allows time resolutions on the order of one minute, although due to noise associated with changes in the background level of ozone and NO_2 , data are frequently averaged over several minutes. The method is subject to interference from several sources and to incomplete conversion of some organic peroxy radicals to NO_2 . The sensitivity of the instrument to humidity, which causes the sensitivity of the CA to decrease, means that most measurements published prior to 1999 must be reevaluated. With the exception of measurements carried out in extremely dry conditions, the measured concentrations would have been too low (see Chapter 6).

Despite the limitations of this method, it has been the most widely used method, as it is possible to achieve good results at relatively low cost. All RO_x measurements presented in this study were made using a CA, and the technique is discussed in more detail in Chapter 6. The CA used during the current study is described in Chapter 7.

5.3 IMR-MS/CIMS

The Ion Molecule Reaction-Mass Spectrometry/Chemical Ionisation Mass Spectrometry² technique has been used for measuring a variety of trace gases, e.g. OH [Eisele and Tanner, 1991, 1993; Tanner *et al.*, 1997], H₂SO₄, DMSO and MSA(g) [Berresheim *et al.*, 1993; Eisele and Tanner, 1993]. Recently it has been used for airborne measurements of peroxy radicals [Reiner *et al.*, 1997, 1998, 1999]. Other groups are also using instruments to measure RO_x based on this approach [Cantrell, 2001].

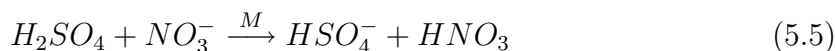
In order to measure peroxy radicals, the radicals first react with added NO and SO₂ in a chain reaction which results in the conversion of SO₂ to gaseous SO₃.



The chain reaction ends with the conversion of SO₃ to sulphuric acid:



This is then detected using ion molecule reaction-mass spectrometry (IMR-MS), which involves the reaction with nitrate ions to produce HSO₄⁻ ions:



This method has the advantage that the high sensitivity of the IMR-MS technique and low background levels of sulphuric acid allow measurements even with short chain lengths and measurement times [Reiner *et al.*, 1997]. However, due to branching of the reaction of RO₂ with NO and the incomplete conversion of some of the resulting RO species to HO₂³, it suffers from similar drawbacks to the conventional chemical

²The method is referred to by different names by various authors, but is essentially the same in both cases, c.f. Ion Molecule Reaction-Mass Spectrometry (IMR-MS) [Reiner *et al.*, 1997, 1998, 1999]; Chemical Ionisation Mass Spectrometry (CIMS) [e.g., Eisele and Tanner, 1991; Tanner *et al.*, 1997].

³The conversion of organic oxy radicals to HO₂ in reaction 5.1 and the various pathways by which this can proceed has been discussed in Chapter 3.

amplifier technique. Thus, it necessarily involves incomplete conversion of RO_x radicals to sulphuric acid. Nevertheless, due to the low chain lengths involved (typically less than 10 [Reiner *et al.*, 1997, 1998]) the error introduced by these factors is less than in the CA. Switching between N_2 and O_2 as carrier gas allows HO_2 and RO_2 to be differentiated [Hanke *et al.*, 2001], as do changes in the amounts of NO and SO_2 added in the inlet [Cantrell, 2001].

5.4 LIF-FAGE

A further technique involves the addition of NO to the air sample to produce OH quantitatively from the peroxy radicals. The OH radicals are then detected using the Laser Induced Fluorescence - Fluorescence Assay by Gas Expansion (LIF-FAGE) technique [e.g., Hard *et al.*, 1992; Kanaya *et al.*, 1999]. The detection of OH involves expansion of the air sample to a pressure of a few Torr, followed by the excitation of the OH radicals using a laser ($\lambda = 308 \text{ nm}$). The excited radicals emit fluorescent radiation at the same wavelength, which is detected perpendicular to the excitation beam using a photomultiplier [Hard *et al.*, 1984]. Parrish and Fehsenfeld [2000] have suggested that, due to the time scales involved for the conversion reaction, this technique allows the measurement of HO_2 , but not of RO_2 . This technique is currently used by several groups, including Pennsylvania State University [Martinez *et al.*, 2001] and Forschungszentrum Jülich [F. Holland, *personal communication*] to measure both OH and HO_2 concentrations.

5.5 Deviation from photostationary steady state (PSSD)

A different approach used by a number of authors is to calculate the RO_x concentration from the deviation of the observed O_3 concentration from that to be expected for the equilibrium between NO_x and O_3 [e.g., Cantrell *et al.*, 1993a, 1996d; Carpenter *et al.*, 1998]. As discussed in Section 2.1, in the absence of peroxy radicals the ozone concentration under photostationary steady state conditions can be derived using equation 2.4:

$$[\text{O}_3]_{\text{equil}} = \frac{j_{\text{NO}_2} \cdot [\text{NO}_2]}{k_{2,3} [\text{NO}]} \quad (5.6)$$

The reaction of peroxy radicals with NO (Reactions (2.18) and (2.20)) disturbs this equilibrium by pushing it towards higher concentrations of NO_2 and O_3 . A modified equation allowing for these deviations can then be written as

$$\Psi_{ox} = \frac{j_{\text{NO}_2} \cdot [\text{NO}_2]}{k_{2,3} [\text{NO}]} - [\text{O}_3] \quad (5.7)$$

where Ψ_{ox} is termed the “missing oxidant” and represents the deviation of the ozone concentration due to free radicals [Jenkin and Clemitshaw, 2000]. It is essentially the amount of oxidising free radicals expressed as the equivalent concentration of ozone. Assuming that the deviation is due to the reaction of RO_x with NO, it is equal to

$$\Psi_{ox} = \frac{k_{2.18}[HO_2]}{k_{2.3}} + \frac{\sum k_i[RO_2]_i}{k_{2.3}} \quad (5.8)$$

By assuming that the reaction rates for HO_2 and organic RO_2 are approximately equal, the total RO_x concentration can be approximated by

$$[RO_2] \approx \frac{k_{2.3}}{k_{2.20}} \Psi_{ox} = \frac{k_{2.3}}{k_{2.20}} \left(\frac{j_{NO_2} \cdot [NO_2]}{k_{2.3}[NO]} - [O_3] \right) \quad (5.9)$$

Comparisons of peroxy radical concentrations calculated using this technique with measurements using the chemical amplifier have led to reasonable agreement under some circumstances [Cantrell *et al.*, 1993a]. However, for situations in which the radiation changes rapidly, or in the vicinity of NO_x sources, the rapid changes in the measured parameters mean that the conditions for the photostationary state are not fulfilled. Thus, the deviation calculated under such conditions would reflect the changing conditions, and not necessarily the influence of peroxy radicals.

Carpenter *et al.* [1998] compared the RO_x concentrations calculated using the PSSD method with the results of a chemical model. The results of PSSD estimates were at times two orders of magnitude greater than the model calculations. Measurements made at the same time by Clemitshaw *et al.* [1997] and Penkett *et al.* [1999] tended to support the model calculations. However, the CA measurements were not corrected for relative humidity, and unless the measurements were made under very dry conditions, this would imply the need for a substantial upwards correction of the measured RO_x concentrations. Furthermore, the modelling results indicate that there is still a problem in explaining the high results from the PSSD technique. Thus, although this technique may be useful under certain conditions, it would appear to be inappropriate for evaluating RO_x measurements.

5.6 Atmospheric measurements

Peroxy radical measurements have been made in the atmosphere by a growing number of groups since the development of appropriate measurement techniques began. Measurements have been made under a wide range of conditions, ranging from clean air measurements at coastal sites in both hemispheres [e.g., Monks *et al.*, 1996, 1998, 2000; Carpenter *et al.*, 1997; Cantrell *et al.*, 1996a; Penkett *et al.*, 1999], at sea [Weißenmayer, 1994; Weißenmayer and Burrows, 1994], or at high altitudes [Zanis *et al.*, 1999], over measurements made at remote sites [e.g., Cantrell *et al.*, 1993a; Behmann *et al.*, 1994], to measurements in the vicinity of cities [e.g., Mihelcic *et al.*, 1993; Weißenmayer *et al.*, 1995; Handisides *et al.*, 1996a, 2000]. These have shown

large differences in RO_x concentrations at different sites and under different conditions. Clean air sites have generally low concentrations, whereas concentrations of up to 300 pptv have been observed in regions with high biogenic emissions [*Cantrell et al.*, 1993a]. Airborne measurements using IMR-MS [*Reiner et al.*, 1998, 1999] and MIESR [*Mihelcic et al.*, 1985] have also been reported and suggest a decrease in concentration with height.

The measurements at clean air sites cited above have found concentrations to be below about 10 pptv for very clean air masses, and have shown the dependence of RO_x concentrations on the primary production of OH. Other measurements in more polluted environments have shown a good correlation between the observed change in the O_3 concentration and the estimated production via the reaction between RO_x and NO [*Penkett et al.*, 1999; *Weißmayer et al.*, 1995]. Thus, these measurements agree well with current understanding of photochemical processes involving RO_x radicals.

The majority of ambient measurements reported in the literature are ground based measurements made using the chemical amplifier technique [e.g., *Weißmayer*, 1994; *Weißmayer et al.*, 1995; *Cantrell et al.*, 1993a, 1996c; *Carpenter et al.*, 1997; *Monks et al.*, 1996]. Prior to 1999, measurements made using the CA did not take into account the effect of relative humidity. This effect, which will be discussed further in Section 6.5, causes the sensitivity of the CA to be overestimated, so that these measurements can at best be considered to be lower estimates of the real concentration. Therefore, although they contribute to our knowledge of general relationships, they can no longer be considered accurate measurements of the peroxy radical concentration and should be interpreted as surrogates for the total RO_x concentration.

5.7 Conclusions

Each of the methods currently in use have their individual strengths and weaknesses. None of the techniques currently available differentiate between individual organic peroxy radicals, although several do differentiate between HO_2 and organic RO_2 . MIESR probably represents the most accurate method used so far, however logistical problems and cost have prevented it from entering widespread use. The most widely used method is the chemical amplifier technique, which, despite certain drawbacks, is a practical technique for making measurements of the total RO_x concentration.

Measurements of peroxy radicals made under a wide range of different conditions have already made a useful contribution to our understanding of photochemical oxidation in the troposphere. The present study is a further contribution to our understanding of the effect of peroxy radicals on ozone production. It was undertaken on the edge of the Rhine-Main region, and reflects conditions in a rural region which is at times influenced strongly by anthropogenic emissions from nearby urban areas. The peroxy radical measurements were made using a chemical amplifier, and were corrected using published estimates of the dependence on humidity. The method and the instrument will be further discussed in the following two chapters.

Chapter 6

The chemical amplifier technique for measurements of peroxy radicals

Peroxy radicals are typically present in the atmosphere at concentrations up to a few hundred pptv. Due to this relatively low concentration, their high reactivity and short lifetimes, peroxy radicals are difficult to measure directly. The Peroxy Radical Chemical Amplifier (CA) is an instrument for the quasi-continuous measurement of the total concentration of peroxy radicals and oxy radicals in the gas phase ($\text{RO}_x = \text{HO}, \text{HO}_2, \text{RO}$ and RO_2 , where R is an organic rest). The chemical amplifier measures peroxy radicals indirectly, and involves a chain reaction between the peroxy radicals and added NO and CO in which NO is oxidised to NO_2 . The resulting NO_2 is subsequently detected on the basis of its chemiluminescent reaction with luminol.

The chemical amplifier was initially proposed as a potential method for the measurement of peroxy radicals by *Cantrell and Stedman* [1982]. This was followed shortly afterwards by the construction of the first CA by *Cantrell et al.* [1984]. Chemical amplifiers based on the same principle have since been built by several groups [e.g., *Hastie et al.*, 1991; *Cantrell et al.*, 1992, 1996b; *Weißmayer et al.*, 1995; *Heitlinger*, 1997; *Carpenter et al.*, 1997; *Clemishaw et al.*, 1997; *Handisides*, 1995]. A number of improvements to the basic design have been proposed by several groups, in an attempt to improve its performance and to reduce its sensitivity to interference by other atmospheric components, notably PAN.

Two international intercomparison campaigns were held in Europe in 1994 and 1996 (Peroxy Radical Intercomparison Experiment (PRICE) I and II, [*Volz-Thomas et al.*, 1996, 1999; *Heitlinger et al.*, 1997; *Heitlinger*, 1997]) aimed at characterising the CA and comparing it with an independent method (MIESR; see Chapter 5). The results of these campaigns illuminate some of the limitations and problems associated with this technique. Several recent studies have sought to describe and quantify the effect of water vapour on the amplification factor [*Mihele and Hastie*, 1998, 2000; *Mihele et al.*, 1999; *Reichert*, 2000]. The consequences of these studies for the current work will be discussed following a description of the CA technique.

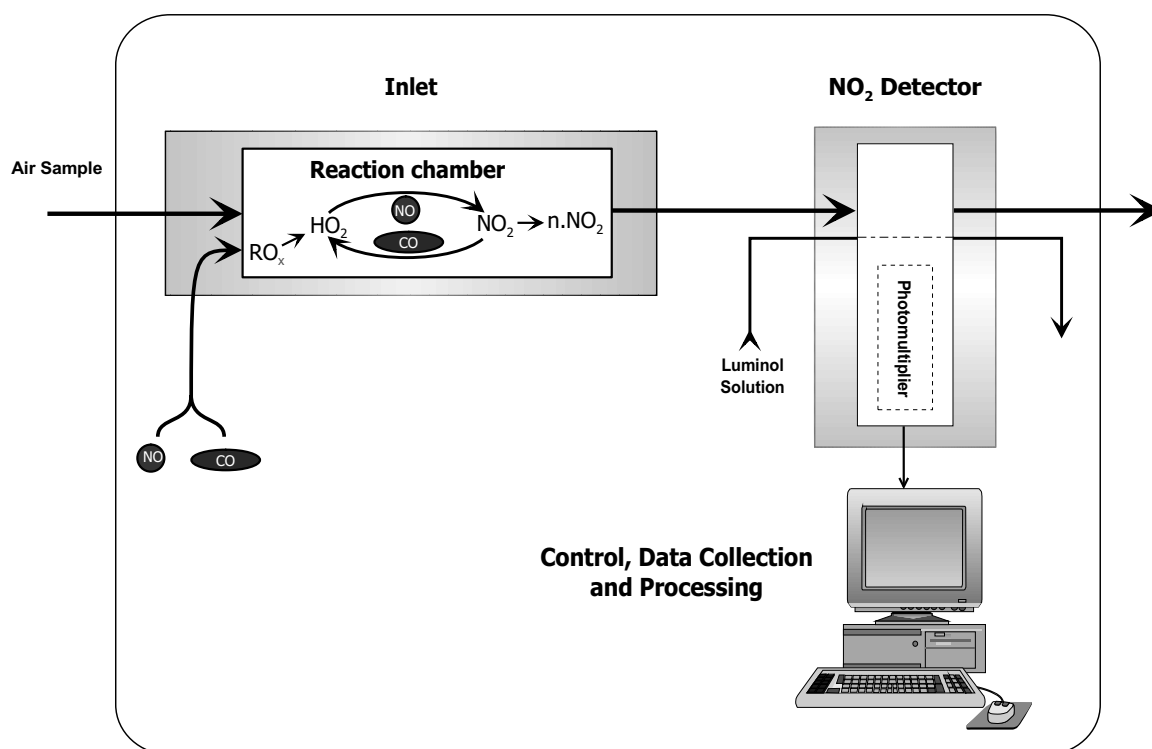
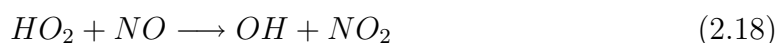


Figure 6.1: Schematic representation of the peroxy radical chemical amplifier.

6.1 Measurement principle

Ambient peroxy radicals react in the inlet of the chemical amplifier with added NO, resulting in the conversion of NO to NO₂. The addition of CO allows the production of further NO₂ in a chain reaction, so that a single peroxy radical results in the production of a much larger number of NO₂ molecules. The resulting NO₂ is subsequently detected and quantified on the basis of its chemiluminescent reaction with luminol. The ambient RO_x concentration can be calculated from the measured NO₂ concentration if the amplification factor and the response of the luminol detector to NO₂ are known. Both are regularly determined by calibration. Figure 6.1 illustrates schematically the basic function of the CA.

The production of NO₂ in the presence of ambient RO_x relies on the chain reaction involving the hydroperoxy radical, HO₂, NO and CO:



This reaction is repeated n times before the radicals are lost in chain terminating reactions, resulting in the production of n molecules of NO₂ for each initial HO₂

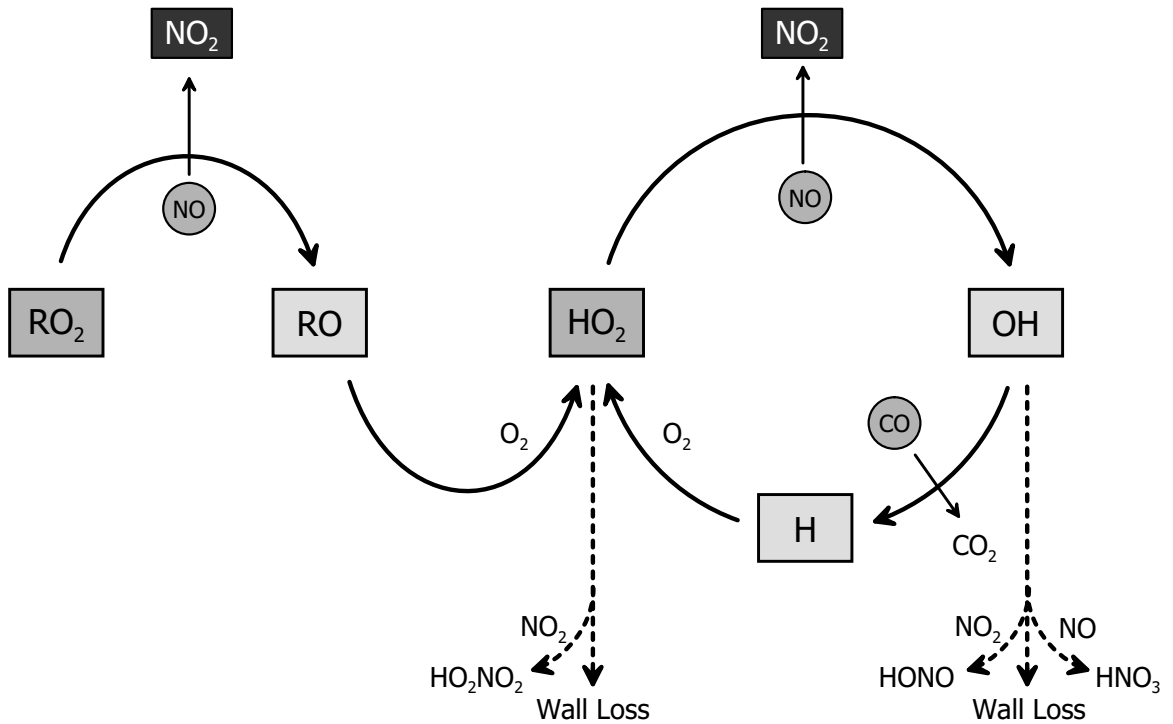
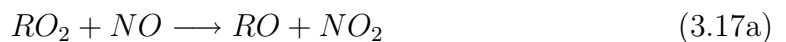


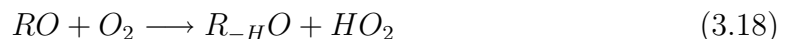
Figure 6.2: Schematic representation of the chain reaction chemistry in the CA inlet, which results in n NO_2 molecules being produced for each ambient RO_x radical.

radical. This can be seen in Figure 6.2, which also shows how organic peroxy radicals also contribute to the cycle by conversion to the HO_2 radical.

Organic peroxy radicals react with NO in an analogue fashion to produce NO_2 :



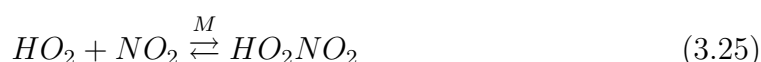
In contrast to the OH radical, the organic oxy radical, RO , does not react with CO . This means that the amplification of the NO_2 signal due to RO_2 is dependent on the conversion of the RO radical to the HO_2 radical (see subsection 3.2.1). After generation of the HO_2 radical the chain reaction proceeds as above. For non-tertiary alkoxy radicals, this occurs via H extraction by O_2 and yields a carbonyl product ($R_{-H}O$) as a byproduct:



This step does not proceed efficiently for some oxy radicals, which reduces the efficiency of the CA for these peroxy radicals, and is discussed further in Section 6.3.

The length of the resulting chain reaction is determined by the relative rates of the chain propagation and termination reactions. The termination reactions include reactions with the walls of the reaction chamber, as well as reactions between radicals. Some of these have already been discussed in previous chapters (see sections 2.2.1 and

3.3). The most important radical-radical reactions at the high NO_x concentrations in the reaction chamber are those between OH, HO_2 and NO_x :



Due to the rapid rate of Reaction (3.3) between OH and CO, the concentration of OH is approximately 100 times less than that of HO_2 , so that Reaction (3.25) is the most important of these loss reactions. Losses due to reactions between the peroxy radicals themselves can be neglected, as the concentrations of NO and NO_2 in the inlet are many times higher than in the atmosphere, and the rates for peroxy-peroxy reactions are relatively slow.

The NO_2 from the amplification reaction and from interfering sources is subsequently measured using a luminol¹ detector, which will be described further in the following chapter, and the signal is processed to obtain the corresponding RO_x concentration.

6.2 Signal modulation

The NO_2 arriving at the luminol detector is not only derived from the chemical amplification process, but, due to the combined influence of ambient NO_2 and ozone titration, is also present in the air sample as background NO_2 . NO_2 is typically present in the atmosphere on the Kleiner Feldberg at concentrations ranging up to 60 ppbv [c.f. *Handisides et al.*, 1999, and Chapter 9 in the current work]. At the high NO concentrations present in the inlet, any ozone in the ambient air sample reacts completely with NO, which results in the NO_2 concentration at the detector increasing by an amount equal to the original O_3 concentration. Furthermore, NO_2 is added to the air flow before the detector to ensure the detector is operating in the linear region (see Section 7.1.2). Taken together, these NO_2 sources result in a background NO_2 concentration which is significantly higher than the amount of NO_2 produced by RO_x radicals. This background NO_2 signal is accounted for by modulating the signal between a measurement and a background mode. This is achieved by switching the amplification reaction on and off. Assuming that the background concentration remains nearly constant, the difference between the signals from these two modes results in a demodulated signal which is essentially due to the presence of peroxy radicals (ΔNO_2).

¹5-amino-2,3-dihydro-1,4-phthalazinedione, also known as 3-aminophthalhydrazide.

Cantrell et al. [1984] initially achieved this modulation by replacing the flow of CO with nitrogen gas during one half of the measurement cycle, so that the OH radical was not cycled back to HO₂. However, as *Hastie et al.* [1991] have shown, peroxyacetyl (PA) radicals resulting from the thermal decomposition of PAN in the tubing also take part in the chain propagation reaction, and provide an additional source of NO₂ during the measurement mode. Depending on the air temperature and the ambient concentration of PAN, this can be a significant effect, as 2 ppbv PAN would generate the same amount of NO₂ at 298 K as 5 pptv radicals.

In order to compensate for this additional source of radicals in the detector, RO₂ amplification is switched off during the background mode by moving the addition point for CO downstream [*Hastie et al.*, 1991]. In the absence of CO, the OH radicals rapidly recombine with other radicals, especially NO. Thus, they are no longer available to take part in the amplification process after CO is added, and the chain reaction is not sustained for ambient RO_x. The presence of CO during both modes means that PA radicals produced by PAN decomposition undergo amplification during both halves of the cycle. By keeping the distance between the two addition points short, nearly equal numbers of PA radicals are amplified in each mode. Thus, the effect of PAN is almost entirely cancelled out during demodulation. The presence of CO during both modes has the further advantage of ensuring that the air sample arriving at the detector always contains the same concentration of CO and NO, thus minimising any effect of these components on detector sensitivity. The CA built for the present study [*Handisides*, 1995] uses this modulation technique as PAN concentrations of nearly 6 ppbv have been observed at Kleiner Feldberg during summer.

The resulting modulated signal which is the raw output of by the CA is shown in Figure 6.3 for the 45 minutes following an NO₂ calibration. The measurement was made shortly after midday on a sunny day during an ozone episode. The effect of the peroxy radicals is seen clearly in the modulated signal. The signal during each mode is made up of contributions from the various sources mentioned above, and these contributions are represented schematically in Figure 6.4 on page 61.

The detector signal during the measurement mode (S_{Det}^1) can be considered to be the sum of the following components:

$$S_{Det}^1 = S_{NO_2^{amb}} + S_{O_3} + S_{RO_x} + [a(T) + b(T)]S_{PAN} + S_{misc}. \quad (6.3)$$

where S_{Det}^1 is the signal at the detector during the first half cycle,
 $S_{NO_2^{amb}}$ is the signal due to ambient NO₂,
 S_{O_3} is the signal due to the titration of ambient ozone by NO,
 S_{RO_x} is the signal due to the presence of peroxy radicals,
 $a(T)$ is the fraction of PAN molecules which dissociate between the two addition points at temperature T,
 $b(T)$ is the fraction of PAN molecules which dissociate between the second addition point and the NO₂ detector,
 S_{PAN} is the signal which would result from the complete thermal dissociation of PAN in the tubing and the subsequent participation of the

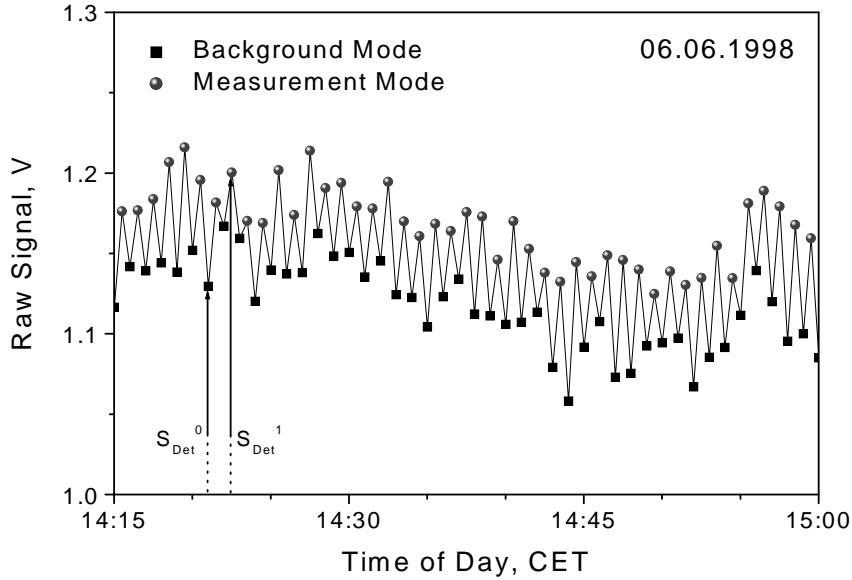


Figure 6.3: Measured signal output from the CA for a fine weather period. The signal during Background Mode, S_{Det}^0 , is represented by a solid square; the Measurement Mode, S_{Det}^1 , by a gray circle.

$S_{misc.}$ resulting PA radicals in the chain reaction, and is any remaining signal due to the detector, for example, the PMT dark current, the offset due to NO_2 added to the air sample, and any other sources of interference.

The detector signal during the background mode of the measurement cycle (S_{Det}^0) is analogously the sum of the relevant components, as seen in Figure 6.4(b),

$$S_{Det}^0 = S_{\text{NO}_2^{amb}} + S_{\text{O}_3} + b(T)S_{PAN} + S_{misc.} \quad (6.4)$$

The demodulated signal (ΔS) can then be calculated as the difference between these two signals:

$$\begin{aligned} \Delta S &= S_{Det}^1 - S_{Det}^0 \\ &= S_{\text{RO}_x} + a(T)S_{PAN} \end{aligned} \quad (6.5)$$

When $a(T)S_{PAN}$ is sufficiently small this can be approximated by

$$\Delta S \approx S_{\text{RO}_x} \quad (6.6)$$

This is achieved by keeping the distance between the addition points short.

The amount of NO_2 produced by the chain propagation reaction due to RO_2 ($\Delta[\text{NO}_2]$) can then be calculated from the resulting demodulated signal on the basis of the sensitivity of the detector to NO_2 :

$$\Delta[\text{NO}_2] = s\Delta S \quad (6.7)$$

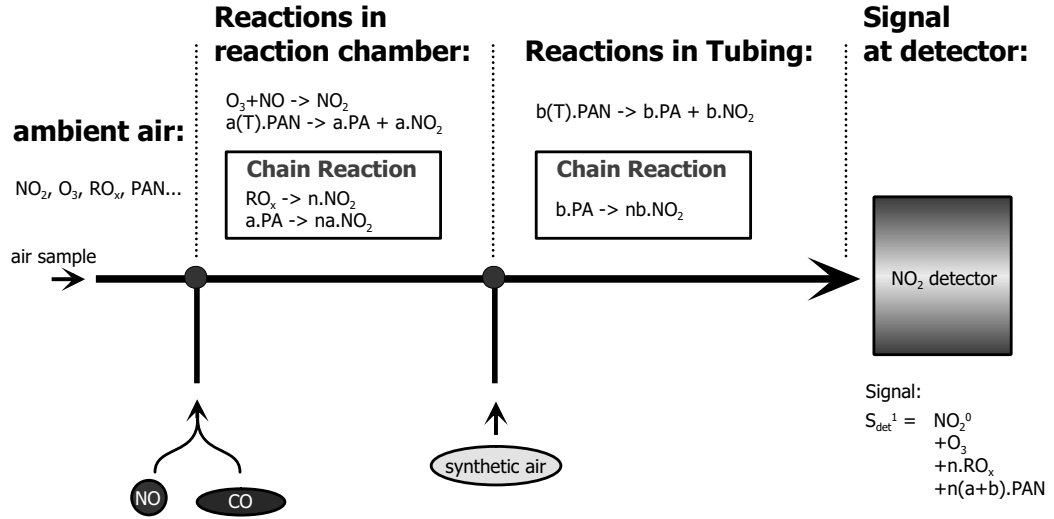
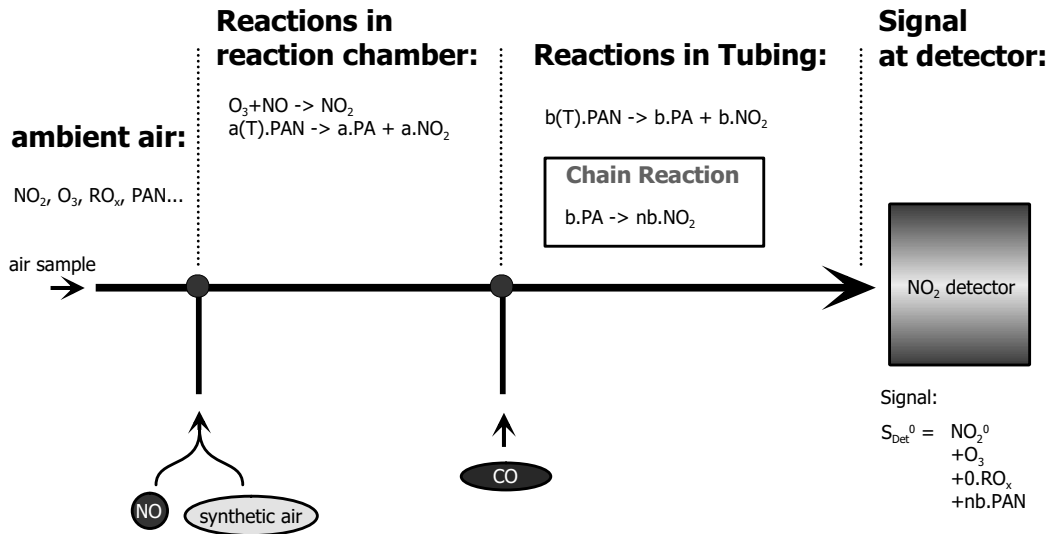
(a) Measurement mode of measurement cycle; amplification of RO_x signal is active(b) Background mode of measurement cycle; amplification of RO_x signal is inactive

Figure 6.4: Schematic representation of the two modes in the measurement cycle which lead to the modulated NO_2 signal. The NO_2 signal consists of components due to background NO_2 , the titration of ozone, and amplification of both ambient RO_x and peroxy acetyl radicals resulting from thermal decomposition of PAN in the tubing. The demodulated signal ΔS equals the difference between the signals for each of the two modes ($a(T)$ is typically negligibly small):

$$\Delta S = S_{\text{Det}}^1 - S_{\text{Det}}^0 = n \cdot \text{RO}_x + na(T) \cdot \text{PAN}$$

where s is the sensitivity of the detector to NO_2 in ppbv NO_2 per volt, and ΔS is the demodulated signal in volts. This can in turn be converted to the equivalent peroxy radical concentration using the amplification factor:

$$[\text{RO}_x] = \frac{s\Delta S}{CL} \quad (6.8)$$

where CL = the effective amplification factor, i.e., the chain length of the amplification reaction. These conversion factors are determined regularly by calibration.

6.3 The amplification factor

The amplification factor, or chain length (CL), corresponds to the average number of NO_2 molecules produced per RO_x radical and is dependent on a number of factors related to instrument design and operating conditions. The most significant factors are:

- the wall loss rate, which is affected by the surface properties of the reaction chamber and inlet, and their surface area,
- the concentrations of NO and CO added to the reaction chamber,
- the concentrations of several ambient gas compounds, notably ozone, NO_2 , and water vapour, which influence the gas phase reactions in the reaction chamber, and
- the speciation of RO_x radicals in the air sample.

These factors can interact with each other, so that, for example, the loss rate to wall surfaces in the reaction chamber also affects the sensitivity of CL to the concentration of HO_2 and NO_x .

The various factors affecting CL can be subdivided into two categories, which overlap to a certain degree:

- Those which affect the rate of the chain propagation reactions, and
- those which primarily have an influence on the termination reactions.

The concentration of CO added to the reaction chamber is an example of the first category, whereas the ambient concentrations of O_3 , HO_2 and NO_x fall into the second category. NO, which is added at the beginning of the reaction chamber, affects both reaction rates, and both the initial NO concentration and the relative rate of wall loss determine the dominant effect. The interplay of these factors has been extensively modelled by several authors [*Cantrell et al.*, 1984, 1993b; *Hastie et al.*, 1991; *Clemishaw et al.*, 1997], and the most important results relevant to instrument design are summarised in this section. RO_2 speciation and water vapour, both of which

are dependent on the ambient operating conditions, and are not primarily a function of instrument design also have significant effects on the amplification reaction. These will be considered separately in the following sections.

An increase in the NO concentration added to the inlet at a constant CO concentration leads initially to an increase in chain length, as the reaction rate between HO₂ and NO increases. However, after the optimum level has been reached, any further increase in the NO concentration leads to an increase in the ratio of OH to HO₂, with a subsequent increase in the relative termination rate due to the formation of HONO (Reaction (2.10)). High NO levels lead to an increase in reactions of oxy radicals with NO, hence retarding their conversion to HO₂ (see Section 3.2.1). This results in a fall off in CL at higher NO mixing ratios [Cantrell *et al.*, 1993b; Clemishaw *et al.*, 1997]. The existence and exact position of this maximum depends on the relative wall loss rate, with the maximum shifting to progressively higher NO concentrations for higher wall losses.

CL initially increases as the CO concentration is increased, but after reaching a plateau it remains constant. The initial increase is due to the increasing proportion of OH radicals which take part in the chain propagating reaction with CO, as opposed to undergoing a terminating step with NO. However, at higher CO concentrations, the amplification factor is limited by the ratio between the conversion of HO₂ to OH and the loss rate of HO₂, neither of which are CO dependent.

The rate of the termination reactions increase as a result of increases in the concentrations of several compounds. High levels of both HO₂ and NO₂ lead to a shortening of the chain reaction via Reactions (2.6) and (3.25). The NO₂ concentration is determined by the ambient concentrations of NO₂ and O₃, as well as by the chain reaction itself. Models show that this effect remains under 10% for initial HO₂ mixing ratios of up to 200 pptv [Hastie *et al.*, 1991]. This places an upper limit on the radical mixing ratios which can be used to calibrate the CA. NO₂ produced by the titration of ambient O₃ can be a problem for sensitive systems with low wall loss rates, in which termination reactions dominate. However, Hastie *et al.* showed that for a CA with a similar design to the instrument used for the current work, the effect of 100 ppbv ozone on the amplification factor is at the most 10 %.

In absolute terms, high wall loss rates lead to rapid HO₂ loss and cause CL to decrease. However, they also mean that CL is less sensitive to changes in the rates of the termination reactions, and is also less sensitive to changes in the wall loss rate itself. Hence, high wall loss rates relative to the radical termination reactions result in a more stable CL, and a trade off between k_{wall} and CL becomes necessary.

The insights gained from these simulations have led to an optimisation of CA operating conditions, with NO and CO mixing ratios in the inlet for most instruments typically lying in the range 2 - 4 ppmv and 4 - 10 %, respectively [c.f. Heitlinger, 1997]. In contrast, there is considerable variety in inlet design, due to different compromises between long term stability and amplification factor.

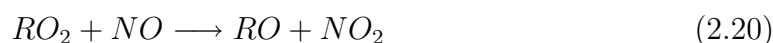
6.4 Organic peroxy radicals

Due to the large number of precursor VOCs, a large number of organic RO₂ radicals are potentially present in ambient air, with widely varying relative concentrations and physicochemical properties. This affects the efficiency with which they are detected by the CA. As a result, the effective amplification factor is a function of the properties and relative concentration of the individual radical species in the air sample. Differences in the efficiency with which different species are converted to HO₂ provide an intrinsic limit on the degree to which the concentration obtained from the CA signal can be considered to be a measure of the total peroxy radical concentration.

The differences in the sensitivity of the CA to different peroxy radicals are due to the following factors:

- Differences in rate and branching ratio of the initial reaction with NO.
- Differences in wall loss rates for HO₂ and organic radicals.
- Non-propagation of the chain reaction for some organic peroxy radicals.

The reaction rate with NO varies somewhat for different radicals (see Section 2.2), although for the two most abundant species, HO₂ and CH₃O₂, the rate coefficients are quite close. However, the reaction proceeds via two channels, only one of which leads directly to NO₂ production (see Section 3.2.1):



For a given peroxy radical, the relative importance of these two pathways helps determine the amplification factor for that peroxy radical. Recent recommendations for the branching ratio of smaller RO₂ radicals conclude that for the most common atmospheric peroxy radical, CH₃O₂, less than 0.5% react via Reaction (3.17b) [Tyndall *et al.*, 2001]. For C₂H₅O₂ the ratio is <1.4%, whereas for the peroxyacetyl radical (CH₃C(O)O₂) it is much higher, about 20±10%. This indicates that for the simplest peroxy radicals this alternative reaction pathway is likely to have little impact on the CA. For some larger peroxy radicals, the second channel becomes more important and results in a lower sensitivity to these radicals. Thus, the detection efficiency of the CA depends on the relative importance of this pathway.

Wall loss rates in the CA inlet also vary for different peroxy radicals. For most RO₂ radicals the wall loss rate is relatively low, but the loss rate in the inlet has been shown to be significantly higher for HO₂ radicals [Mihele *et al.*, 1999]. This may also apply to radicals with polar groups. As HO₂ is used to calibrate the CA in this study, loss rates in the inlet are taken into account in the calibration process. However, this has the consequence that loss rates for organic RO₂ radicals may be overestimated.

Some organic oxy radical products of the reaction between RO₂ and NO, e.g., tertiary oxy radicals, are not converted to HO₂ by CO and therefore do not contribute

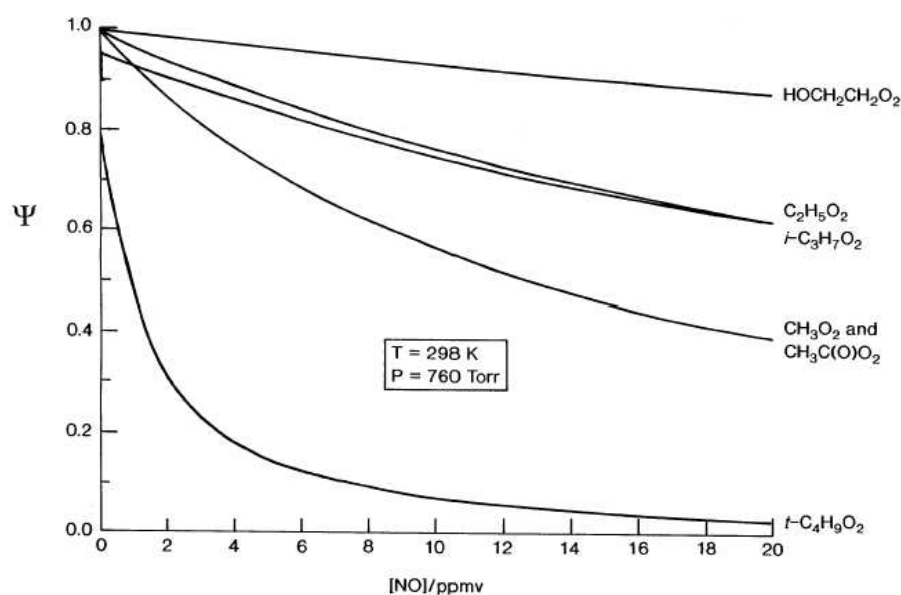


Figure 6.5: Idealised fractional yields of HO₂ (Ψ) for a series of RO₂ radicals as a function of NO concentration in the absence of heterogeneous removal (taken from *Ashbourn et al.* [1998]).

to the subsequent propagation reaction. Other organic oxy radicals are converted to HO₂ with much lower efficiency, due to competing reactions with NO :



In contrast, alternative decomposition and isomerisation pathways which result in the production of HO₂ may be available for some oxy radicals, and some of these proceed even faster than the reaction with O₂. Due to the wide range in fractional yields of HO₂ for different RO₂ radicals, the relative abundance of the different radicals in the ambient atmosphere plays an important role in determining the degree to which the CA provides an accurate measure of the total RO_x concentration.

The effect of these factors on the CA is not straightforward and needs to be considered further to evaluate the CA's usefulness for atmospheric measurements.

Heitlinger [1997] has shown that the RO_x concentration obtained from the detector output is a complicated function of amplification factor (CL), loss rate in the inlet (ϵ), and detector efficiency² (δ_i) for each RO₂ radical present, and any effect due to

²The term conversion efficiency is to be preferred, as strictly speaking the detection efficiency is only equal to the conversion efficiency when wall loss rates are neglected.

interference by other substances, e.g., PAN($\kappa[\text{NO}_2]$).

$$[\text{HO}_2] + \sum_i [\text{RO}_2]_i = f(\Delta[\text{NO}_2]) = f(\text{CL}, \varepsilon_{\text{HO}_2}, \frac{[\text{HO}_2]}{\sum_i [\text{RO}_2]_i}, \varepsilon_{\text{RO}_{2i}}, \frac{\delta_i [\text{RO}_2]_i}{\sum_i [\text{RO}_2]_i}, \kappa[\text{NO}_2]) \quad (6.9)$$

The detector efficiency is itself a function of the chemical properties of the radical under consideration and its radical products.

Theoretically, in order to calculate the true total peroxy radical concentration, each of these parameters would need to be known exactly. However, many of these parameters are unknown, e.g., the reaction coefficients for many peroxy radical species, and the identities and relative concentrations of the RO_x radicals present in the atmosphere, are currently unmeasurable. Simulations using chemical models show that they can vary considerably, depending on the precursor compounds from which they result. *Heitlinger* concluded that the CA method could only be used to determine the total RO_x concentration when δ_i lay close to unity for all RO_{2i} radicals involved.

This requirement may be fulfilled during most daytime measurements, as the main peroxy radical species are frequently HO₂ and methyl peroxy (CH₃O₂) radicals [c.f. *Mihelcic and Volz-Thomas*, 1994; *Ashbourn et al.*, 1998], and the assumption can be made that tertiary peroxy radicals do not contribute significantly to ozone production. However, the oxidation of many biogenic compounds results in a large number of peroxy radicals, some of whose chemical properties are quite different from those of the simpler radicals. Consequently, a potentially wide range of detector efficiencies is to be expected for the products of more complex oxidation mechanisms, especially those involving night-time chemistry.

The detection efficiency for the most common organic peroxy radical (CH₃O₂) was calculated to be about 80%, whereas, for the tertiary butyl peroxy radical, $\delta_{(\text{CH}_3)_3\text{CO}_2}$ was only about 22% at 3 ppmv NO [*Heitlinger*, 1997]. This value for CH₃O₂ agrees well with measurements made during PRICE II [*Heitlinger et al.*, 1997; *Heitlinger*, 1997]. The results of chemical simulations presented by *Jenkin et al.* [1996] and *Ashbourn et al.* [1998] show that the idealised fractional yield of HO₂ (Ψ) for a number of peroxy radicals is also a function of the concentration of NO. Ψ can be significantly less than unity for some RO₂, as seen in Figure 6.5.

Jenkin et al. [1996] modelled the response of a CA for the development of an air mass over five days along a trajectory typical for summertime pollution episodes in the UK. The results indicated that while the response does vary somewhat, it does not vary as much as might be feared. The study suggested that during daylight, the fractional response of a CA should exceed 90%. At night, however, the response should drop to 70-80%. These calculations only took gas phase chemistry into account, so that the influence of varying heterogeneous loss rates also needs to be considered.

Laboratory measurements of the fractional response of the CA described by *Clemishaw et al.* [1997] to a series of RO₂ radicals allowed the combined effect of heterogeneous loss and gas phase processes to be measured directly [*Ashbourn et al.*, 1998]. They indicated that, for all the organic radicals measured the total fractional

response relative to HO_2 lay below unity. However, the measured fractional yield was considerably higher than when calculated by simulations which considered only gas phase reactions. This was due to wall losses in the inlet, which were found to play a significant role in reducing the signal for HO_2 and more polar radicals.

These results provide experimental support for the simulations of *Jenkin et al.*, and suggest that the proportion of daytime peroxy radicals measured by the CA is likely to be between 70 and 80 % of total RO_x . The RO_2 radicals used in the study were representative of those formed by the OH initiated oxidation of hydrocarbons and oxygenates, and hence are probably representative of daytime populations. Other factors probably limit the fractional response of other classes of peroxy radicals, e.g., β -nitro-oxy peroxy radicals resulting from night-time chemistry, and tertiary peroxy radicals. The results of recent inter-comparison experiments with the MIESR or IMR-MS also suggest that the CA has a response of approximately 80% [*Hanke et al.*, 2001; *Volz-Thomas et al.*, 2001].

6.5 The effect of water vapour on the amplification factor

A further parameter which has a significant effect on the efficiency of the CA is the presence of water vapour, as has been shown in several very recent studies [*Mihele and Hastie*, 1998, 2000; *Mihele et al.*, 1999; *Reichert*, 2000]. This effect results in a reduction of the dry air amplification factor with an increase in the relative humidity (RH). Measurements by *Mihele et al.* [1999] showed a decrease in CL relative to dry air ($\sim 1\%$ RH) of approximately 50% at ca. 40% relative humidity. As measurements in the atmosphere are almost always made at much higher relative humidities than exist in the inlet during calibration, the reduced amplification factor needs to be taken into account in calculating the total RO_x concentration. As a result, most CA measurements prior to the discovery of this effect must be recalculated using corrected amplification factors.

This effect has the further consequence that the signal to noise ratio (SNR) is very low during episodes with high relative humidity, leading to a high detection limit. Thus detection of RO_x at high humidity levels becomes very difficult. This has been observed during measurements made in cloud on Kleiner Feldberg. RO_x concentrations were almost always below the detection limit under such conditions. This was interpreted as due to the increased loss of HO_2 to a water film which is assumed to form on the inner walls of the inlet under such conditions. The amplification factor and detection limit were observed to recover after cloud dissipation.

Mihele and Hastie [1998] and *Mihele et al.* [1999] carried out a series of experiments in which they measured the CA amplification factor at different relative humidities by adding humidified air to the air flow from the radical source just inside the CA inlet. A significant decrease in the chain length of the amplification reaction was observed with increasing humidity. Figure 6.6 shows their results contrasted with results from two other groups.

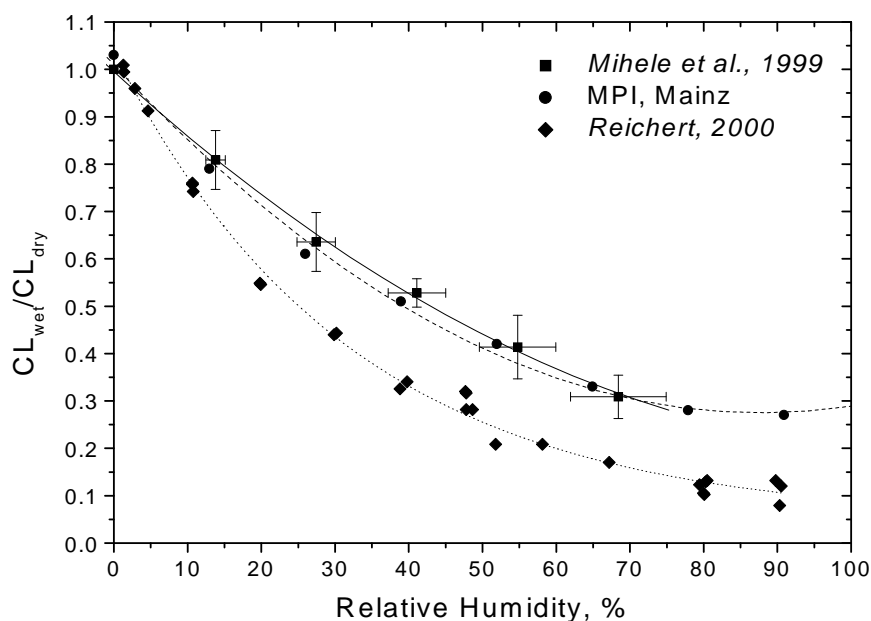


Figure 6.6: The ratio of the amplification factor in humid air to that in dry air (CL_{wet}/CL_{dry}) plotted against the relative humidity (RH) of the air sample. Data from *Mihele et al.* [1999], *Reichert* [2000], and MPI für Chemie (Mainz).

Investigations of the water effect have also been carried out by *Reichert* [2000] using the CA from the University of Bremen, and a specially designed humidifier and radical source arrangement. The results confirmed the dependence of the amplification factor on relative humidity, but measured an even greater decrease in CL with increasing relative humidity than was observed by *Mihele et al.* [1999], as can be seen in Figure 6.6. The experimental arrangement used by *Reichert* involved production of HO_2 radicals in air with a carefully controlled relative humidity. The concentration of HO_2 radicals produced in the humidifier/radical source was controlled by adjusting the UV light intensity.

Both sets of results followed a similar curve for the region above approximately 30% RH. The major difference between the two curves below this point lay in a rapid decrease of the CL_{wet}/CL_{dry} ratio measured by *Reichert* [2000] between 0 - 30 % RH. This could not be readily explained by *Reichert*.

Although differences in the experimental arrangements could be responsible for these differences, it is also possible that differences in the construction of the two CAs used in the experiments may be responsible; *Mihele et al.* used 1/4" Teflon tubing for the inlet, whereas the CA used by *Reichert* has a glass reactor. As the differences were observed at low relative humidities, they may be due to differences in the surface properties of the different inlets. This may be related to the establishment of a water monolayer, which has been shown by *Pankow* [1997] to occur on a clean quartz surface at about 30% RH. At higher RH, the wall loss rates should converge,

and other factors, i.e. gas phase reactions, may then outweigh the effect of surface properties. This may explain the parallel nature of the curves observed at $\text{RH} > 30\%$. Unpublished measurements made at the Max Plank Institut für Chemie (MPI) in Mainz [T. Klüpfel, *personal communication*] using a larger Teflon tube for the CA inlet and the experimental approach of *Mihele et al.* showed surprisingly good agreement to those of *Mihele et al.*, as seen in Figure 6.6. This suggests that the nature of the inlet surfaces may be the critical factor in determining the behaviour at low RH.

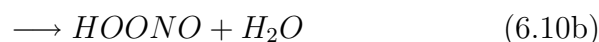
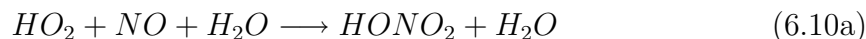
While the agreement between the groups is significant, the differences also show that further investigations of the effect of water on the CA response are necessary. Such investigations should concentrate on differences between various CA designs and surface materials, and on ascertaining any differences associated with two experimental techniques themselves. Although the experimental technique of *Reichert* is considerably more sophisticated and avoids potential problems due to mixing in the inlet, the difference in materials used for the inlet is a possible source of difference between the two sets of results.

The exact source of this dependence on humidity is also uncertain, but three factors have been considered:

- an increase in the wall loss rate,
- an increase in gas phase termination reactions, such as Reactions (2.10), (3.25) and (2.6), and/or
- a decrease in the effective gas phase chain propagation reactions, (2.18) and (3.3).

Mihele et al. found that heating the walls of the reaction chamber to drive water off the inner walls led to a decrease in the sensitivity of CL to water vapour. This indicates that the nature of the reactor walls plays a significant role in determining the sensitivity to water vapour. However, increasing the NO concentration so that gas phase termination reactions would dominate caused less change in the dependence on humidity than expected, and suggests that the gas phase reactions also play a role.

Two potential pathways for a termolecular chain termination reaction with NO were proposed by [*Mihele et al.*, 1999] to explain the observed effect:



The observed water dependence were simulated in a chemical model by setting the reaction rate of either of the two paths equal to about $2.1 \times 10^{-31} \text{ cm}^6 \text{ molec}^{-2} \text{ s}^{-1}$. Model simulations by *Reichert* [2000] confirmed that wall losses alone could not explain the observed effects, and proposed a series of reactions involving either water clusters, $(\text{H}_2\text{O})_k$, or the HO_2 adjunct reacting with NO to form a larger complex. These reactions would lead to a change in the propagation reaction rates. The IMR-MS method (see Section 5.3), does not show any water dependence, which suggests

that the use of CO in propagating the chain reaction may be the cause of this effect. However, such instruments have a low chain length, which would minimise any effect on the amplification factor due to the chain reaction chemistry.

It is currently uncertain as to whether experimental or design differences are responsible for the differences between the published results on the sensitivity of the CA to water vapour. The inlet used by *Mihele et al.* [1999] uses 1/4" Teflon tubing for the inlet and reaction chamber and is very similar to the inlet of the CA used in the current study. Due to this similarity of design, the published data on CA sensitivity to water vapour of *Mihele et al.* [1999], supplemented by the unpublished data from MPI, were used to correct the RO_x measurements made during the current study. Direct measurements of this effect were not carried out as part of the current study, as the cause of the differences between the various published studies needs to be clarified first. Consequently, the error associated with this correction is quite large and is a major component of the total uncertainty in the measurements (see Section 7.4).

6.6 The interpretation of RO_x measurements using the CA

The results of previous studies discussed here show that the amplification factor used to calculate the total RO_x concentration from the measured NO₂ signal is subject to several sources of uncertainty, of which the two most important sources are

- differences in the chemical properties of HO₂ and RO₂ radicals, and
- the sensitivity of the amplification factor to water vapour.

Both modelling and experimental results discussed in this chapter indicate that differences in the properties of various radicals should not be a problem for daytime measurements. The CA effectively measures the ability of the various RO_x radicals in an air sample to convert NO to NO₂. Thus, the measured concentration should be interpreted as the HO₂ concentration which would produce an equivalent amount of NO₂ in the same time interval. This is related to the true RO_x concentration, although the exact relationship is determined by the unknown composition of the peroxy radical population. Therefore, CA measurements should be considered to be a measure of the total concentration of all alkoxy and peroxy radical species, weighted according to their short term ozone production capacity³.

The dependence on relative humidity creates difficulties under conditions with high relative humidity, as the detection limit can become too high to detect the peroxy radicals. However, for drier conditions such as those experienced during episodes of intense photooxidation, the appropriate amplification factor can be obtained by correcting the dry air value using the sensitivity to water vapour based on *Mihele et al.* [1999].

³This should not be confused with the ozone creation potential, which is commonly referred to in the literature, and which is a measure of the amount of ozone produced by the complete oxidation of an initial VOC [e.g., *Derwent et al.*, 1996].

Chapter 7

The IMG chemical amplifier

A peroxy radical chemical amplifier (CA) using the technique discussed in the previous chapter was built for the current study during 1994 and 1995 at the Institute for Meteorology and Geophysics (IMG) of the Johann Wolfgang Goethe-University, in partial fulfillment of a work contract with the Hessisches Landesamt für Umwelt und Geologie (HLUG; Bureau for the Environment and Geology of the State of Hesse) [Handisides, 1995; Handisides *et al.*, 1996b, 1998, 1999, 2000]. It is closely based on the design described in *Hastie et al.* [1991] and operated by the peroxy radical group of the Institute of Environmental Physics, University of Bremen, under Professor John Burrows [Weißbenmayer *et al.*, 1995]. The design of the IMG-CA is described in Section 7.1, followed by a description of the calibration techniques in Sections 7.2 and 7.3. Section 7.4 completes the chapter with a discussion of the uncertainty associated with the measurements made using the CA.

7.1 Description of the IMG Peroxy Radical Chemical Amplifier

The IMG chemical amplifier is designed as a ground-based instrument for measuring the total RO_x concentration in the atmosphere. As discussed in the previous chapter, this is achieved by the reaction of RO_x radicals with NO and CO in the inlet, resulting in a modulated NO₂ signal. This technique lends itself to a modular design, which has been implemented in such a way that the CA consists of the following main components:

- the inlet,
- an NO₂ detector,
- an Automated Calibration Unit (ACU),

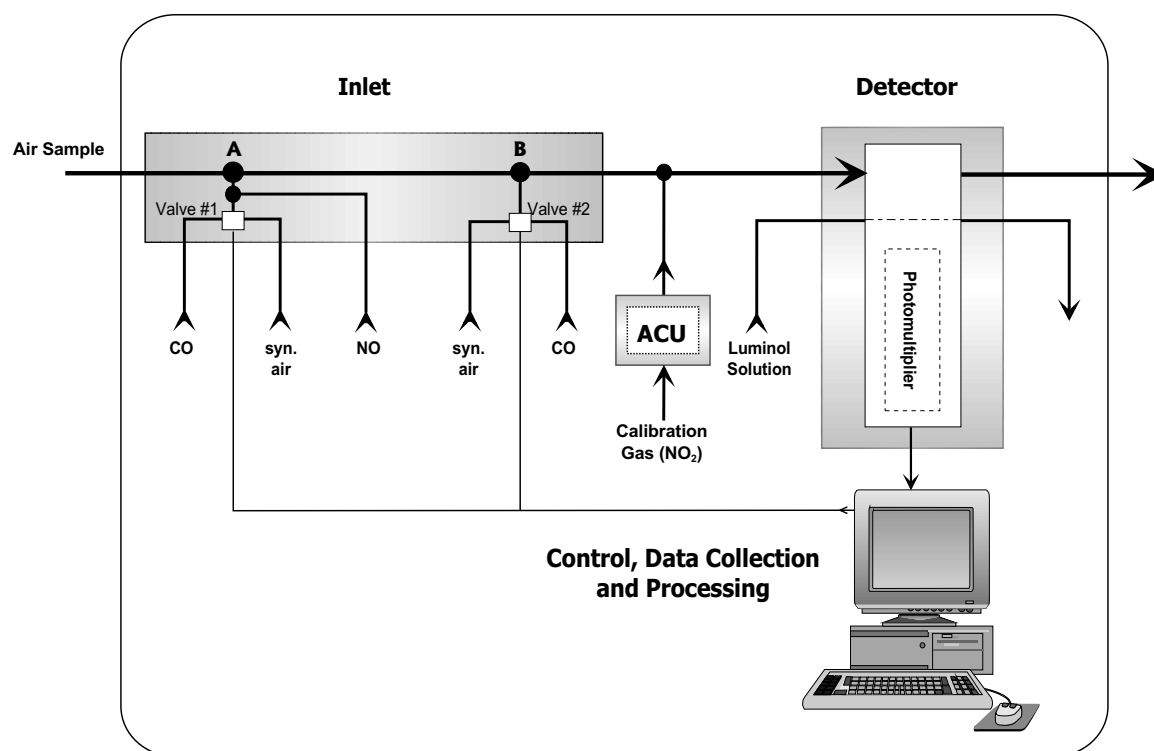


Figure 7.1: Schematic representation of the chemical amplifier used in the current study. ACU denotes the Automated Calibration Unit.

- and the control and data acquisition system.

The inlet is comprised of an intake and a reaction chamber in which peroxy radicals react with NO, resulting in NO₂ production. The chain reaction with NO and CO (see Section 6.1) also amplifies the NO₂ signal due to RO_x by a factor of 50-150. The signal would otherwise be vanishingly small in relation to the level of background NO₂. Solenoid valves and control electronics alternately add CO and synthetic air at each of two T-junctions, thereby modulating the NO₂ signal to allow background affects to be subtracted from the signal. The detector measures NO₂ on the basis of the chemiluminescent reaction between NO₂ and luminol. The ACU allows the automatic calibration of the detector every two hours. The control electronics and the data acquisition system complete the instrument and are responsible for switching the valves controlling the flow of CO and synthetic air in the inlet and of calibration gas in the ACU, as well as for collecting and storing the signal from the detector. The main components of the chemical amplifier are represented schematically in Figure 7.1 and the most important parameters of the chemical amplifier are summarised in Table 7.1. Each of the four main components is described in more detail in the following subsections.

The inlet has been mounted on the roof platform of a container since 1996, at a height of ca. 1.7 m above the platform and ca. 10 m above ground level (see Chapter

Table 7.1: Main characteristics of the peroxy radical chemical amplifier

Inlet

Flow rate of NO (300 ppmv in N ₂)	0.010 slpm
Flow rate of CO (grade 2.0)	0.18 slpm
Flow rate of synthetic air (80% N ₂ , 20% O ₂)	0.18 slpm
Mixing ratio of CO in reaction chamber	10%
Mixing ratio of NO in reaction chamber	1.67 ppmv
Length of intake	5 cm
Length of reaction tube	1.6 m
Reaction tube and intake:	
material	PFA Teflon
outer diameter	1/4" (6.35 mm)
inner diameter	5/32" (3.97 mm)
Time in intake	0.02 s
Time in reaction tube	0.66 s
ε_{HO_2} , estimated	0.05
Total length of tubing between Inlet and NO ₂ Detector	10 m
Tubing:	
outer diameter	1/4" (6.35 mm)
inner diameter	3/16" (4.83 mm)
Time between inlet and detector	5.6 s
Range of the amplification factor or chain length	50 - 150

NO₂ Detector

Flow rate of the air sample	1.61 slpm
Flow rate of NO ₂ added to main flow	0.020 slpm
Mixing ratio of NO ₂ from permeation tube (normal operation)	ca. 1.7 ppmv
Resulting mixing ratio of NO ₂ added to main flow	ca. 17 ppbv
Total flow rate through detector	2 slpm
Operation voltage of PMT	-1000 V

Timing

Length of measurement cycle ^a	1 min.
Dead time after switching	5 s

^aEach cycle consists of two modes, a measurement and a background mode, each of which lasts 30 s

8). All other main components were operated inside the container. The supplies of NO, CO, N₂ and synthetic air required by the CA were stored in a gas bottle locker at the side of the containers. Colour coded nylon tubing was used for the gas supply lines. Prior to 1998, low purity CO (CO 2.0, Alphagas) stored in aluminium bottles was used for the CO supply. Aluminium bottles were used to minimise interference due to ferric carbonyl compounds which can form in steel bottles. Steel bottles (CO 2.0, AGA Gas) were used in 1999, with no noticeable effect on the signal. A reducing trap filled with iodine coated active charcoal (Riedel de Haan, R180060500G) was used to remove any residual carbonyl compounds in the gas supply. Synthetic air (6.0 grade) and N₂ (5.0 grade) were supplied variously by Messer Griesheim and AGA Gas. The NO mixture (nominal mixing ratio: 300 ppmv in N₂) was supplied by Messer Griesheim. Two traps containing ferric sulfate heptahydrate (Fe₂SO₄·7H₂O, Merck, 3965, p.a. grade) were installed in the gas supply line to remove any NO₂ in the NO supply resulting from the reaction of NO with residual O₂ in the gas bottles (Reaction 2.5). They were situated before the MFC and just before the inlet. All gas flow rates were controlled using Hastings Mass Flow Controllers¹ (MFC; Series HFC-202) and Control Units (Model 400).

Teflon PFA 440HP tubing was used for all flow lines carrying either sample gas or NO₂ calibration gas. The outer diameter was 1/4" (6.35 mm) for most flow lines, and 1/8" (3.18 mm) for the few exceptions. All fittings in contact with NO₂ or sample air were also PFA Teflon (Galtek). The gas tubing between the inlet and detector had an internal diameter of 0.190" (4.83 mm) and a length of ca. 10 m, which at a total flow rate² of 1.98 slpm³ resulted in a residence time in the tubing after leaving the inlet of 5.5 seconds.

A constant flow of 0.020 slpm NO₂ is added to the main flow line shortly before the detector by means of the ACU. This ensures that even at low levels of background NO₂ the signal is in the linear region of the detector (see Section 7.1.2).

7.1.1 Inlet

The inlet of the CA is shown schematically in Figure 7.2. It consists of a short intake, followed by a reaction chamber in which the peroxy radicals react with NO and CO, together with control components for switching the flow paths of CO gas and synthetic air between the two addition points. This allows the CA to switch between measurement and background modes. Synthetic air is added at the opposite T-junction to CO to dampen any pressure surges caused by switching. The short intake decouples

¹Mass Flow Controllers measure gas flow on the basis of mass, as opposed to volume, so that all flow rates are automatically corrected to standard temperature and pressure (STP: 273 K, 1013 hPa).

²The total flow rate includes the flow of sample air plus the added CO, NO and synthetic air. The flow rate of sample air is equal to the total flow rate minus the flow of added gas, i.e. 1.61 slpm.

³slpm = standard litre per minute, flow rate normalised to STP.

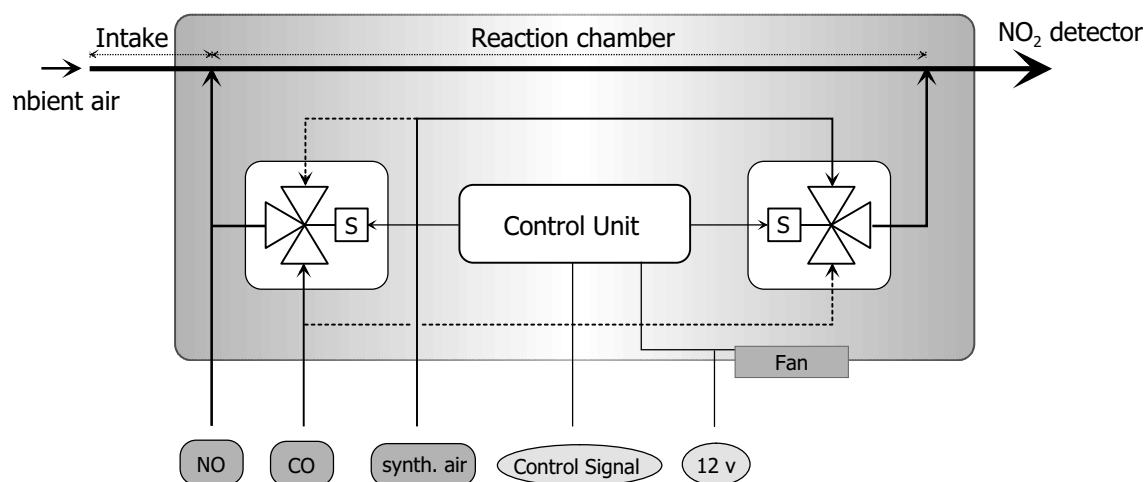


Figure 7.2: Schematic representation of the inlet. The two valves are solenoid actuated and are controlled by signals from the digital output of the ADC-16 card. Solid lines show the default gas flow in measurement mode; the changed flow through the valves during background mode is indicated by dashed lines.

the reactor slightly from the atmosphere, ensuring that CO and NO are not lost from the reactor during wind gusts, and that the air sample is not influenced by radical loss on the housing. It is situated in front of the T-union addition point for NO and CO/synthetic air which marks the beginning of the reaction chamber. Both intake and reaction chamber consist of PFA Teflon tubing with an outside diameter of 1/4" (6.35 mm) and an inner diameter of 5/32" (3.97 mm). All internal fittings are also PFA Teflon. The intake is ca. 5 cm long, and the reaction chamber has a length of 1.6 m. This results in a total inlet volume of 19.8 ml and a residence time of 0.68 s.

CO and synthetic air are switched using Teflon coated solenoid valves (Galtek, 203-3414-115). They are electrically actuated (12 v, 12 W) using power relays (Conrad Electronics, 194-565) controlled by the system software. Solenoid valves and power relays are both mounted inside the inlet housing. The entire inlet is housed in a plastic housing and is shielded from direct sunlight by an opaque outer housing. A fan mounted on the base of the inner housing provides ventilation to prevent overheating due to the valves.

Teflon was selected for the inlet on the basis of its practicality, and to provide consistency over the measurement period. The amplification factor deteriorates over time due to aerosol deposition in the inlet, but is quantified by regular calibration. The Teflon tubing in the inlet was replaced after the amplification factor dropped below ca. 50, although this was delayed as long as possible. The inlet tended to be more stable with a lower amplification factor than when it was frequently changed to achieve a high amplification factor.

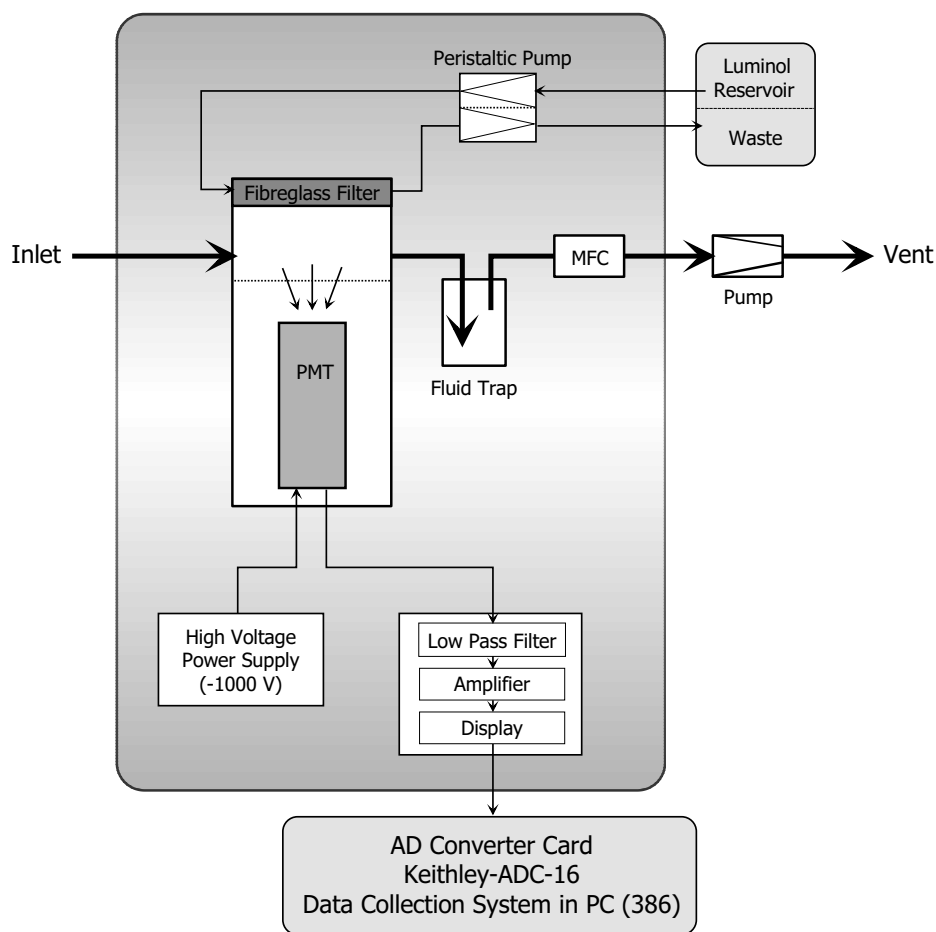


Figure 7.3: Schematic representation of the NO₂ detector. PMT denotes the photomultiplier; MFC is a mass flow controller.

7.1.2 NO₂ detector

NO₂ is detected on the basis of its chemiluminescent reaction with luminol in a detector based on the design of *Maeda et al.* [1980] and *Wendel et al.* [1983]. The detector was custom built for the CA and is shown schematically in Figure 7.3.

The detector consists of a head-on type photomultiplier tube (PMT, Hamamatsu R268; power supply EGG Ortec 456H, -1000 V) and a vertically mounted fibreglass filter wick (Millipore GF/D fibreglass filter, 6.0 cm diameter) over which an alkaline solution containing luminol (5-amino-2,3-dihydro-1,4-phthalazinedione) is pumped. The solution contains 5×10^{-4} M luminol (Sigma-Aldrich A-8511), 5×10^{-2} M sodium sulphite anhydride (Na₂SO₃; Fluka 71989) and 0.1% 2-propanol (2-C₃H₇OH; Fluka 59300) in 4×10^{-2} M potassium hydroxide (KOH; Fluka 60028). The sodium sulphite reduces the sensitivity of the solution to ozone, and the 2-propanol improves the NO₂ sensitivity in a similar way to the methanol used by *Wendel et al.* [1983]. The solution is stored away from light in an air tight bottle prior to use. During use, the sensitivity

gradually decreases with time and this is accelerated at high temperatures. The aging process is probably due primarily to the evaporation of propanol, as adding 2-propanol to the aged solution was found to cause an immediate improvement in sensitivity.

A multiple headed peristaltic pump (Ismatec; MS-CA4 820) is used to pump the solution over the wick and to remove the used solution⁴. The wick is mounted vertically against an inert Teflon plate, with the solution flowing over the wick from top to bottom. The sample air passes over the wick with the chemiluminescent reaction between NO₂ and luminol occurring on its surface. The chamber is sealed by an o-ring which also holds the filter element firmly in place. The wick is changed at irregular intervals whenever the precipitation of luminol causes the sensitivity of the detector to deteriorate.

The reaction with NO₂ results in the oxidation of luminol and produces radiation in the wavelength range 400-500 nm [Cantrell *et al.*, 1993b]. This is detected by a head-on PMT with a peak response at 420 nm, operated at -1000 V. The photomultiplier is mounted in a metal housing at right angles to the surface of the wick and faces the reaction chamber through a quartz window, sealed by an o-ring. The resulting current signal is converted into a voltage signal and amplified using a high impedance operational amplifier circuit with low pass filter. The output is displayed in relative units on a digital display unit and is converted to a digital signal by a 16-bit AD converter card in the PC-based control and data acquisition system (see Section 7.1.3).

Although the exact mechanism of the reaction between luminol and NO₂ is still not clear, it appears to involve two NO₂ molecules [Cantrell *et al.*, 1993b; Heitlinger, 1997; Konrad, 1997], which leads to a nonlinear signal at low concentrations of NO₂. It has been proposed by Konrad [1997] that the reaction proceeds via the attachment of two NO₂ molecules to a luminol molecule, followed by oxidation of the complex by O₂ to 3-aminophthalate. As NO₂ is poorly soluble, the solution of the second NO₂ molecule is the rate limiting factor. The rate reducing effect of NO could also be explained by a reaction of this complex with NO [Heitlinger, 1997].

A quadratic polynomial was found to fit the calibration curves measured for the IMG-CA. An example of a calibration curve with pronounced nonlinearity is shown in Figure 7.4 on the next page. This nonlinearity was not observed during all calibrations, but where present it was taken into account during calibration of CL, see section 7.3. At higher concentrations the detector response was nearly linear. This nonlinearity can be a major source of error for absolute measurements of NO₂. To avoid this effect, the NO₂ detector was calibrated every two hours using a four point calibration at NO₂ levels similar to those experienced during measurements. As the detector response approaches linearity over smaller ranges and at higher concentrations, a linear fit to this calibration data was used for demodulating the signal.

⁴Tygon tubing (0.38 mm i.D.) is used to provide the flow of solution to the detector, while Pharmamed tubing (0.51 mm i.D.) is used to remove the spent solution. The longer lifetime and higher capacity of the Pharmamed tubing helps prevent flooding of the chamber due to failure of the tubing.

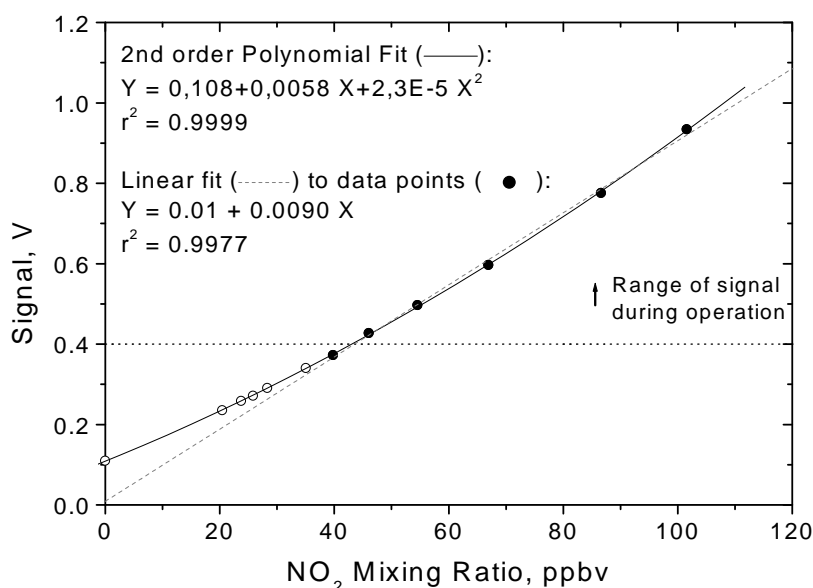


Figure 7.4: Typical NO_2 calibration curve for the NO_2 detector exhibiting a slight nonlinearity, from 9 August, 1999. Parameters are shown for a 2nd order polynomial fit and for a linear fit to the solid points. The minimum signal level observed during that day's measurements is represented by a dotted line.

To further ensure that the detector operated in the linear region, NO_2 was added to the air stream before the detector, so that the concentration of NO_2 at the detector was lifted slightly. The demodulated signal due to RO_x radicals is then described by the linear relationship

$$\Delta S \approx \frac{1}{a} \Delta[\text{NO}_2] \quad \text{for } [\text{NO}_2] > b \quad (7.1)$$

where $a = \frac{1}{s}$ (see Equation 6.7 on page 60) is the detector response in V ppbv^{-1} , and b is the concentration at which the signal becomes linear. The NO_2 concentration is lifted further by NO_2 produced during the titration of ozone in the inlet, so that this condition is generally satisfied during normal operation. Although the nonlinearity of the detector is important for absolute NO_2 measurements, such as are necessary during determination of CL, it is not expected to be significant for the demodulated signal measurements. The detector response to NO_2 was determined regularly as outlined in Section 7.2.

7.1.3 Data acquisition and control system

The control and data acquisition system is a PC-based system which operates under MS-DOS on a 386 computer using the custom-written software "rox.exe". The software programme was written using Quick Basic and compiled as an executable file.

Besides carrying out data acquisition, the programme is responsible for controlling the valves in the inlet, as well as for running an automated calibration routine for the NO₂ detector every two hours.

The system uses a 16-bit integrating Analogue-Digital Converter (ADC) card from Keithley (ADC16) both for data acquisition and to actuate the relays controlling the valves. The signal is integrated by the ADC16 over ca. 60 ms to ensure repeatability even in noisy environments, allowing a sampling frequency of up to 16 Hz. The voltage signal from the NO₂ detector is acquired with 16 bit resolution and is averaged over a default period of 25 seconds. Data is written to disk during the dead time immediately following completion of a mode. The digital outputs control the solenoid valves in the inlet and the ACU by means of power relay switching circuits (DC solid state relay from Conrad Electronics; 19 45 65) which switch the approximately 1 A required by the valves.

The ADC parameters, timing and file path are stored in a configuration file which can be edited using the programme. This allows the length of the measurement cycle and the dead time between modes to be adjusted for the current system characteristics. The dead time between modes is 5 seconds by default, during which data acquisition is suspended to avoid the effects of pressure surges.

The mean detector signal, standard deviation, total gas flow rate through the detector, and information about valve position is written to disk for each data point after each mode. The software system starts automatically after each computer reboot, so that the control system will restart after a power outage without the need for manual intervention. Further details are provided in Appendix A.1.

7.1.4 Data analysis software

The CA data files are subsequently analysed using the custom programme “`modsig.exe`”. The programme converts the voltage signal from the detector to a demodulated signal and to an NO₂ concentration using the calibration data contained in the data file. The programme was written using Borland C/C++ (Version 5) and runs under Win95, or higher. Further details of the programme can be found in Appendix A.2.

The data files to be processed are first read into dynamic memory, whereby data from the automated calibration procedure are extracted from the file and analysed to determine the sensitivity of the NO₂ detector. This information is then used after demodulation to convert the signal into the equivalent NO₂ signal (ΔNO_2).

The demodulation procedure involves first determining the background signal and then subtracting it from the signal during measurement mode. This process is shown schematically in Figure 7.5 for the demodulation of 15 minutes of raw data. The average background signal (S_{det}^0) is obtained by averaging the background mode detector signal ($S_{det,t}^0$) over two measurement cycles. Changes in NO₂ and O₃ levels at time

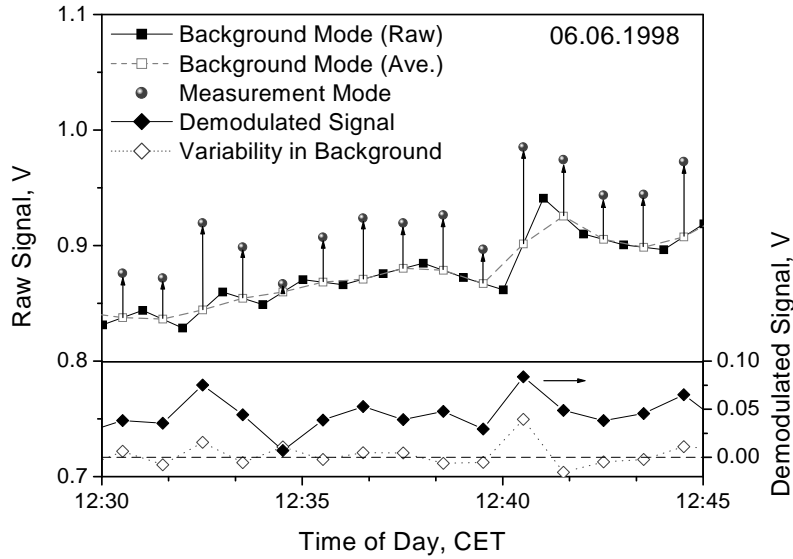


Figure 7.5: Example of the demodulation procedure for a signal from 6 June 1998. The original data are shown by the solid squares (background mode), and the shaded circles (measurement mode). The open squares represent the average background signal, S_{det}^0 , which is defined in the text; the arrows in the upper frame represent the difference between the modes due to RO_x . In the lower panel, the solid diamonds are the resulting demodulated signal, and the open diamonds represent S_{noise} .

scales longer than the measurement period are thus taken into account:

$$S_{det}^0 = \frac{S_{det,t0}^0 + S_{det,t1}^0}{2} \quad (7.2)$$

This is then subtracted from the measurement mode signal (S_{det}^1) to obtain the raw demodulated voltage signal, which is due to ambient peroxy radicals:

$$S_{demod} = S_{det}^1 - S_{det}^0 \quad (7.3)$$

During periods for which S_{demod} is small, changes in the background could make a contribution to the demodulated signal. This spurious signal, referred to here as background noise, is calculated as

$$S_{noise} = \frac{S_{det,t1}^0 - S_{det,t0}^0}{2}$$

and is compared with the demodulated signal during evaluation of the data. The data was only used on days for which S_{demod} is significantly greater than S_{noise} .

The demodulated signal can then be converted into the equivalent NO_2 signal by multiplying S_{demod} by the detector response derived from the NO_2 calibration data from the automated calibration procedure described in Section 7.2.1. The procedure

provides a four point calibration, with the detector sensitivity determined using a linear fit of the measured signal versus the added NO₂ concentration. The time series for the NO₂ sensitivity factor is averaged using a three point running mean to account for outliers and for calibration points corrupted by changes in the background during the calibration.

The demodulated signal is automatically evaluated for outliers on the basis of a comparison of the observed instantaneous changes in the background signal with the average level of change for the entire day or night period. Rapid changes in the background signal are thus taken into account. These could otherwise contribute to an increased error in the peroxy radical signal, which is normally much smaller than the background. The variance in the background is much higher during the day than during the night [c.f., *Clemitshaw et al.*, 1997], so that the average nocturnal level of change is considered separately to that during the day. A data point is rejected when the observed change in the background signal is greater than three times the average difference in the background signal for the appropriate time period.

The processed data were output as one minute values and as ten minute averages, which were then used for the data analysis. Ten minute averages lying further than 5σ from the average daytime or night-time values were also rejected in order to remove extreme outliers from the data set. The peroxy radical concentration was subsequently calculated using Equation 6.8. The NO₂ sensitivity and the effective amplification factor required for the calculation were determined by calibrating the NO₂ detector and CA inlet as described in the following sections.

7.2 Calibration of the NO₂ detector

The NO₂ detector was calibrated regularly using three different procedures at different time scales:

- an automated calibration procedure, using two NO₂ permeation tubes with differing permeation rates, provides a four point calibration every two hours,
- a manual calibration, involving the step-wise dilution of NO₂ from a third permeation tube, allows the linearity of the detector to be checked, and
- a regression of the background signal versus the total concentration of O₃ and NO₂, which allows the results of the automated procedure to be corrected.

The NO₂ for the first two procedures were provided using permeation tubes (Vici Dynacal wafer devices). The permeation tubes were kept in two ovens⁵ at a constant temperature of 30°C. The tubes were continually bathed in a flow of N₂ gas (5.0

⁵The ovens for the CA were built based on the design and using printed circuit boards for the control electronics provided by Werner Haunold of the Zentrum für Umweltforschung.

Table 7.2: List of NO₂ permeation tubes used during the current study.

Id. number	Average Permeation Rate ng min ⁻¹	Period of Use
90F3 #50240	53.1	Aug. 1994 - July 1997
	76.3	July 1997 - June 2000
60F2 #66099	33.5	Sept. 1994 - July 1997
	67.9	July 1997 - June 2000
40T3 #59438	406.4	July 1995 - Nov. 1998
40T3 #79203	420.4	July 1999 - Aug. 2000

grade). The permeation rates were periodically determined gravimetrically using a Sartorius 2474 analytical balance, and calculating the weight change. The permeation tubes used during the project and their average emission rates are shown in Table 7.2.

The use of permeation tubes for calibration purposes is not without problems. The temperature must be kept stable over long periods, and due to the low permeation rates, they can only be determined as averages over several weeks or months. However, the concentration is better defined than for other practical alternatives, such as gas bottles, which have limited life times. Titration of O₃ with NO, such as is used for the calibration of the TECAN NO_x analyser (see page 104), is not suitable for constant use and also involves the addition of excess NO, which could affect detector sensitivity.

7.2.1 Automatic calibration procedure

The automatic calibration procedure was carried out every two hours and involves adding different concentrations of NO₂ to the flow of ambient air, which provides the background level. This allows the response of the detector to be determined at ambient signal levels, thus avoiding the non linearity effect observed at lower NO₂ concentrations. A linear fit through the calibration data gives the NO₂ sensitivity (s) which is required to calculate the equivalent NO₂ concentration from the observed signal.

An Automated Calibration Unit (ACU) which was designed for the CA allows NO₂ from two permeation tubes to be added in varying combinations to the flow of sample air. The ACU is shown schematically in Figure 7.6. The ACU consists of several three-way Teflon coated solenoid valves (Galtek), each of which controls the flow of NO₂ from one permeation tube, directing it into the main sample flow or to a vent. The solenoid valves are switched by power relays which are in turn controlled by digital signals from the ADC-16 card. A total of four calibration points (including a null point) is possible using two permeation tubes. The NO₂ concentration is held for four minutes at each level to allow the signal to stabilise, so that the four point calibration procedure lasts a total of 12 minutes. The detector signal is averaged and

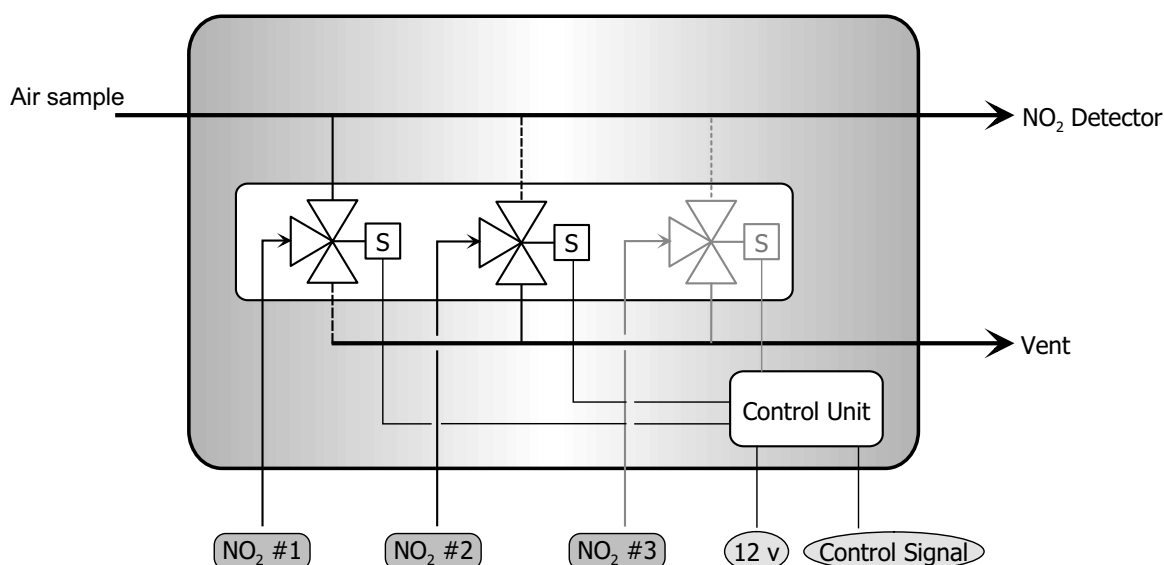


Figure 7.6: Schematic representation of the **A**utomated **C**alibration **U**nit. The unit was designed to allow for up to three NO₂ sources; only two are currently implemented. S denotes the solenoid actuated valves. The default configuration is shown by the solid lines; the alternative positions used during calibration are indicated by dashed lines.

recorded every 30 seconds. The set of measurements at a given NO₂ concentration is analysed, and any points for which the probability of them belonging to the data set is less than 1% are rejected. The NO₂ concentration typically requires 30 - 60 seconds to stabilise after switching, so that the first point at each NO₂ concentration level is frequently rejected due to transient pressure effects and mixing times.

During analysis of the calibration data, the measured signal is associated with the corresponding NO₂ concentration and a linear regression is carried out for the data set, as shown in Figure 7.7. The resulting detector sensitivity is used in turn to calculate the NO₂ concentration from the demodulated voltage signal. The calibration is carried out every two hours to allow changes in the detector sensitivity to be accounted for.

In some cases the background signal changes significantly during calibration due to changes in the NO₂ or O₃ content of the ambient air. This introduces a major source of error into the detector sensitivity at this calibration point. This can be detected as a low correlation coefficient for the calibration point. Before being used to convert the demodulated signal, the conversion factors are also averaged using a three point running average which is weighted by the correlation coefficient. This reduces the error introduced by individual calibration points with a changing baseline.

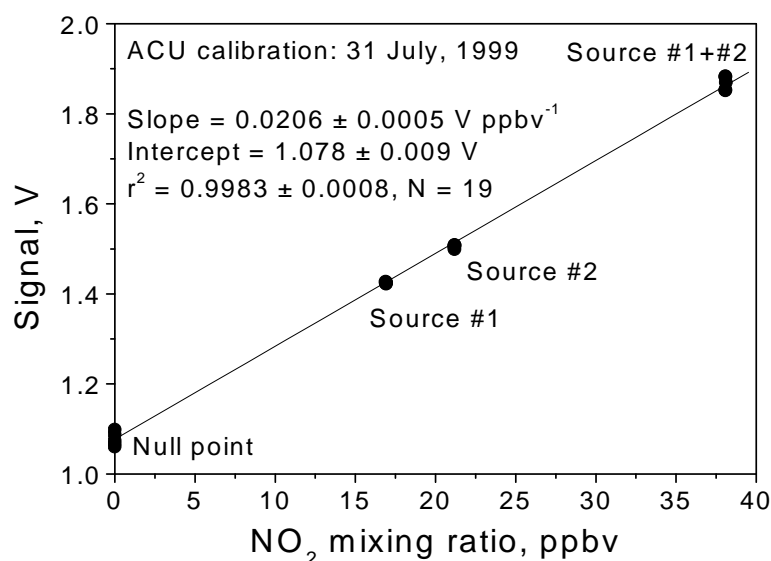


Figure 7.7: Typical data for calibration of the NO₂ detector: ACU calibration from 12:00, 31 July, 1999.

7.2.2 Calibration of detector linearity

In addition to this two hourly calibration, the CA is periodically calibrated manually using NO₂ from a permeation tube with a significantly higher permeation rate than those of the tubes used for the automated procedure. NO₂ from the permeation tube is diluted with synthetic air and is vented through a Teflon T-union attached to the CA intake. The total flow rate is always greater than the sample flow of the CA, so that ambient air does not enter the CA during calibration. The flow rate of synthetic air is successively increased, resulting in a step wise dilution of the NO₂ concentration. This method allows the detector to be calibrated over a much greater range of NO₂ concentrations than is possible using the ACU. The NO₂ concentration covers almost the entire range of NO₂ concentrations found during ambient measurements, whereby it is the detector response at low concentrations which is required to characterise the detector's nonlinearity. Figure 7.4 on page 78 shows an example of a calibration plot obtained using this method.

The NO₂ concentration at the inlet is then plotted against the voltage signal, and the sensitivity parameterised for the entire range of NO₂ concentrations. While this nonlinearity does not affect the demodulated signal, it is important for determining the amplification factor, as described below. A calibration of detector linearity is carried out at intervals of about one week.

7.2.3 Correlation of background signal with measured oxidant levels

While the ACU allows relative changes in the detector sensitivity to be accounted for, it is not an absolute calibration method, as NO_2 losses in the tubing, which could change with time, cannot be accounted for. This is overcome using the background signal, which is a natural byproduct of CA operation. The principal source of the background signal is the titration of ambient ozone by high concentrations of NO in the inlet, resulting in the production of NO_2 . A small contribution towards the background signal is made by ambient NO_2 and an even smaller random contribution by other components. These minor contributions can essentially be neglected. As the titration of ozone results in a stoichiometric conversion of NO to NO_2 , the background NO_2 signal should be equal to the sum of the observed mixing ratios of O_3 and NO_2 in ambient air, offset by the NO_2 added to the air flow to ensure linearity. Thus, a plot of the NO_2 mixing ratio obtained from the detector vs the sum of the mixing ratios of O_3 and NO_2 in ambient air should ideally have a slope of unity. In reality, a deviation from unity is observed due to losses in the tubing, etc. The response of the detector is normalised to the total mixing ratio of O_3 and NO_2 by using the slope of the plot to correct the data.

7.3 Calibration of the inlet

The amplification factor of the chemical amplifier is determined by calibrating the inlet with HO_2 radicals produced in a calibration source on the basis of the photolysis of water vapour at 185 nm. The HO_2 concentration is calculated using the measured concentration of ozone resulting from the concurrent photolysis of molecular O_2 at the same wavelength. The calibration source used in this project is based on a similar radical source originally described by *Schultz et al.* [1995]. Similar sources are used for calibration purposes by a number of groups, and one such source was tested during the PRICE II campaign [*Heitlinger*, 1997]. The working principle of such sources is summarised below.

7.3.1 HO_2 radical source

The radical source is shown in Figure 7.8 and consists of a 1 m quartz tube through which synthetic air containing 1 ppmv CO and a small amount of water vapour flows. Water vapour and O_2 are photolysed at 184.9 nm to form HO_2 radicals and O_3 . The light source is a PenRay Hg/Ar UV lamp (LOT-Oriel 6035) situated approximately 10 cm from the open end of the tube. Water vapour is added to the synthetic air as it flows through a glass frit in a humidifier unit. A defined amount of deionised water (Milli-Q)

is pumped onto the glass frit using a variable speed peristaltic pump (Ismatec, MS-4 Reglo 8-100 with black/orange Tygon tubing) operated near its minimum capacity.

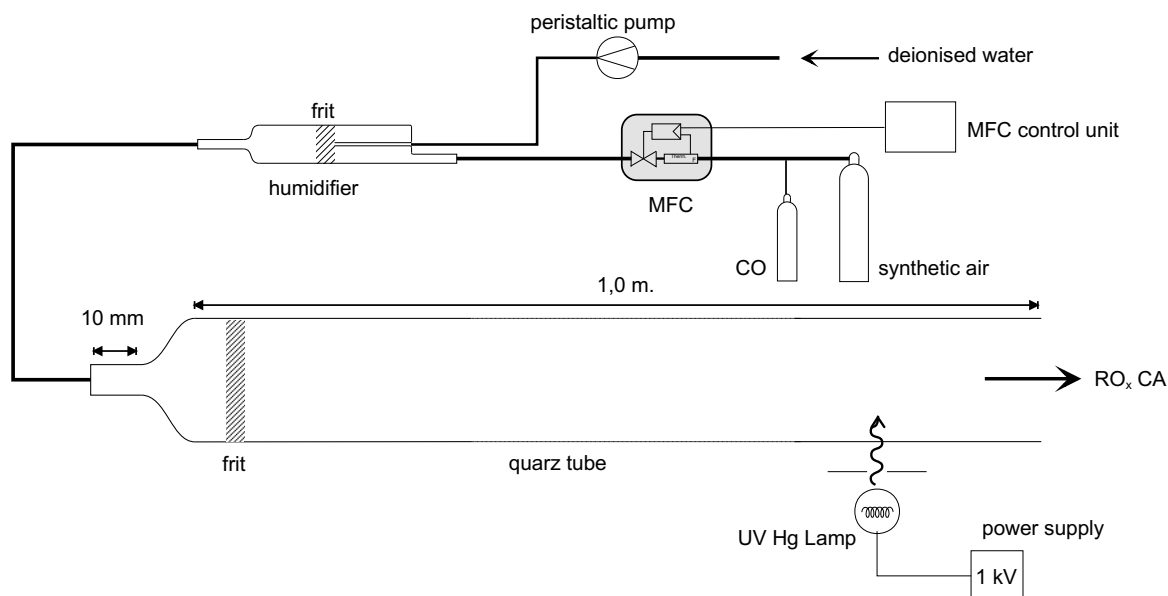
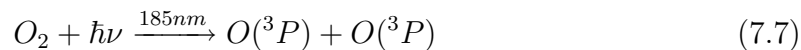


Figure 7.8: Schematic representation of the HO_2 radical source used for determining the amplification factor.

HO_2 is produced following the photolysis of water vapour by the 184.9 nm emission line to produce atomic H and OH radicals. The addition of a small amount of CO (1 ppmv) ensures that the OH radical is converted exclusively to HO_2 , again via an H atom, so that two HO_2 radicals are produced per H_2O molecule:



Ozone is produced independently at the same wavelength, following the photolysis of molecular oxygen:



The concurrent production of HO_2 and O_3 provides a means of determining the HO_2 concentration produced by the source. The local production rates of HO_2 and O_3 are defined by the primary photolysis steps

$$P_{\text{HO}_2} = \sigma_{\text{H}_2\text{O}}^{185} \cdot \phi_{7.4}^{185} \cdot \Theta^{185} \cdot [\text{H}_2\text{O}] \quad (7.9)$$

$$P_{\text{O}_3} = \sigma_{\text{O}_2}^{185} \cdot \phi_{7.7}^{185} \cdot \Theta^{185} \cdot [\text{O}_2] \quad (7.10)$$

where Θ^{185} is the photon flux at 184.95 nm,
 ϕ_i^{185} is the quantum yield of Reaction (*i*), and
 σ_X^{185} is the respective absorption cross section.

When diffusion and chemical loss terms are ignored, the ratio between the concentrations of HO₂ and O₃ is equal to the ratio of the time integrated production rates. The ratio of HO₂ and O₃ is approximately independent of factors controlling the absolute concentration, i.e., photon flux, flow rate and geometry [Schultz *et al.*, 1995], so that the ratio is effectively determined by

$$\frac{[HO_2]}{[O_3]} = \frac{\int \sigma_{H_2O}^{185} \cdot \phi_{7.4}^{185} \cdot \Theta^{185} \cdot [H_2O] \cdot dt}{\int \sigma_{O_2}^{185} \cdot \phi_{7.7}^{185} \cdot \Theta^{185} \cdot [O_2] \cdot dt} = \frac{\sigma_{H_2O}^{185} \cdot \phi_{7.4}^{185} \cdot [H_2O]}{\sigma_{O_2}^{185} \cdot \phi_{7.7}^{185} \cdot [O_2]} \quad (7.11)$$

The quantum yield is unity for both reactions under atmospheric conditions [Vermeil *et al.*, 1967; Washida *et al.*, 1971]. However, two radicals, or molecules, are produced in each reaction, so that $\phi_{7.4}^{185}$ and $\phi_{7.7}^{185}$ are effectively both equal to two and thus cancel out.

Schultz *et al.* [1995] used the NASA/JPL recommended value [DeMore *et al.*, 1994] from the review by Hudson and Kieffer [1975] of $5.5 \times 10^{-20} \text{ cm}^{-2}$ for the absorption cross section of water vapour, and a value of $0.96 \times 10^{-20} \text{ cm}^{-2}$ for O₂ derived from Washida *et al.* [1971]. The latter value was shown by Lanzendorf *et al.* [1997] to have been derived incorrectly, the correct value being $2.2 \times 10^{-20} \text{ cm}^{-2}$. Both these cross sections have been revised by more recent studies.

The absorption cross section for H₂O was measured by Yoshino *et al.* [1996] between 120 and 188 nm and the value at 185 nm was determined to be $10.1 \times 10^{-20} \text{ cm}^{-2}$. However it has been suggested by Cantrell *et al.* [1997] that these measurements were affected by high signal to noise ratios at the longer wavelengths. They obtained a slightly lower value of $(7.14 \pm 0.2) \times 10^{-20} \text{ cm}^{-2}$ at 184.9 nm using a low pressure Hg lamp. Independent measurements of the cross section between 183 and 193 nm by the same authors using a scanning double monochromator system obtained a comparable value of $(6.78 \pm 5 \%) \times 10^{-20} \text{ cm}^{-2}$ at 185 nm. These lower values are also supported by measurements made by Hofzumahaus *et al.* [1997] of $7.0 \times 10^{-20} \text{ cm}^{-2}$ and an unpublished measurement of $7.13 \times 10^{-20} \text{ cm}^{-2}$ made by John Crowley at MPI-Mainz [cited by Hofzumahaus *et al.*, 1997]. Recent measurements by Creasey *et al.* [2000] also agree very well with the value of Cantrell *et al.*, with a value of $(7.22 \pm 0.22) \times 10^{-20} \text{ cm}^{-2}$ being determined at 184.9 nm and 25°C. An average value of $(7.2 \pm 0.3) \times 10^{-20} \text{ cm}^{-2}$ based on the studies by Cantrell *et al.* [1997] and Creasey *et al.* [2000], was used in the current study.

Recent work has shown that the effective cross section of O₂ is subject to considerable uncertainty, and ideally should be determined independently for each experimental configuration. Lanzendorf *et al.* [1997] showed that the cross section for O₂ is affected by the operating conditions of the Hg lamp and presented absorption cross sections for lamps under typical and cooled operating conditions. This result has been underlined by Creasey *et al.* [2000], who has shown that the cross section

should be determined regularly for each individual UV lamp. The emission spectrum for the Hg lamp is not a perfect line emission, but undergoes spectral broadening, and lies on the steep flank of the R11 rotation line of the Schumann-Runge bands for O₂. The absorption cross section is thus very sensitive to changes in the emission spectrum. For similar operating conditions to those of the radical source used here, several authors report absorption cross sections for O₂ in the range 1.1 - 1.4 × 10⁻²⁰ cm⁻² [Lanzendorf *et al.*, 1997; Hofzumahaus *et al.*, 1997; Creasey *et al.*, 2000]. As it is no longer possible to determine the exact cross section for the UV lamp used in the study, the value for $\sigma_{O_2,eff}^{185}$ of $(1.16 \pm 0.20) \times 10^{-20}$ cm⁻² obtained by Creasey *et al.* [2000] for similar operating conditions was used in the current work.

Using these values for the absorption cross sections of H₂O and O₂, the ratio of the concentration of HO₂ to the O₃ concentration can be calculated using

$$\frac{[HO_2]}{[O_3]} = f \cdot \mu(H_2O) \quad (7.12)$$

where f is a constant defined by

$$f = \frac{\sigma_{H_2O}^{185} \cdot \phi_{7.4}^{185}}{\sigma_{O_2}^{185} \cdot \phi_{7.7}^{185} \cdot \mu(O_2)} = 31.0 \quad (7.13)$$

and $\mu(X)$ is the mixing ratio ($\mu(O_2) = 20\%$).

Calculations and measurements by Heitlinger [1997] and Hofzumahaus *et al.* [1997] have shown that the spectral lines at 254 nm and at 194 nm, either of which could theoretically also lead to a change in the HO₂/O₃ ratio due to ozone photolysis or production, have negligible effect on the ratio.

7.3.2 Calculation of the amplification factor

At the high NO concentrations in the inlet, ozone reacts completely with NO to produce NO₂, so that the signal during the CA background mode is essentially due to the ozone produced in the radical source. The measurement and background signals were then converted to their equivalent NO₂ concentrations and used in equation 7.12 to determine the amplification factor, CL:

$$\frac{[HO_2]}{[O_3]} = \frac{\frac{[NO_2]_{demod}}{CL}}{[NO_2]_{bkgrd} - [NO_2]_{null}} \quad (7.14)$$

$$\implies CL = \frac{[NO_2]_{demod}}{[NO_2]_{bkgrd} - [NO_2]_{null}} \cdot \frac{1}{f \cdot \mu(H_2O)} \quad (7.15)$$

When the detector response is linear, a constant conversion factor is used to convert the signal into the equivalent NO₂ concentration. As this conversion factor is used for concentrations in both the denominator and the numerator, it cancels out

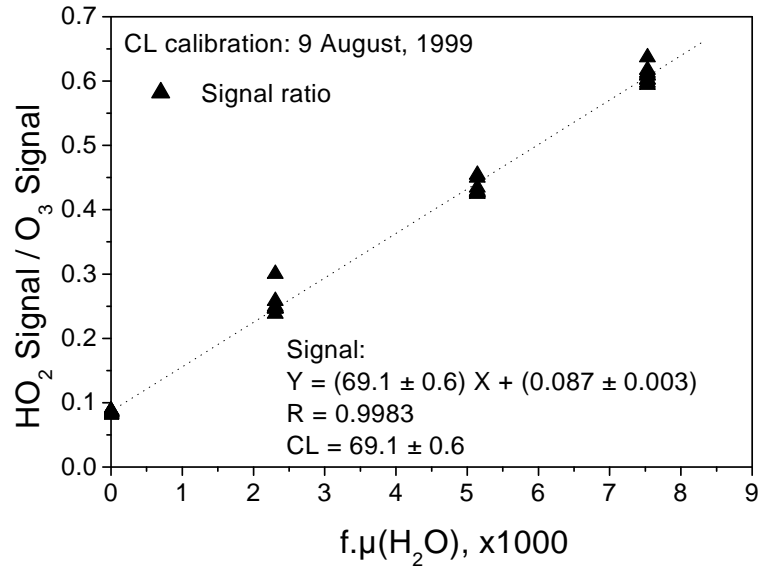


Figure 7.9: Typical data for calibration of the amplification factor: CL calibration using the HO₂ radical source, on 9 August, 1999.

in Equation 7.15, so that the appropriate signal can be substituted for the NO₂ concentration to calculate CL. However, any nonlinearity in the response of the NO₂ detector, which was discussed in Section 7.1.2, means that the signal should be converted to the equivalent NO₂ concentration, and these NO₂ concentrations should be used when calculating CL. Neglecting this nonlinearity was found during the PRICE I campaign to be the major cause for disagreement between the calibration results for different groups [Volz-Thomas *et al.*, 1999]. In the current study, the signals were converted to NO₂ concentrations using the nonlinear parameterisation obtained during the linearity test.

Measurements using the radical source have shown that a small, spurious modulated signal is present when the UV lamp is switched on in the absence of water vapour. This non-zero signal is probably due to water vapour and other impurities in the synthetic air used. Similar effects have been observed by other groups [Burrows, *personal communication*; Heitlinger, 1997] and can reach an equivalent water mixing ratio of up to 11 ppmv [Heitlinger, 1997]. Furthermore, measurements of similar radical sources using MIESR indicated the presence of organic peroxy radicals, even in the absence of water vapour, and this was attributed to the presence of impurities in the synthetic air, which were photolysed to produce organic RO₂. This spurious signal needs to be taken into account when calculating the amplification factor using Equation 7.15, whereby the demodulated signal measured in the absence of added water should be subtracted before calculating CL.

The CA was calibrated in the current work by varying the HO₂ concentration and deriving CL from a plot of the ratio of the signals (or ΔNO₂) vs μ(H₂O), as shown

in Figure 7.9. CL was then derived from the line of best fit. The HO₂ concentration was varied by changing the supply of water to the humidifier, thereby changing $\mu(\text{H}_2\text{O})$. This technique means that the effect of impurities in the synthetic air only contribute an offset to the plot and do not affect the determination of CL. The effect of nonlinearity due to high HO₂ concentrations has also been taken into account (see Section 6.3). The inlet was calibrated weekly during the summer measurement period, weather conditions permitting.

7.4 Error analysis

The uncertainty in the RO_x measurements can be estimated by applying error propagation techniques to Equation 6.8 on page 62 for calculating the RO_x mixing ratio.

$$[RO_x] = \frac{s\Delta S}{CL} \quad (6.8)$$

The uncertainty is estimated using the error propagation equation:

$$\sigma_{RO_x}^2 = \sigma_s^2 \left(\frac{\partial[RO_x]}{\partial s} \right)^2 + \sigma_{CL}^2 \left(\frac{\partial[RO_x]}{\partial CL} \right)^2 + \sigma_{\Delta S}^2 \left(\frac{\partial[RO_x]}{\partial \Delta S} \right)^2 \quad (7.16)$$

where σ is the standard deviation of the denoted quantity, and the various variables are defined as in Equation 6.8. Although some uncertainties in the following analysis are estimated values and not true standard deviations, unless noted otherwise they are treated as standard deviations for the purposes of the error propagation calculations. This simplifies to

$$\frac{\sigma_{RO_x}}{[RO_x]} = \sqrt{\frac{\sigma_s^2}{s^2} + \frac{\sigma_{CL}^2}{CL^2} + \frac{\sigma_{\Delta S}^2}{\Delta S^2}} \quad (7.17)$$

The relative uncertainty is defined as the standard deviation divided by the respective quantity. The total uncertainty is composed of both experimental uncertainties, which determine the precision of the measurements, and of systematic errors in the measurements and associated conversion coefficients, which contribute to the accuracy of the measurements. The uncertainties will be discussed below in terms of the instrumental errors, e.g. calibration uncertainties in the amplification factor (CL) and the detector response to NO₂, and those associated with ambient measurements, which affect the demodulated signal.

Table 7.3 summarises the current best estimate of the uncertainties in the quantities used to calculate the RO_x mixing ratio. The precision includes the estimated uncertainties or observed variations associated with the measurements, whereas the estimated accuracy also includes systematic errors.

Table 7.3: Estimated uncertainties in s and CL . These are used to calculate the total RO_x mixing ratio. The precision and accuracy are relative uncertainties for the given quantity. These are then combined using error propagation to obtain the relative uncertainty in s and CL .

	Precision, %	Accuracy, %
NO₂ Calibration		
Permeation rate	5	5
Dilution factor	0.5	2.5
Regression (single calibration)	8	8
Background Correction	1	1
NO₂ sensitivity, σ_s	7	8
CL Calibration		
f		18
H ₂ O mixing ratio	3.5	5.5
Nonlinearity of the NO ₂ detector	4	4
Regression	2.5	2.5
CL, σ_{CL}	6	20
Total Instrumental Uncertainty, in dry air		
	9	22
Water Effect		
Relative Humidity = 50%		40
Relative Humidity > 60%		50
CL, σ_{CL}, 50% RH	6	60
CL, σ_{CL}, 60% RH	6	70
Total Instrumental Uncertainty, including water dependence of CL		
at 50% RH	10	61
at 60% RH	10	70

7.4.1 Uncertainty due to calibration

The instrumental uncertainty is considered here to be defined by the uncertainties in the calibration of the CA with NO₂ and HO₂. The uncertainties in each of the calibration coefficients are discussed below.

Uncertainty in NO₂ detector sensitivity

The overall uncertainty in the detector sensitivity (s ; see Equation 6.7 on page 60) determined using the ACU is due to uncertainties in the following parameters:

- The permeation rate of the NO₂ sources. The precision was approximately 5% during 1998-1999.
- The dilution factor. This was determined from the uncertainties in the flow rates, with a precision of better than 0.5% and an accuracy of less than 2.5%.
- The statistical error in the slope of the regression fit used to calculate s .

The statistical error in the regression fit defines the precision of the calibration. This takes into account changes in the background NO₂ concentration during calibration, which is the main source of uncertainty in calibrations using the ACU. The uncertainty was averaged over all calibrations made during 1998 to 1999 and was about 8% for a single calibration. This was then averaged over three subsequent calibrations. The NO₂ sensitivity was also corrected for losses in the tubing by calibrating the signal against variations in the background. The uncertainty was calculated from the statistical uncertainty in this regression and amounted to approximately 1%. Thus, the overall precision of the NO₂ response is estimated to be $\pm 7\%$, with the total uncertainty from all these sources estimated to be about $\pm 8\%$.

Uncertainty in CL

The amplification factor, CL, is determined using Equation 7.15. The uncertainty in the amplification factor is made up of contributions from the following factors:

- the photon fluxes for H₂O and O₂; these are used to calculate the conversion constant f in Equation 7.13, and thence the HO₂ concentration,
- the water mixing ratio. This uncertainty is primarily caused by the variability in the flow rate of water, about 3.5%, and the estimated error in the flow rate along the tube, which has an estimated precision of about 0.2% and an accuracy of better than 2%;
- the parameterisation of the detector nonlinearity, and
- the statistical error in the regression fit to the calibration data, which is estimated to be about 2.5%.

The photon fluxes for H₂O and O₃ have a large degree of uncertainty, and the uncertainties were calculated using published values. They make the greatest contribution to the uncertainty in the amplification factor in dry air. The nonlinearity of the NO₂

detector was only apparent during some calibrations. As a result, the estimated uncertainty of 4% represents a maximum uncertainty from this source. Taking these sources of uncertainty into account, the overall precision of the CL calibrations in dry air is estimated to be about 6%, and the total estimated accuracy is about 20%.

7.4.2 Uncertainty in ambient measurements

The ambient measurements are also affected by the ambient operating conditions, which introduce further uncertainties. The most important sources of uncertainty are:

- the sensitivity of the amplification to humidity,
- changes in the background signal, and
- the unknown mix of RO_x radical species present in ambient air.

The largest source of uncertainty is the sensitivity of the CA to ambient water vapour, which was discussed in the previous chapter. Due to the paucity of published studies of this dependency, and differences in the absolute values at high RH (see Figure 6.6), the associated error is difficult to estimate. The results of *Reichert* [2000] lie 40% below those of *Mihele et al.* [1999] at 60% RH, although the quoted uncertainties in the individual measurements are much lower. Until the reasons for this difference are ascertained, the relative uncertainty introduced by the water effect is considered here to be defined by the difference between these two curves, expressed as the relative uncertainty in the parameterisation of the *Mihele et al.* data used here. It is conservatively estimated to be 50% or greater at relative humidities above 60%, and 40% at 50% relative humidity. The accuracy of RH measurements is estimated by the DWD to be up to 10%, however this is outweighed by the large uncertainty in the curve defining the changing sensitivity with humidity. This effect represents a range of possible values, rather than the standard deviation of the sensitivity factor. Consequently, this uncertainty must be added directly to the uncertainty in CL for dry air, rather than by using the equation for standard deviations, c.f. Equation 7.17.

The sensitivity to water results in a very poor SNR on days with high humidity, as the RO_x signal is barely amplified enough to distinguish it from the background fluctuations. For this reason, data from days on which the SNR was less than unity were rejected from the data base. This was mostly the case on days with high humidity.

The background signal results from contributions due to O_3 , NO_2 , and PAN, etc., in the ambient air and must be known when calculating the demodulated signal. Changes in ambient levels of these compounds on a time scale comparable to the modulation period cause a spurious component to be added to the demodulated signal. This causes the signal-to-noise ratio (SNR) to decrease, with an associated increase in measurement uncertainty. The SNR was improved by averaging the data

over ten minutes. These fluctuations vary according to the ambient conditions, so the SNR can vary significantly from day to day. The average level of this fluctuation for the measurements made at Kleiner Feldberg was 9 pptv, and this should be considered to define the average detection limit for the Kleiner Feldberg measurements. At Hohenpeissenberg the SNR was higher, with a detection limit of about 5 pptv.

The response of the CA also varies for different RO_x species. This uncertainty is inherent to most indirect measurements of total RO_x concentrations. As discussed in the previous chapter, the CA probably detects 80-90% of radicals during daytime conditions, although the night-time efficiency may be somewhat lower.

The effective precision of the RO_x measurements cannot be determined using measurements made under calibration conditions, as the changing background signal under ambient conditions is an important additional factor which affects the precision during field measurements. It is currently not possible to differentiate between random fluctuations which limit the precision, such as changes in the background signal, and real fluctuations in the RO_x concentration. The precision of the RO_x measurements under ambient conditions was estimated from the fluctuations of the signal attributed to RO_x between 02:00 and 05:00 CET. At this time of night, the RO_x concentration is at a minimum, although radicals are still present and the presence of night-time chemistry means that real fluctuations in the signal are almost certainly present. The standard deviation is considered to be the maximum absolute precision, although it is not representative of daytime conditions and gives the upper limit of the precision at night. The average standard deviation for these fluctuations was 7 pptv.

7.4.3 Total uncertainty in the measurements

The total uncertainty in the RO_x measurements can thus be estimated from the contributions discussed above. Uncertainties in the calibration procedures result in an estimated precision for the CA in dry air of about 9% and a total accuracy of about 22%. The largest sources of uncertainty were those associated with the photolysis rate of O₂ and the statistical error in the ACU calibration, which was due to changes in the background during calibration.

Under ambient conditions, the accuracy of the measurements is limited by the inadequately known sensitivity of the amplification factor to water vapour, which also affects the SNR and hence the detection limit. This dependence makes the greatest contribution to the overall uncertainty.

Taking all these various factors into account, the combined accuracy of the RO_x measurements is estimated to be approximately 70% for relative humidities above 60%, and about 61% at around 50% relative humidity. The detection limit is estimated to be 9 pptv for average conditions experienced at Kleiner Feldberg. The absolute precision of night-time ambient measurements due to fluctuations in the RO_x level is estimated to be 7 pptv. This would correspond to a relative precision of about 14% at 60 pptv, when the contribution from the calibration coefficients is included.

Chapter 8

Instrumentation and Site

Descriptions

Measurements of peroxy radicals, ozone and several other atmospheric trace gases were made at the Taunus Observatory on Kleiner Feldberg, during the summers 1995 - 1999. An intensive measurement campaign was also held at the Meteorological Observatory Hohenpeissenberg (MOHp), during the period 17 June to 6 July, 2000. During the field campaign, more extensive measurements of atmospheric components were possible due to the wider range of instruments operated at MOHp.

The current chapter provides a description of the two measurement sites, followed by a description of the instrumentation used for the measurements.

8.1 Site description: Kleiner Feldberg

The Taunus Observatory (TO) is operated by the Institute of Meteorology and Geophysics (IMG) on behalf of the Johann Wolfgang Goethe University, Frankfurt am Main, and is situated at a height of 825 m above sea level on the summit of Kleiner Feldberg (50°13'25" N, 8°26'56" E), a mountain on the main ridge of the Taunus Range. Local noon occurs at 12:26 CET. The Taunus Range lies on the northern rim of the relatively heavily industrialised Rhine-Main region, as can be seen in Figure 8.1. The Observatory lies about 30 km northwest from Frankfurt am Main. In contrast, the area for 50 - 100 km to the north of Kleiner Feldberg is only lightly populated and is devoid of major industry.

The area surrounding the Observatory is mainly mixed forest which is crossed by a few main roads. Several smaller towns lie within 5 km of the Observatory. A

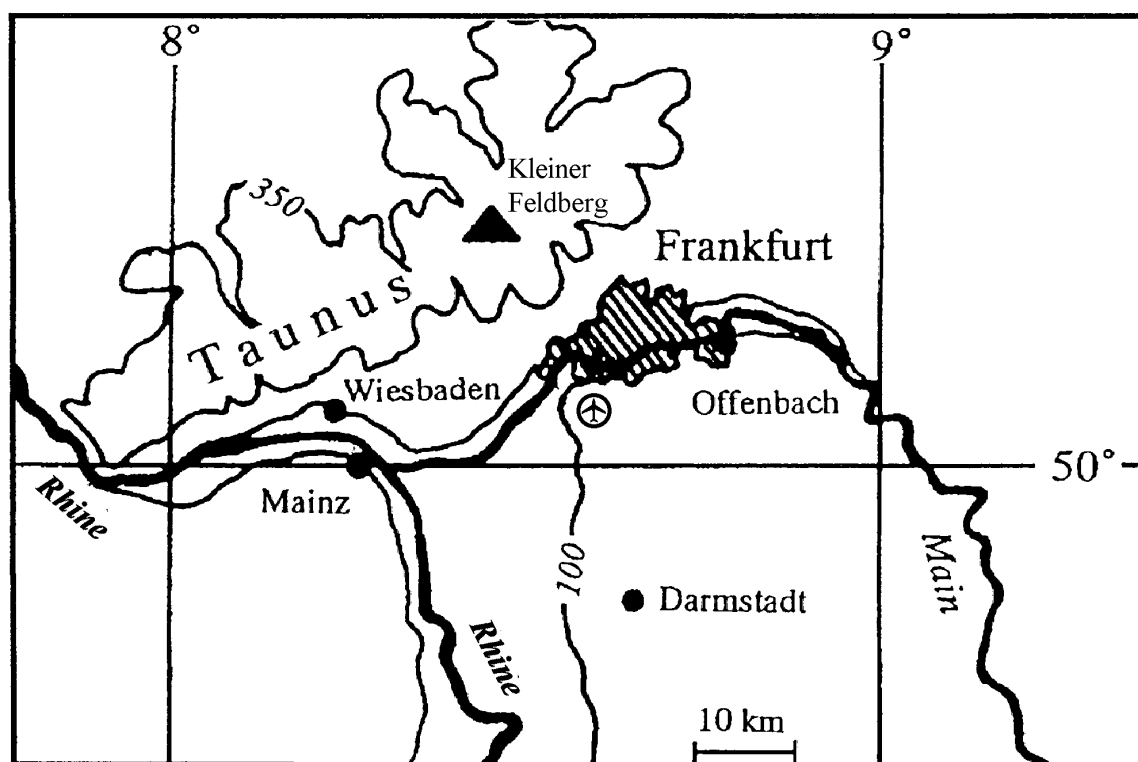


Figure 8.1: Sketch map of central Germany showing the location of Kleiner Feldberg in relation to the Rhine-Main area and the Upper Rhine Valley. The Taunus Range is defined by a contour at 350 m, the Rhine and Main valleys by a 100 m contour. Taken from *Wobrock et al.* [1994].

road passes a few hundred metres from and about 100 m below the Observatory. The road is only lightly frequented, except during weekends, when the Taunus Range is used by relatively large numbers of visitors for recreational purposes. Figure 8.2 shows a topographical map of the vicinity of the Kleiner Feldberg and the site of the Taunus Observatory. Figure 8.3 shows the orography of the Taunus Range. In the near vicinity are two other mountains which influence flow patterns: Großer Feldberg (878 m asl; 1.3 km NE of Kleiner Feldberg) and Altkönig (798 m asl; 2.7 km ESE). The meteorological conditions, including typical flow patterns, will be further discussed in Chapter 9.

The instruments were all situated at or near the summit of Kleiner Feldberg. During 1995 the peroxy radical instrument was located in a container near the summit of Kleiner Feldberg, with the inlet situated on a scaffold approximately 5 m above ground level. In the following year the instrument was moved to a container tower at the summit, where it remained for the following years' measurements. Since 1996 the inlet has been situated on the southwestern side of the tower platform at approximately 8 m above ground level, and nearly 2 m above the platform. The inlet for the HLUG measurements was situated at a height of about 2 m above the northeastern

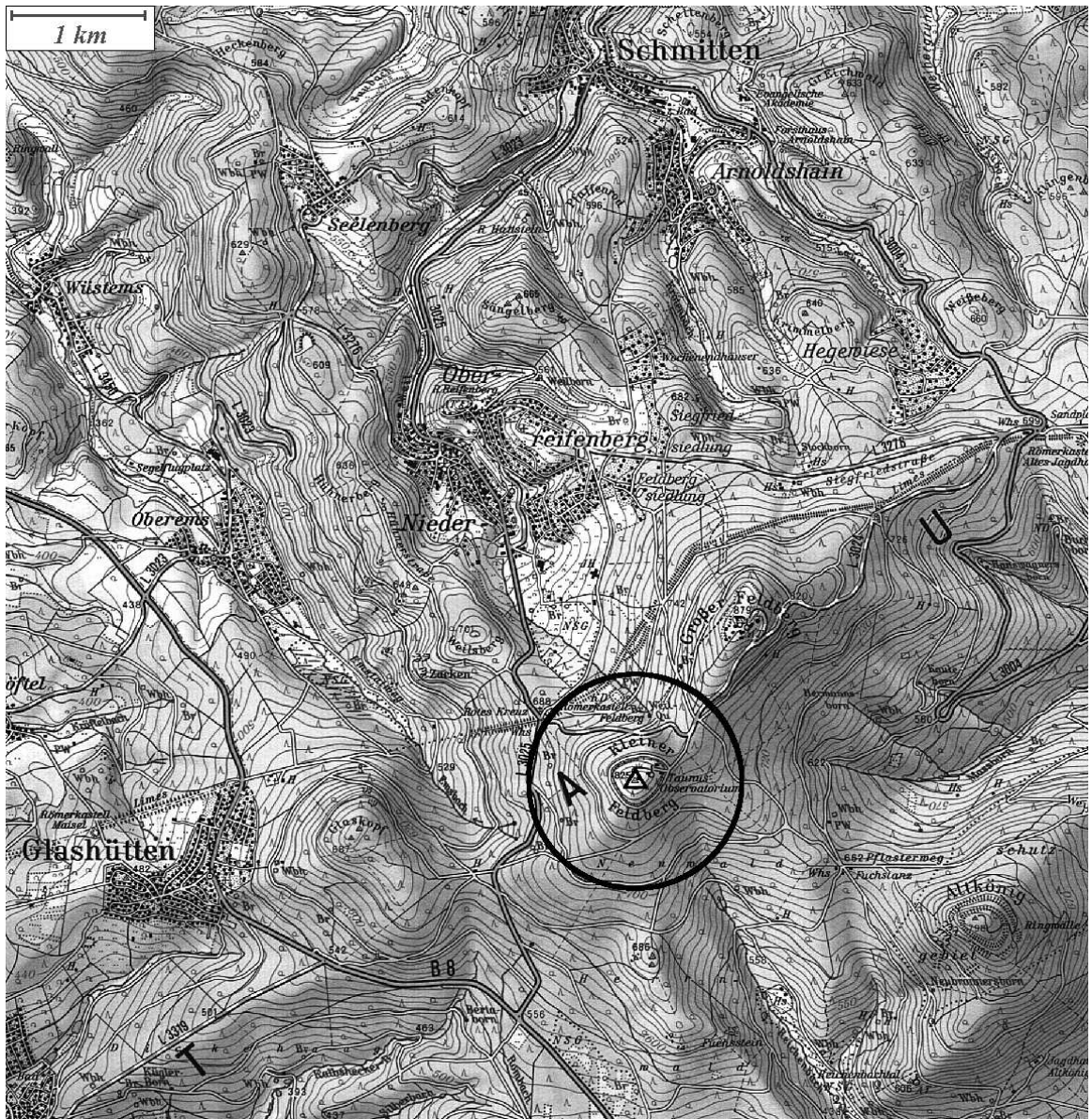


Figure 8.2: Topographical map of the Taunus Range showing the location of the Taunus Observatory on Kleiner Feldberg (825 m a.s.l.). Taken from the topographical map (1:50 000 scale) of the *Hessisches Landesvermessungsamt* [1995].

side of the platform.

The summit of Kleiner Feldberg is covered with low lying vegetation, which mainly consists of grasses and low blueberry bushes, with a few smaller trees. Larger trees, mainly 15-20 m high conifers, surround the summit at a distance of approximately 30 m from the containers, depending on direction. These can be seen in the background in Figure 8.4, which shows the container tower. A sporadically used access road allows vehicle access to the summit for the purposes of equipment transport. An

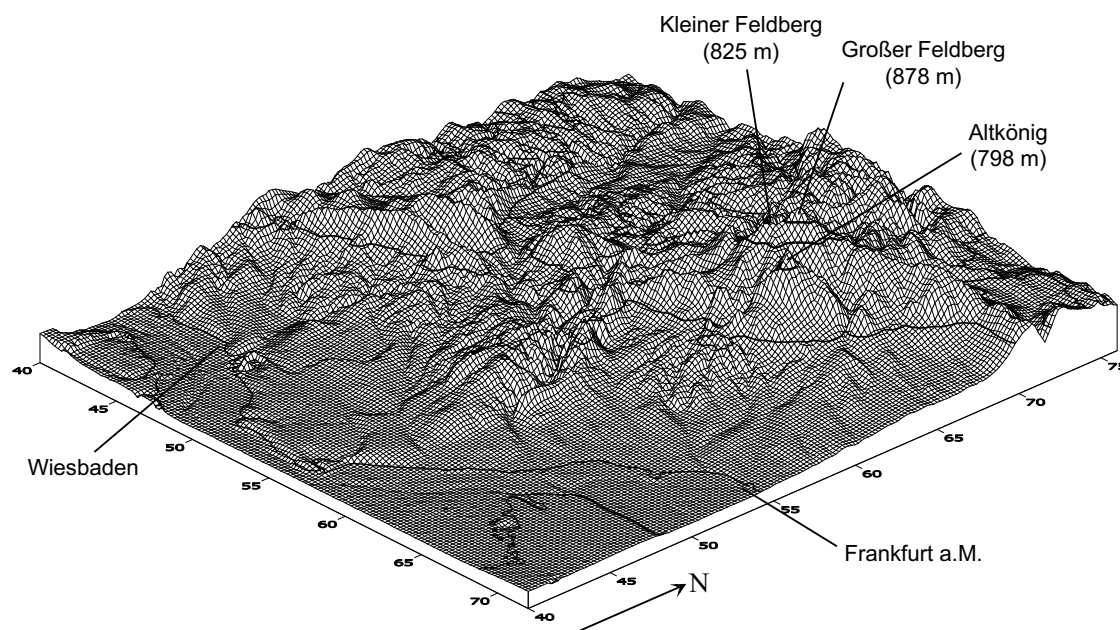


Figure 8.3: Orography of the Taunus Range in the region around Kleiner Feldberg (825 m a.s.l.). The contours are at 100, 350, 700 and 800 m a.s.l.

aerial photo of the measurement site (Figure 8.7 on page 108) shows the Taunus Observatory with the measurement sites marked. A summary of relevant climatic data for Kleiner Feldberg is provided in Table 8.1.

Table 8.1: Climate data for the summer months for Kleiner Feldberg in the Taunus Range [Deutscher Wetterdienst, 1999].

Month	Ave. Temperature (2m) °C	Ave. Precipitation mm	Total Sunshine hours
April	4.5	78.9	151.6
May	8.9	86.7	185.1
June	12.0	100.0	183.7
July	13.8	87.1	201.7
August	13.8	88.2	191.0
September	10.9	70.3	144.6



Figure 8.4: Photo of the container tower on Kleiner Feldberg used for measurements after 1996. The photo is taken from the south. The CA intake is marked by the letter ‘R’ and the mast used by the DWD by ‘M’. Photo courtesy of Dr R. Kurtenbach, Wuppertal University.

8.2 Site description: Hohenpeissenberg

The Meteorological Observatory Hohenpeissenberg is a hilltop weather station operated by the Deutscher Wetterdienst (DWD) in southern Bavaria, approximately 50 km north of the Alps. A wide range of atmospheric measurements are made at the site as part of its dual role as weather station and as global background station in the Global Atmospheric Watch (GAW) programme of the World Meteorological Organisation (WMO). Details about the observatory and the GAW programme can be found at the MOHp website (<http://www.dwd.de/research/mohp/mohp.html>). Figure 8.5 is a map of Southern Bavaria showing the location of the observatory. The Observatory is situated at 975 m above sea level, just below the summit of Hohenpeissenberg (47°48' N, 11°02' E, 988 m a.s.l.) and approximately 300 m above the surrounding countryside. Local noon occurs at 12:16 CET. The observatory is predominantly surrounded by forest and pasture, as can be seen in the photo of the Observatory in Figure 8.6. A car park at the summit of Hohenpeissenberg lies slightly above and

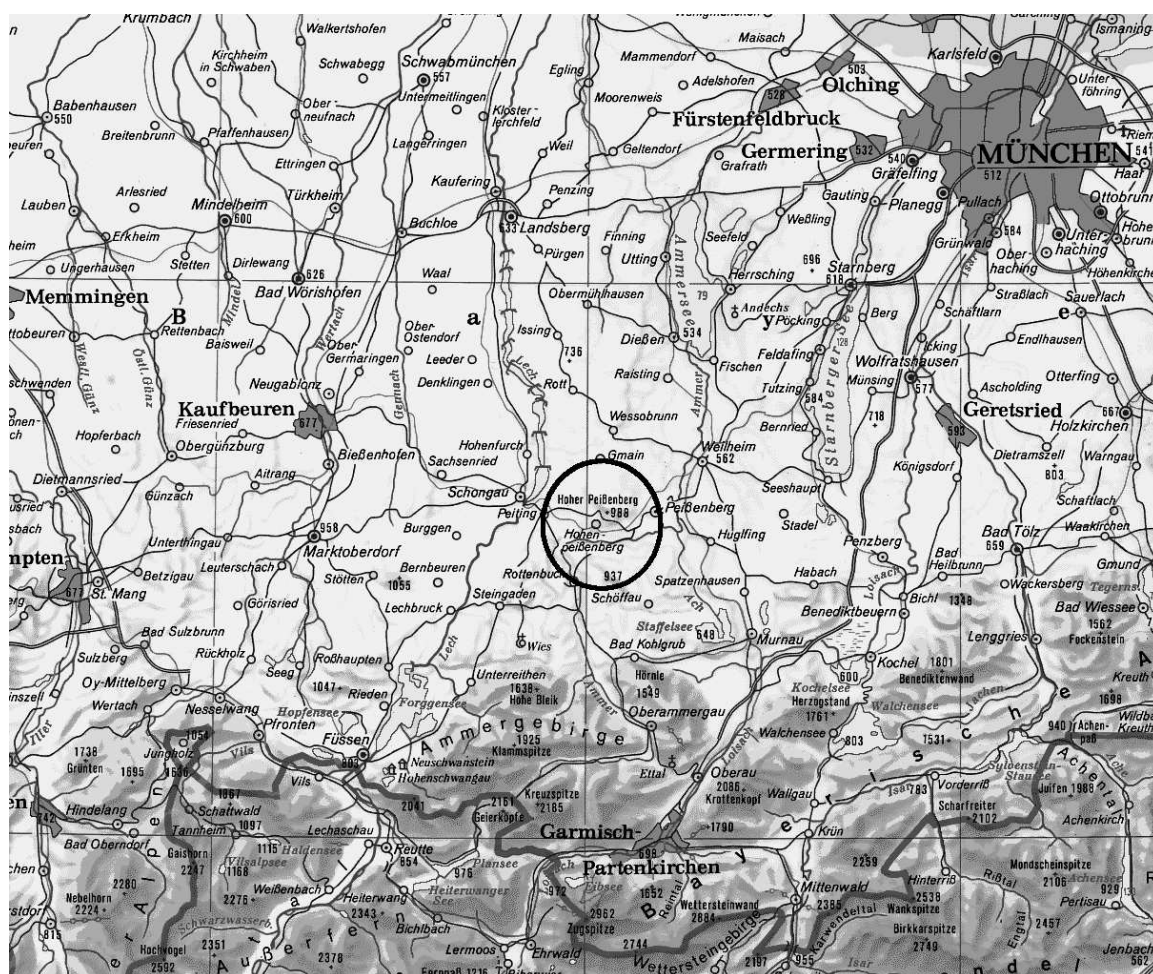


Figure 8.5: Map showing the location of the Meteorological Observatory Hohenpeissenberg (975 m a.s.l.) in southern Bavaria. Map produced using Geothek-Weltatlas 3.0, ©Ed. Hoelzel, Wien, (<http://www.hoelzel.at>), used by permission.

to the east of the Observatory at a distance of approximately 200 m and is heavily frequented by visitors during the summer. The access road to the summit lies on the opposite side of the mountain to the observatory.

The peroxy radical measurements were made on the roof of a container tower, approximately 10 m above ground level. The CA was situated in one of the containers, as were the other instruments whose data are presented here. The instrument inlets were also on the container roof. Meteorological measurements were made in a meteorological garden within 50 m of the container tower.



Figure 8.6: View of the Meteorological Observatory Hohenpeissenberg from the summit of Hohenpeissenberg towards WNW. Photo from the MOHp website.

8.3 Measurements of atmospheric trace gases

The measurements at Kleiner Feldberg were made using instrumentation operated by the IMG, and supplemented by further data from the measurement networks operated by the HLUG and the DWD. Table 8.2 provides a summary of the main instruments at Kleiner Feldberg used during the study. Peroxy radical measurements were made using the chemical amplifier described in Chapter 7. With the exception of the peroxy radical measurements, all other measurements were made using commercial instruments.

During the joint measurement campaign at MOHp, data from the regular measurement programme were used alongside the CA measurements. The instrumentation used during the measurement campaign is summarised in Table 8.3. All instruments, apart from the CA, were operated by DWD personnel. All data evaluation and quality control for these instruments were also carried out as part of the DWD measurement programme. Further details of the instrumentation at MOHp can be found at the

Table 8.2: Summary of instruments used at Kleiner Feldberg during 1998 and 1999.

Component	Instrument	Measurement method	Provided by
ATMOSPHERIC COMPONENTS			
RO _x	Chemical Amplifier ^a	Chemical amplification	HLUG ^b
Ozone	Dasibi 1008RS	UV Absorption	IMG
NO _x	Monitor Labs 8810M	Chemiluminescence	HLUG
	Monitor Labs	Chemiluminescence, Mo converter	HLUG
SO ₂	TECAN / Eco- physics	Chemiluminescence, photolytic converter	Meteorology Consult GmbH
	Horiba Monitor Labs	UV absorption	IMG
PAN	MetConsult ^c	UV absorption	HLUG
RADIATION			
Global radiation	Kipp & Zonen CM10	Moll thermopile	IMG
j _{O¹D}	MetConsult	filter radiometer	IMG
j _{NO₂}	MetConsult	filter radiometer	Meteorology Consult GmbH

^aFor a description of the Peroxy Radical Chemical Amplifier see Chapter 7.

^boperated by IMG

^cInstrument built by Meteorology Consult GmbH.

MOHp website (<http://www.dwd.de/research/mohp/mohp.html>).

The following sections describe the instruments and measurement techniques used at Kleiner Feldberg. The instruments used at MOHp for the measurement of VOCs and OH/H₂SO₄ are also described in more detail, as they are important to the interpretation of the campaign data.

8.3.1 Ozone

Ozone data made available by the HLUG were used as the primary data source. The instrument used for the measurements was a Monitor labs 8810M ozone analyser which was regularly calibrated by personnel from the HLUG. Gaps in the data were filled, where possible, using ozone data from a Dasibi 1008-RS ozone analyser that

Table 8.3: Summary of instrumentation used during the intensive measurement campaign at Hohenpeissenberg during June and July, 2000. With the exception of the CA measurements, all measurements were carried out by the DWD.

Component	Instrument	Measurement method	Temporal Resolution
TRACE GASES			
RO _x	Chemical Amplifier	Chemical amplif.	10 min.
Ozone	Thermo Instruments/ Dasibi	UV absorption	10 min.
NO _x	EcoPhysics	Ozone chemiluminescence	10 min.
NO _y		CO reduction & ozone chemiluminescence detector	10 min.
SO ₂	Thermo Instruments	UV fluorescence	10 min.
H ₂ O ₂ , ROOH		fluorescence	10 min.
CO	Thermo Instruments	IR spectroscopy	10 min.
VOC		GC	1 hr - 1 day
OH / H ₂ SO ₄		CIMS	5 min.
RADIATION			
Global radiation	Kipp & Zonen CM11	Moll thermopile	10 min.
j _{O¹D}		filter radiometer	10 min.
j _{NO₂}		filter radiometer	10 min.

was also operated during most of the measurement period. The Dasibi data were normalised to the HLUG data.

Both instruments operate on the basis of UV absorption by ozone. The detection limit is approximately 1 ppbv ($2 \mu\text{g m}^{-3}$) and the precision approximately 2 ppbv ($4 \mu\text{g m}^{-3}$).

8.3.2 NO_x

NO_x was measured during the study using two different instruments, both of which use the chemiluminescent reaction of NO with O₃ to determine the NO concentration. The NO₂ concentration is determined following the quantitative conversion of NO₂ to NO. A multi-stage measurement cycle allows the measurement of both NO and NO_x using the same detector. The principal differences between the two instruments are the methods used to reduce NO₂ to NO, and their respective sensitivities.

Horiba analyser: During the period 1995-1997, all NO_x data were obtained using a Horiba NO_x analyser, which was operated and regularly calibrated and maintained by the HLUG. In this instrument, NO₂ is reduced to NO using a Molybdenum converter. A major disadvantage of this method is that HNO₃ and other reactive nitrogen compounds (NO_y) are also reduced to NO, so that the resulting NO_x concentration contains an ill-defined contribution from these other compounds. The NO detection limit of 1 ppbv also proved to be too high to be used to calculate the ozone production rate, as in the presence of ozone this level was rarely exceeded.

TECAN/Ecophysics: In 1998 and 1999, a highly sensitive TECAN/Ecophysics NO_x analyser was available by Meteorology Consult GmbH for the NO₂ measurements. This instrument also works on the basis of the chemiluminescent reaction of NO with ozone, but uses a photolytic converter for the reduction of NO₂ to NO, so that exclusively NO₂ is reduced.

The TECAN analyser was calibrated during 1999 using a calibration system modified in cooperation with Meteorology Consult GmbH. NO with a well defined concentration from a gas bottle (Messer Griesheim) is used for the NO calibration. It is then partially oxidised by gas phase titration with ozone to produce a known NO₂ concentration. Ozone is produced in a photolysis chamber by the photolysis of the molecular oxygen in synthetic air using a UV lamp. The presence of excess NO ensures that a further oxidation of NO₂ to NO₃ does not occur, thus enabling the NO₂ concentration to be calculated. The NO₂ conversion efficiency and sensitivity to NO of the TECAN analyser can then be determined.

During 1999, the conversion efficiency of the photolytic converter lay in the range of 42-47 %. The TECAN had a detection limit for NO of approximately 15 pptv. The measurement error for NO is determined mainly by the uncertainty in the gas mixture used for calibration. According to the manufacturer, this uncertainty is approximately $\pm 5\%$. This contributes to an estimated uncertainty for NO₂ of about $\pm 10\%$.

8.3.3 PAN

Measurements of PAN were made using a gas chromatograph (GC) produced by Meteorology Consult GmbH. The measurements were made in cooperation with Meteorology Consult GmbH on behalf of the HLUg. The PAN-GC takes a sample every ten minutes, which is then analysed in an electron capture (EC) detector. The GC was regularly calibrated using PAN produced in a calibration unit. This involved the photolysis of acetone to produce peroxyacetyl radicals, which subsequently reacted with NO, producing PAN. The PAN concentration was determined by the concentration of NO. The estimated relative error is approximately $\pm 20\%$ [*R. Schmitt, personal communication*].

8.3.4 SO₂

Measurements of SO₂ were used for air mass characterisation. Measurements were available from two instruments: a Horiba ambient SO₂ monitor (APSA 350E) belonging to the IMG, and a Monitor Labs SO₂ monitor operated by the HLUg. The APSA 350E has a detection limit of 1 ppbv. The measurement error has not specifically been taken into account, as the measurements were only used as an indicator for changes in air mass.

8.3.5 OH/H₂SO₄ (MOHp)

Measurements of OH and H₂SO₄ are made using the CIMS technique as described in Section 5.3 for the measurement of HO₂. The instrument at Hohenpeissenberg is described in detail in *Berresheim et al.* [2000]. Depending on air quality and desired sensitivity and precision, the OH radicals are titrated with SO₂ containing the heavy isotope ³⁴S, to allow them to be differentiated from atmospheric H₂SO₄, which contains mainly the lighter ³²S (96 %). The OH radicals are titrated to H₂³⁴SO₄, which is ionised by the nitrate ion to H³⁴SO₄⁻. The HSO₄⁻ and nitrate ions are propelled into a collision dissociation chamber, where they are freed from the associated ligands before passing through a quadrupole mass filter to an electron multiplier detector. The concentration of the original H₂SO₄ and OH can then be calculated from the ratios of the respective HSO₄⁻ ions to the nitrate ion,

$$[H_2SO_4] = F \frac{\{H^{32}SO_4^-\}}{\{NO_3^-\}} \quad (8.1)$$

$$[OH] = F \frac{\{H^{34}SO_4^-\}}{\{NO_3^-\}} \quad (8.2)$$

where F is a constant determined by calibration and the braces denote the signal strength. For conditions with relatively low levels of H₂SO₄, ³²SO₂ is added to titrate

the OH radicals, and the OH concentration is determined by taking the difference between the signal with and without added $^{32}\text{SO}_2$, analogous to the technique used in the CA,

$$[\text{OH}] \approx F \frac{\{\text{HSO}_4^-\}_{\text{TS}} - \{\text{HSO}_4^-\}_{\text{BS}}}{\{\text{NO}_3^-\}} = F \frac{\Delta\{\text{HSO}_4^-\}}{\{\text{NO}_3^-\}} \quad (8.3)$$

where TS and BS denote the total signal and background signal, respectively. Measurements are integrated over five minutes. The instrument is calibrated using the photolysis of water vapour to produce equal amounts of OH and HO₂ radicals. The concentration of the OH radicals can be calculated on the basis of the photolytic process in a manner analogous to that described in section 7.3 for the calibration of the CA¹. Currently the measurements are estimated to have a precision, accuracy and detection limit of 44 %, 30 % and 3×10^4 molecules cm⁻³, respectively, for H₂SO₄, and of 52 %, 40 % and 5×10^5 molecules cm⁻³, respectively, for OH. The method also allows other components, such as methane sulphonic acid (MSA), to be measured as well.

8.3.6 VOCs (MOHp)

Two gas chromatography (GC) systems are operated in parallel at MOHp to measure VOCs. Due to the large number of compounds present in the atmosphere, many with very low mixing ratios, only about 80 different compounds are routinely measured, as the data evaluation is an extremely time consuming operation. During normal operation, measurements are only made once a day. However, during the intensive period from 17 to 20 July measurements of over 40 species were made every one to three hours during the daytime hours.

Both systems are housed in a container immediately under the intake, at approximately 12 m above ground level, and share a common intake system. An ozone trap removes ambient ozone from the air sample in order to avoid oxidation of the sample in the GCs.

The first GC system (GC-1) uses a Nafion dryer before the sample passes through a cryogenic trap with glass beads at 85 K. The sample is then desorbed at 473 K and passed through a GC column with a Flame ionisation detector (FID). The system is used to detect light VOCs with two to eight carbon atoms (C2-C8).

The second system (GC-2) uses an adsorption trap (Carbotrap C+B) at 313 K to collect the sample. This is then desorbed at 503 K, and, after cryogenic focussing at 97 K and separation in the column, the VOCs are detected by both an FID and Mass Spectrometer (MS). This system is optimised for the detection of VOCs with between five and thirteen carbon atoms (C5-C13). The overlap between the systems allows enhanced quality control.

¹The principle difference between the two radical sources is the conversion of the OH radicals to HO₂ in the source used for the CA calibration.

8.4 Radiation measurements

Measurements of the following parameters were made at Kleiner Feldberg during the study in order to quantify the radiative contribution to the photochemical processes. Measurements at MOHp used similar instruments.

8.4.1 Global radiation

Global radiation measurements were made during 1996 and 1997, and again during 1999, using a Kipp and Zonen CM-10/CM-11 pyranometer belonging to the aerosol group of the IMG. Various factors, such as temperature and the position of the sun, contribute to the measurement error, which is estimated at less than $\pm 5\%$.

8.4.2 Photolysis rates

Photolysis rates were measured for both O_3 (j_{O^1D}) and for NO_2 (j_{NO_2}). The photolysis of O_3 is probably the most important step in tropospheric photochemistry and leads to the production of the OH radical, as mentioned in Chapter 2. This is, in turn, the most significant source of peroxy radicals in the troposphere and thus serves as an important estimate of photochemical activity. As discussed in Chapter 3, the peroxy radical concentration in polluted conditions should be proportional to j_{O^1D} . NO_2 photolysis is also involved in ozone chemistry, as it is the step leading directly to ozone formation. As a result, it is used in the current study as a further measure of the photochemically active UV radiation.

j_{O^1D}

The ozone photolysis rate, j_{O^1D} , has been measured since 1996 using a filter radiometer produced by Meteorology Consult GmbH and described by Rüb [1999]. Calibration parameters were unavailable for later measurements following repair work on the filter radiometer made necessary by lightning damage. Thus, the detector signal is used directly as a substitute for the hemispheric actinic flux with the spectral characteristic of ozone photolysis. The measurements are for this reason given in units of “Volts”.

The relative error for the detector measurements using the radiometer was estimated by Rüb [1999] to be approximately $\pm 5\%$. Uncertainties in the spectral response of the radiometer lead to an estimated error for the hemispheric actinic flux with the same spectral characteristics as j_{O^1D} of up to $\pm 10\%$.

²The contributing factors with their associated error, as given by the manufacturer, are as follows: Temperature (-10 - +40 °C), $< \pm 1\%$, Irradiance (up to 1000 W/m⁻²) $< \pm 1\%$, combined azimuth and cosine response ($>10^\circ$ sun altitude) $< \pm 3\%$.



Figure 8.7: Aerial photo of the Taunus Observatory. The large circle shows the measurement site for the peroxy radical and other measurements for the period 1996-99. The RO_x measurements in 1995 were made in a container marked by the smaller circle at the top. The meteorological garden, where most of the measurements of the DWD were made is marked by a square and the letter M. The wind measurements of the DWD were made on a mast slightly to the right of the large circle.

j_{NO_2}

A filter radiometer from Meteorology Consult GmbH was used for measurements of the photolysis rate of j_{NO_2} . It was calibrated during 1999 on Kleiner Feldberg by comparison with a master radiometer (No. 505) operated by Meteorology Consult. The estimated error in the j_{NO_2} measurements is less than $\pm 5\%$, and is mainly due to uncertainties in the chemical actinometry [Kraus *et al.*, 1998].

8.5 Meteorological parameters

Meteorological measurements were made during the period 1995 - 1997 using instruments belonging to the IMG. The principal data for the years 1998 and 1999 were

Table 8.4: Summary of the principle meteorological parameters for the years 1998 and 1999, together with their resolution and maximum error.

Parameter	Resolution	Maximum Error
Temperature (2m)	0,1 K	$\pm 0,2$ K
Dew point Temperature (2m)	0,1 K	$\pm 0,3$ K
Relative humidity (2m)	1 %	± 10 %
Precipitation	0,1 mm	± 1 mm
Sunshine hours	Sensor dependent	6 ' /h
Visibility	1 m	≤ 5 km: 200 m > 5 km: 500 m
Wind direction	3,6°	10°
Wind speed	0,1 m s ⁻¹	0,5 m s ⁻¹

made available by the DWD as part of a cooperation contract with the IMG. Supplementary data were supplied by the HLUg.

The IMG instruments were situated on a mast on the western side of the container tower (see Figure 8.7). This was also used by the HLUg for their meteorological measurements. The mast used by the DWD lies to the north of the containers and is slightly below the summit of Kleiner Feldberg. Further measurements were made in the meteorological garden of the DWD, which is situated at approximately 812 m a.s.l. and is marked by the letter 'M' in Figure 8.7. The difference in position could lead to slight differences in the values obtained from the various sources, particularly for wind measurements. However, it is not expected that this will have any significant effect on the results. The principle meteorological parameters supplied by the DWD are shown in Table 8.4, together with the associated resolution and estimated error.

8.6 Data Collection

Several different data collection systems were used at Kleiner Feldberg during the period covered by the current study. For the period 1995 - 1997, a computer controlled Hewlett Packard HP3497A Data Collection System was used to collect the raw data, which was subsequently saved on a Hewlett Packard PC equipped with interface board and appropriate software. The HP3497A system used a 20 channel, 27 bit analogue/digital converter. The data represent one minute averages.

This system was damaged in July 1997 by lightning, and was replaced in 1998 by a system based on Combilog 1020 data loggers (Theodor Friedrichs & Co.). The Combilog data loggers each have 8 analogue channels with 16 bit resolution. One

minute averages are written to a 2 MB flash disk. The data file is subsequently transferred to a PC for analysis using standard software. The data loggers were used for the standard instrumentation operated by the IMG, as well as to record the signal from the HLUG ozone analyser with a higher temporal resolution than is provided by the HLUG measurement network.

The meteorological data from the DWD was transferred as 10 minute averages from an automatic data system (MIRIAM-U; DWD) to a PC operated by the IMG. The measurements were extracted from the encoded 10 minute data provided by the MIRIAM-U system and converted to ASCII format using the programme `datenaus.exe`.

Part III

Peroxy radical measurements at Kleiner Feldberg and Hohenpeissenberg: Results and Interpretation

Overview

This part summarises the measurements of O_3 , RO_x and other components and parameters at Kleiner Feldberg during the summers 1998 - 1999, and during an intensive measurement campaign at Hohenpeissenberg in June 2000. The measurements at Kleiner Feldberg are used to establish diurnal profiles for the most important trace gases, and to investigate the statistical relationships between the various parameters. Ozone production rates are calculated on the basis of the reaction between RO_x and NO during the course of the day, and are compared with the observed change in the ozone concentration. The Hohenpeissenberg measurements were made in cooperation with the Meteorological Observatory Hohenpeissenberg, and are used as a basis for a steady state radical balance model.

Chapter 9 presents the measurements at Kleiner Feldberg and interprets them on the basis of their interactions. Average profiles are presented for several parameters, including O_3 and the total RO_x concentration. The statistical relationships between them are discussed.

The data from Kleiner Feldberg were then used as input for a simple diagnostic model for calculating the expected ozone production from the measured parameters. The model and the results are presented in Chapter 10, along with a comparison between measured and calculated ozone concentrations. The results are used to calculate the diurnal profile of the ozone production rate and this is compared with the average observed rate of production. The comparison suggests that deposition plays a significant role in limiting the observed ozone concentration.

The measurements at Hohenpeissenberg are presented in Chapter 11. The measurements included both OH and RO_x radical measurements, as well as their most important precursors. A steady state radical balance model was used to model the observed concentrations of OH and RO_x and to establish the relative importance of the various sources and sinks. The model is outlined and the results are compared with the observations.

Ozone data from the UBA and HLUG networks have also been analysed in order to investigate the role of larger scale events in determining the local ozone level. The results of this analysis are presented in Chapter 12. Average profiles show that photochemical ozone production plays an important role at the local level during summer. However, meteorological processes associated with the breakdown of the nocturnal boundary layer appear to determine significant features of the diurnal profiles. The spatial representativity of ozone measurements at Königstein (near Kleiner Feldberg) has been calculated by comparison with other German stations. The results suggest that, during the daytime, the events causing the day to day changes in the ozone level are fairly homogenous over relatively large areas.

Chapter 9

Field measurements at Kleiner Feldberg

Field measurements of atmospheric photooxidants were made at Kleiner Feldberg each summer from 1995 to 1999. Interpretation of the measurements at Kleiner Feldberg concentrates on periods for which the Ecophysics NO_x analyser was available, i.e. the summers of 1998 and 1999. Although measurements from an Horiba NO_x analyser operated by the HLUG were available for earlier years, the mixing ratio of NO was frequently below the detection limit using this instrument and these measurements could not be used to calculate the ozone production rate.

Figures 9.1 and 9.3 show the daily averages of the trace gas measurements at Kleiner Feldberg for the summer months June to September during 1998 and 1999. As was discussed in Chapter 3, the sensitivity of the CA to water vapour results in large fluctuations in the background signal and in a higher detection limit for RO_x on days with high relative humidity (RH). For this reason, average RO_x mixing ratios are only shown for days on which the maximum was significantly higher than the variance in the background signal.

The change in ozone level (ΔO_3) is used as a measure of local diurnal photochemical production. It is defined as the difference between the average mixing ratio of O₃ in the afternoon (15:30 - 16:30 CET) and in the morning (09:00 - 10:00 CET). A negative value indicates that the mixing ratio of ozone in the afternoon was lower than in the morning. This is an indicator that ozone production is outweighed by meteorological processes on that day.

Figures 9.2 and 9.4 show the daily averages of the meteorological parameters at Kleiner Feldberg during the same time period. The values for global radiation, actinic flux (O¹D) and j_{NO_2} are averages over the period between the beginning of

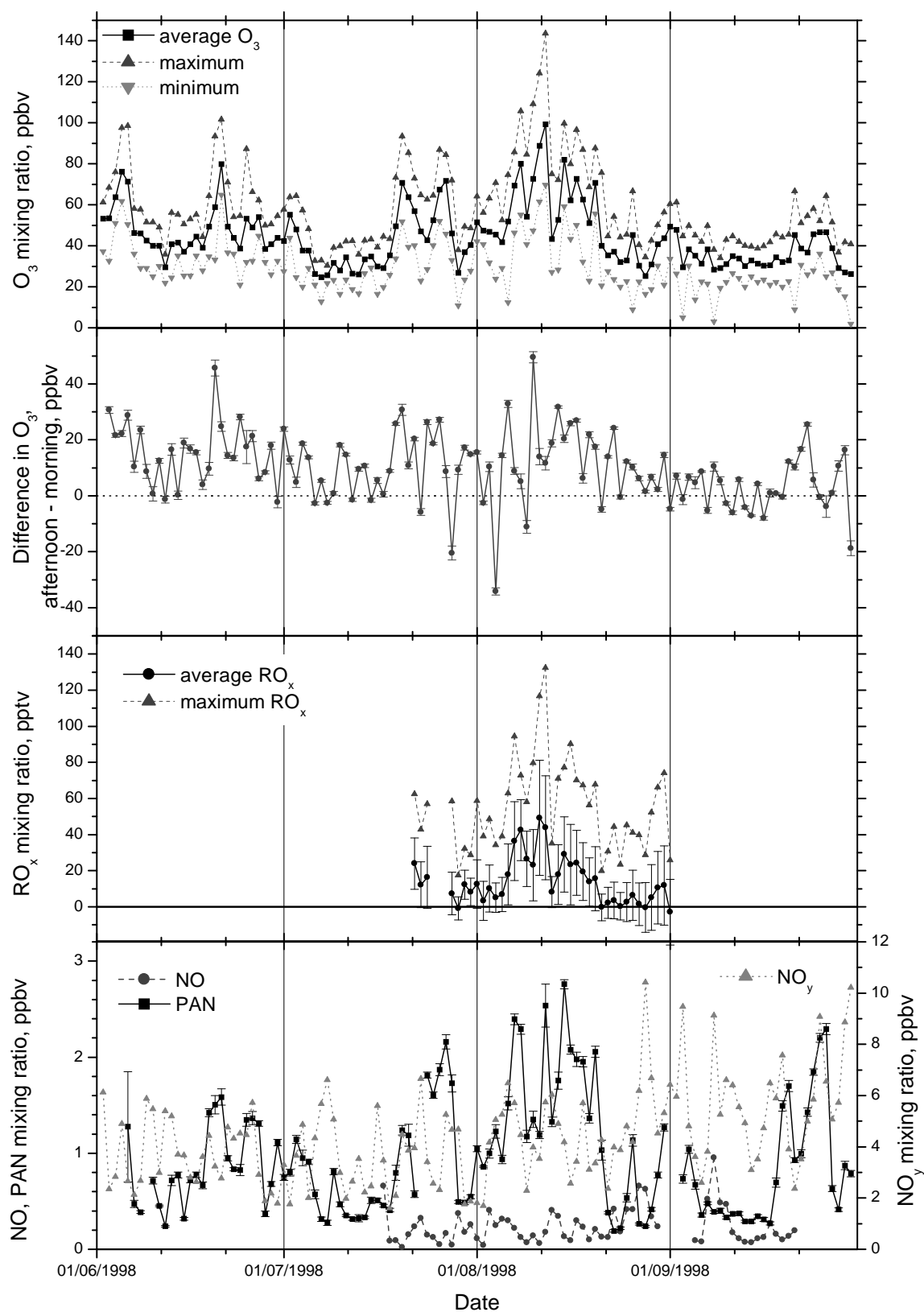


Figure 9.1: Daily averages for the mixing ratios of RO_x , O_3 , NO_x , PAN and the change in ozone level (ΔO_3) at Kleiner Feldberg for June to September, 1998. The NO_y data is derived from the 30 minute averages provided by the HLUg.

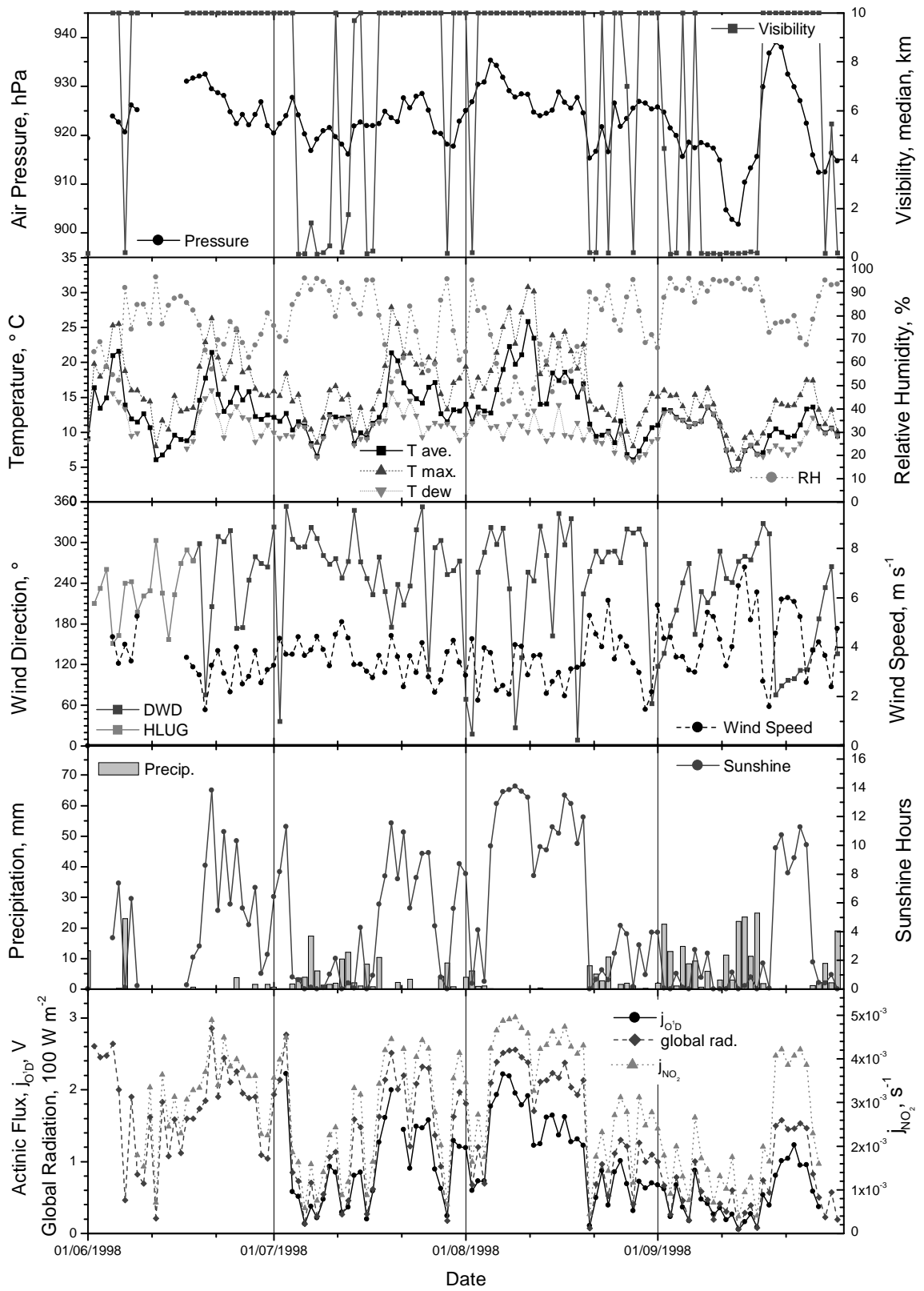


Figure 9.2: Daily averages of the most important meteorological parameters at Kleiner Feldberg for June to September, 1998.

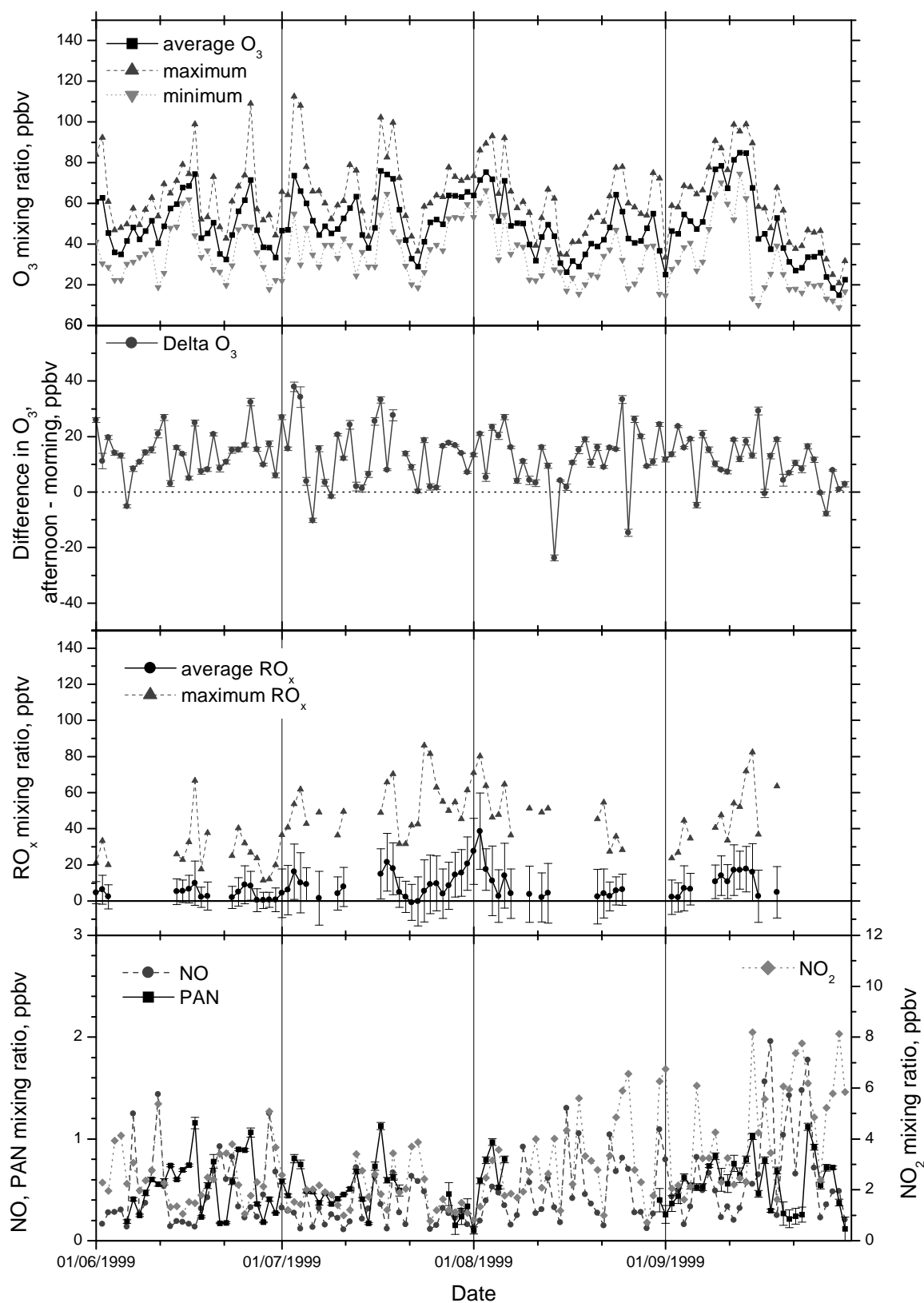


Figure 9.3: Daily averages for the mixing ratios of RO_x , O_3 , NO_x , PAN and the change in ozone level (ΔO_3) at Kleiner Feldberg for June to September, 1999.

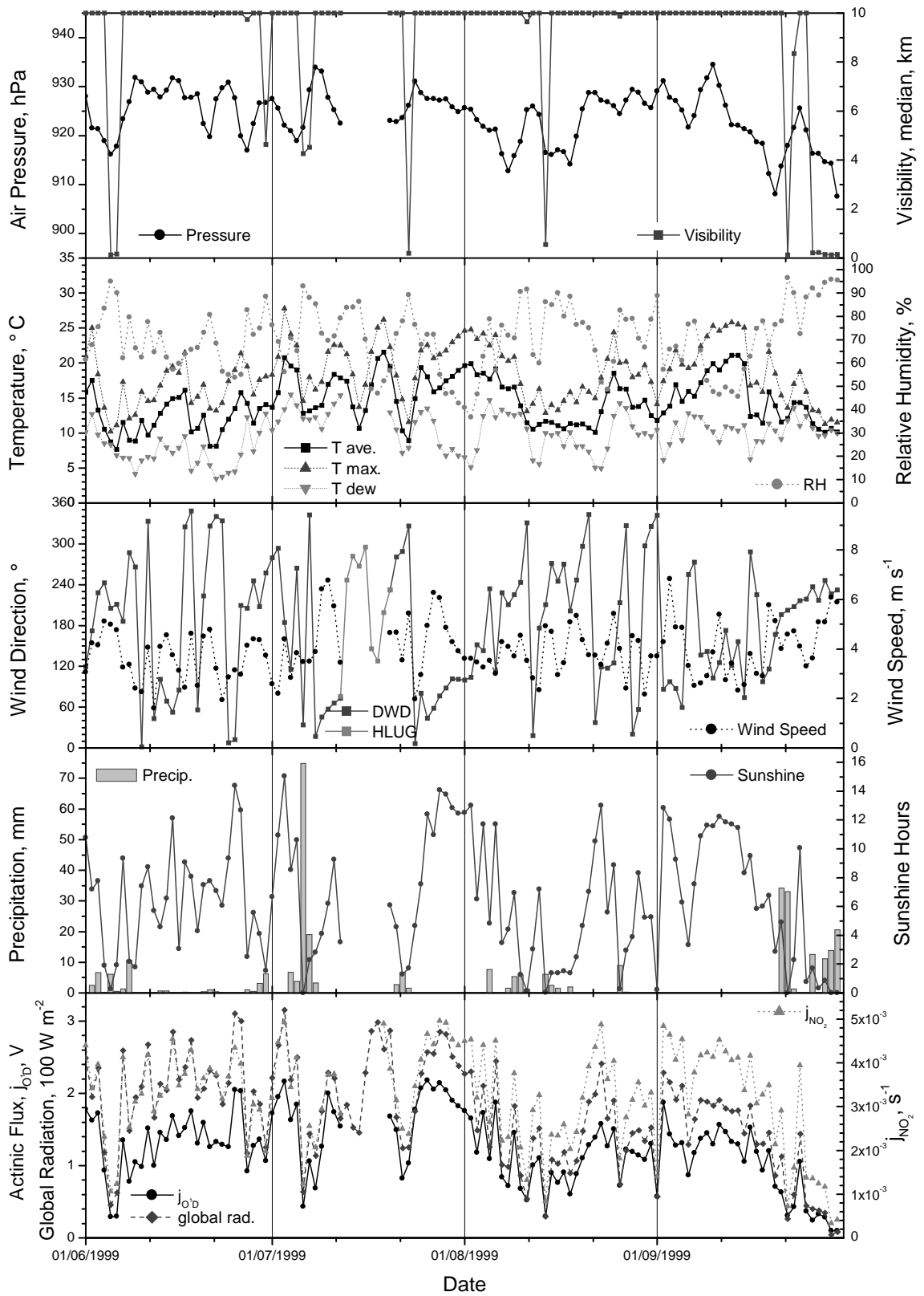


Figure 9.4: Daily averages of the most important meteorological parameters at Kleiner Feldberg for June to September, 1999.

the civil twilight¹ in the morning and its end in the evening. Thus, the averages are proportional to the total amount of radiation reaching the respective detectors over the course of the day.

Episodes of high ozone levels were experienced during both years. In 1998, 10 minute maximum O₃ mixing ratios exceeded 90 ppbv² on a total of 11 days during 7 separate episodes³. During one of these episodes, from 9 to 11 August, the highest ozone mixing ratios for the measurement period were observed, with a peak 10 minute mixing ratio of over 140 ppbv (280 $\mu\text{g m}^{-3}$) on 11 August. This episode occurred during an extended period of fine weather which lasted from 5 to 20 August, with Europe lying under a stable high pressure system. Levels of over 60 ppbv⁴ were observed during 12 episodes totalling 48 days. Moderately high ozone levels were observed more frequently during the 1999 measurement season, but on only one day did the 10 minute mixing ratio exceed 110 ppbv slightly (3 July). The 60 ppbv level was exceeded during 15 episodes totalling 67 days during 1999, and the 90 ppbv level during 10 episodes totalling 15 days.

As is to be expected, episodes with the highest ozone mixing ratios occurred during periods of high radiation and temperature, low RH and no precipitation, i.e., during stable fair weather periods associated with anticyclonic weather conditions and high pressure systems over central Europe. Such episodes were also associated with high mixing ratios of RO_x and PAN and slightly lower NO₂. These episodes generally ended with a change in the mesoscale weather situation. However, the weather situation was weakly cyclonic during several shorter episodes, which were typically brought to an abrupt end by the arrival of frontal disturbances associated with the general cyclonic conditions.

9.1 Diurnal profiles

Diurnal profiles were calculated for various atmospheric components and meteorological parameters and are shown in Figure 9.5. They were obtained by averaging the individual profiles for all days for which the maximum RO_x concentration was greater than the variation in the background signal (see discussion on page 115; the days used are those for which an average RO_x concentration is shown in Figures 9.1 and 9.3). The data set contained 106 days. Two profiles are shown for RO_x. The lower profile was calculated using all days in the data set. The upper curve was calculated using

¹The civil twilight is defined as the period, during which the solar zenith angle has the value $90^\circ \leq \Theta \leq 96^\circ$.

² $\approx 180 \mu\text{g m}^{-3}$; Under current German law, the public must be informed of possible health risks whenever this level is exceeded for one hour or more.

³An episode is defined here as a period during which the maximum 10 minute mixing ratio exceeded a given level on one or more consecutive days. On a number of occasions several episodes occurred in rapid succession with a break of only one day between them.

⁴ $\approx 120 \mu\text{g m}^{-3}$; At this level, health problems first occur for some sensitive individuals.

only days for which the 10 minute maximum was above 60 pptv (26 days). The NO_2 and NO_x profiles only include data from 1999.

The process of averaging the diurnal profiles over a sufficiently long time interval amplifies features which are dependent on the relative time of day, such as ozone production. Features caused by factors which operate on time scales longer than 24 hours are averaged out, so that their effect essentially disappears for a sufficiently large data set. The synoptic weather pattern is one such factor. Although it can cause large changes in the ozone concentration, it is independent of the time of day, so that the average diurnal profile should essentially be free of its influence.

All components considered exhibit pronounced diurnal profiles, all of which are asymmetric to local noon. Ozone, RO_x and PAN, all of which have strong photochemical sources, have maxima in the afternoon. NO has a morning maximum, while the profile for NO_2 is more complex and reflects its role as an intermediate in the relevant reaction schemes.

The diurnal profile for ozone shows a long drop in the ozone level overnight, with the minimum concentration around 07:00 to 08:00 CET. This is followed by a rise of approximately 13 ppbv during the day until a relatively broad maximum is reached in the mid afternoon. After 17:00 to 18:00 CET, the concentration drops gradually. The daytime rise in ozone levels is due to the photochemical production of ozone via RO_x and also advection from other areas. The rising flank during the morning corresponds well to the period for which RO_x levels are rising or at their peak. Photochemical ozone production due to the reaction of RO_x and NO will be examined further in the following chapter.

The diurnal profile for RO_x starts to rise shortly after sunrise, a few hours earlier than it does for ozone, and reaches a broad maximum of about 20 pptv centred at 14:00 CET. A steep flank drops off towards evening, with a tail extending into the night. The night-time level does not drop to null on average, dropping from a value of about 5 pptv at 21:00 CET to a minimum of 1-2 pptv just before sunrise. The presence of these non-zero concentrations, even in the absence of radiation, could be due to stable organic radicals which only react slowly (see the following subsection), but may also be due to night-time production of RO_x radicals via NO_3 radicals and O_3 .

The broad shoulder in the morning RO_x profile is due to the rapid reaction of the RO_x radicals with the high NO concentrations at this time of day. This depresses the RO_x mixing ratio in the morning and is responsible for its relatively slow build up. Increasing O_3 levels cause the NO mixing ratio to drop after 12:00, and allow RO_x to accumulate. Concentrations of RO_x precursors, i.e. VOCs, are also expected to increase during the day, which will also contribute to the shape of the profile. Increased biogenic VOC emission, e.g. of isoprene, occurs from vegetation at high temperatures, and evaporation of anthropogenic VOCs also increases as the temperature rises. The maximum RO_x concentration coincides well with the occurrence of the temperature maximum at around 15:00 CET, and suggests that the emission of VOC plays a role in determining RO_x levels. Further evidence for the role of VOCs was found during

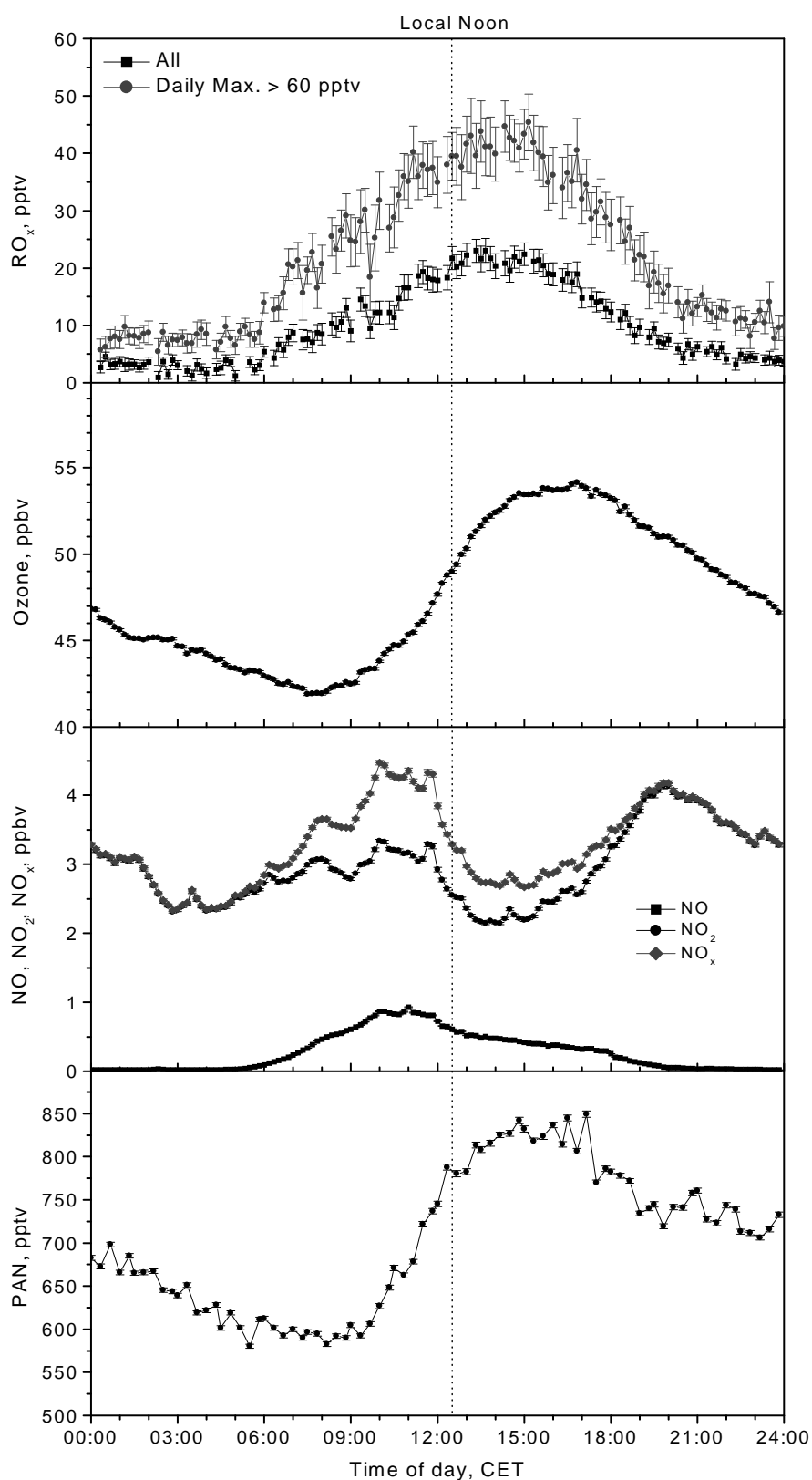


Figure 9.5: Diurnal profiles for several trace gases at Kleiner Feldberg: RO_x , O_3 , NO , NO_2 , total NO_x , and PAN. The error bars represent the standard error in the average over the data set. Local noon is at 12:26 CET and is marked by the vertical dotted line.

the measurements at Hohenpeissenberg. These measurements will be summarised and discussed further in Section 11.1.

The mixing ratio of NO is highest between 09:00 and 12:00 CET in the morning, due to the breakdown of the nocturnal boundary layer and upwards mixing of polluted air. After the establishment of the convective boundary layer, the NO levels are gradually depleted during the afternoon, and rapidly drop after photochemical recycling drops off after 18:00. NO₂ also builds up slightly during the morning as it is produced in the reaction between NO and RO_x, and is transported from lower altitudes. As ozone and solar radiation levels rise during the morning, NO and NO₂ levels drop off in the late morning and afternoon. PAN production also consumes NO₂, although the conversion of NO₂ to PAN represents a temporary loss of NO_x from the system, whereas NO₂ photolysis merely involves a cycling of NO_x. The observed net production of PAN, which averages about 250 pptv per day, does not explain the observed decrease in total NO_x of nearly 2 ppbv on its own. Further processes, such as the production of further organic nitrates with relatively short life times, are required to account for this observed decrease during the afternoon.

9.1.1 Relationship between RO_x and solar radiation

A major source of RO_x radicals is the oxidation of VOCs by OH radicals, which are primarily produced by the photolysis of O₃ by UV radiation. Although further chemical interactions should cause deviations, a close relationship is to be expected between the diurnal profiles of RO_x and of UV radiation, especially at those wavelengths involved in O₃ photolysis. This was investigated by comparing the RO_x profile and normalised profiles for several different parameters of solar radiation in different wavelength regions, i.e. global radiation, j_{NO_2} , and the actinic flux for ozone photolysis, together with its square root. The profiles are shown in Figure 9.6. The baseline for the radiation curves has been positioned to correspond to the RO_x mixing ratio between about 03:00 and 04:00 CET. The radiation curves have been normalised and scaled for easier comparison with the RO_x profile.

The RO_x profile has the same general shape as the profiles for radiation, however the maximum is shifted towards the afternoon. Significant deviations can be seen in both the late morning and the evening.

Before 07:00 CET, the RO_x curve shows good agreement with the curve for j_{NO_2} , and the RO_x level starts to rise quicker than is to be expected for production via the primary production of OH radicals. This may be due to early OH production due to the photolysis of HONO, which can accumulate overnight. This occurs at wavelengths up to 572 nm and would occur before OH radicals are produced via ozone photolysis.

During the morning the RO_x profile generally falls below the radiation curves. As was discussed above, this is due to its reaction with NO, which depresses the RO_x concentration.

In the afternoon, a further deviation from the radiation profiles is observed, with

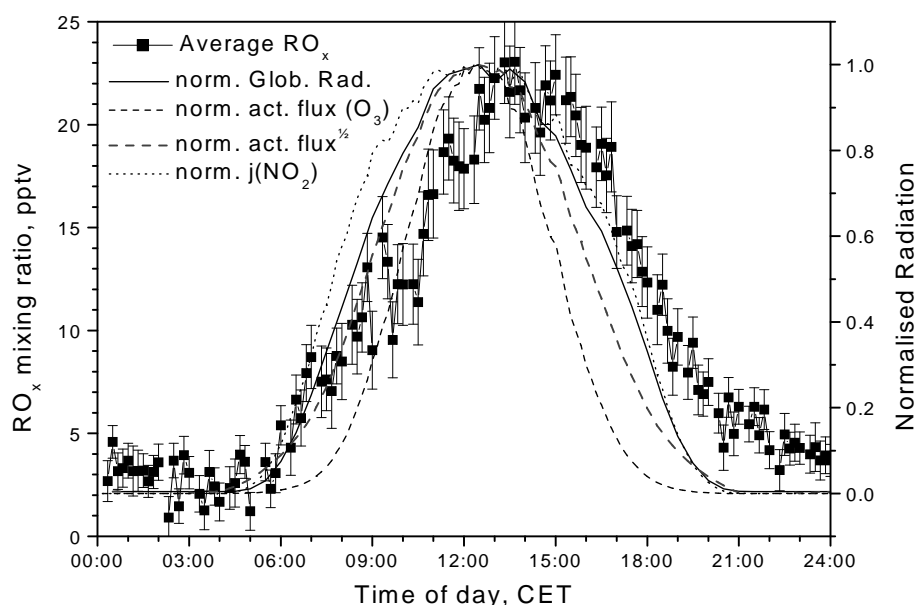


Figure 9.6: Comparison of the average diurnal profile of RO_x with normalised average profiles for four parameters of solar radiation: global radiation, j_{NO_2} , actinic flux for O₃, and the square root of the actinic flux.

the RO_x profile lagging the radiation and gradually tailing off towards evening. An average mixing ratio of approximately 3-5 pptv RO_x was still observed at midnight. A similar tail has also been observed in a number of other studies [e.g., *Monks et al.*, 1996; *Zanis et al.*, 1999; *Cantrell et al.*, 1992]. For clean air conditions, this can be attributed to the long lifetime of organic RO₂ in the absence of NO and HO₂. At low NO mixing ratios, RO₂ is no longer removed by reaction with NO and only reacts slowly with other RO₂ species. In contrast, HO₂ is rapidly removed from the atmosphere in the evening by self reaction and reaction with RO₂.

The high levels of RO_x during the night may also be due to RO_x production via night-time oxidation of VOCs by NO₃ and O₃. *Cantrell et al.* [1992] attributed the tail effect observed during the ROSE campaign to such night chemistry. While night chemistry is possibly responsible for maintaining high RO_x levels at night, the similarity of the tail observed in these average profiles to those observed by *Monks et al.* [1996] suggests that peroxy radical combination reactions under low NO conditions are responsible for the slow decrease in RO_x mixing ratios.

Several studies found a correlation between RO_x levels and $\sqrt{j_{O^1d}}$ for clean conditions at maritime and mountain sites for days with NO concentrations close to zero [*Penkett et al.*, 1997; *Carpenter et al.*, 1997; *Reiner et al.*, 1999]. Under such conditions, O₃ destruction predominated, and the predominant reactions were those between O₃ and HO₂, Reaction (2.19), and between the peroxy radicals, Reactions (3.28), (3.29) and (3.30). The same studies found a correlation with j_{O^1d} on days with

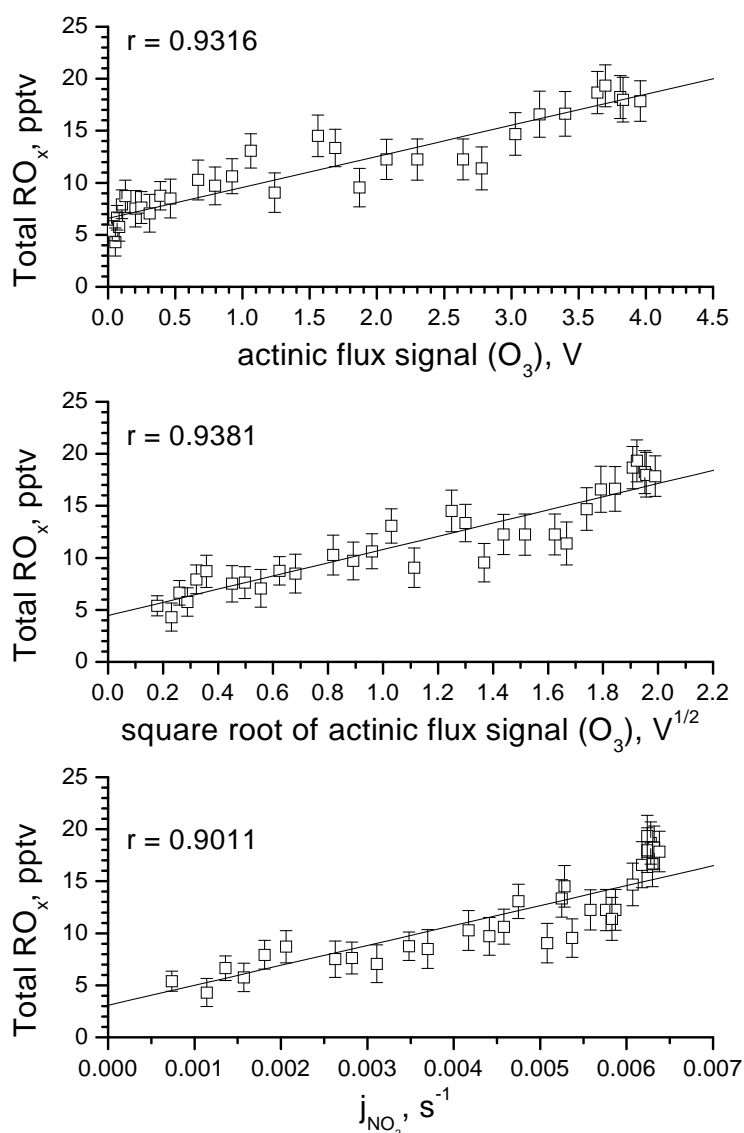


Figure 9.7: Scatter plot of 10 minute average peroxy radical mixing ratios vs normalised averages of the actinic flux signal for ozone, the square root of the ozone actinic flux signal, and j_{NO_2} . Each point represents a 10 minute average between 06:00 and 12:00 CET. Linear fits of the data and the correlation coefficient, r , are also shown. The linear fits were weighted using the standard error in the RO_x mixing ratios.

higher levels of NO, and with net ozone production. This was attributed to the dominating effect of the reaction between RO_2 and NO. *Zanis et al.* [1999] used a simple chemical model to show that an intermediate regime also exists, with NO mixing ratios between about 20 and 100 pptv, for which a correlation with $\sqrt{j_{O^1d}}$ was possible even during ozone production.

Figure 9.7 shows a scatter plot of the average 10-minute RO_x concentration versus j_{NO_2} , the actinic flux signal for ozone and its square root. The straight line represents the line of best fit for the data. Only data for the morning were used in the plot, as production processes are only expected to dominate during this period. The data showed no statistically significant difference between the correlations with the actinic flux signal of ozone and its square root. However, both were more significant than the plot for j_{NO_2} at the 95% significance level⁵. The good correlation indicates that even in the relatively polluted environment at Kleiner Feldberg, the production of OH via O_3 photolysis is the major factor determining the buildup of RO_x . However, it was not possible to test the results of *Zanis et al.* using these results. The deviation from linearity indicates that other parameters, such as NO, do have a slight impact on the morning RO_x profile, but that radiation driven production is the dominating parameter.

9.1.2 Summary

The main features of the diurnal RO_x profile can be summarised as follows:

- RO_x mixing ratios reach their minimum value of 0-2 pptv in the early morning between 02:00 and 05:00 CET.
- The buildup of RO_x during the morning is best described by the production of OH due to ozone photolysis; however, the rapid reaction with NO causes the profile to drop below the expected linear fit during mid-morning.
- Photolysis of HONO may cause an initial pulse of OH just after solar radiation first becomes available between 04:00 and 05:00. This may be the cause of the initial rise in RO_x between 05:00 and 07:00 CET.
- The maximum RO_x mixing ratio is reached in the early afternoon. This can be attributed to decreasing NO concentrations allowing RO_x accumulation, as well as increased production due to the increased supply of VOCs.
- RO_x mixing ratios drop off slowly towards the evening. The removal of NO by titration with ozone, and the rapid reaction of HO_2 with ozone and other radicals means that the predominant removal process for the organic radicals is combination with other RO_2 radicals. Night-time production via NO_3 and O_3 oxidation of VOCs may contribute to non-zero night-time concentrations.

⁵An F-test was applied to the data using the procedure of *Zanis et al.* [1999]. This was true even when the period before 11:00 a.m. was considered.

9.2 Weekend Effect

The data from Kleiner Feldberg was also averaged according to the day of the week to throw further light on the so-called “weekend effect”. This effect has been observed in ozone measurements at a number of German stations [c.f. *Fricke*, 2000]. It is an indicator of the effect of anthropogenic emissions on the levels of trace gases, as these are the only factors which can be expected to show a variation on a one week timescale. As discussed for the diurnal average profiles, the effects of mesoscale meteorological processes should average out over time, as they are independent of the day of the week. Similarly, natural emissions should not on average show any dependence on the day of the week. Thus, any observed variation provides information on any impact due to human activities. As anthropogenic emissions still occur at the weekend, it is only their rate relative to the nearly constant natural emission rate which varies in the course of the week. Consequently, without knowing the total emission rates the two types of emission source cannot be totally separated, so that this method does not allow an estimate of the relative importance of anthropogenic versus natural processes. However, the presence of a regular pattern does indicate whether human activities have any impact on photochemical oxidant levels.

An analysis of the Kleiner Feldberg data shows that there is indeed a small but significant “weekend effect” for NO_x and O_3 , although these are inversely correlated. Figure 9.8 shows the weekly profiles for RO_x , NO_x and O_3 , and average mixing ratios for each day of the week. The NO , O_3 and RO_x data were calculated using both 1998 and 1999 data, however there was no significant difference when only 1999 data were used. NO_2 data were only available for 1999. The average NO_x values for the weekends were found to be significantly different from the average weekday concentration using a standard T-test, whereby the difference was most significant for Sunday. For O_3 , the difference between the weekend and the entire week was not significant, but was significant when only the latter part of the week is considered. The most significant difference is in all cases between Sunday and the period Wednesday to Thursday, and until Friday for O_3 .

The average mixing ratios of both NO and NO_2 are lowest on Saturday and Sunday, whereby the Saturday values of NO_2 are only slightly lower than those on Monday or Friday. For NO_2 , the average mixing ratio was 1.56 ppbv, which was only half of the average of 3.31 ppbv for the working week. The corresponding mixing ratios for NO were 0.13 ppbv for Sunday and 0.325 ppbv for the average weekday. Saturday and Monday appear to represent transition days between the working week and the weekend for primary emissions. In contrast, the average daily ozone mixing ratio is highest on Sunday. The highest mixing ratios are observed on average on Saturday afternoon. The average ozone mixing ratio on the weekend was just over 49 ppbv on both days, and the average weekday mixing ratio was 46.8 ppbv.

The high NO_x mixing ratios during the week can be attributed to the higher level of emissions during the working week. These result from greater transport and industrial activity. The lowest values are reached on Sunday due to a decrease in the

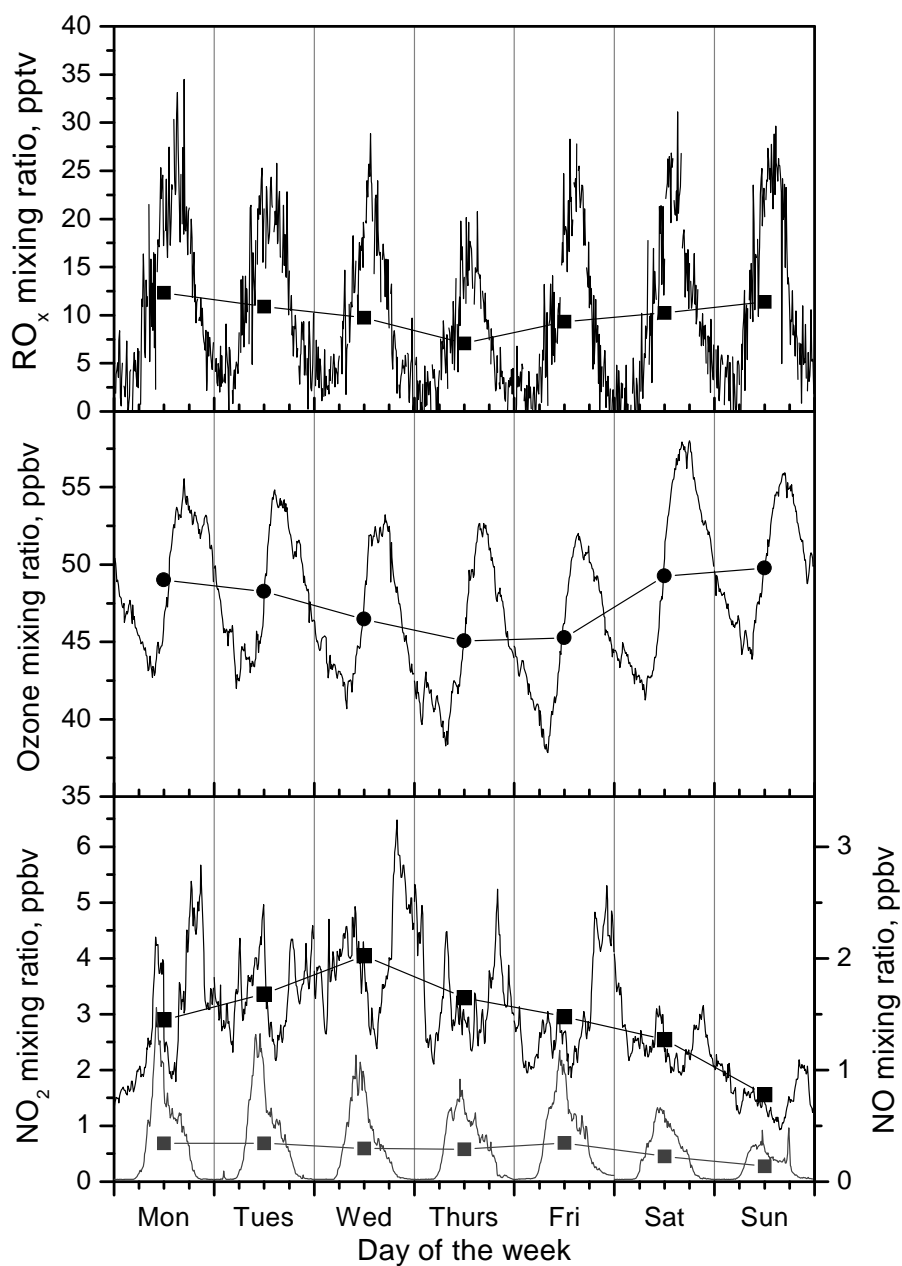


Figure 9.8: Average weekly profile for the mixing ratios of O_3 , RO_x , NO and NO_2 . All data represent 10 minute average mixing ratios averaged over the period June - September, 1999. NO and NO_2 were measured using a TECAN NO/ NO_2 analyser; the O_3 data is from the HLUG measurement network.

amount of emissions over the weekend. During fine weather periods, large numbers of cars carry weekend visitors to the Taunus. These do not seem to affect the NO_x measurements, which suggests that the measured NO and NO_2 values appear to reflect the regional situation more strongly than the local situation. However, the amount of such leisure time traffic may simply be too small on average to affect the results.

The weekend effect on ozone is more difficult to explain, although it has also been observed at other German stations. *Fricke* [2000] suggested that the higher weekend concentrations may be due to the delay which is necessary to allow production and transport of O_3 to the measurement site. However, this would require a delay of several days for the ozone production, which seems unrealistically long. They may also reflect less chemical destruction of ozone due to anthropogenic emissions, although this is probably only a minor factor.

A more likely explanation is provided by the isopleth representation of the model results which were presented briefly in Chapter 1 (see Figure 1.1 on page 6). Such studies have shown that, when NO_x levels are high enough, any moderate reduction in initial NO_x concentrations will lead to an increase in O_3 levels. Depending on the initial levels, only a major reduction in NO_x levels or a reduction in VOCs would lead to an eventual decrease in the peak ozone concentration. Such a regime is referred to as VOC limited, because only reductions in VOC emissions would result in a reduction in ozone levels. Measurements by *Hidy* [2000] indicate that this regime applies in eastern Germany. This also seems to be the case in the present situation, where the reduced NO_x emissions at the weekend are accompanied by higher O_3 levels.

The RO_x data shows less difference between weekend and working week. The minimum of 7 pptv occurs on Thursday, with much higher levels of around 10 pptv found at the beginning and end of the week. With the exception of the lower values on Thursday, a pattern is not clearly discernible. This suggests that biogenic emissions from the surrounding forests, which are not subject to a dependence on the day of the week, may dominate the supply of biogenic precursors. As RO_x levels are sensitive to the levels of both precursor and reaction partners, the observed variation is probably due to the interaction between the two. Higher levels of NO during the week could contribute to the lower RO_x levels towards the middle of the week, although this should be at least partially offset if anthropogenic VOC were a major source of RO_x precursors.

Taken together, the above mentioned variation in ozone and NO_x concentrations over the course of the week suggests that human activities have a measurable impact on observed mixing ratios at Kleiner Feldberg. Increased levels of NO_x during the week are representative of the higher levels of anthropogenic emissions. In contrast, levels of ozone increase at the weekend. This makes it clear that reductions in NO_x emissions do not automatically lead to reduced ozone levels. Much larger reductions in NO_x emissions than occur during the weekend appear necessary if net ozone levels are to be reduced.

9.3 Statistical relationships between components

The data series for 1998 and 1999 was investigated to determine whether statistical relationships between the atmospheric trace gases and meteorological parameters were present. A number of plausible statistical relationships consistent with known characteristics of the photochemical system were found. The most important relationships of O_3 and RO_x are discussed below. In most cases, a linear relationship was found to be the most significant. This was confirmed by carrying out a further series of statistical tests based on Spearman, Kendall [e.g., *Schönwiese*, 1992] and trans-information theory [*Weingartner*, 1985]. Even in cases where a nonlinear fit appeared more appropriate, the nonlinear fit was not statistically more significant than the linear correlation. The degree to which two quantities are correlated is given by Pearson's correlation coefficient⁶, r .

The data set used for the statistical tests was selected from the measurements at Kleiner Feldberg during 1998 and 1999. All days for which there was an incomplete set of meteorological data or no ozone data were excluded from the data set. Most of the time series for atmospheric components had gaps, partly due to instrumental downtime. Reducing the data set further to eliminate these gaps would have resulted in very small data sets, and the results would not have been as statistically significant. Hence, the data set was used despite the incompleteness of the data for the atmospheric components. Comparisons using smaller data sets indicated that this did not lead to a distortion of the results. The statistical significance of the correlations, which is dependent on the sample size, is quoted in the following tables of results. A smaller data set containing only data from ozone episodes was also investigated. The results from this analysis were similar to those for the larger data set, however they were statistically less significant due to the smaller size of the data set.

9.3.1 Ozone

The parameters for the linear relationship between the daily maximum ozone mixing ratio and various parameters are presented in Table 9.1. Plots of the most important relationships with meteorological parameters are shown in Figure 9.9. The plots for the atmospheric components are shown in Figure 9.10 on page 135.

The maximum ozone mixing ratio is correlated well with all of the meteorological parameters considered, except wind speed. The correlation with RH is strongly negative. These correlations do not necessarily reflect causal relationships, but may merely reflect a common dependence on weather conditions. Similar relationships were found by *Grosch and Schmitt* [1994] using a 6 - 12 year data set for several UBA stations.

⁶This is properly known as the Pearson product-moment coefficient of correlation and is described in all standard statistics textbooks [e.g., *Schönwiese*, 1992]. The square of r can be interpreted as the fraction of the total variation of y which is described by fitting a line of the form $y = ax + b$ to the data.

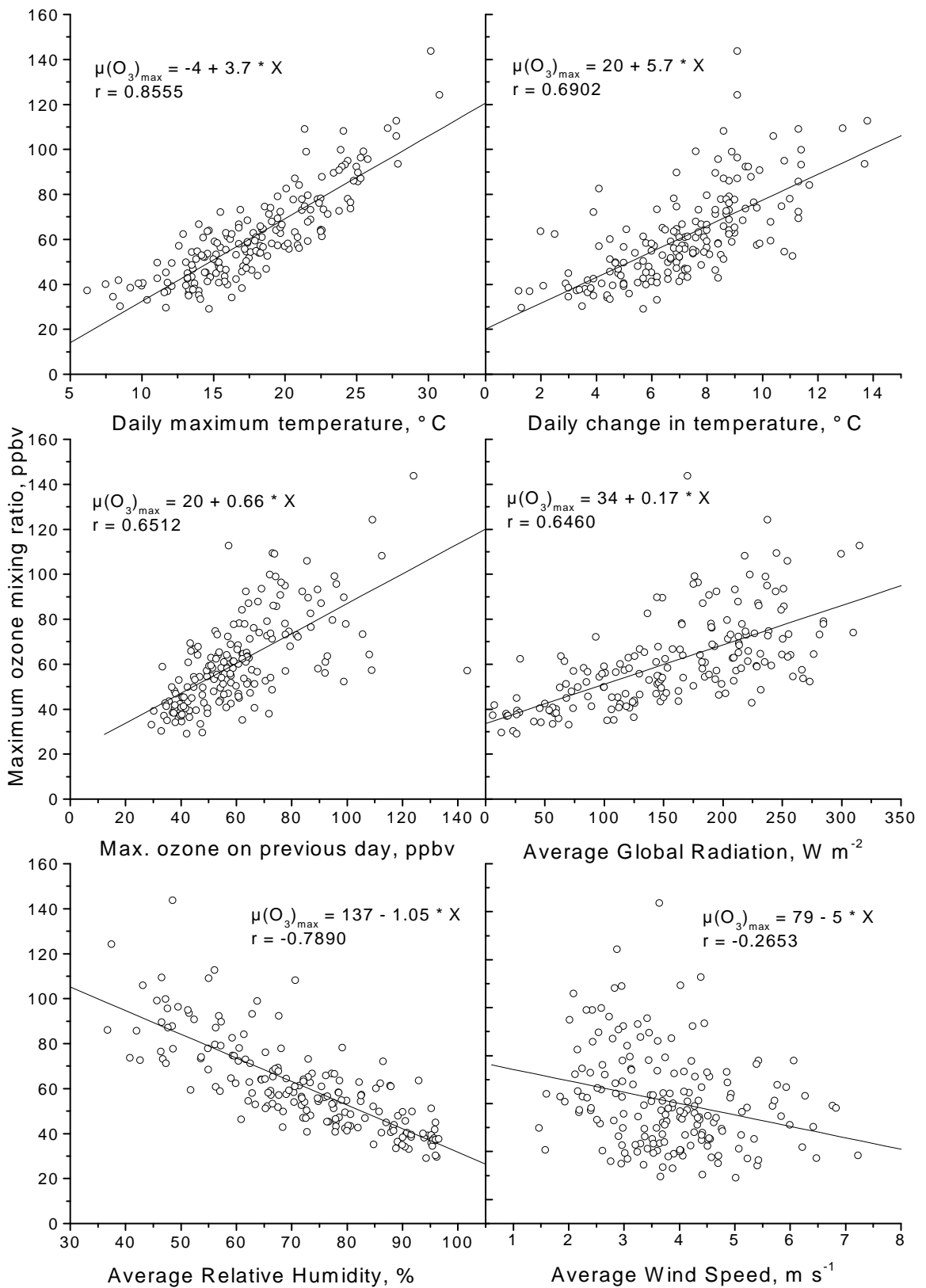


Figure 9.9: Plots of the correlation of the maximum mixing ratio of ozone with various meteorological parameters.

Table 9.1: Correlations between the maximum daily mixing ratio of O_3 and the average daily mixing ratio of RO_x , PAN and NO_x , and various meteorological parameters at Kleiner Feldberg for a data set from the summers of 1998 and 1999. Line of best fit: $Y = A + B \cdot X$; correlation coefficient, r ; number of days, N ; significance, S .

Maximum ozone mixing ratio (Y)

X	A	B	r	N	S, %
max. temperature	-4	3.7	0.8555	180	> 99.99
change in temperature	20	5.7	0.6902	180	> 99.99
glob. radiation	34	0.17	0.6460	180	> 99.99
ave. j_{NO_2}	37	7600	0.4779	180	> 99.99
ave. act. flux (O_3)	41	19	0.5046	180	> 99.99
relative humidity	137	-1.05	-0.7890	180	> 99.99
sunlight hours	41	3.1	0.6998	180	> 99.99
wind speed	79	-5	-0.2653	180	> 99.9
average RO_x	54	1.5	0.7251	81	> 99.99
max. RO_x	40	.61	0.6293	82	> 99.99
ave. PAN	47	19	0.5109	145	> 99.99
ave. NO	69	-17	-0.3022	156	> 99.9
ave. NO_2	73	-3.5	-0.3311	102	> 99.9

As has been observed in many other studies, the maximum ozone mixing ratio is best correlated with the daily maximum temperature. A linear fit explains 73% of the variability in the maximum ozone level. [Grosch and Schmitt, 1994] found that the relationship between ozone and maximum temperature was best described using a cubic polynomial. However, a polynomial fit brought no significant improvement in the correlation coefficient for the data set used in this study. This may be due to the limited range of temperatures in the data set in the current study, as the nonlinearity in the data used by Grosch and Schmitt only became apparent below 10°C. Only a few data points in the current data set had temperatures below 10°C, and they suggest a nonlinear relationship. A nonlinear fit was not significantly better than a linear fit for the data set used here. The observed relationship is in both studies purely statistical, and only serves to describe the observed relationship. The real physical link between temperature and ozone is more complex, and is undoubtedly nonlinear.

The good correlation between temperature and ozone is only partially due to the influence of temperature itself on ozone production. The amount of scatter in the plot for these, and all other, quantities shows that other factors also affect the observed ozone level. These include the influence of other meteorological and physicochemical factors which affect both temperature and ozone production. A primary factor is the intensity of solar radiation. Table 9.2 shows the correlations between the radiation parameters measured at Kleiner Feldberg and the daily maxima of both temperature

Table 9.2: Correlations between various radiation parameters with the maximum temperature and maximum ozone mixing ratio at Kleiner Feldberg for a data set from the summers of 1998 and 1999. Linear correlation: correlation coefficient, r . Number of days, $N = 180$ for all correlations.

Parameter	T_{\max}	$O_{3\max}$
	r	r
glob. radiation	0.6607	0.6460
ave. j_{NO_2}	0.5156	0.4779
ave. act. flux (O_3)	0.5481	0.5046
sunlight hours	0.7330	0.6998
c.f. T_{\max}		0.8555

and ozone. They are slightly better correlated with temperature. Radiation has both a direct and an indirect effect on the photochemical production of ozone, but it also supplies thermal energy to the atmosphere, leading to higher temperatures. Consequently, the correlation between radiation and temperature, although less than that between ozone and temperature, is quite high. Thus, weather situations with high average levels of photochemically active radiation are associated with ozone production and high temperatures. The reverse applies to the correlation with relative humidity. RH is high during episodes with a lot of cloud and high precipitation, leading to reduced radiation, temperatures and ozone production.

Temperature exercises a direct influence on ozone production via the temperature dependence of the chemical reactions leading to ozone production. In addition, VOCs have a higher partial pressure at higher temperatures. This leads to increasing emission rates of both anthropogenic and biogenic VOCs as temperature increases. Both these effects contribute to higher ozone production as the temperature rises, and contribute to the positive correlation observed here.

Wind speed is only weakly correlated with ozone levels, although the trend is towards lower levels at higher wind speeds. Dilution and vertical transport at high wind speeds contribute to a well mixed atmosphere, and cause a decrease in ozone levels. Both ozone and its precursors undergo dilution equally, so both ozone levels and ozone production can be expected to decrease at high wind speeds. Lower wind speeds are also more common in high pressure systems, which will contribute to the observed trend. However the statistical relationship is weak, with only about 7% of the variance in ozone explained by the wind speed. A weak relationship between ozone levels and wind direction was also observed. This will be discussed in Section 9.4.

Lines of best fit were also derived for the relationships between ΔO_3 and the same set of parameters. As defined on page 115, ΔO_3 is the difference between the average mixing ratio in the afternoon (14:00 - 18:00 CET) and in the morning (07:00 - 09:30

Table 9.3: Correlations between ΔO_3 and the average daily mixing ratio of RO_x , PAN and NO_x , and various meteorological parameters at Kleiner Feldberg for a data set from the summers of 1998 and 1999. Line of best fit: $Y = A + B \cdot X$; correlation coefficient, r ; number of days, N ; significance, S .

ΔO_3 (Y)						
	X	A	B	r	N	S, %
	max. temperature	-7	1.0	0.4718	178	> 99.99
	change in temperature	-8	2.7	0.6312	178	> 99.99
	glob. radiation	-0.3	0.072	0.5208	178	> 99.99
	ave. j_{NO_2}	2	3100	0.3745	178	> 99.99
	ave. act. flux (O_3)	3	7	0.3939	178	> 99.99
	relative humidity	31	-0.27	-0.4030	178	> 99.99
	sunlight hours	5	1.1	0.4940	178	> 99.99
	wind speed	18	-1.6	-0.1688	178	> 95
	average RO_x	15	0.008	0.0086	81	-
	max. RO_x	15	-0.001	0.0027	82	-
	ave. PAN	9	3	0.1812	143	> 95
	ave. NO	12	-0.2	0.0083	154	-
	ave. NO_2	15	-0.7	-0.1326	102	~ 80

CET). The parameters for the linear fits to the data are shown in Table 9.3. As can be seen by comparing Tables 9.1 and 9.3, the relationship with ΔO_3 is considerably weaker than the corresponding relationship with the maximum ozone mixing ratio. Some parameters have a direct causal influence on ozone photochemistry, so that a stronger correlation than observed was expected. For example, radiation, and the mixing ratios of NO and RO_x , directly influence ozone production, whereas PAN is a product of reactions which occur under the same conditions as ozone production. However, all quantities used here are daily averages, which do not reflect the temporal development on shorter time scales. ΔO_3 may be influenced strongly by short term, small scale fluctuations, by factors such as mixing and transport, and also by the interaction between these factors. Thus, it seems to be a poor parameter to describe the meteorological situation leading to ozone production. Its relationship to photochemical production will be discussed in Chapter 10. In contrast, the ozone maximum appears to be more representative of processes operating over a longer time scale, as discussed below on page 136, and is well correlated with quantities describing the overall weather system.

The daily average RO_x mixing ratio is well correlated with the ozone maximum ($r=0.7251$; see Figure 9.10), but has almost no correlation with ΔO_3 . RO_x has a causal relationship to the ozone concentration via its reaction with NO, so that it could be expected to be better correlated with the change of ozone concentration. The good

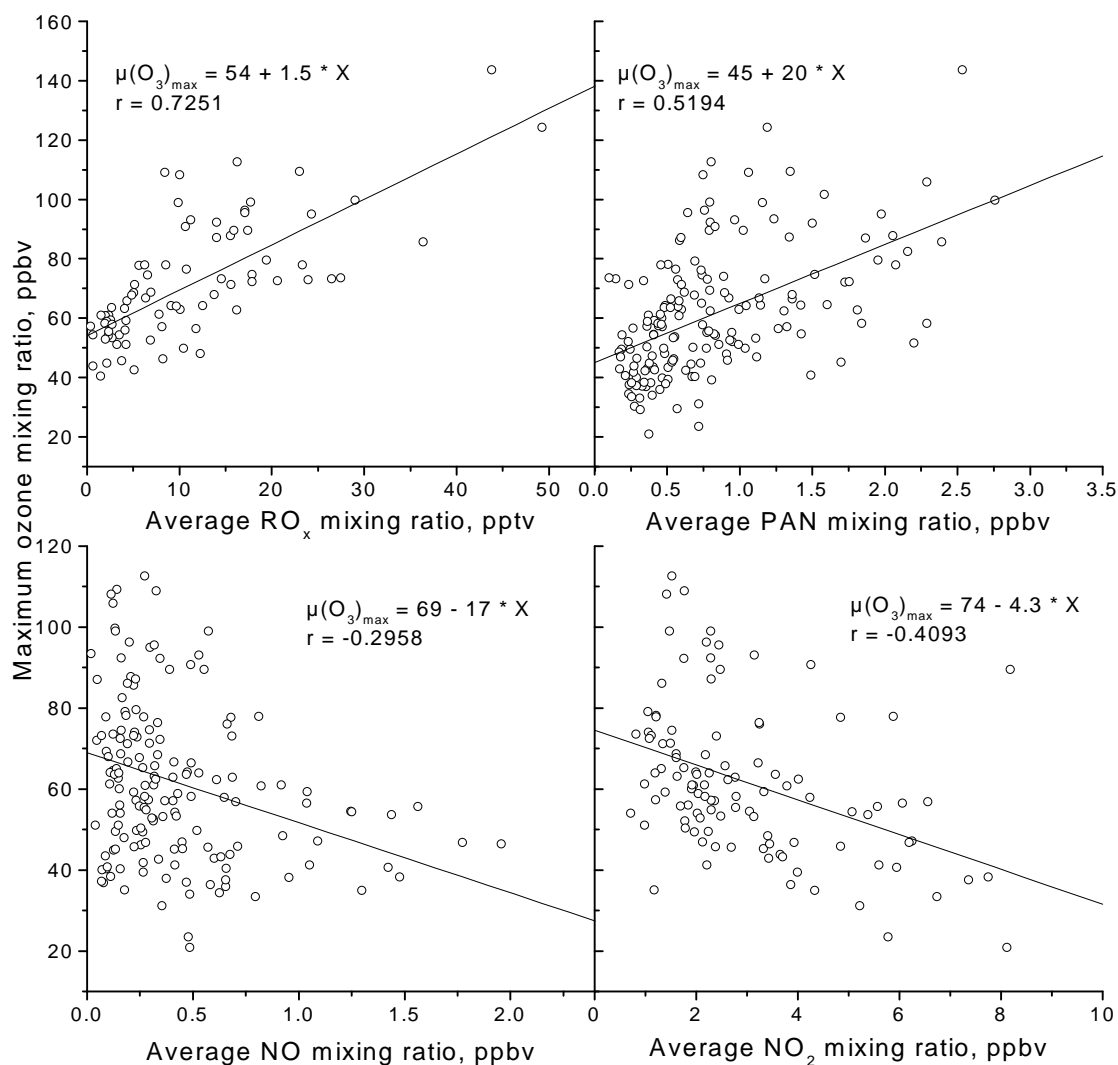


Figure 9.10: Plots of the correlation of the maximum mixing ratio of ozone with the average daily mixing ratios of RO_x, PAN, NO and NO₂.

correlation with the ozone maximum suggests that the overall weather situation plays the dominant role in determining both parameters. Thus, this relationship probably reflects the fact that both ozone and RO_x require stable fine weather periods to reach significant levels. The maximum RO_x level is not as well correlated with either the maximum ozone mixing ratio or ΔO_3 . This is probably due to the fact that the RO_x maximum can be a short term response to ambient conditions. RO_x radicals are short lived relative to ozone, so that levels fluctuate quite rapidly as concentrations of precursors and reaction partners change. One of their primary precursors, the OH radical, has a much shorter lifetime and is extremely sensitive to changes in radiation. Thus, the maximum mixing ratio of RO_x reflects ambient conditions on a short time

scale and is a poor indicator for conditions over the entire course of the day. It may have only a cursory effect on ozone production, and this is reflected in its weaker relationship to both the maximum level of O_3 and to ΔO_3 .

PAN also exhibits a significant correlation to the ozone maximum. PAN is produced by Reaction (3.12) between RO_2 radicals and NO_2 under similar conditions to those associated with ozone production. As was observed for RO_x , the correlation of PAN with ΔO_3 is much weaker than with the O_3 maximum. However, in contrast to RO_x , this is the result of PAN's relatively long life time, which allows it to accumulate from day to day. Thus, it is not as strongly dependent on daytime processes as ΔO_3 , resulting in a poor correlation.

Ozone has quite a weak relationship to both NO and NO_2 , despite the fact that NO_x is the direct precursor of ozone. NO_2 , as the immediate precursor to ozone, is destroyed in the reaction step leading to ozone production, which contributes to the slight negative correlation. However, the concentration of NO_2 does not necessarily reflect the amount of recycling it undergoes, which can be considerable during episodes of intense VOC oxidation. Furthermore, ozone is also dependent on the presence of other precursors, i.e. VOCs and RO_x . The negative correlation with NO may reflect the rapid reaction between O_3 and NO . However, the relationship is more complex, as the reaction of NO with RO_x leads to increased ozone production. Thus, the relationship between these three compounds is highly complex, and a clear relationship between the variables is not expected.

Persistence

Ozone episodes in Central Europe normally occur during periods of high pressure influence. During such episodes, the ozone level builds up from one day to the next, until a change in the meteorological conditions brings the episode to a close and causes the ozone level to drop. Thus, there should be a relationship between the ozone level on any given day and the maximum on earlier days. This was investigated by correlating the maximum ozone mixing ratio observed on each day (day 0) with the maximum ozone level on each of the previous days. A time lag of 1 to 14 days was investigated, whereby the correlation coefficient decreased nearly monotonically over this period. Figure 9.11 shows the correlation coefficient plotted against the time lag in days.

As expected, a significant correlation with the ozone maximum on the previous day was found, with over 40% of the variance in the ozone maximum on day 0 explained by the variation in the ozone maximum for the previous day ($r = 0.6519$). The correlation decreases rapidly with time. Thus, the ozone level on the preceding day appears to play an important role in determining the maximum ozone level reached on any given day. Any change in ozone level occurs relative to a base level which is determined largely by the level on the previous evening. Although, meteorological processes cause a drop in the ozone level overnight, the overlying reservoir layer and subsequent downwards

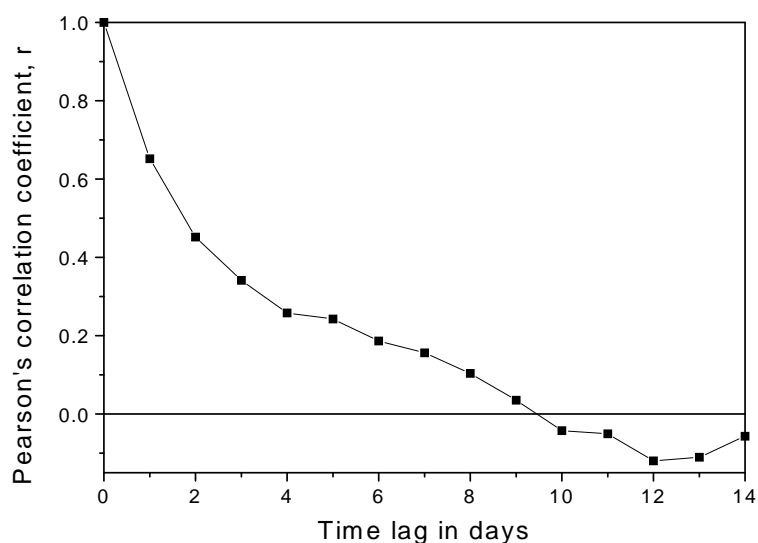


Figure 9.11: Plot of the Pearson's correlation coefficient, r , versus the time lag for the autocorrelation between the ozone maximum on day 0 and the maximum on the n th preceding day. Maximum 10 minute ozone values from the HLUG station on Kleiner Feldberg were used for the analysis. The data set included a total of 195 days from the period June to September, 1998 and 1999.

mixing after sunrise help reestablish the ozone level at an elevated layer during ozone episodes. Furthermore, weather patterns which are conducive to ozone formation tend to be slow moving, so that during such episodes the weather pattern can be expected to persist for several days, contributing to this effect.

9.3.2 RO_x

The parameters for the linear correlations between the average daily RO_x mixing ratio and several other quantities are presented in Table 9.4. Scatter plots for the correlations are shown in Figures 9.12 and 9.13. The daily average mixing ratio on two days can be seen from the plots to have been negative. They have been included in the data set, although they have no physical meaning. Random fluctuations can lead to such small negative average values on days with very low concentrations, so that rejecting them would ignore any instrument-based offset.

The correlations with RO_x are weaker for most quantities than those with ozone. The correlation coefficients for PAN, NO and wind speed are all slightly higher than the corresponding parameters for ozone, but the significance level of the correlations with RO_x is somewhat lower due to the smaller number of data points. As was the case for ozone, the statistical relationships partly reflect the influence of the fine weather conditions necessary for RO_x production. This is particularly true for all the

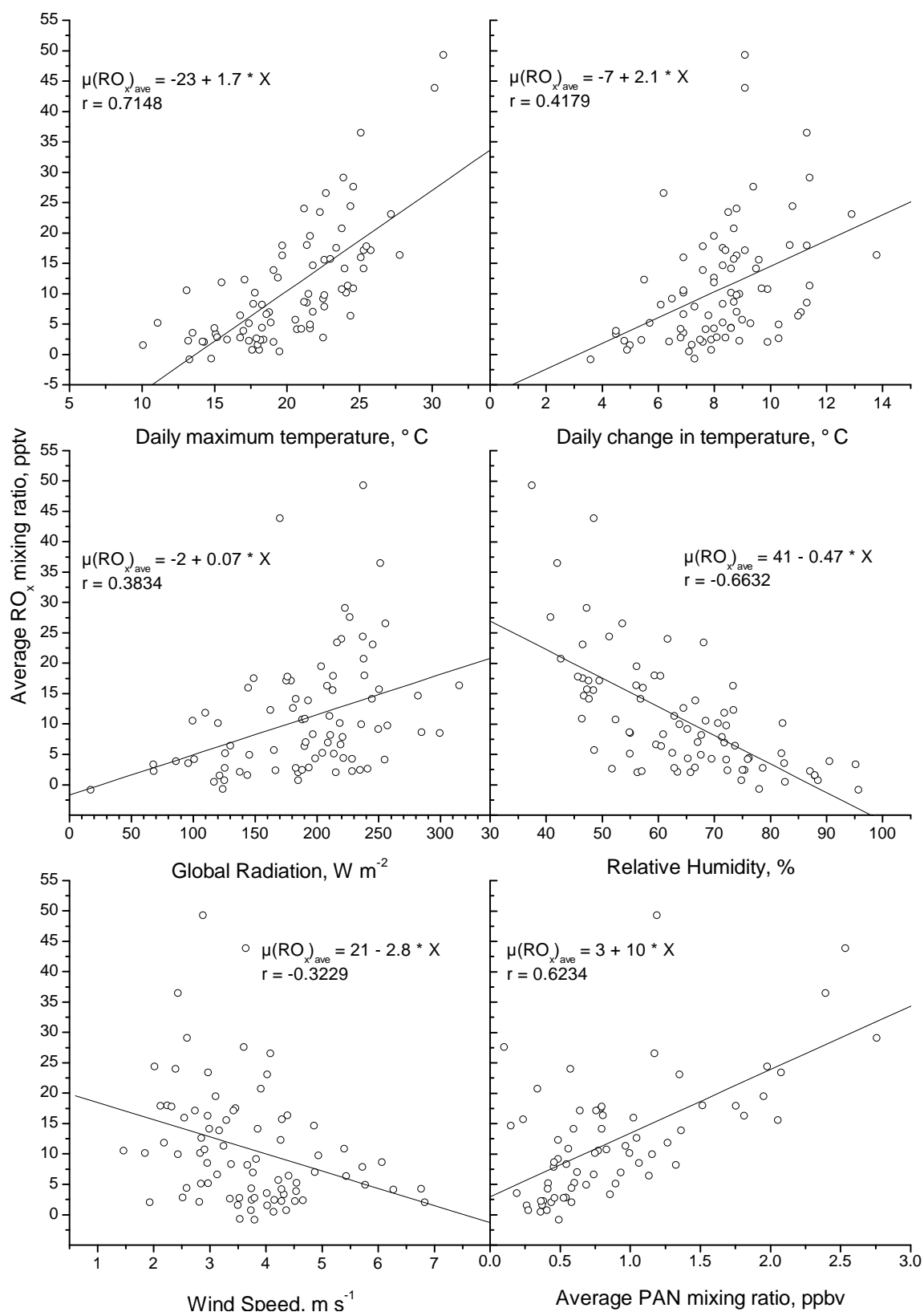


Figure 9.12: Plots of the correlation of the average daily RO_x mixing ratio with several meteorological parameters and with the average PAN mixing ratio.

Table 9.4: Correlations between the average daily RO_x mixing ratio and the mixing ratio of PAN and NO_x , and various meteorological parameters at Kleiner Feldberg for a data set from the summers of 1998 and 1999. Line of best fit: $Y = A + B \cdot X$; correlation coefficient, r ; number of days, N ; significance, S .

Average RO_x mixing ratio, pptv (Y)

X	A	B	r	N	S, %
max. temperature	-23	1.7	0.7148	81	> 99.99
change in temperature	-7	2.1	0.4179	81	> 99.9
global radiation	-2	0.06	0.3834	81	> 99.9
ave. j_{NO_2}	-5	4000	0.4339	81	> 99.99
ave. act. flux (O_3)	2	67	0.3185	81	> 99.5
relative humidity	41	-0.47	-0.6632	81	> 99.99
sunlight hours	0	1.3	0.5597	81	> 99.99
wind speed	21	-2.8	-0.3229	81	> 99.5
ave. PAN	3	10	0.6234	68	> 99.99
ave. NO	17	-18	-0.4045	80	> 99.9
ave. NO_2	10	-0.8	-0.1773	58	~ 80

meteorological parameters, for which the same considerations as for ozone apply.

RO_x has a much shorter lifetime than ozone and is consequently much more sensitive to changes in the ambient conditions. Thus, changes in radiation or in the concentrations of precursors or reaction partners, e.g. VOCs and NO, have an immediate impact on observed mixing ratios. These all operate on time scales much shorter than one day, which contributes to the scatter in the plots. Again similar to ozone, temperature is the parameter which is correlated best with RO_x , as it is a proxy for the conditions which underlie many of these relationships.

PAN is a direct product of the reaction of peroxyacetyl radicals with NO_2 , so a good correlation with RO_x is to be expected. However, PAN has a much longer lifetime than RO_x , allowing it to accumulate and undergo transport, so that the measured concentrations need not be directly related to its in-situ production. Thus, this correlation probably reflects not only the chemical relationship between RO_x and PAN, but also their common dependence on fine weather periods.

The negative correlation with NO is readily explained by the fact that the reaction with NO is the main sink for RO_x . Thus the presence of higher NO concentrations results in shorter lifetimes for RO_x radicals and prevents them from accumulating further.

The correlation between NO_2 and RO_x is quite poor. Further tests show that NO_2 correlations with other meteorological parameters and with PAN are generally poor, although it is well correlated with NO ($r = 0.6455$; $N = 121$). The relationship with NO is not surprising, as NO is the main source for NO_2 and they are also

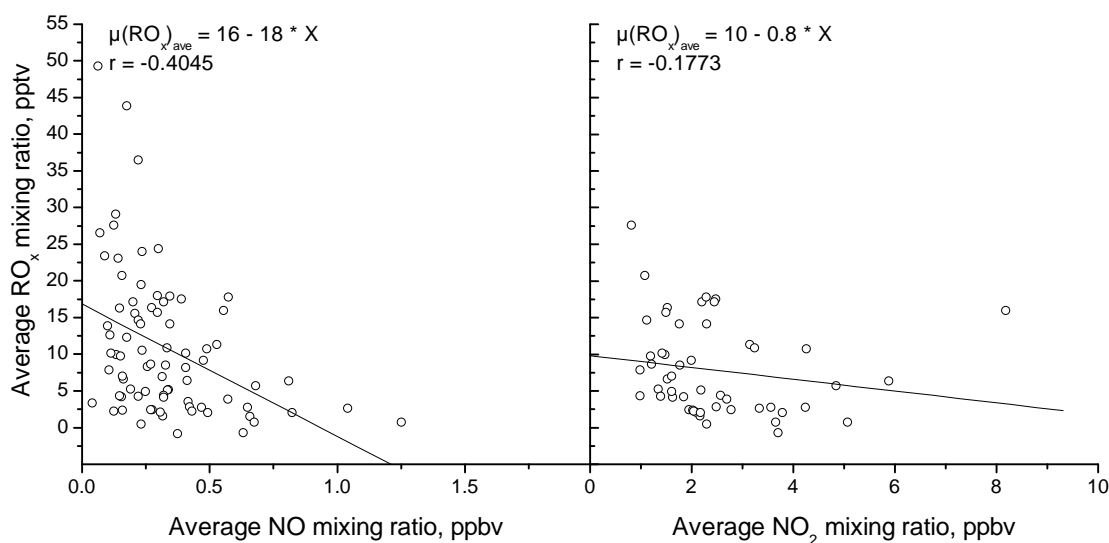


Figure 9.13: Plots of the correlation of the average RO_x mixing ratio with the average daily mixing ratios of NO and NO₂.

related via photochemical cycling. The weakness of the correlation with other trace compounds is more surprising, as NO₂ is the precursor of both O₃ and PAN, and is the product of the reaction between RO_x and NO. However, its role as an intermediate and the multitude of the interactions means that none of the relationships is strong enough to alone explain the variation in NO₂. Thus, simple statistical relationships are inadequate to explain the complexity of the NO₂ interactions.

Although these statistical relationships with the daily RO_x mixing ratio are consistent with known relationships, other quantities, such as VOCs, also need to be considered. The supply of VOCs, in particular, is a limiting factor for the production of RO_x radicals. However, due to the nonlinear nature of VOC oxidation, this is unlikely to be well described by a linear relationship.

9.4 Effect of wind direction

The wind patterns at Kleiner Feldberg are strongly influenced by the orography of the surrounding hills belonging to the Taunus Range (see Section 8.1). As can be seen in Figures 8.7 and 8.3, several valleys lead to Kleiner Feldberg, resulting in the air flow being channelled through these valleys and along the main ridge of the Taunus range. The primary wind channels are along the NE-SW axis of the Taunus ridge, up the Reichenbachtal from the SE, the Maßborntal from the ESE, the Emstal from the WNW, and from the NNW over Ober and Nieder Reifenberg. Each of these channels is apparent in the combined wind rose in Figure 9.14 for the months June to September

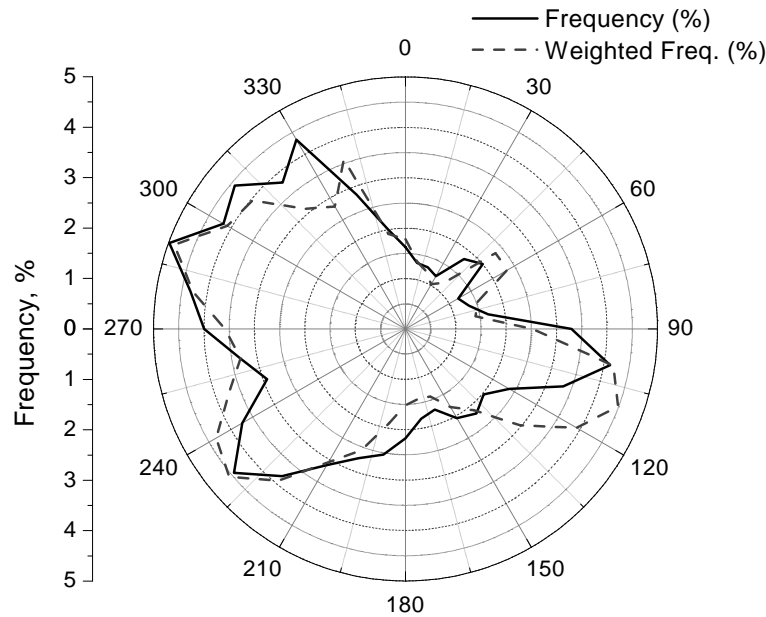


Figure 9.14: Wind rose for the combined period June to September, 1998 and 1999. The black lines represent the frequency of wind for a given direction, the dotted lines represent the weighted frequency (see text).

of 1998 and 1999, whereby the wind came mostly from the westerly quadrants. In 1998 the wind was mainly from the northwest sector (over Oberreifenberg and the Emstal), whereas in 1999 the most frequent wind directions were from the WSW along the Taunus ridge, or up the Maßborntal from Oberursel to the ESE.

The dashed line in Figure 9.14 represents the frequency, f , with which the wind came from a given direction ($\theta = x$), weighted by the wind speed ($v(\theta)$):

$$f_{(\theta=x)} = \frac{\sum v_{(\theta=x)}}{\sum_{\theta=0}^{360^\circ} v} \quad (9.1)$$

If the weighted frequency is higher than the average frequency, which is denoted by the black line, then winds from this sector had higher than average wind speed. Similarly, a lower weighted frequency indicates a below average wind speed. Low wind speeds are associated with longer residence times in the locality of Kleiner Feldberg, whereas air masses associated with high winds spend less time in the near vicinity of the station. As a result they may be more representative of conditions in the surrounding region or from even further away. For both years, lower than average wind speeds were associated with wind from the NW quadrant and from SSE, which suggests that air parcels from this sector may be more strongly influenced by local sources. Wind from along the ridge or from Oberursel have higher than average wind speeds, which may result in a greater contribution from air parcels originating farther away.

Measurements of CO and H₂ at Taunus Observatory in winter 1996-7 by *Wetter*

[1998] showed that the sectors with the highest CO concentrations were those from Oberursel to the east, from the direction of Wiesbaden to the SW, and from Oberreifenberg to the north. He did not, on average, observe significant increased CO mixing ratios directly from Frankfurt. He suggested that the higher mixing ratios from Oberursel represented air containing polluted air from Frankfurt-Hanau-Offenbach which had been channelled through the Maßborntal between Großer Feldberg and Altkönig, a hill lying between Frankfurt and Kleiner Feldberg.

Although these measurements were made during winter, it is to be expected that similar results should apply during summer to air from the various sectors. Accordingly, air from the SW and ESE should contain pollutants from the Rhine-Main industrial regions. Air from the NW should be considerably freer from pollutants, as, with the exception of smaller towns such as Oberreifenberg, there is mainly forest for 50-100 km to the north of Kleiner Feldberg. Overall, the analysis of the current data was consistent with the interpretation of *Wetter* [1998].

Wind roses for several different atmospheric components are shown in Figure 9.15. The data set included all days for which measurements of the individual components were available. Each day was classified according to the average wind direction, and average mixing ratios were calculated for each sector. The sectors encompassed 30° for all components except RO_x . Due to the smaller number and uneven distribution of days for which RO_x averages were available, the sectors used in the wind rose for RO_x were 45° wide. The average mixing ratio for all days in the data set was also calculated and is shown as a dotted circle in the same colour as the corresponding component.

The wind roses for NO and NO_2 show maxima from the SW and from Oberreifenberg to the NNW. The maxima to the NW are probably due to emissions from local sources, such as traffic, being channelled to Kleiner Feldberg. The high mixing ratios from the SW possibly reflect the combined contributions from local emissions in Königstein and the surrounding main roads, as well as industrial emissions from the Rhine-Main region. The lower mixing ratios to the NE and W can be attributed to the fact that anthropogenic emissions from these regions are likely to be at a minimum from both these directions, as they are represent largely forested areas. Wind from these regions possibly represent the natural background level of these precursors.

Air masses from the SE contained only average NO_x mixing ratios, but may reflect regional concentrations resulting from traffic and industry in Frankfurt and surrounding areas. A further source of NO_x is likely to be the A5 motorway, which passes to the east of Kleiner Feldberg and carries a lot of traffic. These sources appear to contribute to the average NO_x values, although high average values are not observed from this direction. However, the wind roses for both temperature and solar radiation also have broad maxima towards the east, and may indicate that the wind during fine weather episodes came predominantly from the east and SE.

The wind rose for RO_x has a similar shape to those for NO_x , although the highest mixing ratios were observed for wind from the S instead of from SW. Higher than average mixing ratios were also observed from the NW, and are probably due to the

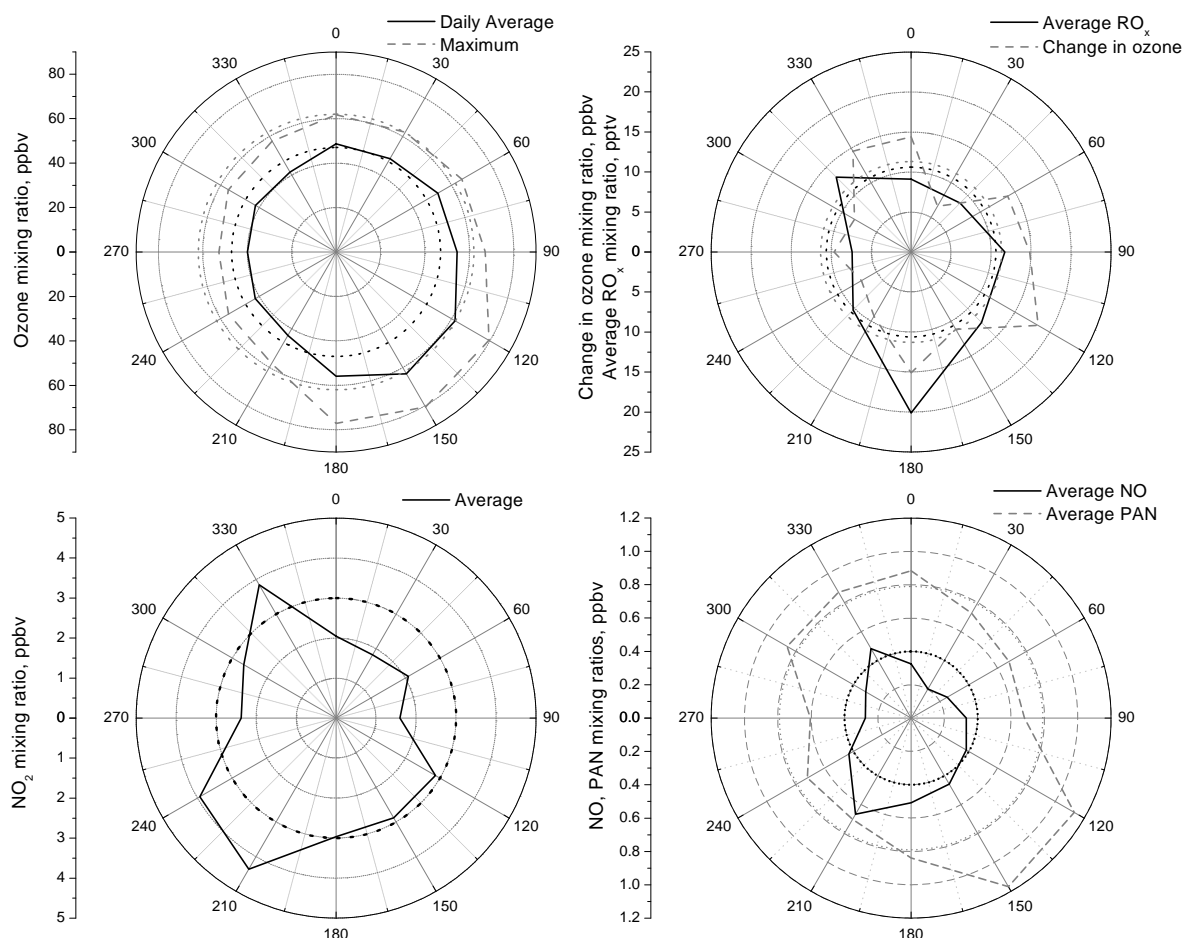


Figure 9.15: Wind roses for the average daily mixing ratios of O_3 , RO_x , NO , NO_2 and PAN , and ΔO_3 . The dotted circles represent the direction independent average mixing ratios of the respective components.

same local sources as for NO_x . The highest mixing ratios were from the south, with only average mixing ratios apparent in air masses from the SE. As is the case for NO_x , minimum mixing ratios were associated with wind from the NE or W. The data points for $\theta = 0^\circ$ and 180° represent measurements on only three and four days, respectively, so that they may not be as reliable as the other points, which are averages over nine or more days. However, the wind rose for ΔO_3 also has a maximum from the south, which indicates that the RO_x peak to the south is real, even if it may not be as pronounced as shown here. With the exception of this dominant maximum to the south, there is much less relative variation in the wind rose for RO_x than was observed for NO_x . This is consistent with the fact that RO_x is dependent on other sources than NO_x . VOC emission from the surrounding forests is a potential source which would dampen any directional dependence.

The wind roses for the secondary photooxidation products, O_3 and PAN , both

have a slightly different shape. Maximum mixing ratios are associated for both compounds with a broad peak to the SE. The shape of the wind rose for ozone is almost indistinguishable from that of temperature, which reflects the strong relationship between these two parameters. This suggests that wind from the SE was predominantly associated with the fine weather periods. Such air masses appear to have already undergone photochemical processing, resulting in enhanced O_3 and PAN levels, but only average levels of NO_x and RO_x .

Slightly above average mixing ratios of PAN were observed from the NW, similar to NO_x and RO_x , although levels from the SW were below average. The maximum to the NW may correspond to recent processing of local NO_x and VOC emissions, leading to a buildup of PAN. It does not appear to reflect aged air parcels as it is not associated with high O_3 mixing ratios, which may require longer processing times. Temperatures from this sector were also lower, so that PAN would have had a longer lifetime on such days. This would allow PAN to accumulate more quickly, but would also allow PAN originating farther away to contribute to the air masses arriving at Kleiner Feldberg. However, the higher NO_x mixing ratios from this direction suggest that local sources are important for this sector. Therefore, it is proposed that this peak to the NW, which is evident in most wind roses, is due to local emissions of VOCs and NO_x from Oberreifenberg and traffic in this sector. A local source in this direction is supported by the wind rose in Figure 9.14, which shows that wind from this sector was associated with slightly lower than average wind speeds.

In conclusion, the wind roses indicate that raised ozone levels are mostly associated with the transport of processed air from the east to southeast during fine weather periods. Such air masses mostly reach Kleiner Feldberg from the valley leading from Oberursel to Kleiner Feldberg. Polluted air was also associated with wind from the SW. However, air from this sector shows little evidence of processing and appears to be associated with days with low solar radiation input and low pressure systems. Evidence is also found for a local source of NO_x and VOC to the NW.

9.5 Conclusions

Average diurnal profiles showed that the main features of the daily behaviour of RO_x can be readily explained in terms of their reaction with NO , which is rapid during the morning. This causes a shift of the maximum towards afternoon. This is consistent with the diurnal O_3 profile, which shows an average production for the measurement period of around 13 ppbv per day. The period of maximum net ozone production corresponds well with the period of increasing or maximum RO_x levels. The photochemical production of ozone due to the reaction of RO_x with NO will be investigated further in the following chapter.

The statistical relationships between ozone, its precursors and the meteorological

conditions were investigated using the measurements at Kleiner Feldberg during the summer months of 1998 and 1999. Although the ozone maximum is well correlated with the average mixing ratio of RO_x radicals, this cannot be attributed solely to the role played by RO_x radicals in O_3 production. Both O_3 and RO_x are produced under similar meteorological conditions, and these meteorological processes contribute significantly to the observed statistical relationships. The daily maxima in the mixing ratios of both O_3 and RO_x correlate best with temperature. Temperature appears to be the best proxy for the weather conditions under which photochemistry can take place.

Chapter 10

Predicting ozone

Due to the health risks associated with high ozone concentrations, considerable effort is put into predicting ozone concentrations during the summer months. A variety of approaches are currently in use by various environmental agencies for predicting ozone concentrations on the following day. These range from elaborate chemical models to empirical or statistical methods. The latter are a relatively cost-effective approach to the problem. One of the aims of this project was to investigate the possibility of improving the current methods by taking into account the information on photochemical production of ozone provided by the RO_x measurements.

Peroxy radicals are responsible for the photochemical production of O_3 during the daytime and are the primary cause of the elevated ozone concentrations observed during the summer. Measurements of RO_x and NO concentrations allow the ozone production rate to be calculated. The daily contribution of photochemical production to the ozone concentration is then equal to the integral of the ozone production rate over the course of the day. The ozone production due to RO_x has been calculated using the measurements at Kleiner Feldberg and are presented below. The degree to which photochemical ozone production alone is responsible for the observed increase in the ozone mixing ratio during the daytime is then considered.

Knowledge of the photochemical production may allow improvements in the accuracy of ozone forecasts, at least for short term forecasts. Due to their short lifetimes, taking peroxy radicals measurements into account is unlikely to improve the ability of long term forecasts to predict ozone concentrations.

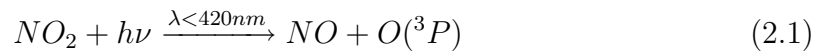
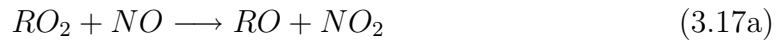
Grosch and Schmitt [1994] have shown that a simple statistical model with only three input parameters is capable of explaining 50-80% of the total variance in the ozone concentration at 49 German stations¹. Their model used a multiple linear fit to the maximum temperature for the day of interest, as well as the maxima of temperature and ozone concentration from the previous day. A similar statistical model

¹The model was parameterised independently for each station.

is presented for Kleiner Feldberg. The morning measurements of RO_x concentrations are then used to extend the model. This is used to predict the ozone concentration for that afternoon and the results are compared to the observed values.

10.1 Calculation of ozone production

Local photochemical ozone production results from the conversion of NO to NO_2 via its reaction with peroxy radicals, and the subsequent photolysis of NO_2 , as discussed in Chapter 2,



The ozone production rate can be approximated by

$$\frac{d[O_3]}{dt} \approx k^*[NO][RO_2]_{total} \quad (2.23)$$

$$\approx k^*[NO][RO_x] \quad (10.1)$$

where $[RO_x]$ is the total concentration of RO_x radicals as measured using the chemical amplifier (CA), and k^* is the average rate coefficient for the reaction between NO and RO_2 . k^* is theoretically the weighted average of the reaction rates of each RO_x radicals present in the atmosphere with NO. The average should be weighted by the relative abundance of the relevant RO_x radicals. As HO_2 and CH_3O_2 are the two most common peroxy radicals [Mihelcic and Volz-Thomas, 1994; Ashbourn et al., 1998], k^* can be assumed to be approximately equal to the average reaction rates for the reactions of these two peroxy radicals with NO. In this study, $k^* = 8 \times 10^{-12} \text{ cm}^3 \text{ molecule}^{-1} \text{ s}^{-1}$.

The amount of ozone resulting from local production during the day is equal to the integral of the local production rate over the entire day. The ozone concentration at time t_i as a result of local photochemical production alone can then be calculated by adding the ozone concentration at sunrise to the daytime photochemical ozone production:

$$[O_3]_{calc,t_i} \approx [O_3]_{t_0} + \int_{t_0}^{t_i} \left(\frac{d[O_3]}{dt} \right)_{pc} dt \quad (10.2)$$

$$\approx [O_3]_{sunrise} + \sum_{t_0}^{t_i} (k[NO]_i[RO_x]_i) \Delta t \quad (10.3)$$

where pc denotes photochemical production, t_0 is 00:00 CET and $[O_3]_{sunrise}$ is the ozone concentration at sunrise.

NO_2 represents a reservoir which, in the absence of photochemical production, is in equilibrium with ozone and NO. The reaction of O_3 with NO leads to an increase in the amount of NO_2 in this reservoir, whereas photolysis of NO_2 results in the production of O_3 . Small changes in the ozone concentration occur as a result of fluctuations in the NO_2 reservoir. This needs to be accounted for when calculating the ozone concentration [Weißmayer *et al.*, 1995]. Thus, the change in the NO_2 concentration at a given time of day, t_i , relative to the NO_2 concentration at sunrise² was subtracted from the calculated O_3 concentration to obtain the adjusted O_3 concentration for that time of day:

$$[\text{O}_3]_{calc}' = [\text{O}_3]_{sunrise} + \sum_{t_0}^{t_i} (k[\text{NO}]_i[\text{RO}_x]_i)\Delta t - ([\text{NO}_2]_{t_i} - [\text{NO}_2]_{sunrise}) \quad (10.4)$$

where $[\text{NO}_2]_{t_i}$ is the NO_2 concentration at time t_i . This assumes that any deficit has been completely photolysed to O_3 , and that any surplus is completely due to the reaction of O_3 with NO. The resulting equation is essentially a simplified null order diagnostic model for the photochemical change of the ozone concentration.

10.2 Observed change in ozone mixing ratio vs modelled ozone production

The photochemical production of O_3 was calculated on the basis of Equation 10.3 using the measured data from Kleiner Feldberg for the summer of 1999. The data set used for this calculation included the measurements of RO_x , NO, NO_2 and O_3 concentrations on all days of the summer of 1999 for which measurements were available for the entire daylight period and for which the maximum global radiation was over 600 W m^{-2} . The latter criterium ensured that only days with suitable conditions for photochemical ozone production were included in the data set. This criterium was fulfilled on 52 days. NO_2 data were used to calculate adjusted O_3 concentrations using Equation 10.4. Both sets of results have been compared with the observed change in the ozone concentration, ΔO_3 . This was defined on page 115 as the difference between the average mixing ratio of ozone on the afternoon (15:30 - 16:30 CET) and in the morning (09:00 - 10:00 CET).

Figure 10.1 presents a plot of the total daily ozone production calculated using Equation 10.3 vs ΔO_3 . A linear fit to the data is also shown. Figure 10.2 shows a similar plot for the total daily photochemical O_3 production corrected by the effect of fluctuations in the NO_2 reservoir using Equation 10.4. The correlation coefficients for

²The one-hour average concentration for the hour beginning at the start of civil twilight in the morning was used as the base concentration.

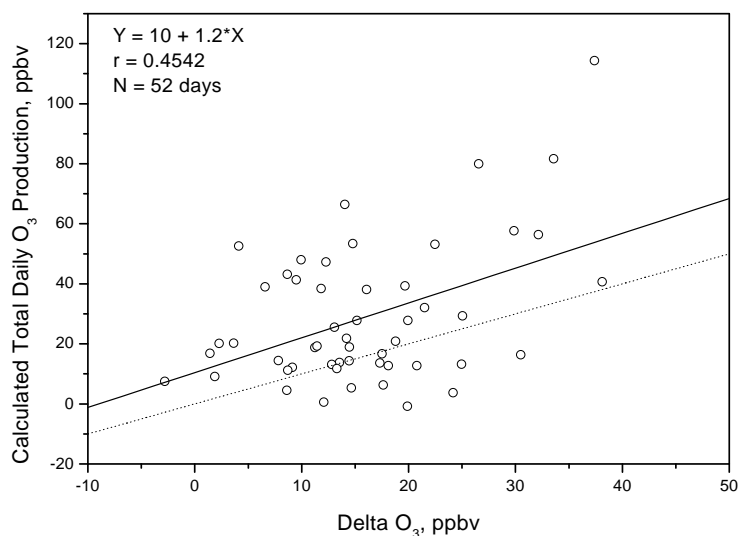


Figure 10.1: Plot of ΔO_3 vs the total daily photochemical O_3 production calculated on the basis of the reaction between RO_x and NO . The dotted line represents the 1:1 gradient.

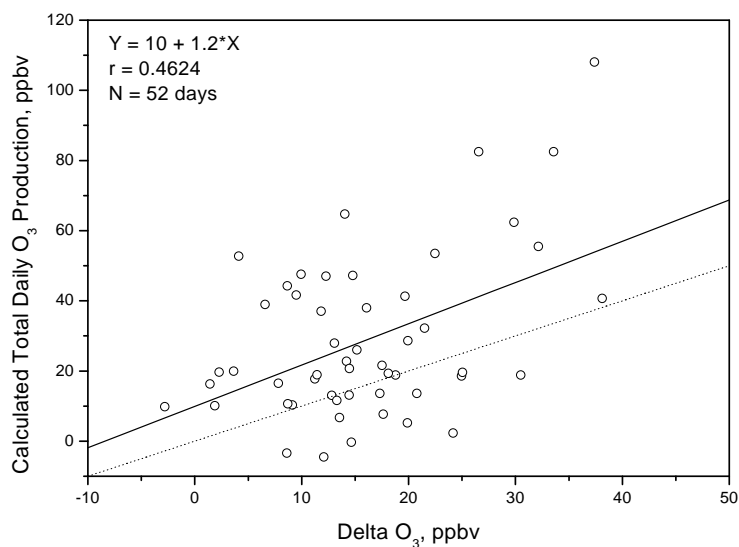


Figure 10.2: Plot of ΔO_3 vs the total daily photochemical O_3 production calculated on the basis of the reaction between RO_x and NO , and corrected for the change in NO_2 . The dotted line represents the 1:1 gradient.

both plots are quite low. The variance in the total calculated daily ozone production explains just over 20% of the observed variance in the daily change in the ozone concentration, ΔO_3 . Although inclusion of the effect of the NO_2 reservoir on the O_3 mixing ratio was found to improve the shape of the calculated daily profiles, its

inclusion has little effect on the total calculated O_3 production. The inclusion of NO_2 results in only an extremely small improvement in the correlation between the calculated O_3 production and ΔO_3 , which considers the net effect over the entire day.

The line of best fit shows that the total calculated daily ozone production overestimates the actual change in the ozone concentration by about 20%. The plot shows a wide degree of scatter around this line, with the calculated ozone production up to three times the observed change on some days. On other days, the calculated ozone production is nearly zero, although ΔO_3 was over 20 ppbv on some of these days.

These results show that the calculated photochemical ozone production is not a reliable indicator for ΔO_3 when considered alone. Other factors such as advection and changes in the meteorological conditions probably have an effect on the daily change in the ozone concentration. The data set has been filtered for several parameters, such as wind speed, which is related to advection, however no parameter could explain the observed results on its own.

10.3 Diurnal profile of ozone production

The average effect of daytime processes was investigated by comparing the average rate of ozone production to the average observed rate of change of the ozone mixing ratio as a function of time of day. The calculated profiles of photochemical ozone production were averaged over the 52 day data set used in the previous section to suppress the effect of non diurnal processes. The average rate of change in the measured ozone mixing ratio was also calculated for the data set. The daily profiles of the average ozone production rate and the average rate of change in the ozone mixing ratio are shown in Figure 10.3. The smoothed lines represent a fit to the data using a Fast Fourier Transform (FFT) low-pass filter. The data points were smoothed on a time scale of one hour for the upper panel, and at 2 hours for the lower panel on account of the greater scatter in the signal.

The upper panel shows the diurnal profile of the calculated ozone production and the change in the observed ozone mixing ratio over the course of the day. The inclusion of the influence of the NO_2 reservoir has little effect on the smoothed profile, although the plot has considerably more scatter when the influence of NO_2 is included. This suggests that, as mentioned above, NO_2 does improve the agreement with the observed values on a short time scale, particularly during the early morning and late evening, however on time scales of over one hour it has very little effect on the ozone profile. The calculated ozone production rate has a maximum rate of approximately 5 ppbv h^{-1} at midday, and falls away to zero after 18:00 at night and before 06:00 in the morning.

The rate of change of the observed O_3 mixing ratio is negative before 08:00 in the morning and after 17:00 in the afternoon. Loss processes predominate during this period of the day, as NO and HO_2 mixing ratios are very low. The main loss process

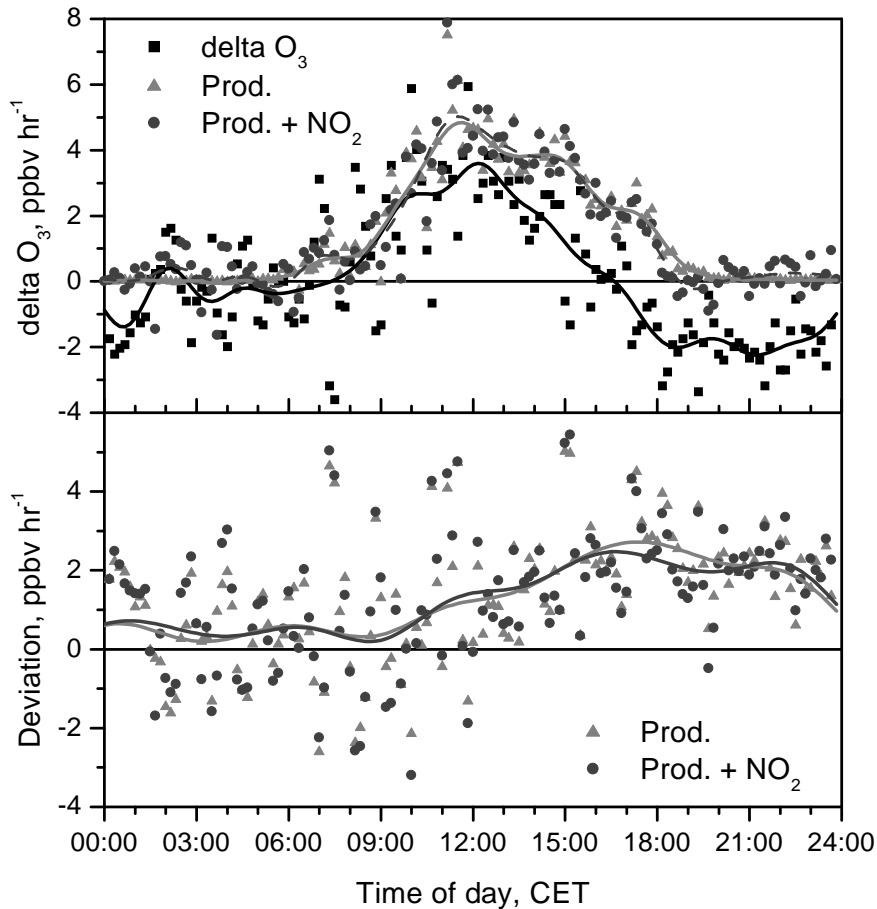


Figure 10.3: Average diurnal profile of the measured change in the ozone mixing ratio and the calculated ozone production (upper panel); and the deviation of the calculated production from the observed change in O₃ (lower panel). Each data point is a ten-minute average expressed as the hourly change in the mixing ratio. In each panel, the calculated ozone production is plotted both with and without the effect of NO₂. The smoothed curves are a fit to the data plots using FFT; the FFT time scale was 1 hour for the upper panel and 2 hours for the lower panel.

responsible for the night-time loss of ozone is probably deposition, although advection of polluted air due to the anabatic wind system during the early evening may make a contribution. The highest loss rate of 2.2 ppbv h⁻¹ occurs between 18:00 and 21:00. After 02:00 a.m. the rate of change is nearly zero.

During the day the rate of change of the O₃ mixing ratio is positive and is over 3 ppbv h⁻¹ at midday. The diurnal profile has a similar shape to the profiles for the calculated rate of ozone production. This can be seen in Figure 10.4, which shows the measured rate of change in the O₃ mixing ratio plotted against the calculated ozone production rate. The correlation coefficient for the plot of $r = 0.6626$ shows that there is general agreement between the plots. The negative offset and the slope of less than

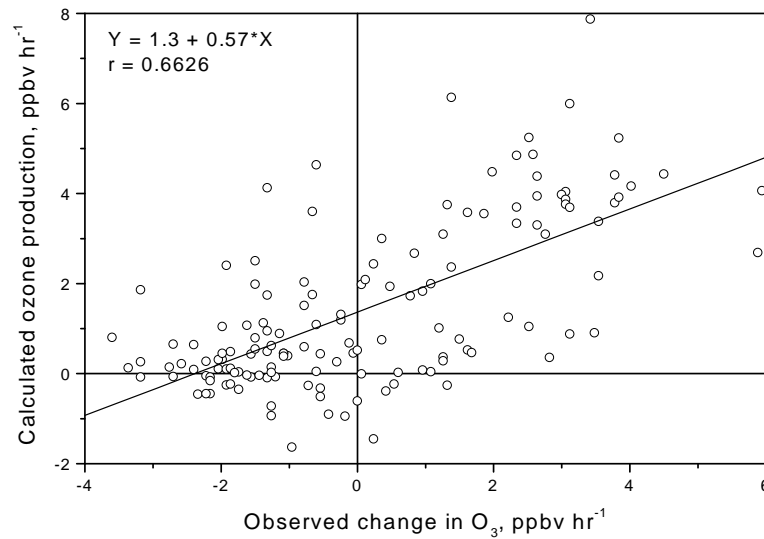


Figure 10.4: Plot of the rate of change of the ozone mixing ratio vs the calculated ozone production rate. The influence of NO_2 is included in the calculated production rate.

unity is due to the presence of loss processes. These reduce the effective production rate during the daytime.

The deviation between the calculated production rate and the observed rate of change is plotted in the lower panel of Figure 10.3. The deviation during the day and in the early evening is higher than during the early morning period. The change in the ozone mixing ratio would be overestimated if model calculations only took the ozone production rate into account. As loss of ozone by reaction with NO is already accounted for by the inclusion of NO_2 in the calculation of the production rate, this deviation is probably caused by meteorological processes associated with the increased convection during the day. Advection associated with the local topography is likely to result in slope winds with the desired diurnal pattern. This should result in the transport of presumably more polluted air from lower altitudes to the summit of Kleiner Feldberg during the late morning and evening. This has a minimum during the late night and early morning, before increasing during the morning. Deposition rates are strongly influenced by the degree of mixing. This is at a maximum during the afternoon, and drops away after sunset. Deposition is therefore likely to contribute to the observed diurnal pattern, but cannot explain the observed deviation on its own. Thus, the primary non-photochemical factors responsible for the diurnal profile of the change in the ozone mixing ratio are likely to be both deposition and transport associated with the diurnal circulation pattern.

In summary, the shape of the average diurnal profile of the ozone mixing ratio for days with high levels of solar radiation is primarily due to the temporal variation in the photochemical ozone production rate. Meteorological processes with a strong

dependence on the time of day, such as deposition and transport, lead on average to an effective reduction in the accumulation rate of O_3 from photochemical production alone by approximately 25-30% during the middle of the day. On any given day, however, the strong variation in meteorological conditions which are independent of the time of day can cause a large deviation from this average pattern. This results in the poor correlation between total daily zone production and the observed change in the ozone mixing ratio which was found in Section 10.2.

10.4 An extended statistical model for predicting ozone concentrations

As the calculated ozone production is not found to be a good predictor for the observed increase in the ozone concentration on its own, the feasibility of using the measured RO_x concentrations in a statistical forecast model for ozone was investigated. As a first step towards a predictive model, the statistical relationships discussed in the previous chapter were used as the basis for establishing a multi-parameter statistical model to describe the maximum afternoon ozone concentration.

All measurements from 1998 and 1999 with a complete set of NO , RO_x and O_3 measurements were included in the data set for the statistical analysis. Data from 103 days were included in the data set. Although ideally only days with obvious photochemical production should have been included in the data set, such a data set would have been too small to allow interpretation of the results. A multiple linear regression was then carried out on the data set. Table 10.1 shows the quantities which were included in the multiple linear regression. The resulting regression included only

Table 10.1: Development of a multiple linear progression to describe the maximum mixing ratio of ozone at Kleiner Feldberg. Data was used from 103 days during the summer months June to September, 1998 and 1999. A near complete data set was available for each of the days.

1	Parameter	3	Correlation Coefficient, r	Explained Variance, %	Increase in r^2 , %
	T_{max}		0.887	78.6	-
	T_{max} $[RO_x]_{ave}$		0.908	82.5	3.9
	T_{max} $[RO_x]_{ave}$ GR_{ave}		0.921	84.8	2.3

Parameterisation:

$$(O_3)_{max} = 2.126 \cdot T + 716.7 \cdot (RO_x)_{ave} + 0.0793 \cdot GR_{ave} + 5.287$$

three quantities as input:

- maximum temperature, T_{max} ,
- the average daily mixing ratio of RO_x , $(RO_x)_{ave}$,
- and the average global radiation, GR_{ave} .

Taken together the three input quantities described nearly 85% of the variance in the maximum O_3 mixing ratio. The inclusion of further quantities did not lead to a significant improvement. This is purely a diagnostic relationship, as neither RO_x nor global radiation can be more readily predicted than O_3 itself. The dominant input quantity is the maximum daily temperature. The inclusion of the mixing ratio of RO_x and global radiation, which are indicators of the level of photochemical production, only marginally increases the declared variance for the maximum O_3 mixing ratio.

The prognostic relationship of *Grosch and Schmitt* [1994] used the maximum temperature of a given day, and the maximum temperature and ozone maximum of the previous day to predict the maximum ozone mixing ratio. The maximum temperature for the day under consideration was derived from weather forecasts. This statistical model proved capable of predicting 50-80% of the cases, in which the ozone maximum exceeded 90 ppbv.

A similar predictive model was established for Kleiner Feldberg using the maximum daily temperature and the ozone maximum from the previous day, $O_{3'_{max}}$. The temperature on the previous day was not found to improve the predictive capability of the forecast and was omitted. The RO_x mixing ratio at different times of the morning, as well as the calculate ozone production up to a given time were also included in the forecast to see if this brought any improvement in its ability to predict the maximum ozone mixing ratio. The results are shown in Table 10.2.

The results show that neither the inclusion of morning RO_x mixing ratios, nor the calculated ozone production for the morning improves the ability to forecast the maximum ozone mixing ratio. The dominant relationship remains the relationship with temperature, which acts as a proxy for both the photochemical conditions and also for the meteorological conditions.

10.5 Conclusions

Although the photochemical ozone production due to the reaction between RO_x and NO describes the daily variation in the rate of change of the ozone mixing ratio quite well, other processes clearly play a significant role. Thus, the photochemical production alone is unable to adequately describe the observed daily change in the ozone mixing ratio.

The inclusion of morning RO_x measurements also provided no significant improvement in the ability of a simple statistical forecast to predict the afternoon maximum

Table 10.2: Improvement of a simple prognosis of the daily maximum O_3 mixing ratio by inclusion of RO_x mixing ratios from the morning of the day under consideration, or calculations of the total ozone production before a given time. The maximum temperature on the day, T_{max} , and the ozone maximum from the previous day, O_{3max}' , are included as forced variables. The RO_x mixing ratios are 1 hour averages for the hour prior to the time shown. The improvement in r^2 is relative to the value including the forced parameters.

Parameter	Correlation Coefficient	Explained Variance, %	Improvement in r^2 , %
T_{max}	0.887	78.6	-
O_{3max}'	0.895	80.1	1.5
$RO_x(09:00)$	0.895	80.1	-
$RO_x(10:00)$	0.896	80.2	0.1
$RO_x(11:00)$	0.896	80.3	0.2
$RO_x(12:00)$	0.896	80.3	0.2
O_3 Prod. (09:00)	0.898	80.6	0.5
O_3 Prod. (10:00)	0.898	80.6	0.5
O_3 Prod. (11:00)	0.897	80.5	0.4
O_3 Prod. (12:00)	0.898	80.6	0.5

O_3 mixing ratio. Improvements in the CA may improve the level of accuracy of these measurements by reducing noise levels, however, the dominance of temperature suggests that even short-term improvements in the predictive ability of such statistical forecasts is unlikely. However, RO_x measurements may become useful for improving forecasts using chemical models. As a first step towards this goal, our understanding of RO_x photochemistry needs to be further tested using measured data. The following chapter investigates the ability of a simple chemical model to model the profiles of RO_x and OH concentrations at Hohenpeissenberg.

Chapter 11

Steady state OH and RO_x model

Peroxy and OH radicals are intimately linked via the catalytic oxidation cycle which leads to the oxidation of VOCs and the production of ozone. A measurement campaign to investigate the photochemistry of OH and RO_x was held at Hohenpeissenberg during June and July 2000. The main aim of the campaign was to make measurements of all the major components involved in this oxidation cycle and to model these radical species using a steady state radical balance model. To achieve this aim, the routine measurements at Hohenpeissenberg were supplemented by measurements of the total RO_x concentration using the IMG-CA, and additional measurements of VOCs were scheduled during an intensive measurement phase. The instrumentation used during the campaign has already been described in Chapter 8.

The main set of peroxy radical measurements were made during the period 18 June to 6 July, 2000. The initial four day period from 18 to 21 June was characterised by fine weather and intense photochemical activity. As a result, an intensive series of measurements including OH, VOCs, O₃, NO_x, H₂O₂ and meteorological parameters were carried out. The main features of the measurements on these five days will be discussed in the following section. This is followed by a description of the steady state model in Section 11.2 and a discussion of the results in Sections 11.3 and 11.4.

The four day episode was marked by a high pressure system over central Europe during the week leading up to 21 June. In most regions of Central Europe, cloudless skies led to higher than normal temperatures. Thunderstorms were recorded near the Alps on 20 June, but these were well to the south of Hohenpeissenberg. This period was followed by an abrupt change on the 22nd as a trough moved over Central Europe, but this was not accompanied by strong frontal activity. Increasing thunderstorm activity on the evening of 22 June brought the episode to an end.

11.1 Measurements at Hohenpeissenberg

The mixing ratios of various atmospheric components are shown in Figure 11.1 for the intensive phase from 18 to 21 June. Figure 11.2 shows the most important meteorological parameters. The mixing ratios of the most important VOCs or groups of VOCs are shown in Figure 11.4 on page 162. Pronounced diurnal profiles were observed for O₃, RO_x, OH, NO, isoprene and the terpenes. Nearly cloudless days resulted in maximum daily temperatures of over 25°C on all days apart from 18 June.

On each day, the profiles of several trace gases contain the signature of a significant transport event during the late morning. Peaks in the mixing ratios of NO and NO₂, and to a lesser extent for CO and SO₂, all suggest that polluted air is being carried by advection to the measurement site. The high NO levels also lead to a dip in the O₃ mixing ratio. On both 19 and 20 June there is also a pronounced peak in the late morning in the mixing ratios of most VOCs. This is evident in the profiles of all VOCs except the group consisting of non-biogenic alkenes. The presence of the signature in the profile for aromatic compounds and the group of alkanes, alkynes and cyclic alkanes, which are predominantly anthropogenic in origin, indicates that it is associated with the arrival of polluted air. Isoprene and terpene mixing ratios also exhibit a peak at this time.

The arrival of this highly polluted air is caused by the breakup of the stable nocturnal boundary layer and the growth of the convective mixed layer during the morning. This allows air which has become enriched in pollutants as a result of their accumulation overnight to be transported upwards from the surrounding area, and its arrival at the measurement site results in the observed peaks in these trace gases.

A further transport event appears to occur after sunset. Levels of O₃, SO₂, CO and NO₂ all show a pronounced peak between about 18:00 and 22:00 CET, although the exact time and duration varies from day to day. On all days the O₃ peak arrives first, and only as it drops does the NO₂ concentration rise. This suggests the advection of relatively fresh pollution to the site, as the wind speed picked up during the evening on each of these days, and turned from north to come from the east at the same time. However, the exact grounds for this event are still uncertain.

Ozone levels were quite high and exhibited a pronounced diurnal profile during the entire period. Maximum mixing ratios increased from approximately 80 ppbv on the evening of the 18th to over 90 ppbv on the 21st.

RO_x exhibited a pronounced diurnal profile over the entire period. The afternoon maximum rose from about 55 pptv on the 18th to around 70 pptv on both 20 and 21 June. Significant levels of up to 10 pptv RO_x were also observed at night. This is probably due to the enhanced night-time oxidation of VOC by the nitrate radical and by O₃, as discussed in Section 2.1.3. The reaction rate with NO₃ and O₃ is much faster for secondary alkenes, such as isoprene and the terpenes, than for other alkenes and other VOCs. Although no NO₃ measurements were available, alkene measurements showed that concentrations of about 50 pptv of biogenic VOCs were present at night, particularly of isoprene, whose emission is temperature dependent. Mixing ratios for

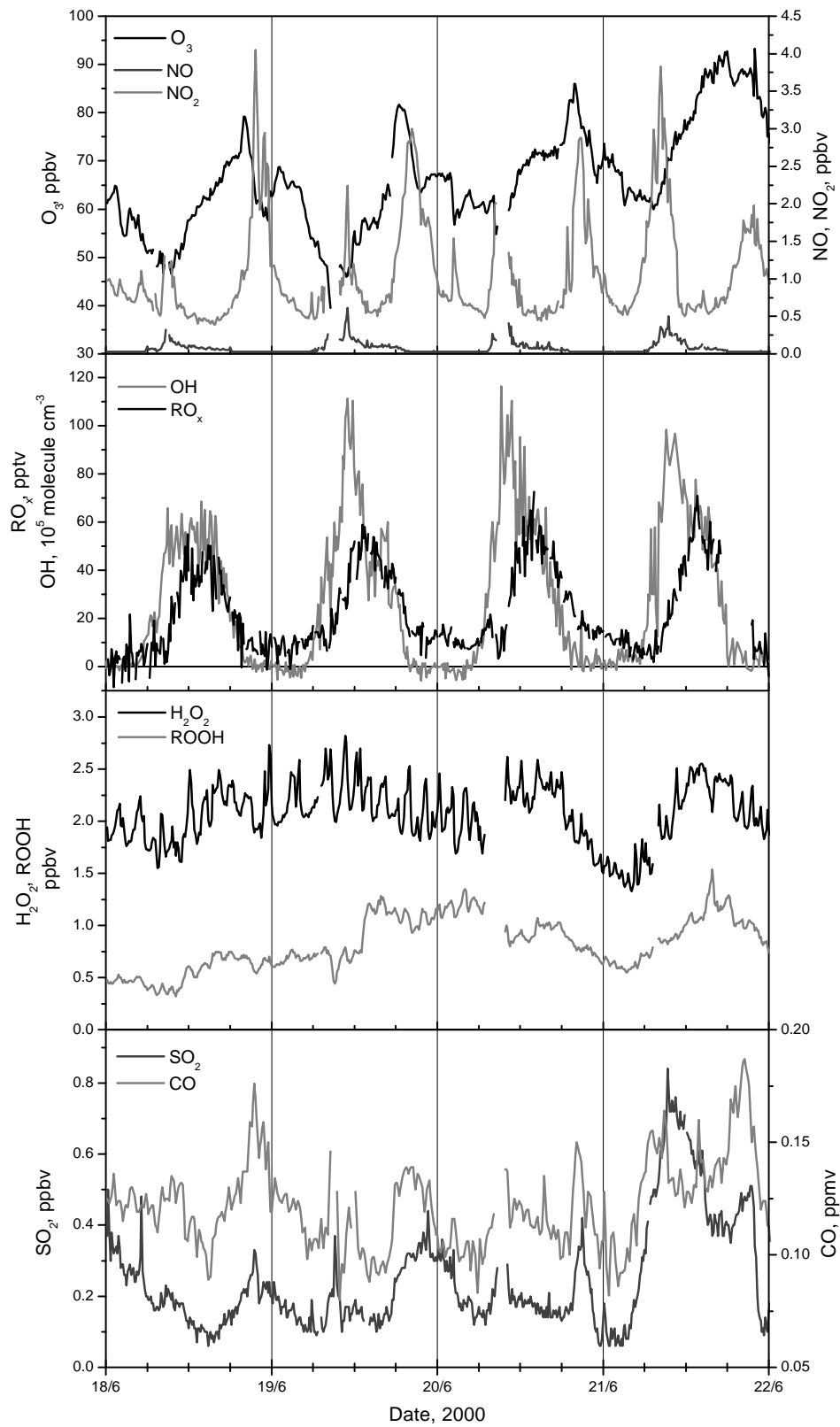


Figure 11.1: Mixing ratios of the most important atmospheric components measured during the intensive phase of the measurement campaign at Hohenpeissenberg from 18 to 21 June, 2000.

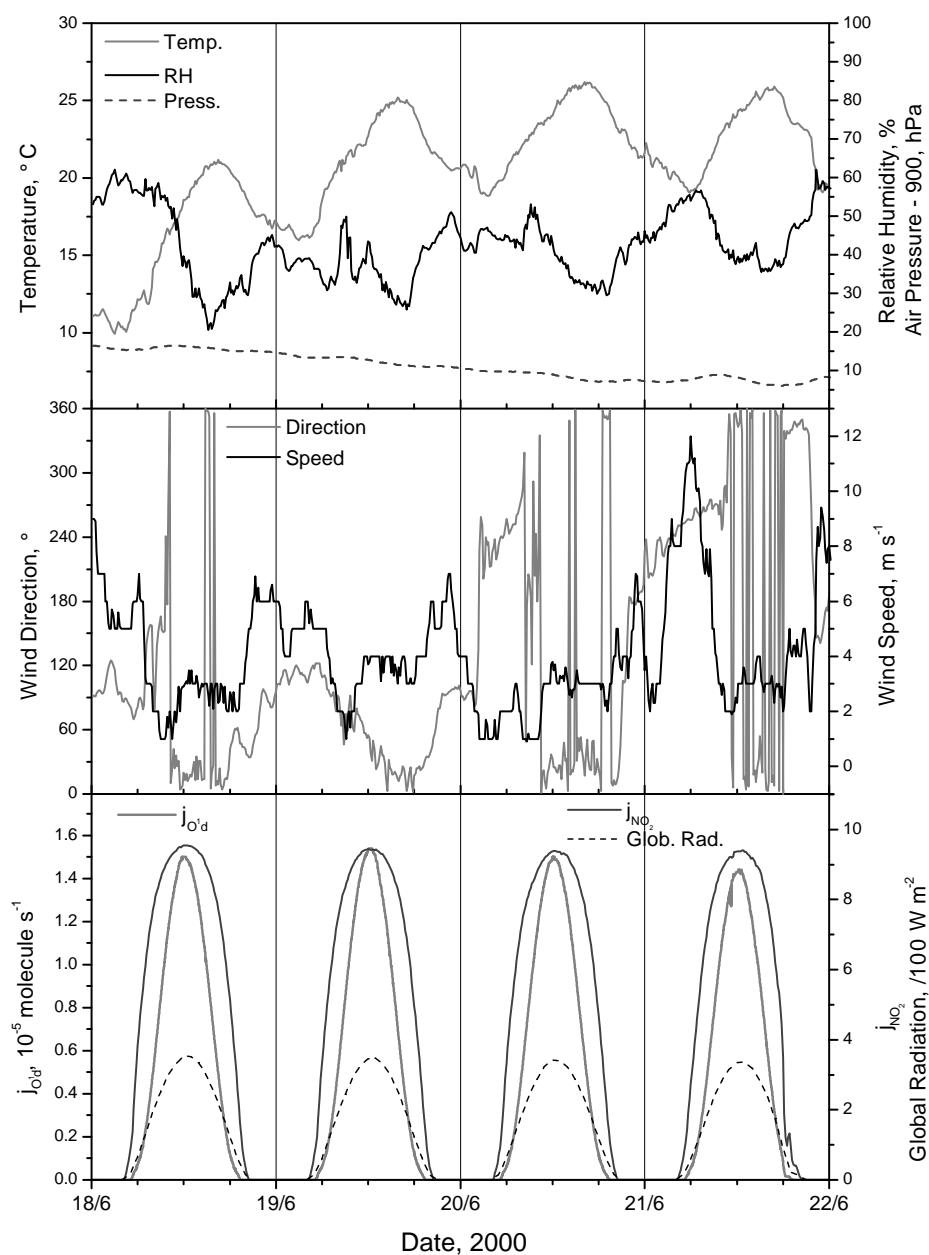


Figure 11.2: Meteorological parameters measured during the intensive phase of the measurement campaign at Hohenpeissenberg from 18 to 21 June, 2000.

total alkenes reached 500 pptv on some nights. This should lead to considerable nighttime oxidation and RO_x production.

The OH radical is the primary cause of VOC oxidation and RO_x formation during the daytime. RO_x accumulates over the course of the day as it is produced by VOC

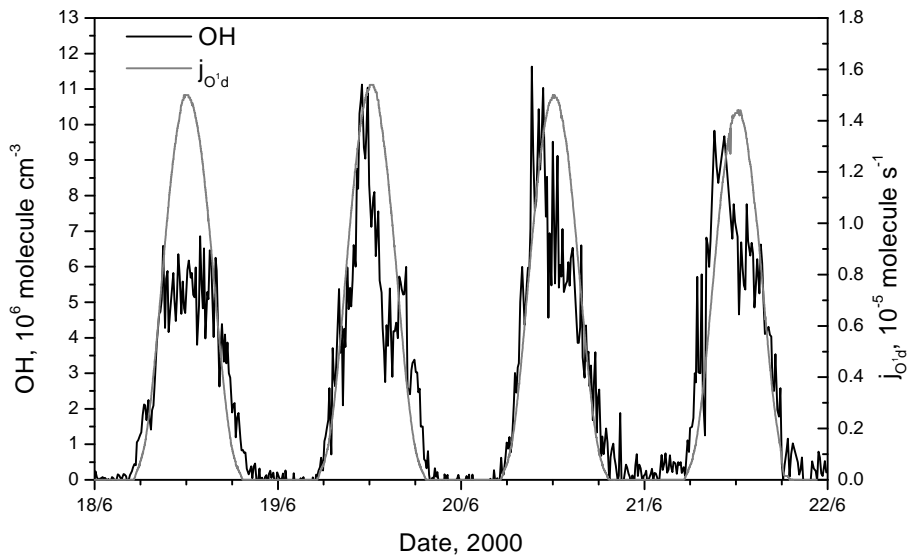


Figure 11.3: Plot of the OH concentration and with the photolysis rate for O_3 , j_{O^1d} .

oxidation, and the maximum OH concentration corresponds to the time point of maximum RO_x production. This results in the OH peak occurring earlier than the RO_x maximum. However, the presence of NO suppresses RO_x levels due to the rapid reaction between the two to produce NO_2 . The maximum mixing ratios of NO occurred during late morning and were associated with the transport of polluted air from the boundary layer. Maximum mixing ratios of over 0.5 ppbv were observed on 19 and 21 June. The RO_x mixing ratio appears to be suppressed by these high NO levels during late morning, and only reaches its maximum value after NO returns to its average daytime level of under 0.2 ppbv. This reaction is responsible for considerable O_3 production during the morning hours.

The OH concentrations also show a pronounced diurnal profile, with maximum concentrations being reached slightly before midday and dropping to essentially zero during the night. The maximum reached 11×10^6 molecule cm^{-3} on the 19 and 20 June. The increase in the OH concentration closely followed the j_{O^1d} profile in the morning, but the two curves deviated towards midday and in the afternoon. A comparison between the profiles for OH and for j_{O^1d} is shown in Figure 11.3.

The profiles of both OH and RO_x have been examined in more detail using a steady state radical balance model, and will be discussed in more detail in the following sections.

The profiles of various groups of VOCs are shown in Figure 11.4. The upper panel shows groups containing VOCs which are mainly anthropogenic in origin. The profiles of isoprene and various terpenes are shown in the lower panel and exhibit marked diurnal variation. They have a broad maximum during the afternoon due to

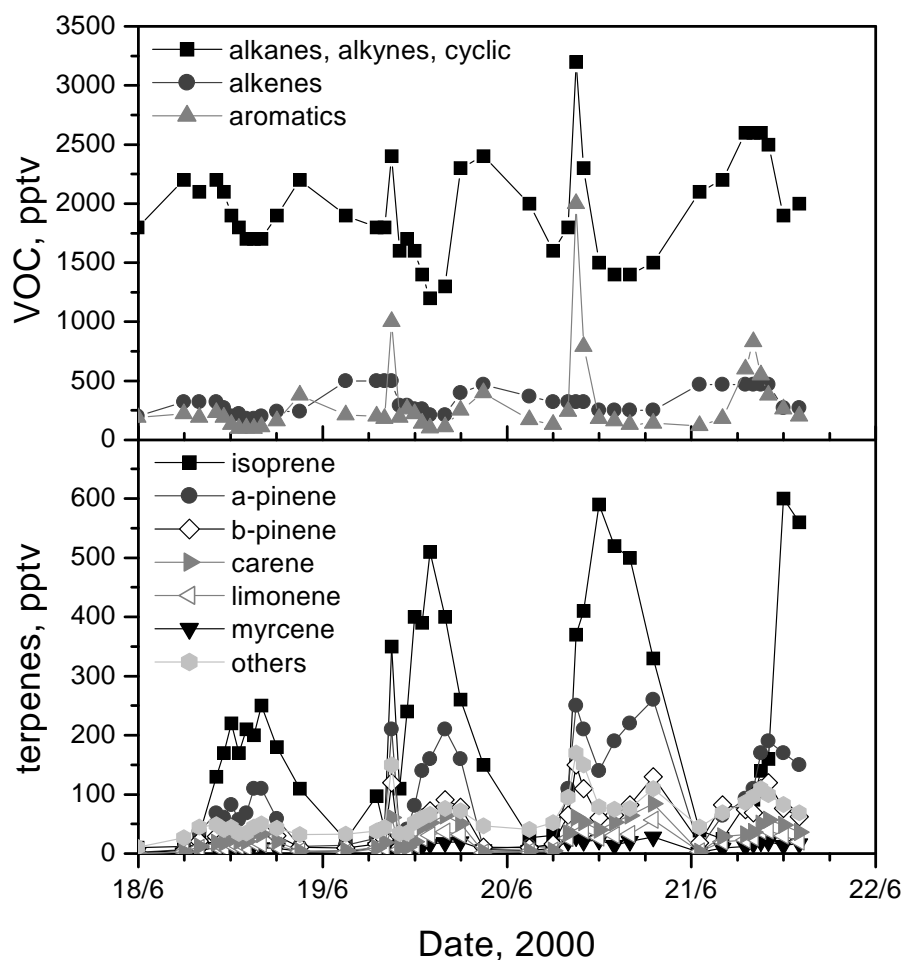


Figure 11.4: Mixing ratios for various groups of VOCs measured during the intensive phase of the measurement campaign at Hohenpeissenberg from 18 to 22 June, 2000. The group labelled alkenes in the upper panel does not include isoprene or terpenes.

the higher afternoon temperatures. Biogenic emissions are sensitive to both radiation levels, which controls the photosynthetic activity, and temperature, which influences the vapour pressure, and hence the amount which is emitted into the atmosphere. The maximum concentrations of isoprene can be seen to follow the progression of temperature on the four days quite well. The VOC measurements were discontinued on the afternoon of the 21st due to a lack of liquid nitrogen for the cryogenic trap.

The other organic compounds exhibit quite a different diurnal pattern, with local minima observed during the early afternoon. This is caused by increased OH oxidation during midday.

The conversion rates due to the reaction with OH have been calculated for individual VOCs together with Christian Plass-Dülmer [*personal communication*] from MOHp. The total VOC conversion rate due to OH is plotted in Figure 11.5, along

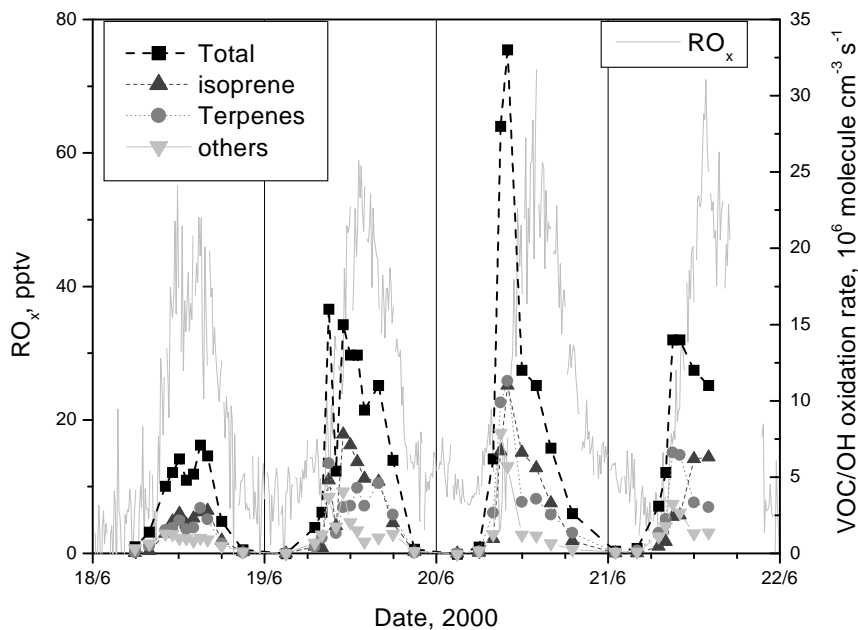


Figure 11.5: Plot of the contributions of isoprene, all other terpenes, and the other NMHCs to the total oxidation rate of VOC by OH. The measured RO_x mixing ratio is shown for orientation.

with the rates for isoprene and the other terpenes. The resulting RO_x mixing ratios are shown in the background. The highest conversion rate for an individual VOC was observed for isoprene. The conversion rate for isoprene alone reached over 10×10^6 molecule s^{-1} on the 20th. The other terpenes also made a significant contribution. Conversion rates for the other VOCs were quite low. The general shape of the RO_x profile is hinted at by the VOC conversion rate, particularly on the 18th. However, the peak in the conversion rate on the late morning is not reflected in the RO_x mixing ratios at all. The shape of the RO_x profile has been further investigated using a steady state model, which will be described in the following section.

11.2 Steady-state radical balance model

The concentrations of OH and RO_2 were calculated using a steady state radical balance model and the measurement data from 18-21 June. The resulting concentrations were then compared to the measured values. The model is only valid if the radical species are in steady state, i.e. that both species are sufficiently short-lived that they remain in equilibrium with the ambient conditions. This implies that the production and loss rates for each of the radicals are approximately equal and opposite. The resulting set of equations describing the balance between production and loss rates can then be solved for the concentration of the radical under consideration.

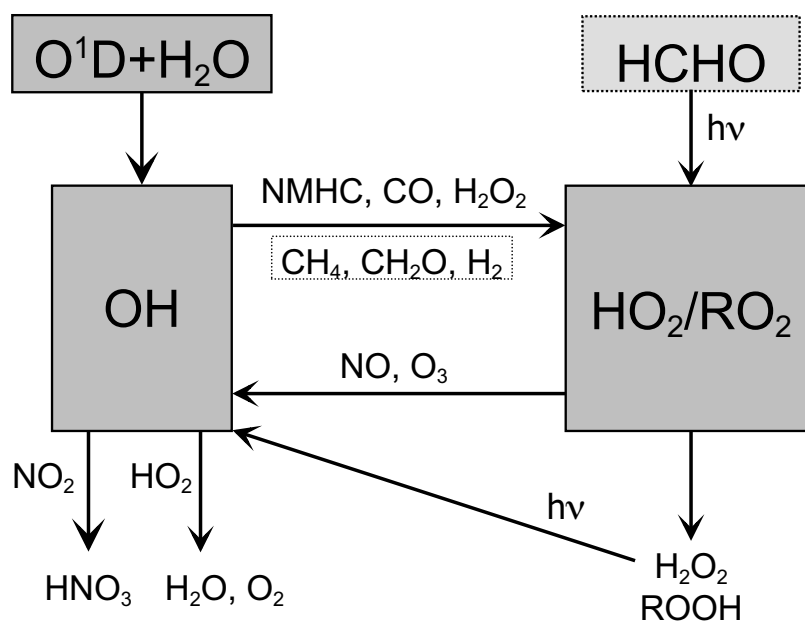


Figure 11.6: Block diagram of the chemistry considered in the steady state calculations. Components whose concentration were approximated are in dashed boxes.

Calculations of the radical lifetime using the calculated radical fluxes showed that this assumption is valid for both radicals during daytime. The lifetime of OH was under 0.5 seconds for the entire period under investigation. RO_x had a considerably longer lifetime, but it only exceeded three minutes during the night (approximately 19:00 to 7:00 CET). The assumption of steady state conditions breaks down at night for RO_x, but night-time concentrations of both radicals were in any case quite low. Thus, the results from the calculations of night-time concentrations can be expected to show large deviations from measurements.

Figure 11.6 is a block diagram of the set of chemical interactions included in the radical balance calculations. Assuming steady state conditions, the rate of change of the radical concentration is close to zero, which implies that the sources and sinks balance exactly:

$$\frac{dR}{dt} \approx 0 = P_R - L_R \quad (11.1)$$

$$\Rightarrow P_R = L_R \quad (11.2)$$

where P_R represents the total production rate for radical R, and L_R is the corresponding loss rate. As loss reactions inevitably involve the reaction of the relevant radical with some other component, an equation which is independent on the RO_x concentration is obtained. This can be solved for R when all other components are known. The concentrations of all trace gases used in the model were measured, with the exception of HCHO, CH₄ and H₂. The concentrations of CH₄ and H₂ were approximated using typical concentrations for the Northern Hemisphere: 1.7 ppmv for CH₄ [Seinfeld and

Pandis, 1998], and 500 ppbv for H₂ [*Novelli et al.*, 1999]. The calculations were then solved for each time point for which VOC measurements were available.

To solve the equations exactly, the speciation and concentration of the various peroxy radicals would be required. As this would make the calculation intractable, the model was simplified by making the assumption that the RO_x population was composed exclusively of 50% HO₂ and 50% CH₃O₂ radicals. Measurements by *Mihelcic et al.* [1993] and *Mihelcic et al.* [2001] have shown that for daytime conditions, HO₂ and RO₂ are present in nearly equal amounts. It is also to be expected that CH₃O₂ makes up a significant proportion of the organic radicals, although the presence of large amounts of other radicals with different reaction constants to those of CH₃O₂ would have some impact on the results.

The production of RO_x radicals via the oxidation of VOCs by O₃ or the NO₃ radical was not included in the model. Ozonolysis of biogenic VOCs could lead to RO_x production, particularly during the day, however the kinetic information on VOC ozonolysis does not readily allow the yield of HO₂ or RO₂ to be calculated. Thus, it is not included in the model. Nitrate oxidation of VOCs was not included either, as no NO₃ measurements were available, and the assumption of steady state is in any case invalid for night-time RO_x chemistry.

The equations and reaction constants used in the steady state model for OH and for RO_x are given in Appendix D.

11.3 OH balance

The resulting profile for OH is shown in Figure 11.7. The triangles represent the initial model results, the line represents the measured OH profile, and the solid squares represent the OH concentration at the time of the calculations. The measured OH concentrations were corrected on the basis of the VOC measurements to allow for reactions in the inlet. While the agreement is good for 20 - 21 June, the concentration of OH was overestimated on the 18th and 19th. The difference was particularly high on the late morning on the 19th; at 10:00 the measured OH concentration was 7.29×10^6 molecule cm⁻³, which was overestimated by 60% by the calculated concentration of 1.2×10^7 molecule cm⁻³. However, the general shape of the profile, including the peaks in the late morning, is generally well reproduced by the steady state calculations on all days.

The calculation was originally made without any allowance for the presence of oxygenated hydrocarbons, such as aldehydes or ketones, which are not measured by the GC system used at Hohenpeissenberg. In order to account for this “missing” VOC, 3 ppbv of formaldehyde, HCHO, was added to the model calculations as a proxy for the oxygenated VOCs. The resulting concentrations are represented by the open diamonds and show much better agreement with the measured results on the 18th and 19th. For example, at 10:00 CET on the 19th the calculated OH concentration

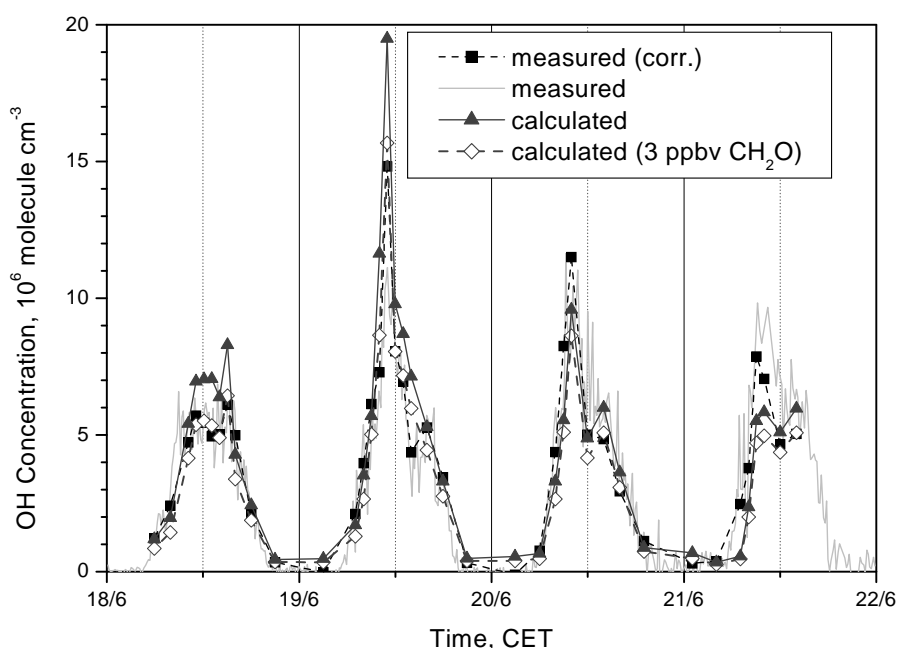


Figure 11.7: Plot of the OH concentration from observations and from steady state radical balance calculations for the period 18-22 June, 2000. Observations corrected for inlet chemistry on the basis of VOC measurements are shown as solid squares. Triangles represent calculations using measured components; open red diamonds include the added effect of 3 ppbv HCHO (see text).

after allowing for HCHO is 8.6×10^6 molecule cm^{-3} , which lies only about 20% above the measured value. However, the addition of HCHO results in the OH concentration being slightly underestimated on the last two days, 20-21 July.

These results indicate the importance of oxygenated VOCs for the OH balance, and that measurements of the most important ketones and aldehydes are necessary for a more complete radical balance. Measurements during the POPCORN campaign in northern Germany by *Benning and Wahner* [1998] found 0.6 to 3.3 ppbv HCHO and 0.1 to 3.8 ppbv CH_3CHO in a maize field during August 1994. The maize crop was severely affected by drought in this summer, so that biogenic emissions were not as high as would normally have been expected [*Plass-Dülmer et al.*, 1998]. *Montzka et al.* [1995] have shown that methyl vinyl ketone (MVK) and methylacrolein (MACR), which are products of isoprene oxidation, can be present during daytime at a combined level of about 50% of the isoprene concentrations. This would correspond to about 2-300 pptv MVK and MACR for the 500 pptv isoprene observed at Hohenpeissenberg. Even higher levels of MVK and MACR relative to isoprene were found by *Lamanna and Goldstein* [1999] at a large distance downwind from an isoprene source. High levels of other oxygenated VOCs have also been found in some studies [e.g. *Goldan et al.*, 1997; *Lamanna and Goldstein*, 1999]. Considering these high concentrations of oxygenated VOCs, the value of 3 ppbv used for HCHO in the current work may in

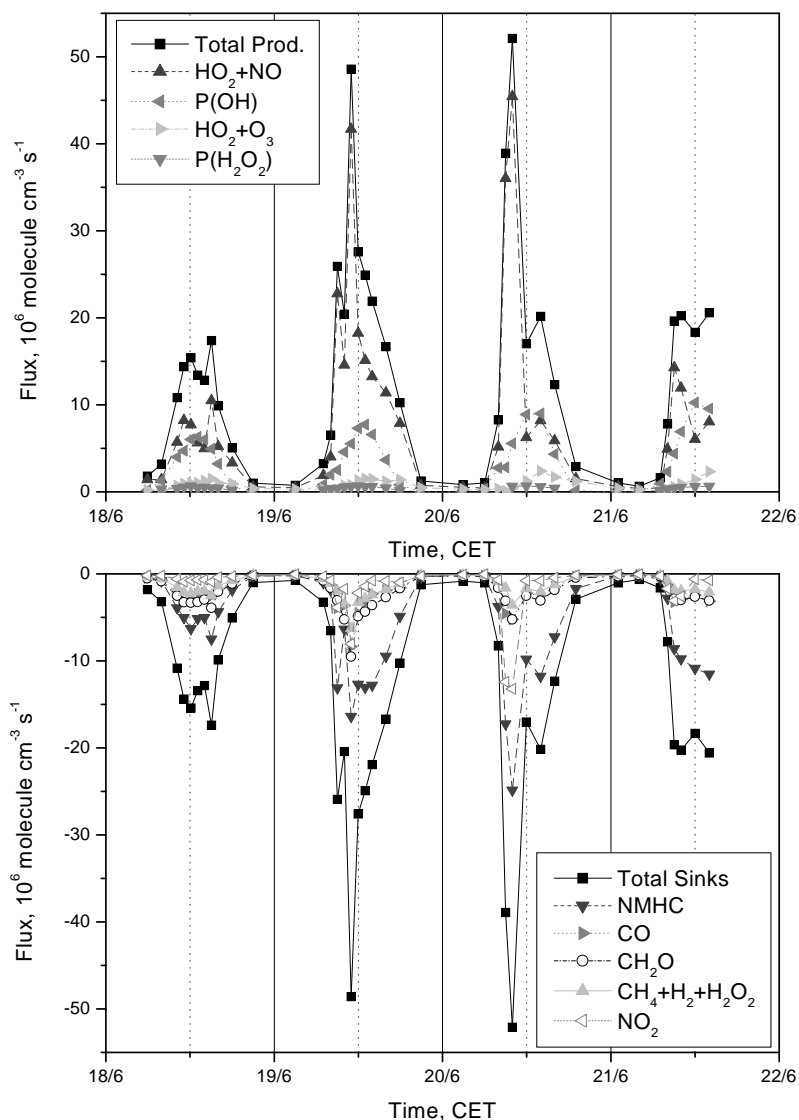


Figure 11.8: Plot of the contributions of various sources and sinks of OH as calculated by the steady state model for the period 18-21 June, 2000. Sources make a positive contribution, sinks are negative. Estimated values were used for HCHO, CH_4 and H_2 concentrations.

fact be too low. It is used in the radical balance purely as a proxy for the oxygenated VOCs, and should not be understood as an estimate of the real HCHO concentration.

The contributions of the individual sources and sinks to the OH concentration were also examined. The contributions are plotted in Figure 11.8 as the flux of OH radicals produced or destroyed by each source or sink pathway. The upper panel shows the contributions of the individual source terms to the total production rate; the lower panel shows the contributions of the sink terms.

The dominant source of OH radicals is the recycling¹ of HO₂ radicals by NO, with over half the OH radicals being produced by this pathway on average. However, this source of OH is highly dependent on the supply of NO, so that on some days the primary production via the photolysis of O₃ produced comparable amounts of OH during daylight hours to that recycled from HO₂. The rapid recycling of HO_x is the cause of the large spikes in the OH concentration during the late morning, which on all days corresponded with the arrival of high NO_x concentrations at the measurement site. Both the reaction of HO₂ with O₃ and the photolysis of H₂O₂ made only minor contributions to the OH concentration.

The main sink for OH was the oxidation of NMHC by the OH radical. The oxidation of CO and an assumed 3 ppbv HCHO consumed nearly equal amounts of OH, while the combined oxidation of CH₄, H₂ and H₂O₂ was of even less significance. The reaction of OH with NO₂ was generally only a minor sink, but during the mid-morning advection of polluted air to the measurement site it was responsible for up to 32% of the OH loss.

11.4 RO_x balance

The results for the steady state model calculations of RO_x are shown in Figure 11.9. The data points are represented using the same key as for the OH calculations. The agreement between the measured and modelled RO_x mixing ratios was very good on all days, considering the large uncertainty in the RO_x measurements. Most of the major features of the profile are well described by the model. The slight dip in the mixing ratio for RO_x at about 8:00 CET is reproduced well on both the 19th and 20th, although an extra peak is apparent at 07:00 CET on the 21st. This feature coincides with a rapid increase in the OH concentration and to the arrival of NO_x rich air.

Adding the influence of 3 ppbv HCHO as a proxy for oxygenated VOCs improved the agreement on the 19th and 20th, but on other days it caused the RO_x concentration to be overestimated. Some such deviation is to be expected, as the mixing ratio of oxygenated VOCs is very unlikely to be constant. Lower mixing ratios of oxygenated VOCs are to be expected on days with less intense photochemistry, such as 18 June. However, although the addition of HCHO increased the difference between measurements and model on the 18th, it improved the agreement for OH. This indicates a possible inconsistency in the data on this day, as on all other days the improvement in fit was consistent for both radical species.

The radical flux through the different pathways was also calculated for RO_x, and is shown in Figure 11.10 using the same key as for OH.

¹The term recycling refers to the fact that OH oxidation is responsible for the majority of HO₂ production. This results in a catalytic cycle of VOC oxidation during which OH and HO₂ are continually “recycled”.

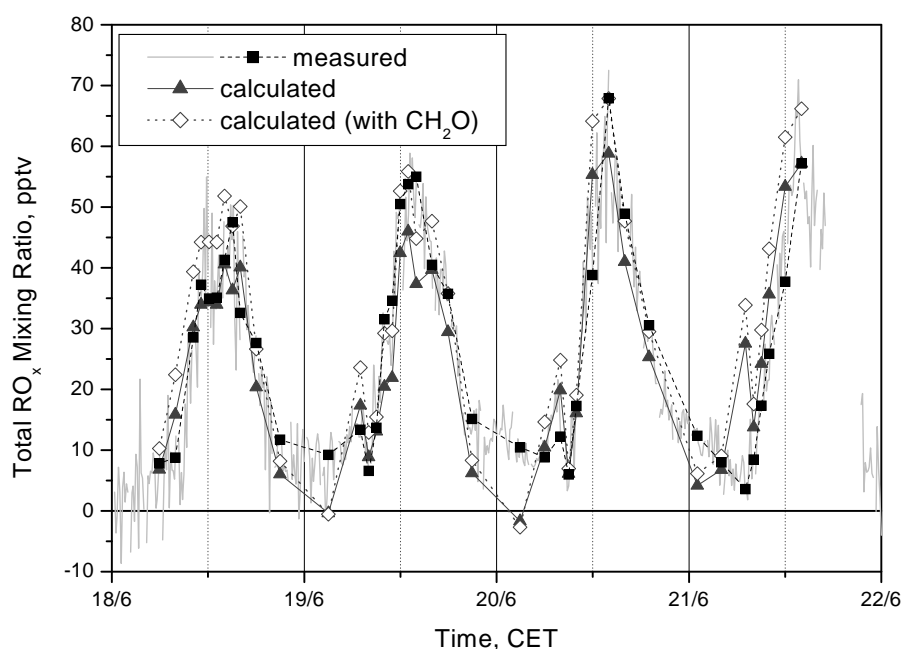


Figure 11.9: Plot of the RO_x concentration from observations and from steady state radical balance calculations for the period 18-22 June, 2000. Observations corrected for inlet chemistry on the basis of VOC measurements are shown as solid squares. Triangles represent calculations using measured components; open red diamonds include the added effect of 3 ppbv HCHO (see text).

The sources for RO_x correspond to the sinks of OH, with the exception of the reaction between OH and NO₂, which leads to the formation of HNO₃ instead of RO_x as in the other reactions. The relative strengths of the source reactions are the same as discussed above for the OH sinks. The production of RO_x radicals via the oxidation of VOCs by O₃, which may play a major role, has not been included for the reasons mentioned above. Thus, the source terms may be somewhat larger than these results show. This would require an upwards revision of the calculated RO_x concentration. The current uncertainty in the correction for the water effect on the CA measurements means that any minor revision should still lie within the range of the RO_x measurements.

By far the most dominant sink for RO_x is the reaction of RO₂ radicals with NO. The resulting massive recycling of RO_x to OH also was responsible for the OH spike in the mid to late morning as commented on above. Due to the dominance of this sink, the relative importance of the other sink reactions is suppressed during the morning, when high concentrations of NO were present. This result confirms that this reaction between RO_x and NO is indeed responsible for the delayed accumulation of RO_x radicals observed during the morning and for the accompanying shift of the maximum to the afternoon, as discussed in Section 9.1.

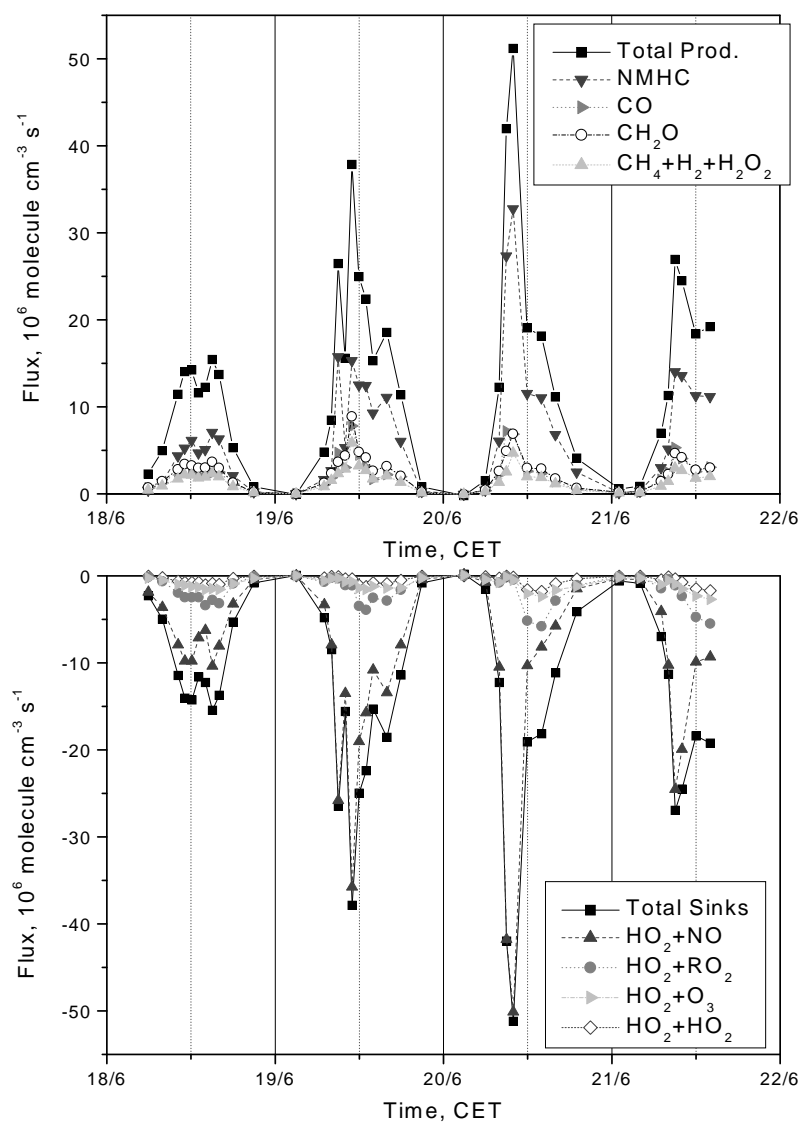


Figure 11.10: Plot of the contribution of various sources and sinks of RO_x as calculated by a steady state model for the period 18-21 June, 2000. Sources make a positive contribution, sinks are negative. Estimated values were used for HCHO, CH₄ and H₂ concentrations.

Following the return to lower NO concentrations after midday, the reactions between peroxy radicals and with O₃ gain slightly in importance, but remain less important than the reaction with NO. The reaction between HO₂ and RO₂ is the most important of these terms in this model, although this is partly due to the fact that the proportion of HO₂ to RO₂ is kept constant. In reality, HO₂ radicals will be lost faster than organic RO₂ radicals. Thus, this result probably overestimates the importance of the reaction involving HO₂. This contributes to the rapid drop observed for the

modelled RO_x mixing ratio, which reaches zero or is slightly negative at night. However, conditions are not steady-state for RO_x at night, so that the modelled results for RO_x cannot be considered valid.

11.5 Conclusions

The measurement of a wide range of trace gases at Hohenpeissenberg during a fine weather period from 18 to 22 June, 2000 allowed interactions between a wider range of atmospheric components to be considered in more detail. The general features of the temporal change in ozone, RO_x , OH, NO_x and VOC could be explained in terms of their interactions, but evidence was also found for the transport processes. The temporal profiles showed that convection associated with the breakup of the nocturnal boundary layer during the late morning led to increased levels of anthropogenic pollutants at the measurement site.

The main features of the diurnal profiles of OH and RO_x could be modelled using a steady state radical balance model. The results showed that OH oxidation of VOCs during the morning and the subsequent rapid recycling of RO_x to OH by reaction with NO is responsible for the prominent morning peak in the OH concentration. It is also responsible for the delayed accumulation of the RO_x radicals and the shift of the maximum mixing ratio to the afternoon.

Although the possible presence of oxygenated VOCs could lead to a change in the absolute magnitude of the OH and RO_x profiles, their basic shape is described well by the limited chemistry included in this model. This gives confidence, that the measurements at MOHp allow a consistent interpretation of the HO_x cycle. The role of oxygenated VOCs, particularly HCHO, does need to be investigated further. The improved agreement between the model and observations achieved by assuming the presence of 3 ppbv HCHO indicates that measurements of the ambient concentrations of this class of compounds are required to adequately test our understanding of the HO_x cycle.

Chapter 12

The climatology of ozone on Kleiner Feldberg

As has been seen in the chapters dealing with the measurements at Kleiner Feldberg, the local photochemical ozone production cannot explain the observed ozone concentration on its own. Other processes, such as those discussed in Chapter 4, also exert a strong influence on the observed ozone concentration. The net effect on the ozone concentration was investigated by analysing ozone data from the measurement networks operated by German environmental agencies over a period of several years. The aim of this analysis was to determine the extent to which ozone measurements can be considered to be representative of long-term, large scale processes.

This analysis was carried out on several temporal and spatial time scales. Firstly, the annual variation in the ozone concentration was analysed to determine the role played by photochemical ozone production at various times of year. This is followed by a discussion of the differences in the average diurnal profiles of the ozone concentration during periods of increased ozone production for three stations which lie within 15 km of each other but at different altitudes. The differences between the stations provide information over changes in the structure of the boundary layer over the course of the day.

Finally, the issue of spatial representativity is considered on a regional scale by considering ozone measurements at 277 German stations. The correlation between the ozone measurements at each of these stations and Königstein is calculated and the relationship with the distance from Königstein is investigated. This allows a “characteristic distance” defining the spatial representativity of the measurements at Königstein to be determined for different times of day.

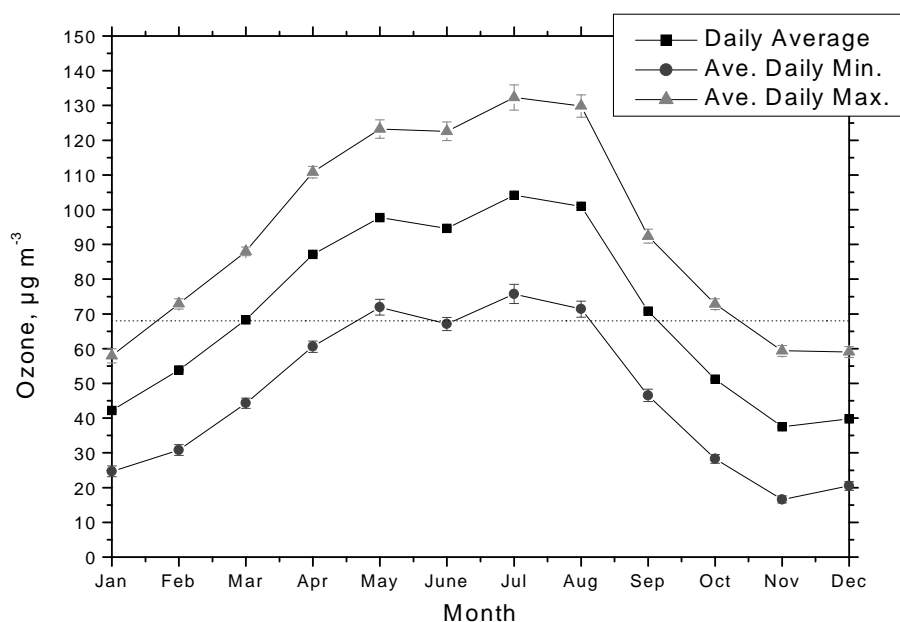


Figure 12.1: Average ozone concentration for each month, measured at Kleiner Feldberg, 1993-99. The dotted line represents the background concentration calculated for 1998 (see text).

12.1 The annual ozone profile

The average ozone concentration at Kleiner Feldberg has been calculated for the years 1993-1999 using half hourly averages from the HLUg measurement station. As can be seen in Figure 12.1, the highest average ozone concentrations occur during the months of May to August. During this period, the high position of the sun and long days leads to more intense photochemical activity. The prevalence of stable high pressure systems during summer also helps create conditions favourable to ozone production. Episodes with higher ozone concentrations can also occur during March and April, but the generally changeable weather and lower insolation during these months means that the ozone concentration is on average lower than during the summer months.

The annual profile is asymmetrical to the solar year, with higher concentrations occurring in the spring time than in the autumn. High ozone concentrations in spring are relatively common in the Northern Hemisphere [Monks, 2000], although their origin is not entirely understood. One process proposed as the source of high spring-time concentrations is the transport of ozone from the lower stratosphere during stratospheric-tropospheric exchange (STE). Various studies have indicated that STE, coupled with a seasonal build up of tracers, including ozone, in the lower stratosphere during winter, may cause increased mass transport into the troposphere during spring [e.g., Holton *et al.*, 1995, and other articles reviewed in Monks, 2000]. However, there

is some doubt as to whether the different mechanisms for STE do indeed show a seasonal preference for spring time transport [e.g., *Beekman et al.*, 1997; *Monks*, 2000]. *Monks* [2000] presents considerable evidence that, although STE does make a contribution, the main origin is photochemical. Measurements at Mace Head show a spring time maximum in the concentrations of six trace gases with quite different sources and sinks [*Derwent et al.*, 1998]. Of the six, only ozone had a significant stratospheric source. *Wang et al.* [1998] have demonstrated on the basis of a comparison between model results and observations that increased ozone levels are caused by a superposition between contributions from STE (with a maximum in January-April) and photochemical production, which peaks between April and June, and that chemistry plays the most important role. The accumulation of ozone precursors such as non-methane hydrocarbons (NMHC) and NO_x reservoir gases during winter may prepare conditions for an increase in photochemical activity as insolation increases during springtime [*Penkett et al.*, 1993]. Although Kleiner Feldberg does not experience a maximum as at some stations, a combination of long range transport and local production could result in the slightly higher ozone concentration observed in May.

Diurnal profiles for the ozone concentration have been calculated for each month of the year using half hour average values of concentration for Kleiner Feldberg for the years 1993 to 1999, and these are shown in Figure 12.2. These profiles reflect the balance between those production, loss and transport processes which are dependent on the time of day. Very little diurnal variation is observed during the winter months (October - February). All months show a slight increase during the morning with a maximum in the early afternoon due to local photochemical activity, but in winter this is a very minor effect. March and September can be considered transition months, and the summer months (April - August) exhibit a pronounced diurnal profile with a minimum shortly after 06:00 CET and a maximum in the early afternoon. On average, maximum concentrations were found in July and August. Afternoon levels were nearly $120 \mu\text{g m}^{-3}$ during these two months, and an average increase of 26-28 $\mu\text{g m}^{-3}$ occurred during the day¹. The direct contribution of local production seems to have been most significant during June, when the daily diurnal increase in ozone was over $29 \mu\text{g m}^{-3}$. Thus, as expected, the diurnal profiles for each month of the year indicate that local photochemical production makes a contribution at all times of year, although its main contribution occurs during summer.

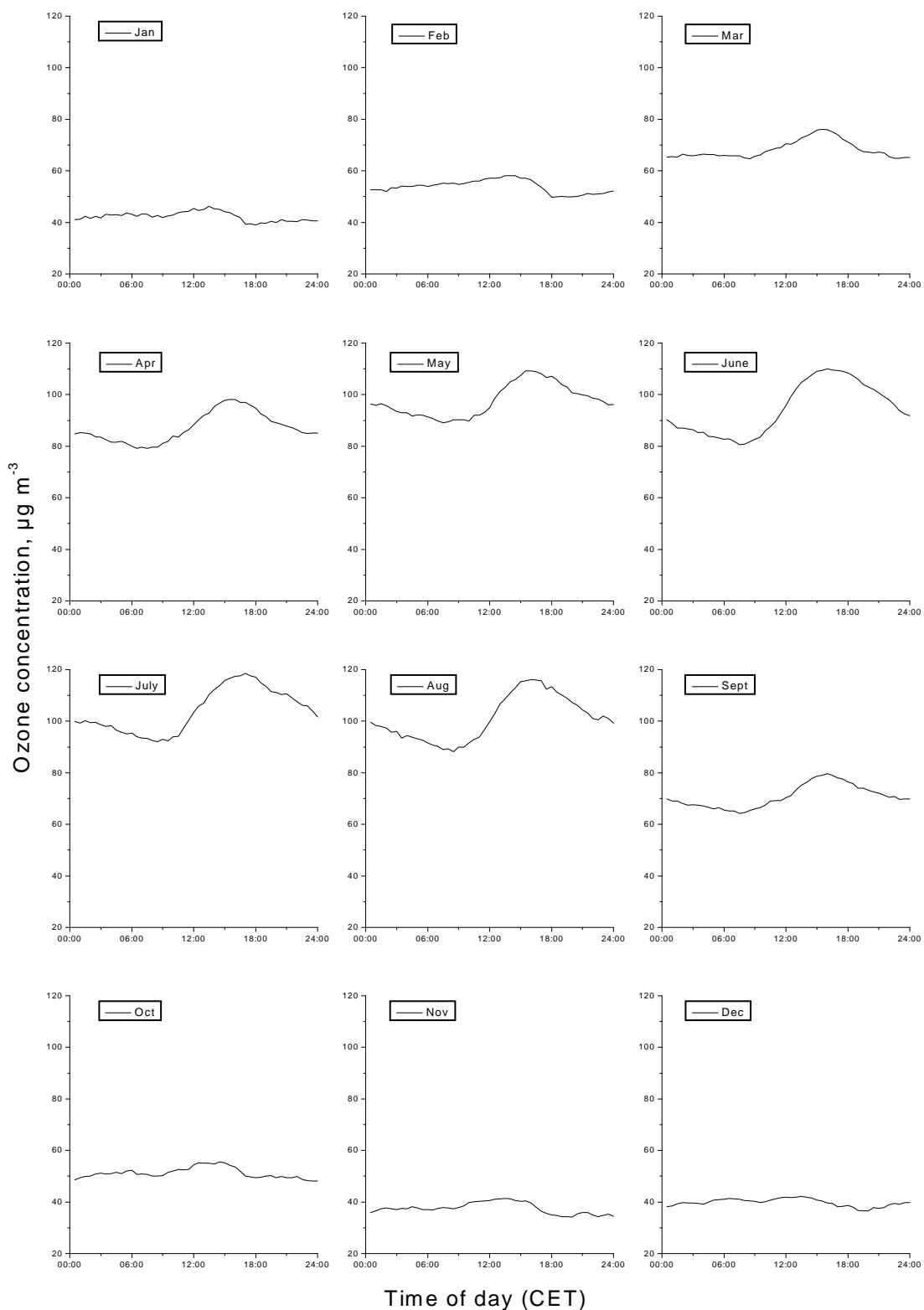


Figure 12.2: Average diurnal ozone profiles for each month of the year, measured at Kleiner Feldberg, 1993-99. The profiles were calculated using half hour ozone concentrations provided by the HLUg.

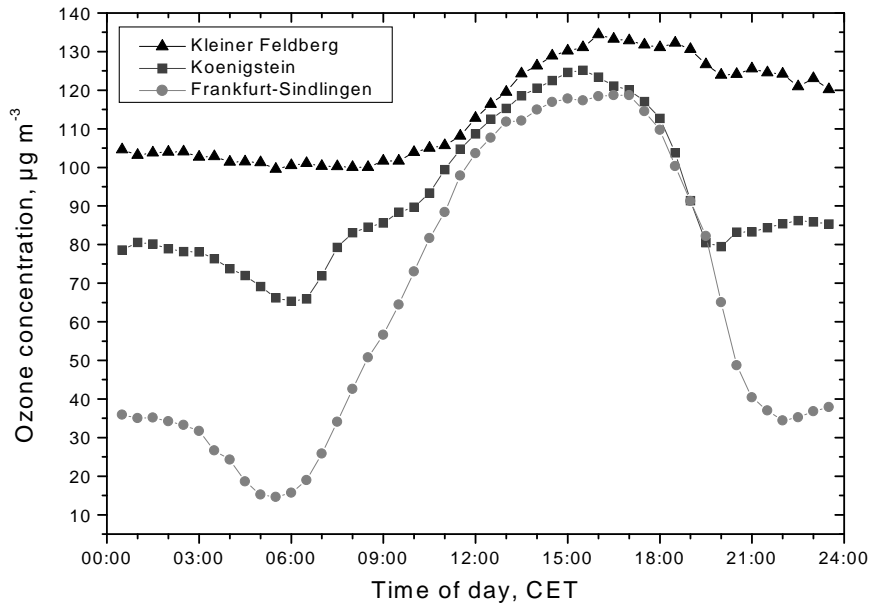


Figure 12.3: Average diurnal profiles for the ozone concentration at three sites during episodes with increasing ozone concentrations: Kleiner Feldberg (825 m a.s.l.), Königstein im Taunus (593 m a.s.l.) and Frankfurt-Sindlingen (96 m a.s.l.). The episodes were selected from the HLUG half hour ozone data for 1993-1997 (Königstein and Sindlingen) and 1993-1999 for Kleiner Feldberg.

12.2 Average diurnal profiles during ozone events

In order to examine the effect of these diurnal processes in more detail, the average diurnal ozone profile was calculated for three stations at various altitudes in the Rhine-Main region. These stations are sufficiently close to each other (<15 km) that they are subject to the same synoptic scale weather situations. These diurnal profiles are shown in Figure 12.3. The profiles are averages of the half hour ozone concentration during a series of selected ozone events. All these events were characterised by increasing ozone concentrations and stable weather patterns. The diurnal profile results from the cumulative effects of those processes which are dependent on the time of day, i.e. photochemical production, deposition, and vertical transport. Advection associated with the local orography can also have a component which is dependent on the time of day. Each of these processes contribute a signature to the diurnal profile.

The most prominent features of the diurnal profiles are the parallel increase in the ozone concentration during the day, and the large differences in the overnight behaviour at the three stations. At all three sites, the concentration decreases overnight.

¹ $\mu\text{g m}^{-3}$ are units of concentration, which is dependent on temperature and pressure, and the trace gas under consideration. Under normal conditions (STP), an ozone concentration of $2 \mu\text{g m}^{-3}$ is approximately equal to a mixing ratio of 1 ppbv.

However, at Kleiner Feldberg (825 m a.s.l.), the decrease is only minor compared with the lower stations. The concentration at the lowest station, Frankfurt-Sindlingen (96 m a.s.l.), reaches its lowest point of around $15 \mu\text{g m}^{-3}$ shortly after dawn, but begins to rise again soon after this. The concentration at Königstein (593 m a.s.l.) parallels that at Sindlingen, although the early morning minimum is slightly later, around 06:00. Prominent at both stations is a dip in the concentration after about 03:00. The overnight decrease at these stations is probably due to the combined effect of deposition and the titration of ozone with NO, which continues to be emitted at night. The dip observed at these stations after 03:00 may be due to depletion of the stable layers formed overnight, to an increase in deposition rates due to increased turbulence around daybreak, or to an increase in the NO concentration. This could in turn be due to increased emissions, but could also be associated with photolysis of NO_x reservoirs, e.g. HONO, by the first solar radiation of the day. NO measurements with the required accuracy are not available for these stations, so that it is not possible to determine whether changes in the NO concentration are responsible. The concentrations at Königstein and Sindlingen both rise after the minimum. The rate of increase in the concentration levels off at around 08:00 - 09:00 CET slightly above the evening level.

The overnight decrease in the concentration at Kleiner Feldberg is much less than at either of the other stations, and only starts to rise again at around 08:30. A slight levelling off between 10:00 and 11:00 follows an initial increase in the ozone concentration. After 11:00, the profiles at all three stations are nearly parallel, with only a relatively small difference in between them. This increase can be attributed to local ozone production during the day. The afternoon maxima are remarkably similar, and increase slightly with altitude. The highest concentration at Kleiner Feldberg is only about $20 \mu\text{g m}^{-3}$ higher than at Sindlingen. This is in contrast to the situation in the early morning when the difference in concentration reaches nearly $90 \mu\text{g m}^{-3}$.

Towards evening the concentration at all three stations sinks, although at Kleiner Feldberg this effect is not pronounced. At Königstein and Sindlingen, the concentration sinks significantly before stabilising at levels of around 80 and $40 \mu\text{g m}^{-3}$, respectively.

Certain features of these profiles can be interpreted as the result of changes in the vertical structure of the atmosphere at different times of the day, which was discussed briefly in Chapter 4. During the day, all three stations lie within the well-mixed convective mixed layer, and experience similar production processes. Differences between the stations are minimal, due to the strong mixing, but stations close to NO_x sources have the lowest concentrations. Sindlingen is an urban station in close proximity to traffic and other anthropogenic sources of NO_x. These sources are progressively less important for the other two stations, which are both forest stations, even though both are still affected to some degree by emissions from traffic.

After sunset, the atmosphere gradually becomes layered, with a residual layer overlying a stable nocturnal boundary layer. These layers affect the stations differently according to their altitude. Kleiner Feldberg appears to be only slightly below

or in the lower residual layer during the night, and experiences only a slight drop in concentration. Both of the lower stations become decoupled from the overlying reservoir layer, and experience longer exposure to NO_x , leading to a rapid drop in ozone levels. Sindlingen remains in the lowest layer overnight and experiences the greatest drop. This layer is probably also strongly affected by deposition, as it is not enriched by mixing from overlying layers as it is during the day.

After sunrise, the growth of the convective mixed layer leads to the increase in the ozone level at the lower stations as the upper boundary of this layer grows upwards. This means that air from increasingly higher levels is mixed with air from the lower layers. At slightly higher levels, this probably causes an initial drop in the ozone concentration due to the upwards mixing of air with low ozone levels and higher levels of pollutants. This can be expected to be followed by an increase in the ozone level as ozone rich air from the overlying levels is mixed downwards. The “plateau” observed at Königstein and Sindlingen probably marks the end of this convective mixing phase phase, and the start of a phase in which photochemical production dominates.

12.3 The background ozone concentration

The hemispheric background concentration of ozone is an important quantity for estimating the contribution of local processes. While this is difficult to measure on the basis of local measurements, particularly in the boundary layer, where local processes and boundary layer processes have an effect on the measurements, the characteristic annual background concentration at a station can be calculated on the basis of ozone and wind speed measurements.

The background concentration reflects the long term balance between STE, average photochemical production or loss, and depositional loss at the station. *Altshuller and Lefohn* [1996] defined the ozone background as the O_3 concentration that would prevail in the absence of domestic anthropogenic emissions. However, as pointed out by *Lin et al.* [2000], such a background is not purely natural, as it can include a sizable contribution associated with intercontinental transport.

In the current study, the ozone background is considered to be the average annual ozone concentration at a station in the absence of any direct contribution from local processes. It can be approximated by analysing the ozone data as a function of wind speed [*Kaminski and Gilge*, 2000a] and determining the concentration at which average concentrations at high wind speeds converge for the summer and winter half years.

Low wind speeds frequently occur under the influence of high pressure systems. These are often associated during the daytime with higher average ozone concentrations in summer, but in winter the low production rates associated with the lower insolation do not balance out the losses. Although loss rates due to deposition and

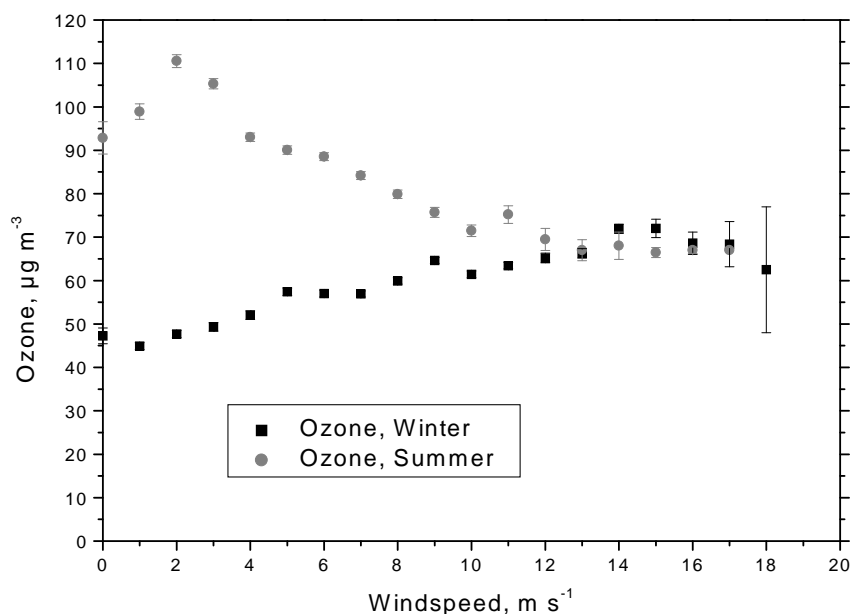


Figure 12.4: Ozone concentration plotted as a function of wind speed for winter (Jan. - March; Oct. - Dec.) and summer (Apr. - Sept.) at Kleiner Feldberg, 1998. The points are average values derived for the half hourly ozone concentrations. The convergence of the two lines at approximately $68 \mu\text{g m}^{-3}$ indicates the background concentration for Kleiner Feldberg.

photochemistry are also lower in winter, production rates still do not exceed the losses. This results in low average wintertime concentrations, even at low wind speeds. Ozone concentrations at low wind speeds are also representative of a smaller area, so that local conditions have a greater affect on the observed ozone level.

In contrast, due to mechanically induced turbulent mixing the air mass is more homogeneous at higher wind speeds. As a result, the ozone concentration is more representative of a larger air mass and, hence, of a larger region. Thus, the average concentration at higher wind speeds can be considered to represent the net contribution of the various sources and sinks, as mentioned above. This can vary from station to station, depending on the degree to which the station is influenced by local sinks or sources. For example, urban stations are likely to be strongly influenced by local emissions even during periods with high wind speeds. In contrast, stations which are closer to the free troposphere are more likely to reflect the average hemispheric ozone background concentration.

The concentration at high wind speeds is found at many stations to be nearly the same during the summer and winter half years. This suggests that such air parcels are well mixed and that, despite the large changes in insolation, the changes in production and loss nearly balance out when averaged over a sufficiently large area.

Figure 12.4 shows a plot of the half hour average ozone concentration at Kleiner

Feldberg as a function of the wind speed for 1998. At high wind speeds the data sets for summer and winter converge and allows the background ozone concentration to be estimated for this station and year. For 1998, the background concentration as defined by this method was found to be approximately $68 \pm 2 \mu\text{g m}^{-3}$.

At very low wind speeds below 2 m s^{-1} , the average concentration during summer is observed in Figure 12.4 to decrease. This may reflect the fact that these very low wind speeds may be primarily associated with night-time conditions, with stable stratification of the boundary layer and impoverishment of the lowest layers. The average concentrations at low wind speeds are higher than the background level during summer, whereas they are lower than the background during winter. This suggests that, as mentioned above, that local production is a major effect during summer, whereas loss processes dominate at Kleiner Feldberg during winter.

The background ozone concentration for 1998 was also calculated for all other stations in the measurement network of the HLUg for which both ozone and wind speed data were available. Figure 12.5 shows the results plotted against altitude. For some stations, insufficient data was available at high wind speeds for the summer and winter curves to converge. In most such cases, the convergence point could be estimated by averaging the nearest points and taking the values at higher wind speeds during winter² into account. At Dillenburg, wind speeds were too low to allow the two curves to converge and the background could not be estimated. In contrast to Kleiner Feldberg, most stations were characterised by relatively low wind speeds, so that this method was hard to apply. As a result, the background concentration at some stations is subject to considerable uncertainty. This was particularly the case for the city/town stations.

The stations in Hesse can be divided into two groups: those with an altitude of less than around 300 m a.s.l., with background concentrations between $46 \mu\text{g m}^{-3}$ for Frankfurt-Ost and Kassel-Süd and 66 in Borcken, and the forest and hill stations above 300 m a.s.l., with background concentrations above $62 \mu\text{g m}^{-3}$. The background values for the city and town stations are severely affected by the loss of ozone due to NO titration at the high NO_x concentrations typical of the city. For the forest and hill stations, the background concentrations lie within the fairly narrow range of $62 \sim 68 \mu\text{g m}^{-3}$. These stations appear to be less exposed to such local loss processes and the background concentrations at these stations probably are influenced to a large degree by the Northern Hemisphere background concentration. These values agree quite well with the European background of $64\text{--}74 \mu\text{g m}^{-3}$ found during the TOR programme [Beck and Grennfelt, 1993, 1994; Scheel *et al.*, 1997]. It is also only slightly below the average concentration of $71 \mu\text{g m}^{-3}$ at the North Sea station Westerland for 1999, which due to its remote site is influenced significantly by the Northern Hemisphere background [Umweltbundesamt, 2000].

Also shown in Figure 12.5 are the background concentrations for Hohenpeissenberg of $80 \mu\text{g m}^{-3}$ in 1998 and for Hamburg-Sasel of around $50 \mu\text{g m}^{-3}$ in 1995 [Kaminski

²The highest wind speeds were all observed during the winter half year.

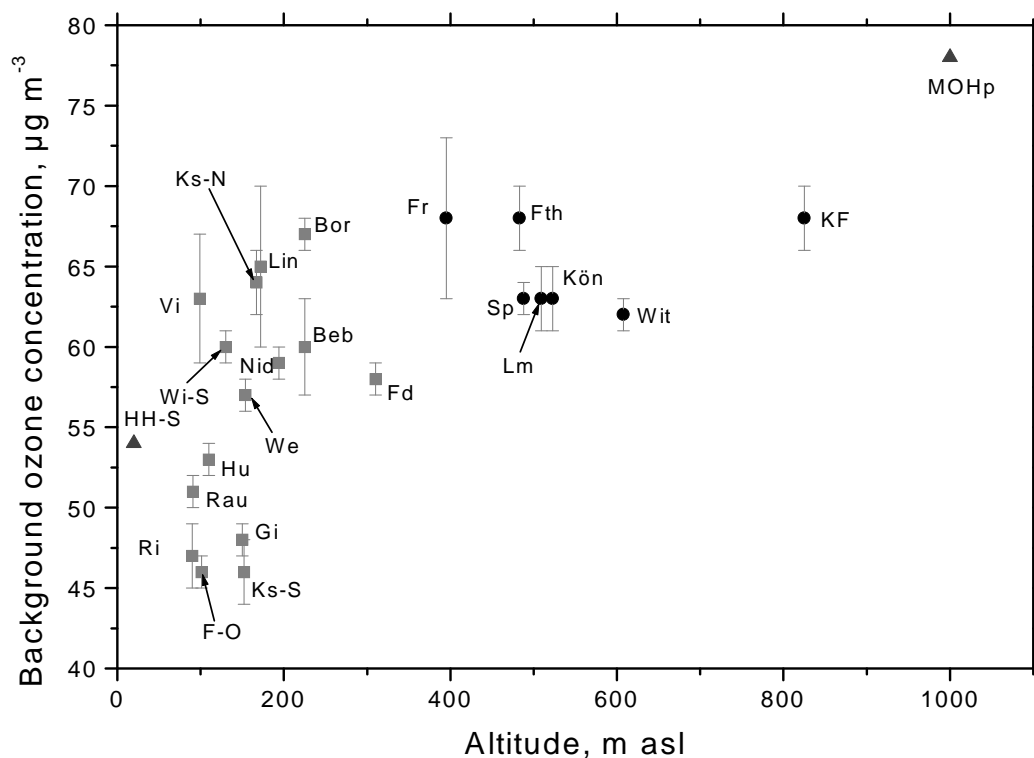


Figure 12.5: Background ozone concentration for 1998 plotted as a function of altitude for all stations in the HLUg measurement network for which both ozone and wind speed data were available. The circles represent forest and hill stations, the squares are stations on or near cities or towns, and the triangles are the two stations referred to in *Kaminski and Gilge* [2000a] (Hamburg-Sasel and Hohenpeissenberg).

Abbr.	Station	Alt.	Abbr.	Station	Alt.
Beb	Bebra	225	Kön	Königstein	523
Bor	Borken	225	Lin	Linden	172
F-O	Frankfurt-East	101	Lm	Limburg	509
Fr	Frankenberg	395	MOHp	Hohenpeissenberg	975
Fth	Fürth	483	Nid	Nidda	194
Fd	Fulda	310	Ri	Riedstadt	90
Gi	Giessen	150	Rau	Raunheim	91
HH-S	Hamburg-South	20	Sp	Spessart	488
Hu	Hanau	110	Vi	Viernheim	99
Ks-N	Kassel-North	167	We	Wetzlar	154
Ks-S	Kassel-South	152	Wi-S	Wiesbaden-South	130
KF	Kleiner Feldberg	825	Wit	Witzenhausen	608

and Gilge, 2000a,b]. The background concentration at Hohenpeissenberg is somewhat higher than observed at remote stations in Hesse. This may be due to an increased contribution of stratospheric air at the higher altitude, as it seems to be somewhat above the values for the European background cited above. Hamburg-Sasel, in contrast, fits well within the range observed at urban sites in Hesse.

Having estimated the background concentration, the average local monthly contribution to the annual ozone background can be estimated for Kleiner Feldberg by comparing the background value for 1998 with the average monthly concentrations shown in Figure 12.1. The months April to August make a positive net contribution due to ozone production, whereas the months October to February contribute to a net decrease in the ozone concentration due to the near absence of ozone production over the continent during winter. As has already been observed for the average daily profiles, March and September are transition months with nearly no net contribution. During the three months November to February, the average maximum ozone concentration remains below the annual background concentration for the station. Comparison of the average background concentration with the average concentration for each month shows that the monthly average for July is 53% higher than the average annual background, whereas during November it is only about 56% of the background.

The average monthly ozone concentrations is a composite of the average background concentration and the effect of local processes at the station. In summer, local photochemical production significantly outweighs loss processes, so that at low wind speeds the average concentration is significantly higher than the background level. In winter the situation is reversed. Loss processes dominate, and the poor mixing of the boundary layer at low wind speeds leads to a decline in ozone levels. This results in the net monthly contributions of the local processes to the hemispheric ozone concentration which is reflected in the average monthly concentrations.

12.4 Spatial representativity of ozone measurements

The previous sections have shown that meteorological processes, which can be expected to be active on a regional scale, have a significant impact on the local ozone observations. In order to estimate the scale length of these processes, the spatial representativity of the ozone measurements was studied using UBA data. The spatial representativity provides information about the relative importance of regional as opposed to local processes. It also gives an indication as to how well the results of local process studies can be applied to other regions which lie further away.

Climatological investigations of spatial representativity have been used to assist climate studies and the optimisation of measurement networks [e.g. *Schönwiese and*

Rapp, 1997; Rapp and Schönwiese, 1996; Rapp, 2000]. They yield quite different results for temperature and precipitation, with monthly average temperature measurements being representative over much larger areas than those of precipitation. This reflects the fact that precipitation is quite sensitive to small scale events, whereas temperature is more likely to reflect the weather situation on a large scale.

A similar approach was used for the analysis of the German ozone data, with the difference that daily one hour averages were used instead of monthly averages. The approach used in the current study involved investigating the fall-off with distance of the temporal correlation coefficients (r_t) between ozone measurements made at each of the German stations and at the HLUg measurement station Königstein, which is situated a few kilometres downhill from Kleiner Feldberg. The temporal correlation coefficients were calculated for the ozone data from Königstein for the period 1993 - 1997 and the one-hour ozone concentration for the same time of day at 277 measuring stations in Germany. The resulting correlation coefficient r_t is a measure of the degree to which day-to-day changes in the ozone concentration at Königstein are representative of changes at the other station, with $(100 \cdot r_t^2)$ % of the variability at the second station explained by the variability of the ozone measurements at Königstein. The correlation was calculated using the data for each hour of the day. This resulted in a daily profile of the time dependent correlation with Königstein, which provides information over the relative importance of local and regional scale processes. All stations belonged to the air quality control networks of the UBA, who provided the data, or to the environmental agencies of the German federal states. Data was only used from stations for which five years data was available.

In the second step, the r_t for each station was then correlated against both the distance of the station from Königstein (r_d) and its height above sea level (r_{alt})³. Figure 12.6 shows examples of the plots of r_t vs distance from Königstein and vs altitude for two times of day. Comparing the two sets of plots, we find that the correlations at 15:00 CET are much more compact than those at 03:00. This is most likely due to the more homogeneous conditions in the boundary layer during the day. In order to further examine this diurnal behaviour, the resulting correlation coefficients (expressed as the square of the coefficient, r^2) are plotted against the time of day in Figure 12.7.

The spatial correlation as expressed by r_d is quite poor overnight and in the early morning (22:00 - 10:00 CET), with r_d^2 less than approximately 0.1 during this period when all stations are included in the correlation. Figure 12.6(a) is typical of the situation during this period. After 10:00 CET the correlation of r_t with distance becomes more compact, see for example Figure 12.6(b), and reaches a maximum $r_d = 0.898$ at 16:00 CET during the mid afternoon. This is due to the effect of insolation which leads to stronger mixing during the day. This results in local effects being subordinated to the large scale situation. The correlation for nearby stations should thus be better, as the stations experience similar weather conditions and are affected

³Neither r_d nor r_{alt} include information about the goodness of the correlation with Königstein directly, but only about the relationship of this correlation to distance and altitude, respectively.

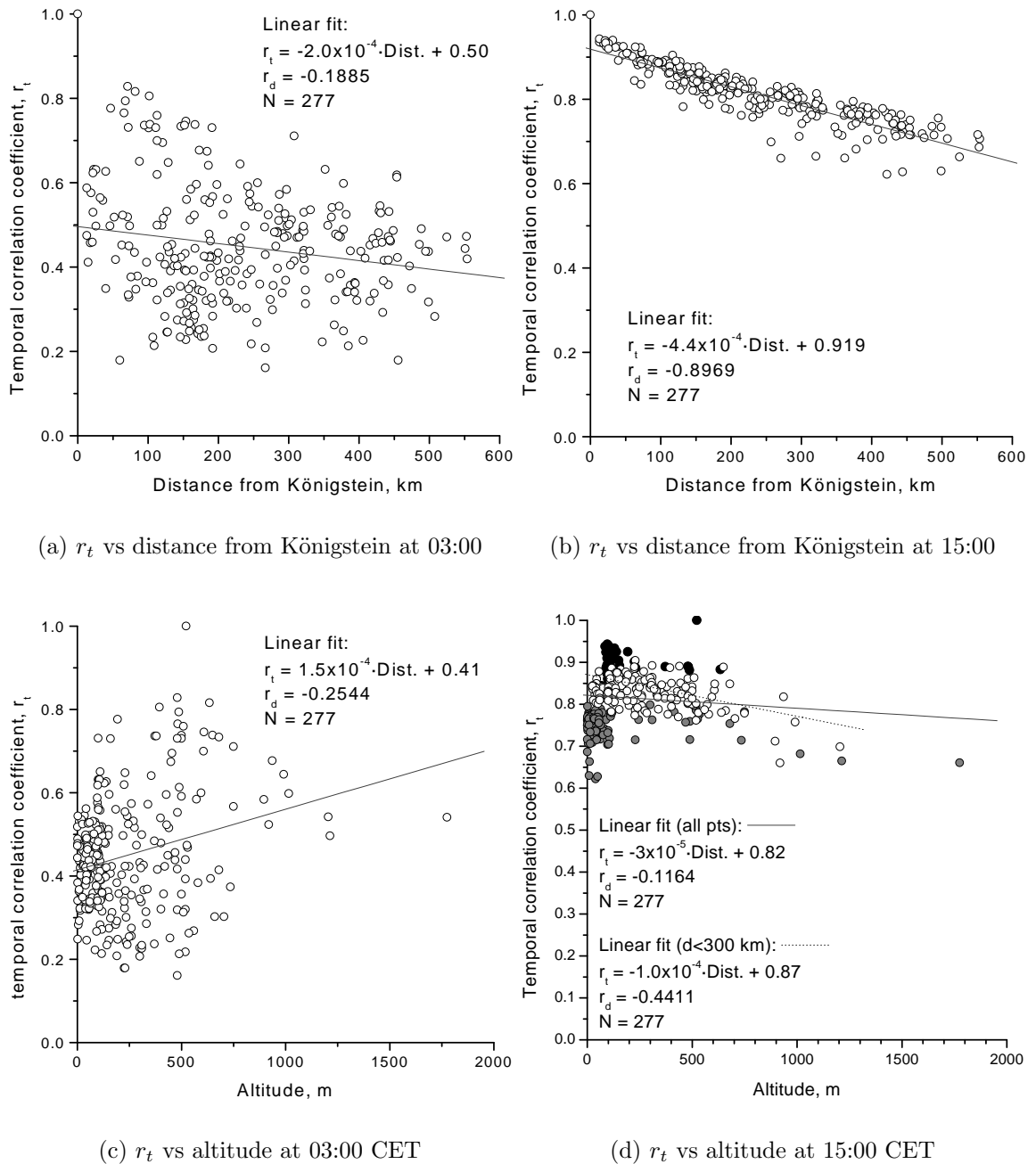


Figure 12.6: Plots of r_t vs distance from Königstein and vs altitude at 03:00 and 15:00 CET for 277 German stations. Data provided by UBA.

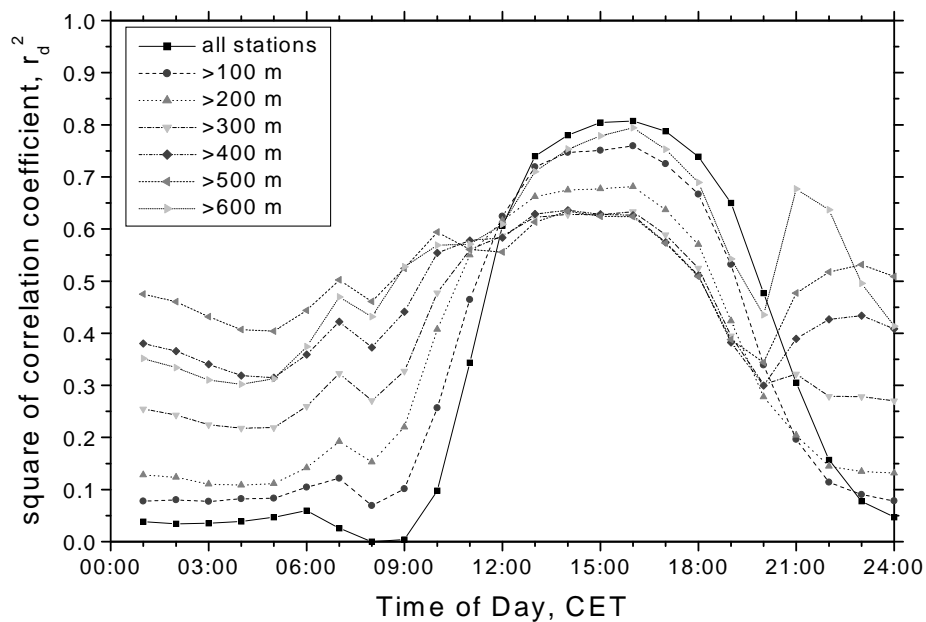
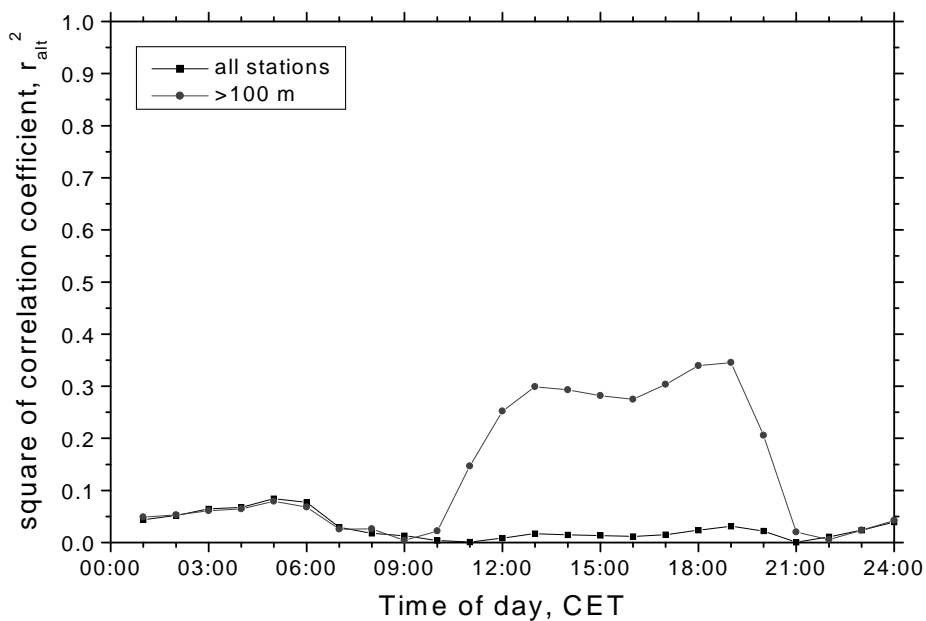
(a) Correlation between r_t and distance from Königstein, r_d^2 (b) Correlation between r_t and altitude, r_{alt}^2

Figure 12.7: Daily profiles of r_d^2 and r_{alt}^2 for 277 German stations. The data set covers the entire period 1993 - 1997. See text for definitions. Data provided by UBA.

by similar sources and sinks.

In contrast, when r_t is plotted against altitude for all stations using a linear fit, r_{alt}^2 is under 0.1 for the entire day. As can be seen by comparing Figures 12.6(c) and 12.6(d), the plot at 15:00 is much more compact, but exhibits a nonlinear behaviour, with a maximum r_t for stations at about 100 m. This nonlinear effect is caused by the uneven distribution of stations at different heights. Most of the low lying stations are relatively far away from Königstein, with a correspondingly low r_t . The stations with the highest r_t are those close to Königstein. This is evident in Figure 12.6(d), in which stations which are further than 300 km from Königstein are shown as shaded points, and those closer than 100 km are black. The relationship between r_t and height is better defined when distant stations, which were mostly also at altitudes under 100m, are left out of the correlation. The dotted line in Figure 12.6(d) shows the linear fit for all stations closer than 300 km, with $r_t = -0.4411$. This shows that the effect of distance from Königstein is much stronger than that of altitude. When only stations above 100 m a.s.l. are considered, the diurnal profile for r_{alt}^2 (see Figure 12.7(b)) is similar in shape to the profile for r_d^2 , but the correlation is nonetheless never as high as for the correlation with distance.

Due to the dominance of the distance from Königstein, the effect of altitude was investigated by calculating a series of diurnal profiles of r_d^2 for those stations above a given altitude. Figure 12.7(a) shows the series of profiles for a range of cut-off heights between 100 and 600 m a.s.l. The resulting profiles suggest that altitude does have a significant effect on spatial representativity. Particularly at night, the effect of stratification seems to cause stations at lower altitudes to be decoupled from the large scale events affecting higher stations. A similar effect was inferred from the average diurnal profiles for Sindlingen, Königstein and Kleiner Feldberg shown in Figure 12.3 on page 177. During the night, the relationship between r_t and distance from Königstein is more significant when only higher stations are included⁴. This suggests that the stations at higher altitudes are more representative of regional conditions at night, and are less strongly affected by local conditions and processes such as deposition and NO_x sources. Thus, overnight ozone concentrations at higher stations may be more indicative for ozone in the residual layer⁵. Lower lying stations are probably more strongly influenced by differences in the distribution of NO_x sources and the reduced vertical mixing.

During the day, differences among the correlations for different cut-off heights become less pronounced, with all the correlations highly significant. A rapid decrease is observed in the correlation after 18:00 CET, which indicates that local changes at this time of day. When only stations above about 400 m are considered, the correlation increases again after 20:00. This may be associated with the establishment of night-time stratification at higher altitudes.

During summer, the overall correlation with distance becomes somewhat stronger.

⁴For the few stations above 600 m, this is only true between 07:00 and 09:00.

⁵see Section 4.3

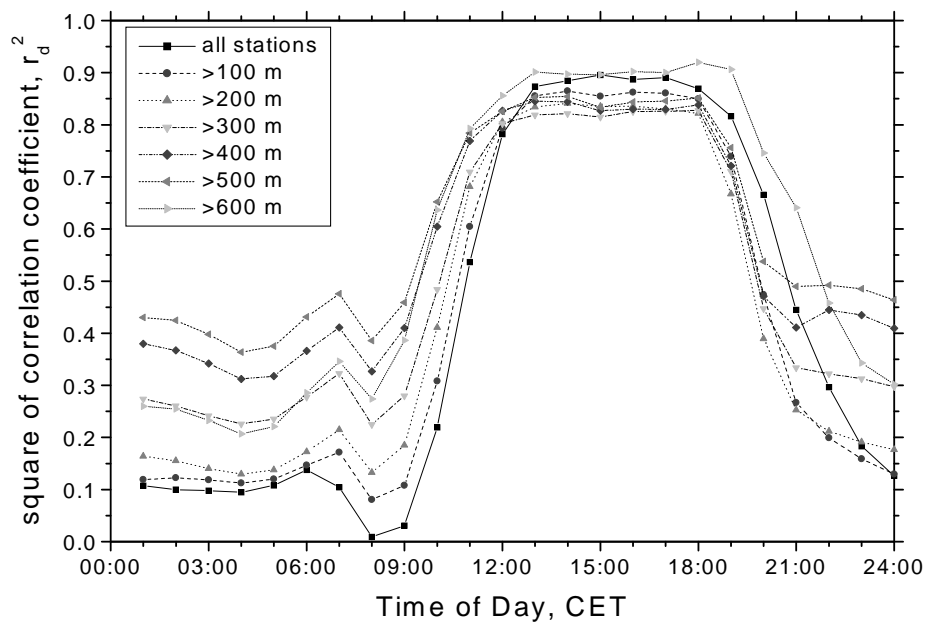
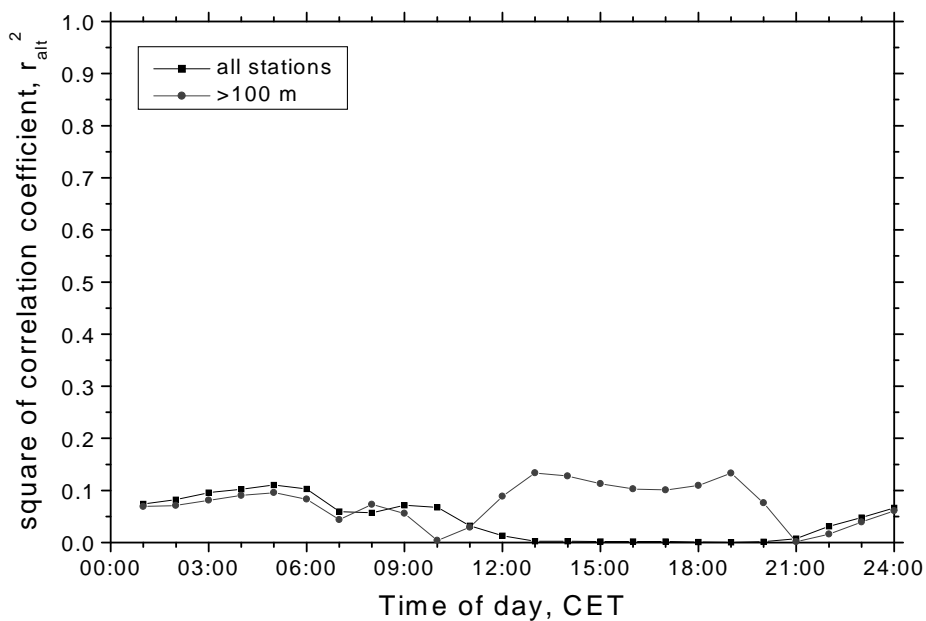
(a) Correlation between r_t and distance from Königstein, r_d^2 (b) Correlation between r_t and altitude, r_{alt}^2

Figure 12.8: Daily profiles of r_d^2 and r_{alt}^2 for 277 German stations. The data set covers the summer period, April to September, 1993 - 1997. Data provided by UBA.

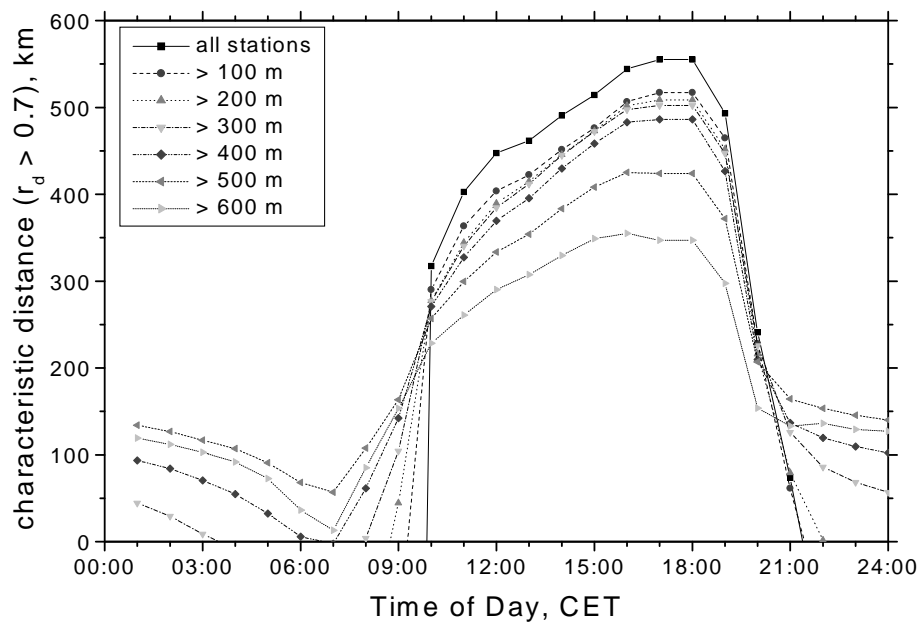
Figure 12.8 shows the diurnal profiles of r_d^2 and r_{alt}^2 for the summer months April to September, 1993-1998. During daytime a compact correlation was found for the relationship with distance, regardless of which stations were included in the correlation, and r_d^2 exceeded 0.8 for the entire period from 13:00 to 18:00 CET. This dominance of the effect of distance means that other factors play much less of a role, so that r_{alt}^2 is below 0.15 for the entire day. This is probably due to the intensive convective mixing during daylight hours in summer, which leads to a fairly homogeneous boundary layer. Stations at all altitudes thus experience similar conditions, so that the day to day changes are most strongly affected by regional factors and differences between stations can be expected to reflect their separation.

At night, the correlation with distance sinks to values similar to those observed for the whole year.

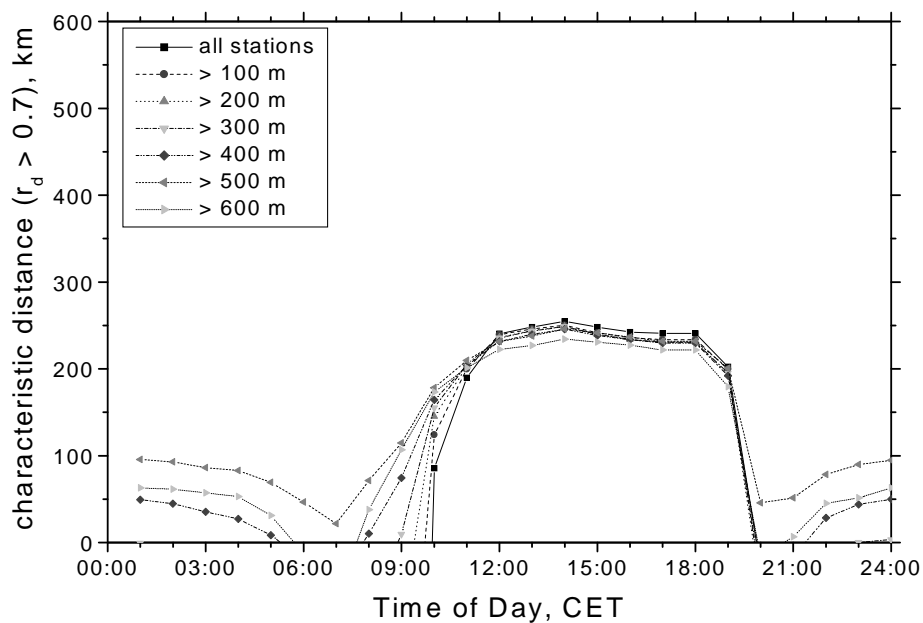
Although the profiles in Figures 12.7 and 12.8 provide information about the dependence of the temporal correlation with Königstein r_t on the distance from Königstein, or on the station altitude, they do not say anything about the region in which the measurements at Königstein can be considered to be representative. In order to quantify the extent of this region, the characteristic distance (D) for the correlation with Königstein was calculated for each time of day. The characteristic distance is defined here as the distance from Königstein at which r_t drops below 0.7, using a linear fit to the data. This corresponds to the point at which 50% of the day to day variance in the ozone concentration at a given time of day is explained by the temporal relationship with Königstein. It can be considered to define the region for which Königstein is representative of the temporal behaviour of the ozone concentration. The resulting diurnal profile of D is shown in Figure 12.9 for both the entire year (12.9(a)) and the summer period (12.9(b)). A series of profiles are also plotted for cases in which only stations above a certain height are considered.

Both profiles have similar shapes to Figures 12.7 and 12.8, with a relatively high value between 11:00 and 19:00 CET, and a much lower level overnight. During the night, Königstein is representative of a much smaller region, and comparison with the profile for r_d^2 in Figure 12.7(a) shows that the relationship is not very robust, i.e., there is considerable scatter in the temporal correlation of individual stations with Königstein, as is seen in Figure 12.6(a). During the day, however, measurements at Königstein are representative of a much larger region, with a radius over 500 km in the late afternoon. Figures 12.7(a) and 12.6(b) show that this region is also well defined.

During summer, the representative region is not as large (Figure 12.9(b)), extending only 250 km from Königstein, but this relationship is much more robust than when the whole year is considered. Furthermore, during summer the extent of the region varies little between 11:00 and 18:00. It appears likely that widespread stratification develops in winter during the daytime, leading to Königstein becoming representative of a larger region. Photochemical production is also at a minimum, so that the ozone level during winter is more strongly influenced by the hemispheric background. This



(a) Characteristic distance at different times of day, whole year



(b) Characteristic distance at different times of day, summer months

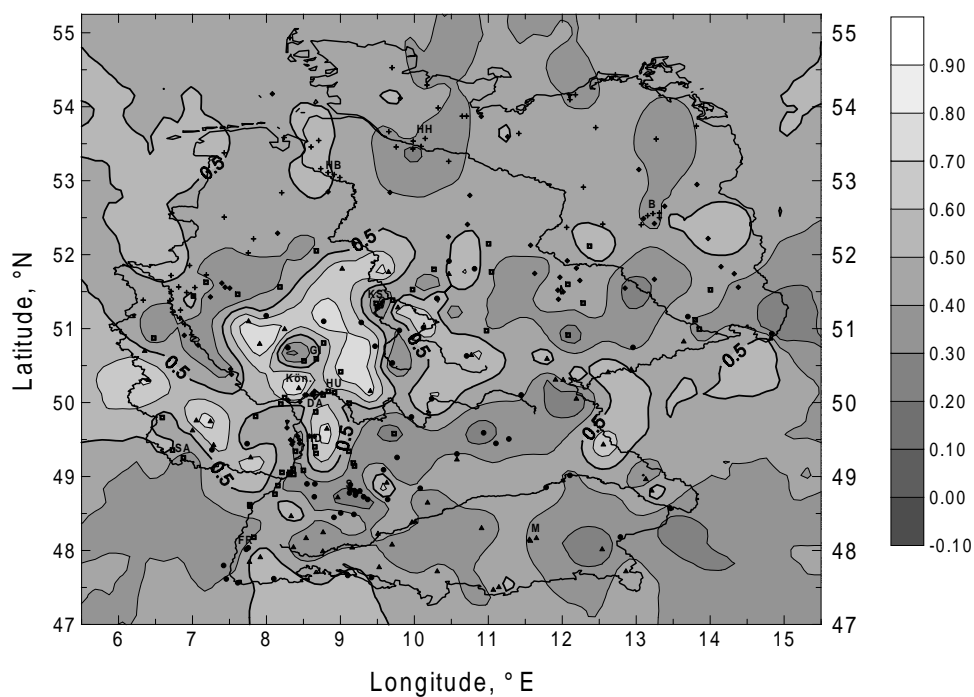
Figure 12.9: Daily profile of the characteristic distance (D , for which $r_t = 0.7$) for 277 German stations relative to Königstein im Taunus.

would also tend to level out the changes over a large area. On the other hand, disturbances due to changing weather conditions are also common, resulting in the observed greater overall scatter in r_t . The representative region during summer is smaller than when the whole year is considered, however the correlation is more compact and applies equally at all heights. As ozone production is significant during summer, the high temporal correlations in this region imply that production follows a similar day to day development within this area. This suggests that the boundary layer during the day is better mixed during summer, so that during daytime the individual stations are more strongly influenced by the air masses typical for the region than by local sources and sinks. During night-time, this intense insolation driven mixing is not present, and the local sources and sinks become more important.

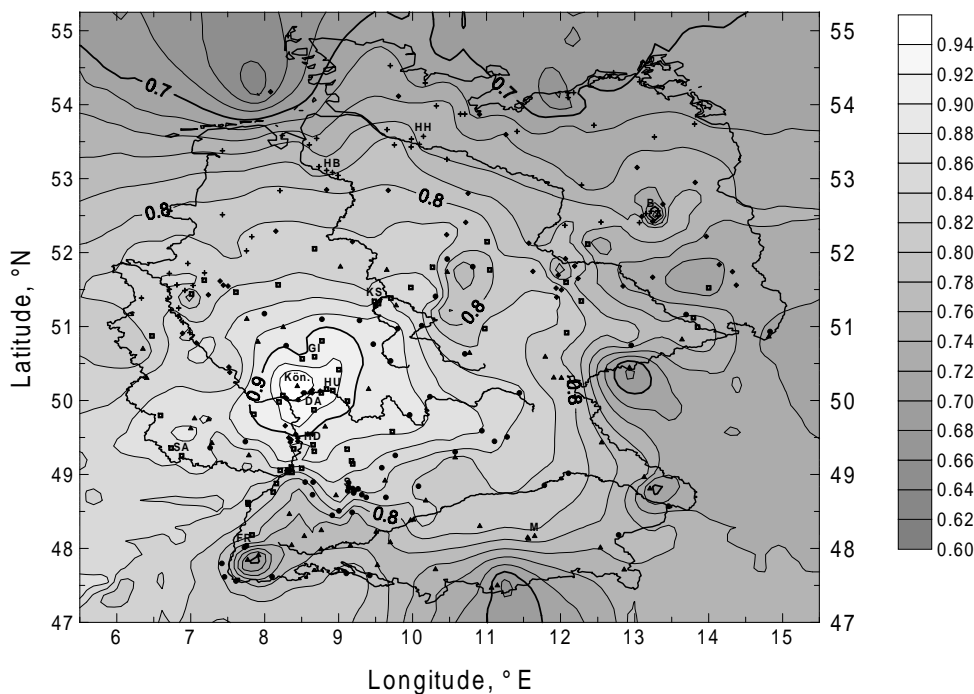
The spatial distribution of the temporal correlation r_t between the ozone concentration at Königstein and the other stations is shown in Figures 12.10 and 12.11 for the whole year and for summer, respectively. The plots show the distribution of r_t at two different times of the day, at 03:00 and 15:00 CET, and were calculated using data from the five year period 1993 - 1997. A marked difference between the daytime and night-time situations is apparent. At 03:00 CET there is no consistent pattern to be seen, with the highest correlations to be found with some of the slightly higher stations in the central German hill country. However, this is not always true, and the correlation drops quickly towards Wetzlar and Giessen, to the north of Königstein. Similar distributions are found for both the entire year (Figure 12.10(a)) and for the summer months (Figure 12.11(a)), although during summer the correlation drops off much more quickly with distance, and large areas to the south and west of Königstein show nearly no correlation. This helps to confirm the picture in which local processes seem to take precedence over large scale events at night, whereas at 15:00 CET a much more well ordered picture of regional emerges.

When the whole year is considered (Figure 12.10(b)), the ozone concentration at Königstein is significantly correlated ($r_t > 0.9$) during the afternoon with the concentration over an area extending from Giessen to Worms in the North - South direction, and from Rüdeshheim to Nidda in West - East extent. The boundary of the area for which $r_t > 0.7$ encompasses almost the entire country. In summer, the regional variation is more pronounced, and the region for which Königstein is representative is more compact. The $r_t > 0.9$ boundary essentially delineates the Rhine-Main region, and the region for which $r_t > 0.7$ extends as far as the Black Forest and the Oberpfalz in the south and west, and to Hannover to the north. Although this is much less than the characteristic distance common for meteorological parameters such as the average monthly temperature or monthly precipitation [e.g., *Schönwiese et al.*, 1986; *Schönwiese and Rapp*, 1997; *Rapp and Schönwiese*, 1996; *Rapp*, 2000], it indicates that regional scale events play a significant role during the afternoon, and that the ozone concentration is strongly influenced by the regional weather situation.

That this is not alone due to regional similarities in ozone production can be seen in Figure 12.12. This shows the spatial distribution of r_t for the difference between the ozone concentration at 16:00 in the afternoon and at 08:00 in the morning. The

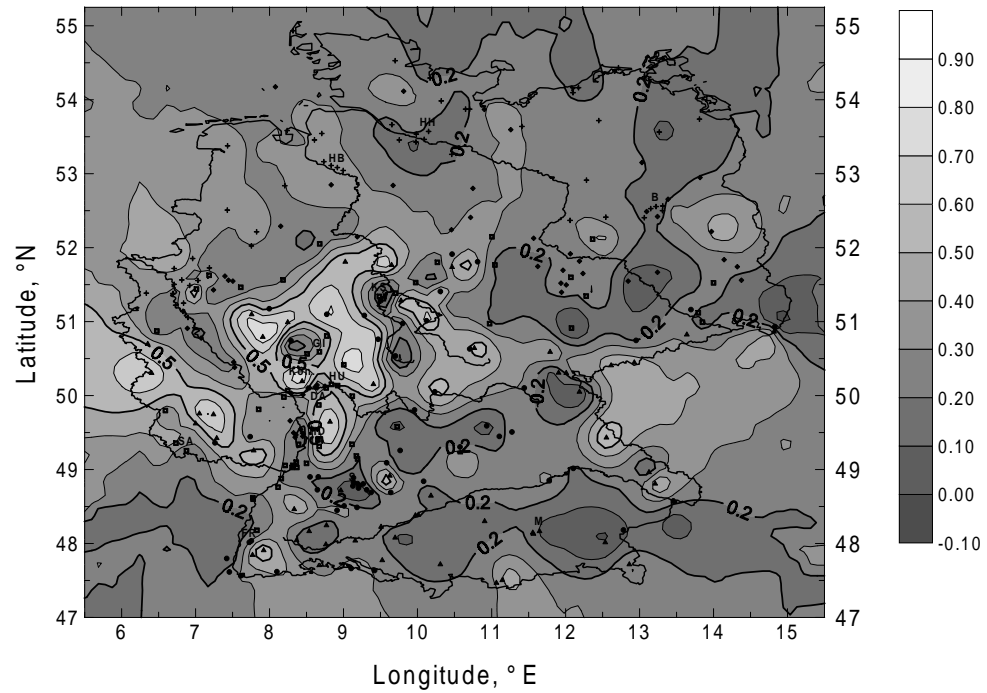


(a) 03:00 CET

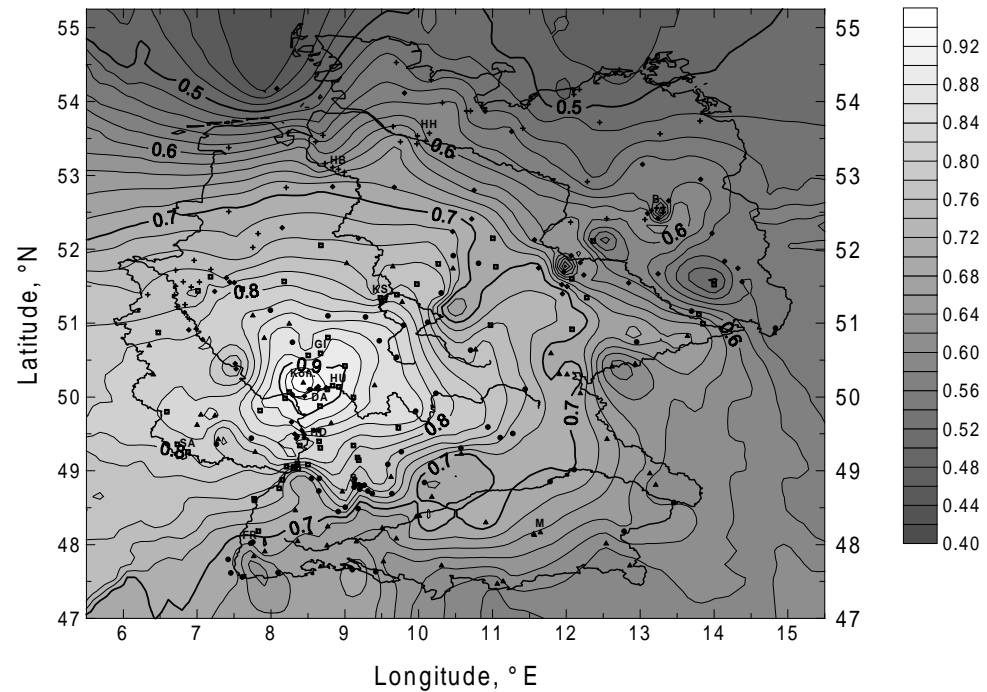


(b) 15:00 CET

Figure 12.10: Distribution of the temporal correlation between the ozone concentrations at Königstein and 276 other German stations for 03:00 and 15:00 CET, respectively. Database was for the whole year, 1993-1997. Data was provided by UBA.



(a) 03:00 CET



(b) 15:00 CET

Figure 12.11: Summertime distribution of the temporal correlation between the ozone concentrations at Königstein and 276 other German stations for 03:00 and 15:00 CET, respectively. Database was for the months April to September, 1993–1997. Data was provided by UBA.

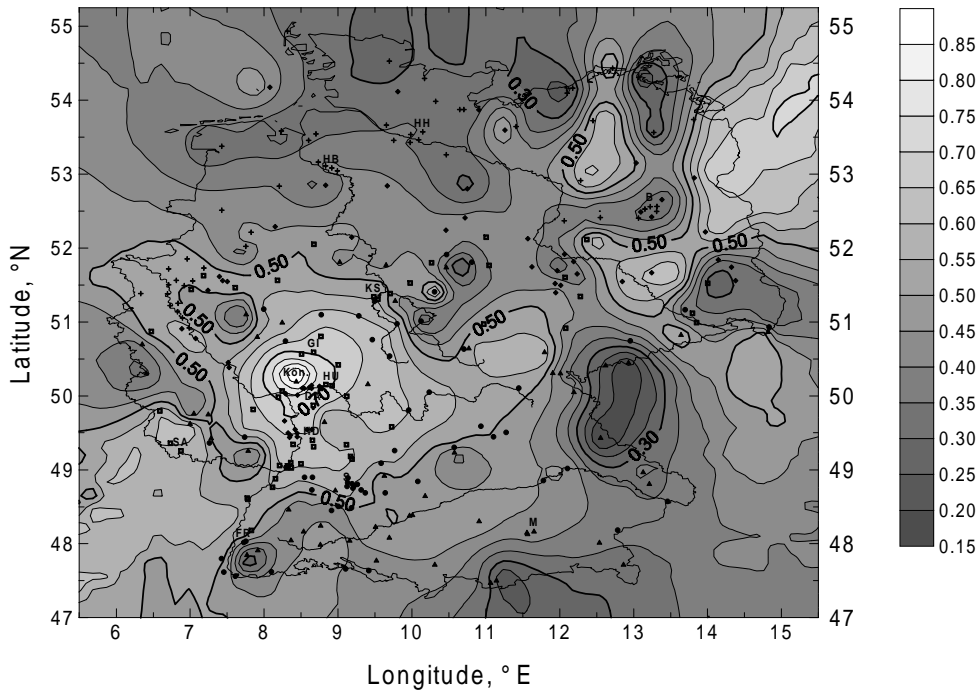


Figure 12.12: Summertime distribution of the temporal correlation between the ozone concentrations at Königstein and other stations in Germany for the difference in mixing ratios between 08:00 and 16:00 CET. UBA data from 277 German stations were used for the summer months April to September, 1993-1997.

correlation with Königstein is quite poor for all stations, with the region defined by $r_t > 0.7$ encompassing only the stations in the Rhine-Main region. It appears that the good regional representativity during the daytime is defined primarily by factors other than ozone production, such as mixing.

In summary, the temporal correlation between the ozone concentrations at Königstein and other stations is significantly correlated with distance from Königstein, and this is most pronounced during the afternoon. This indicates that the wider regional situation is of great importance to the daytime ozone concentration. The correlation of r_t with station altitude is quite poor, which reflects the strong dependence on distance and indicates that altitude is a poor indicator for the change in concentration over time. At night the relationship between r_t and distance breaks down to a large extent, although the effect of atmospheric stratification can be seen in a better correlation with distance for stations at higher altitudes.

12.5 Conclusion

The measurements of the ozone concentration from Kleiner Feldberg show that photochemical ozone production leads to a significant local diurnal increase in ozone concentrations during the summer months. Convective mixing and deposition also play a role in determining the diurnal profile of the ozone concentration, but the importance of these processes varies somewhat for stations at different altitudes, depending on the local circulation patterns. The daily variation at hilltop stations such as Kleiner Feldberg is less than at stations at lower altitude.

The day to day changes in the ozone concentration are controlled largely by processes operating on a regional scale during the daytime. This can be seen by the highly significant correlation of ozone measurements made at Königstein with other stations in the surrounding region, which extends to around 250 km in summer. This is probably due to strong horizontal and vertical mixing, and suggests that conditions only change slowly with distance during the daytime. Production is probably influenced more strongly during the daytime by the weakly changing regional weather patterns than by local emissions, and this is reflected by the strong correlations of both O_3 and RO_x concentrations with temperature. However, other factors besides photochemical production appear to play a strong role in determining the spatial representativity.

Chapter 13

Conclusion

The current work is an investigation into the effect of peroxy radicals on the photochemical production of ozone. Ozone is an important oxidant in the atmosphere which is involved in the oxidation of a large number of compounds. This is important for the self-cleansing of the atmosphere, but can also cause health problems in people and animals and cause damage to plants, etc. Peroxy radicals are radical intermediates in the oxidation of organic compounds, and contribute to an increase in the ozone concentration in polluted air masses.

In order to investigate the complex interactions leading to ozone formation, a series of field measurements of O_3 , RO_x and other relevant trace gases have been carried out at Kleiner Feldberg and Hohenpeissenberg. The RO_x measurements were made using a chemical amplifier, which was built for the purpose of carrying out this research project. Supplementary measurement data were made available by the HLUG and DWD.

These measurements show a number of plausible, yet complex, statistical relationships between the relevant trace gases. The most significant statistical relationship, however, is the already well established correlation between the daily maximum temperature and the maximum ozone concentration. Temperature was also very well correlated with the RO_x concentrations, and was found to be the best proxy for describing the conditions necessary for photochemistry.

As a result, temperature was confirmed as the most important parameter for predicting the ozone concentration. A simple statistical ozone forecast based on temperature and the ozone concentration on the previous day was able to explain about 80% of the variance in the observed maximum ozone concentration. The inclusion of the peroxy radical concentration from the morning under consideration resulted in only a very small improvement in the forecasted afternoon ozone concentration.

This tiny improvement does not justify using the RO_x measurements on an operational basis, which would be associated with considerable additional effort, for ozone

forecasts on the basis of statistical or empirical models. These results suggest that there is unlikely to be much improvement in the predictive ability of statistical models, even when further trace gases are taken into account, and that future improvements can best be achieved by moving to chemical models. Measurements of the RO_x concentration may enhance the ability of chemical models to forecast ozone, however it is likely that other parameters would initially prove to be of greater importance.

The photochemical production of ozone by RO_x radicals nevertheless is one important factor which influences the ozone concentration. This photochemical ozone production was calculated for 52 days with global radiation levels of over 600 W m^{-2} on the basis of the reaction between RO_x and NO . It was able to explain slightly more than 20% of the variance in the increase in ozone during the day. The low level of agreement can be attributed to the role of advection and changing conditions over the course of the day. Average diurnal profiles of the photochemical ozone production rate and the observed rate of change of the ozone concentration have a similar shape. However, loss processes associated with the diurnal circulation pattern and deposition cause a reduction in the observed rate of change in the ozone concentration. The average reduction at noontime was about 25%, when the photochemical ozone production rate was at its maximum of approximately 5 ppbv h^{-1} . At night, the loss processes resulted in a net loss of ozone at a rate of around 2 ppbv h^{-1} . The difference between the photochemical ozone production rate and the observed rate of change of the ozone concentration reached its maximum on the afternoon, which is consistent with the behaviour of deposition and transport processes from the surrounding valleys.

The RO_x measurements were also found to be consistent with the measurements of the OH radical and VOCs at Hohenpeissenberg on the basis of simple radical balance calculations. A steady state model was used to simulate the concentrations of OH and RO_x on the basis of the measured trace gas concentrations and the most important sources and sinks for the respective radical.

The concentrations calculated using the model showed good overall agreement with the observed radical concentrations, and most prominent features of the diurnal profiles could be reproduced by the model. The results showed that the “recycling” of the HO_2 radical to OH by its reaction with NO is responsible for the high concentrations of OH in the late morning, which had previously been the subject of some uncertainty. The reaction of the RO_x radicals with NO was also found to be a major factor in determining the shape of the diurnal profile for the RO_x concentration. This reaction is most rapid during the morning, when NO has its maximum. As a result, the build up of RO_x on the morning is delayed and the maximum RO_x concentration is only reached at about 14:00, after this reaction becomes less important.

The oxidation of NMHCs is at the same time both the most important sink for OH and the major source for RO_x , and reached rates of nearly $35 \times 10^6 \text{ molecule cm}^{-3} \text{ s}^{-1}$. The presence of large isoprene and terpene concentrations at Hohenpeissenberg meant that these compounds, isoprene in particular, dominated this process. The oxidation of other trace gases, e.g. CO , CH_4 , H_2 and H_2O_2 , was much less significant. Differences between the calculated and observed concentrations on some days were interpreted

to suggest that oxygenated VOCs may also be present in sufficient concentrations to influence the observed concentrations. However, this needs to be confirmed by actual measurements of oxygenated VOCs and by more detailed chemical modelling.

The issue of the importance of photochemical ozone production on longer time scales and a regional scale has also been addressed. Data from measurements of the ozone concentration at stations in Germany have been analysed at various spatial and temporal scales to determine the extent to which local ozone production is representative for events on a larger scale.

On a temporal scale, photochemical ozone production is considered to make a net positive contribute to the ozone level for the period April to August. Comparison of diurnal profiles with nearby stations show that these results are not only valid for Kleiner Feldberg, but that during periods of intense photochemical ozone production, daytime production rates are similar at stations at a range of altitudes and in different environments. The influence of layering was found to contribute to differences between the diurnal profiles at the different stations.

The spatial representativity of hourly ozone measurements was investigated using ozone measurement data from all of Germany which was supplied by UBA. The relationship between the ozone concentration at a given station and the ozone concentration at Königstein was found to depend primarily on the distance of the station from Königstein and the time of day. During the day, the relationship between the correlation coefficient and the distance of the station from Königstein was very strong, and decreased slowly with distance. At night, however, no dependence on distance was found, and the correlation coefficient was generally low. This suggests that during the day, mixing of the boundary layer, horizontal transport and the generally widespread nature of high pressure systems contribute to establishing conditions which remain similar over fairly large distances. At night, this pattern breaks down due to layering of the lower troposphere, and regional differences become much more important. A "characteristic distance" for this relationship was introduced and defined as the distance at which the correlation between the measurements at a given station and at Königstein explained less than 50% of the variation in the ozone concentration. This was found to extend about 250 km from Königstein for the greater part of the daylight hours in summer. For the whole year, the characteristic distance was even greater, although the correlation coefficients were in general lower. These results give added confidence that conditions necessary for ozone production and relevant for RO_x chemistry are not only valid on a local scale, but have a wider significance during summer for regional processes.

In summary, the current study was able to confirm the importance of the photochemical ozone production due to the presence of peroxy radicals during summer. The measured RO_x concentrations are consistent with our understanding of the atmospheric photochemistry, and with the results of a simple steady state model for OH

and RO_x radicals. Nevertheless, despite the importance of RO_x for the photochemical production, the measurements did not enable an improved ozone forecast using a simple statistical relationship for predicting the ozone concentration. This emphasises the limitations of the commonly used statistical approach to ozone prognosis, and suggests that chemical modules may be required to achieve an improvement in ozone forecasts.

Zusammenfassung

Diese Studie liefert einen Beitrag zum Verständnis der Rolle der Peroxyradikale bei der Produktion des troposphärischen Ozons. Hierzu wurden Messungen der Peroxyradikale, des Ozons und anderer wichtiger photochemischer Spurengase am Kleinen Feldberg in Hessen und am Hohenpeißenberg in Bayern vorgenommen. Dies ermöglichte die Berechnung der photochemischen Produktionsrate des Ozons, und den Vergleich mit der gemessenen Änderung der Ozonkonzentration. Aufgrund der Messungen am Kleinen Feldberg wurde ein einfaches statistisches Modell zur Vorhersage des Ozonmaximums erstellt. Eine Verbesserung dieses Modells durch die Berücksichtigung der RO_x -Messungen am Vormittag konnte kaum erzielt werden. Am Hohenpeißenberg wurden neben diesen Verbindungen zusätzlich auch das Hydroxyradikal (OH), flüchtige organische Verbindungen und eine Reihe anderer Komponenten gemessen. Die tageszeitliche Entwicklung der OH- und Peroxyradikal-Konzentrationen wurde mit einem Radikalbilanz-Modell berechnet. Die berechneten Konzentrationen stimmen gut mit den beobachteten Konzentrationen überein. Weiterhin wurde die räumliche Repräsentanz der Ozonmessungen untersucht. Dabei wurde festgestellt, dass die Messungen des HLUg nahe Königstein im Taunus im Sommer für eine Region von etwa 200 km in Durchmesser repräsentativ sind.

Trotz seiner niedrigen Konzentration, spielt troposphärisches Ozon eine wichtige Rolle bei der Selbstreinigung der Atmosphäre. Andererseits, führen erhöhte Konzentrationen zu gesundheitlichen Beeinträchtigungen beim Menschen und weiteren Schäden an Pflanzen und Umwelt. Seit den Fünfzigern und Sechzigern Jahren tritt dieses Problem infolge erhöhter Emissionen von Stickoxiden und organischen Verbindungen in vielen Regionen bei starker Sonneneinstrahlung auf. Die Anwesenheit von flüchtigen organischen Verbindungen führt zu der Bildung von Peroxyradikalen (RO_x), die das normale photochemische Gleichgewicht zwischen Ozon und Stickoxiden zu Gunsten erhöhter Ozon-Konzentrationen verschieben. Diese flüchtigen organischen Verbindungen (kurz VOCs genannt, aus dem Englischen “volatile organic compounds”), werden sowohl aus natürlichen als auch aus anthropogenen Quellen emittiert.

Peroxyradikale werden hauptsächlich durch die Oxidierung von VOCs durch die Hydroxyradikale (OH), aber auch durch Ozon und das Nitratradikal, gebildet. Sie reagieren mit NO und bilden NO₂, das durch Photolyse Ozon bildet. Weitere Reaktionen führen zu der Bildung von Nebenprodukten, die die Effizienz der Ozonbildung verringern, aber auch zur Bildung weiterer Peroxyradikale beitragen.

Die vorliegende Arbeit liefert einen Beitrag zum Verständnis dieses Themengebietes. Es wurden an zwei Messorten Messungen einer breiten Palette von atmosphärischen Spurengasen durchgeführt, um die Beziehungen und Wechselwirkungen zwischen diesen Komponenten zu untersuchen.

Insbesondere werden nachstehende Fragen behandelt:

- Ermöglicht die Kenntnis der Peroxyradikal-Konzentration eine Verbesserung der täglichen Ozonvorhersage?
- sind die Peroxyradikalmessungen am Hohenpeissenberg konsistent mit den Messungen anderer Spurenstoffe sind, u.a. des OH-Radikals und der VOCs?
- Sind lokale Messungen der Ozonkonzentration und Prozessstudien für Ereignisse auch im regionalen Maßstab repräsentativ?

Messmethode

Zur Durchführung dieses Projektes wurde ein chemischer Verstärker zur Messung der Gesamt-Peroxyradikalkonzentration gebaut. Im Einlass des Gerätes reagieren die Peroxyradikale mit hinzugefügtem NO und produzieren NO₂ und weitere Radikale, z.B. OH und organische Oxy-Radikale. Diese weiteren Radikale werden größtenteils in einer Reaktion mit zusätzlich hinzugefügtem CO wieder in HO₂ verwandelt, das sich dann weiter mit NO reagieren kann. Dies führt zu einer Kettenreaktion, bei der mehrere NO₂-Moleküle pro RO_x-Radikal gebildet werden. Die Kettenreaktion wird durch Verlust der Radikale durch Oberflächenreaktionen oder durch Schlussreaktionen der Radikale untereinander beendet. Der Verstärkungsfaktor entspricht die Kettenlänge (d.h. die pro Radikal gebildete Anzahl von NO₂-Molekülen). Er wird durch eine Kalibrierung des Gerätes bestimmt, und liegt normalerweise im Bereich von 50-100 NO₂-Molekülen.

Das durch die Kettenreaktion produzierte NO₂ sowie das zuvor bereits in der Luftprobe enthaltene NO₂ wird anschließend mit einem Luminoldetektor nachgewiesen. In diesem Detektor reagiert NO₂ in einer Chemilumineszenz-Reaktion mit einer Luminollösung. Das bei dieser Reaktion emittierte Licht wird mit einem Photomultiplier registriert.

Um zwischen NO₂ (und Ozon) in der Hintergrundluft und NO₂ aus der Oxidationsreaktion mit RO_x zu unterscheiden, wird das im Einlass zugefügte CO zwischen zwei Zuführungspunkten im 30 Sek. Takt hin und her geschaltet. Dadurch wird die Verstärkung des Peroxyradikalsignals ein- und ausgeschaltet. Durch den Abzug des

Hintergrundsignals vom Gesamtsignal erhält man schließlich das NO_2 -Signal, das aufgrund der Peroxyradikale entsteht. Dieses Signal wird mit Hilfe des durch Kalibrierung bekannten Verstärkungsfaktors und der NO_2 -Empfindlichkeit des Detektors in die Peroxyradikalkonzentration umgewandelt.

Um den Verstärkungsfaktor zu bestimmen, wird das Gerät bei kontinuierlichem Betrieb mit HO_2 ¹ einmal pro Woche kalibriert. Das Gerät wird außerdem alle 2 Stunden in einem automatisierten Vorgang mit NO_2 kalibriert. Zusätzlich wird die Linearität des Detektors in unregelmäßigen Abständen überprüft.

Aufgrund des indirekten Messverfahrens misst das Meßgerät die äquivalente HO_2 -Konzentration, die die beobachtete Menge an NO_2 erzeugen würde. Weil die tatsächlich vorhandenen RO_x -Radikale teilweise unterschiedliche physikochemische Eigenschaften haben, ist dieser Meßwert nur eine Annäherung zum "wahren" Wert. Ergebnisse andere Autoren zeigen, dass unter Tageslichtbedingungen dennoch mehr als 90% der Radikale erfaßt werden. Messungen in der Nähe von starken biogenen Quellen können aber zur Unterschätzung der Gesamtkonzentration führen.

Der Verstärkungsfaktor ist von der Konzentration des atmosphärischen Wasserdampfes abhängig. Der in trockener Luft bestimmte Kalibrierfaktor muss deshalb in Bezug auf diese Querempfindlichkeit korrigiert werden.

Die Präzision des Messgerätes wurde aus einer Analyse der Kalibrierdaten auf etwa 10% und die Genauigkeit auf etwa 22% in trockener Luft geschätzt. Unsicherheiten in der Abhängigkeit des Verstärkungsfaktors von der Wasserdampfkonzentration führen zu einer Minderung der Präzision. Nach Berücksichtigung dieser zusätzliche Unsicherheit, beträgt die Präzision der Messungen etwa 61% bei 50% relativer Feuchte, und 70% bei 60% relativer Feuchte.

In den Sommermonaten der beiden Jahre 1998 und 1999 wurden Messungen am Taunus Observatorium der Universität Frankfurt auf dem Kleinen Feldberg durchgeführt. Neben der Peroxyradikalmessungen wurden Messungen von Stickoxiden mit einem hochempfindlichen Analysegerät der Firma EcoPhysics durchgeführt. Weitere Messungen wurden vom Hessischen Landesamt für Umwelt und Geologie (HLUG) und dem Deutschen Wetterdienst (DWD) zur Verfügung gestellt.

Im Rahmen einer Messkampagne im Juni/Juli 2000 am Meteorologischen Observatorium Hohenpeißenberg (MOHp) fanden weitere Messungen statt. Dort waren neben den RO_x -Messungen Messdaten der GAW-Station des DWDs zur Auswertung und Interpretation verfügbar. Als Teil des normalen Messbetriebes werden am MOHp die Konzentrationen von OH, eine Reihe von VOCs, und anderen relevanten Spurengasen bestimmt.

¹als repräsentatives Peroxyradikal. Alle Konzentrationen sind daher als äquivalente HO_2 -Konzentrationen zu verstehen.

Messergebnisse

Die Messungen am Taunus Observatorium fanden in den Monaten Juli bis September der Jahre 1998 und 1999 statt. Für den gesamten Zeitraum wurden mittlere Tagesgänge für RO_x , O_3 , PAN und Stickoxide berechnet. Alle untersuchten Komponenten zeigen an ausgeprägte Tagesgänge. Das Mischungsverhältnis des Ozons erreicht ein Maximum von ca. 65 ppbv zwischen 14 und 17 Uhr MEZ. Der Tagesgang des mittleren RO_x -Mischungsverhältnisses zeigt am Vormittag einen langsamen Anstieg. Das Maximum von durchschnittlich etwa 20 pptv wird um etwa 14:00 MEZ erreicht. Danach geht das Mischungsverhältnis auf ein mittleres nächtliches Minimum von 2-3 pptv zurück. Der Tagesgang des NO -Mischungsverhältnisses zeigt ein Maximum am Vormittag. Durch die Reaktion des NO mit RO_x führt dies zu dem beobachteten langsamen Anstieg der RO_x -Werte.

Um ein Hinweis auf den Einfluß anthropogener Emissionen zu bekommen, wurde der Wochengang von Ozon, RO_x und NO_x ebenfalls untersucht. Der Wochengang des Ozons zeigt einen signifikanten Anstieg am Wochenende. Dagegen nimmt die Konzentration der Stickoxide am Wochenende ab, bedingt durch einen niedrigeren Ausstoß von Verkehr und Industrie. Der Wochengang für RO_x zeigt einen geringen Rückgang gegen Mitte der Woche. Da die RO_x Vorläufer sowohl von biogenen als auch von anthropogenen Ursprungs sind, wird ein Wocheneffekt der anthropogenen Emissionen möglicherweise durch die biogenen Emissionen maskiert. Da einem Anstieg des Mischungsverhältnisses der RO_x -Radikale weitgehend ausbleibt, widerspricht auf dem ersten Blick die Zunahme des Ozonmischungsverhältnisses am Wochenende dem beobachteten Rückgang vom Mischungsverhältnis der Stickoxide. NO_x und RO_x sind die wichtigsten Ozonvorläufer. Dies ist aber durch Modellergebnisse von verschiedenen Autoren erklärbar. Sie zeigen, dass eine Minderung der NO_x -Emissionen zuerst zu einer Zunahme der Ozonkonzentration führt, wenn die NO_x -Konzentration über einem gewissen Schwellenwert liegt. Dieser Zustand wird als VOC-limitiert bezeichnet, da nur VOC-Minderungsmaßnahmen eine sofortigen Minderung des Ozonpegels bewirken. Die Meßergebnisse deuten darauf hin, dass am Kleinen Feldberg eine solche Situation vorgefunden wurde. Dies deutet darauf hin, dass eine Ozonminderungsstrategie in erster Linie auf einer Minderung der VOC Emissionen zielen sollte.

Die statistischen Beziehungen zwischen den verschiedenen meteorologischen und luftchemischen Parametern wurden untersucht. Das Datenmaterial der beiden Jahre enthält eine Reihe plausibler statistischer Beziehungen, die mit bekannten Charakteristika des photochemischen Systems konsistent sind.

Die Tagestemperatur ist die für die Ozon- und RO_x -Konzentrationen bei weitem wichtigste Einflussgröße. Sowohl das Tagesmaximum des Ozonmischungsverhältnisses als auch das mittlere RO_x -Mischungsverhältnis sind mit dem Maximum der Tagestemperatur gut korreliert ($r = 0.856$ für O_3 ; $r = 0.715$ für RO_x). Beide Spurengase werden während Wetterlagen mit hoher Sonneneinstrahlung produziert, die auch mit höheren Temperaturen verbunden sind. Die Temperatur ist daher die beste Ersatzgröße für

photochemische Vorgänge.

Auf der Grundlage der Messungen am Kleinen Feldberg wurde ein einfaches statistisches Modell zur Vorhersage des Ozonmaximums erstellt. Durch die Berücksichtigung der RO_x -Messungen am Vormittag konnte nur eine geringe Verbesserung dieses Modells kaum erzielt werden. Mit den Parametern Temperatur und Ozonkonzentration am Vortag konnte das statische Modell bereits 80% der Variation der Ozonkonzentration erklären. Die zusätzliche Berücksichtigung von RO_x -Messungen und der berechneten Ozonbildung am Vormittag führte lediglich zu einer Verbesserung der erklärten Varianz um 0.5%. Diese minimale Verbesserung rechtfertigt den Einsatz des mit den erheblichen Aufwand verbundenen RO_x -Messgerätes zu diesem Zweck nicht. Diese Ergebnisse deuten daraufhin, dass eine Verbesserung solcher statistischen Modellen durch zusätzliche Spurengasmessungen relativ unwahrscheinlich ist. Weitere Verbesserung der Ozonvorhersagen wird eher durch den Einsatz von gekoppelten chemischen Modellen zu erreichen sein.

Die Ozonbildungsrate auf Basis der Reaktion zwischen RO_x und NO wurde für Tage mit einem Maximum der Globalstrahlung über 600 W m^{-2} berechnet. Die Rolle des NO_2 , das als Reservoir für das Ozon dient, wurde bei der Berechnung der Ozonbildungsrate berücksichtigt. Der beobachtete Ozonanstieg wurde dann mit der über die Zeit integrierten Bildungsrate verglichen. Obwohl die Übereinstimmung an manchen Tagen recht gut war, ist der Korrelationskoeffizient für den Gesamtdatensatz niedrig ($r = 0.46$). Dieses Ergebnis bestätigt, dass neben der lokalen Ozonbildung andere Prozesse eine wichtige Rolle für die Ozonkonzentration spielen.

Die beobachtete Änderung des Ozonmischungsverhältnisses wurde mit dem gemittelten berechneten Tagesgang der Ozonbildungsrate verglichen. Die beiden Tagesgänge haben eine ähnliche Form, aber die eingetretenen Änderungsraten der Ozonkonzentration sind niedriger als die berechneten Ozonbildungsraten. Die Ozonbildungsrate lag bei etwa 5 ppbv h^{-1} um die Mittagszeit, während die beobachtete Änderung des Ozonmischungsverhältnisses bei etwa 3.5 ppbv h^{-1} lag. Der Unterschied zwischen den beiden Kurven ist durch Verlustprozesse, wie z.B. trockene Deposition und Advektion, die nicht berücksichtigt wurden, zu erklären. Am Abend überwiegen die Verlustprozesse. Zu dieser Zeit werden etwa 2 ppbv O_3 pro Stunde abgebaut.

Die Messkampagne am MOHp hatte als Hauptziel, eine Radikalbilanz für OH und RO_x aufzustellen. Hierzu wurden während einer Schönwetterepisode über vier Tage zusätzliche VOC-Messungen vorgenommen. Für diese Messtage wurde ein auf der Annahme des lokalen photostationären Gleichgewichts der Radikale basierendes Modell der Radikal-Konzentration erstellt. Mit Hilfe der Quellen und Senken enthaltende Bilanzgleichung wird dann die Konzentration des Radikals zum Zeitpunkt t bestimmt. Die Annahme eines photochemischen Gleichgewichts ist für OH über dem ganzen Zeitraum erfüllt, während für RO_x sie nur tagsüber gültig ist.

Die Modellergebnisse stimmten im allgemeinen sehr gut mit den Messungen überein. Allerdings wurde die OH -Konzentration an den beiden Tagen 18. und 19. Juni deutlich überschätzt. Beispielsweise, betrug die gemessene Konzentration um

10:00 MEZ am 19.06 7.29×10^6 Moleküle cm^{-3} . Sie wurde um 60% von dem Modell überschätzt, was durch den Einfluss oxygenierter VOCs erklärt werden kann. Als Stellvertreter für diese nicht gemessenen Verbindungen wurde Formaldehyd (HCHO) in einem Mischungsverhältnis von 3 ppbv angenommen. Diese Annahme führte an den zwei Tagen zu einer besseren Übereinstimmung der Spitzenwerten der OH-Konzentration. Im obengenannten Beispiel erniedrigte sich der berechnete Wert auf 8.6×10^6 Moleküle cm^{-3} , und liegt somit nur 20% über dem gemessenen Wert. Der zeitliche Verlauf vom Mischungsverhältnis der RO_x -Radikale wurde sehr gut modelliert.

Die verschiedenen Senk- und Quellterme konnte mit dem Modell abgeschätzt werden. Dies zeigt, dass das sogenannte "Recycling" der HO_2 -Radikale (die Reaktion zwischen HO_2 und NO) die wichtigste Quelle für OH und die wichtigste Senke für RO_x ist. Durch die erhöhte NO -Konzentration am Vormittag wird HO_2 sehr schnell in OH umgewandelt, das wiederum für die VOC-Oxidation und RO_x -Bildung verantwortlich ist. An Tagen mit niedrigerer NO -Konzentration, war der Beitrag der primären OH-Produktion durch die Photolyse von Ozon ähnlich groß wie der Beitrag aus dem "Recycling" von HO_2 . Die wichtigste Senke von OH ist die Oxidation der Nicht-Methan-Kohlenwasserstoffe, gefolgt von der Oxidation von HCHO, CO, und anderen Spurengasen. NO_2 -Oxidation kann eine wichtige OH-Senke während Episoden mit höherer NO_2 -Belastung sein.

Die OH-Quelltermen sind gleichzeitig die bedeutendsten RO_x -Senken, und umgekehrt die OH-Senken die wichtigsten Quellen für RO_x . Als zusätzliche Senken wurden die Reaktionen der Peroxyradikale miteinander berücksichtigt, wobei die wichtigste dieser Reaktionen die zwischen HO_2 und RO_2 ist. Diese Reaktionen sind nur am Nachmittag von Bedeutung. Am Nachmittag verliert die Reaktion mit NO wegen abnehmender NO -Konzentration an Wichtigkeit. Die Oxidation von VOCs durch Ozon und das Nitrat-Radikal wurde nicht berücksichtigt.

Um die Rolle der photochemischen Ozonproduktion auf regionaler Skala zu untersuchen, wurden die Ozonmessungen des HLUG für Hessen, und des Umweltbundesamtes für ganz Deutschland statistisch untersucht. Diese Untersuchung erfolgte auf unterschiedlichen zeitlichen und räumlichen Skalen.

Der mittlere Tagesgang der Ozonkonzentration am Kleinen Feldberg für jedes Kalendermonat zeigt wie erwartet, dass die photochemische Produktion während der Sommermonate am wichtigsten ist. Diese Signatur der photochemischen Ozonbildung wird auch im Winter beobachtet. Die Hintergrundkonzentration für das ganze Jahr am Kleinen Feldberg betrug etwa $68 \mu\text{g m}^{-3}$. Die Monatsmittelwerte für den Zeitraum April bis August lagen alle über diesem Wert, was auf eine Netto-Produktion in diesen Monaten hindeutet. März und September sind nach diesem Kriterium Übergangsmonate, während Oktober bis Februar zu einem Netto-Abbau von Ozon beitragen. Die Hintergrundkonzentration für den Kleinen Feldberg war ähnlich wie anderen hessischen Waldstationen.

Die Ozon-Messdaten von 277 deutschen Messstationen wurden mit den an einer Waldmessstelle nahe Königstein gemessenen Ozonwerten korreliert. Um ein Maß für

die räumliche Variation der Korrelationsgüte zu bestimmen, wurde untersucht, wie diese Korrelationskoeffizient von der Entfernung der Station von Königstein abhängt. Die Stärke der Korrelation nimmt mit der Entfernung der betrachteten Station von Königstein ab. Es zeigte sich allerdings ein stark tageszeitlich abhängige Zusammenhang zwischen den Korrelationskoeffizient und der Entfernung der behandelten Station von der Referenzstation Königstein. Tagsüber war die Zusammenhang mit der Entfernung sehr ausgeprägt, dagegen nachts sehr gering. Dies kann man auf eine gute Durchmischung und räumliche Homogenität der bodennahen Schicht während des Tages zurückführen.

Ein Maß für die räumliche Repräsentanz der lokalen Messungen wurde mit Hilfe des Konzeptes der "charakteristischen Entfernung" definiert. Diese wurde als jene Entfernung von Königstein definiert, ab der der Korrelationskoeffizient einer mittlere Station mit Königstein unter 0.7 sank. Nach dieser Definition ist Königstein im Sommer tagsüber für ein Gebiet von etwa 250 km Durchmesser repräsentativ. Über das ganze Jahr ist es für ein noch größeres Gebiet, von bis zu 550 km, repräsentativ. Dies ist vermutlich auf stärkere Durchmischung, bzw. Homogenität, und geringere photochemische Produktion im Winter zurückzuführen. Diese Ergebnisse deuten darauf hin, dass die Prozesse, die einen wichtigen Einfluss auf die Ozonkonzentration ausüben, auf regionalen Skalen von einigen hundert Kilometern aktiv sind (z.B. an große Hochdruckgebiete gebunden sind).

Zusammenfassend lässt sich sagen, dass die photochemische Produktion von Ozon durch Peroxyradikale im Sommerhalbjahr ein sehr wichtiger Prozess ist. Die gemessene Peroxyradikalkonzentrationen sind mit den aufgrund der chemischen Oxidation der VOCs durch OH berechneten Konzentrationen konsistent. Die Peroxyradikale sind aufgrund ihrer Reaktion mit NO die Ursache der erhöhten sommerlichen Ozonkonzentrationen. Obwohl die Peroxyradikal-Konzentrationen für die chemische Modellierung von Bedeutung sind, tragen Peroxyradikalmessungen nur wenig zu einer Verbesserung der Qualität von kurzfristigen statistischen Ozonprognosen bei. Eine Verbesserung der Ozonprognosen ist daher erst mit dem Einsatz von chemischen Modellen zu erwarten.

Appendix

Appendix A

Description of system software

Two programmes were custom written for controlling the operation of the chemical amplifier (CA) and for converting the signal data into an RO_x signal. The control and data collection programme, `rox.exe`, is responsible for the CA operation, collection and averaging of the signal output, and saving the data to a data file. The second programme, `modsig.exe`, is used to extract the calibration data from the data file and to demodulate the CA output data.

A.1 Control and data collection programme: `rox.exe`

The programme `rox.exe` is written in Quick Basic, a compiled Basic version, for use under DOS on a 80386-based computer (or higher). A simplified version with reduced functionality (`286rox.exe`), was used temporarily during 1995 on a 80286 computer, but will not be described here.

The programme has a modular design, with separate modules controlling the input/output operations. This allows additional modules for other ADC and control cards to be added with only a minimum of change to the core programme. Modules for the Keithley ADC-16 16-bit ADC card, Meilhaus ME-26 12-bit ADC card and a Data Translation DT-2801A data collection unit have been tested. However, only the 16 bit ADC-16 proved suitable for use with the CA. Due to the large background signal, the 12 bit ADC did not have adequate resolution to differentiate between the two signal modes.

The basic function of the programme is outlined sequentially below:

- Programme details, including version number, are shown on the first screen.
- The programme allows the control system to be configured according to the current ADC settings and timing requirements. The configuration details are initially stored in an ASCII file named (`rox.cfg`) in the main directory (`c:\`). If this file is not found then the programme asks the operator for the required

```

                                Momentane Configuration ist wie folgt:

1. A/D Wandlerkarte: Keithley ADC-16
3. Kanalnummer für ROx-Eingang: 0
4. Kanalnummer für Gesamtfluss-Eingang: 1
5. Basisadresse der A/D-Wandlerkarte: 768
7. InputBereich: 3.2767
8. Software Gain: 1

9. Länge der Zyklus: 30
10. Wartezeit nach Ventilschaltung: 5
11. Delay nach Ventilschaltung: 5

12. Anzahl der Eichventile: 2

13. Default-Pfad für Datenspeicherung: \

Nummer der zu ändernden Item eingeben (0 zu verlassen): █
```

Figure A.1: Screen shot of the configuration screen of rox.exe. Settings for the ADC and timing can be altered here.

parameters (default settings can be chosen). The configuration screen is shown in Figure A.1¹. It allows the option of changing the settings, and if this option is taken a screen showing the current configuration appears and allows individual parameters to be changed.

- The address registers of the ADC to be used are initialised on the basis of the configuration parameters, as are the variables for controlling the input and output.
- The default address for the output file is then shown and the file name can be changed if desired. The default file name is “DDMMHHmm.rox”, where DD = date, MM = month, and HHmm is the start time in hour and minutes. The default path for the output data is stored in the configuration file. Data can also be stored on a second data carrier.
- The files are initialised, and a short pause allows an opportunity for the gas flows, peristaltic pump and PMT power supply to be checked.
- The programme commences the measurement cycle and data collection. Data is output to the monitor as well as being written to disk every half cycle to

¹The screen shots are currently all in German, as the CA was built under contract to the HLUG, a German public sector organisation.

avoid data loss during a power outage. A signal is sent to the valve controller in the inlet to switch the valve position every 30 seconds. Data continues to be collected for a few seconds after switching (as the influence of the changed gas flows do not reach the detector for around 5-6 seconds). Data collection is then interrupted for several seconds (default value is five seconds) to allow gas flows to stabilise. During this pause, the data is averaged and the result is written to disk together with the time and date, the valve settings (denoted by 0 or -1), the standard error in the mean, the number of data points used to obtain the average, and the flow rate of gas through the detector. Data collection is recommenced after an appropriate time interval. An example of the data output for one complete cycle for 1 July 1999 is as follows:

```
"07-01-1999 00:19:01 -1 +0.98899 +0.00082 251 +2.0201
07-01-1999 00:19:31 0 +0.99185 +0.00052 251 +2.0178"
```

- Every two hours the system runs an automated calibration procedure as described in Section 7.2.1. Switching of the CO and synthetic air flows at the inlet is interrupted during the calibration, and a signal is sent to the ACU to allow NO₂ containing air from two permeation tubes to either join the main gas flow to the detector or to be vented (see Section 7.2.1). This allows the CA to run through a series of 2ⁿ calibration points, where n is the number of permeation tubes used. Data is collected and written to disk as above. The start and end of the calibration is demarcated by a text to that effect in the output file. The valve setting is also stored to disk by saving the binary value stored in the register controlling the valves (values are -1 to -2ⁿ).
- The timer for the automated calibration procedure can be switched off at any stage by use of the function key "F5". Pressing "F5" a second time restarts the timer.
- The automated calibration procedure can be started at any time by using the function key "F4". This also restarts the timer.
- A new file is started at the end of each day, and at each new start. The new file name is selected according to the default settings.
- The programme can be stopped at any time by using the function key "F3". After double-checking that the programme should be ended, any remaining data is written to disk and the files are closed before control is returned to the operating system.

An entry in the "autoexec.bat" file ensures that the system starts automatically at each reboot, ensuring that the system restarts after a power outage. In such a case, the programme moves automatically through the startup procedure if there is no keyboard input for about one minute. This allows the system to restart even without operator input.

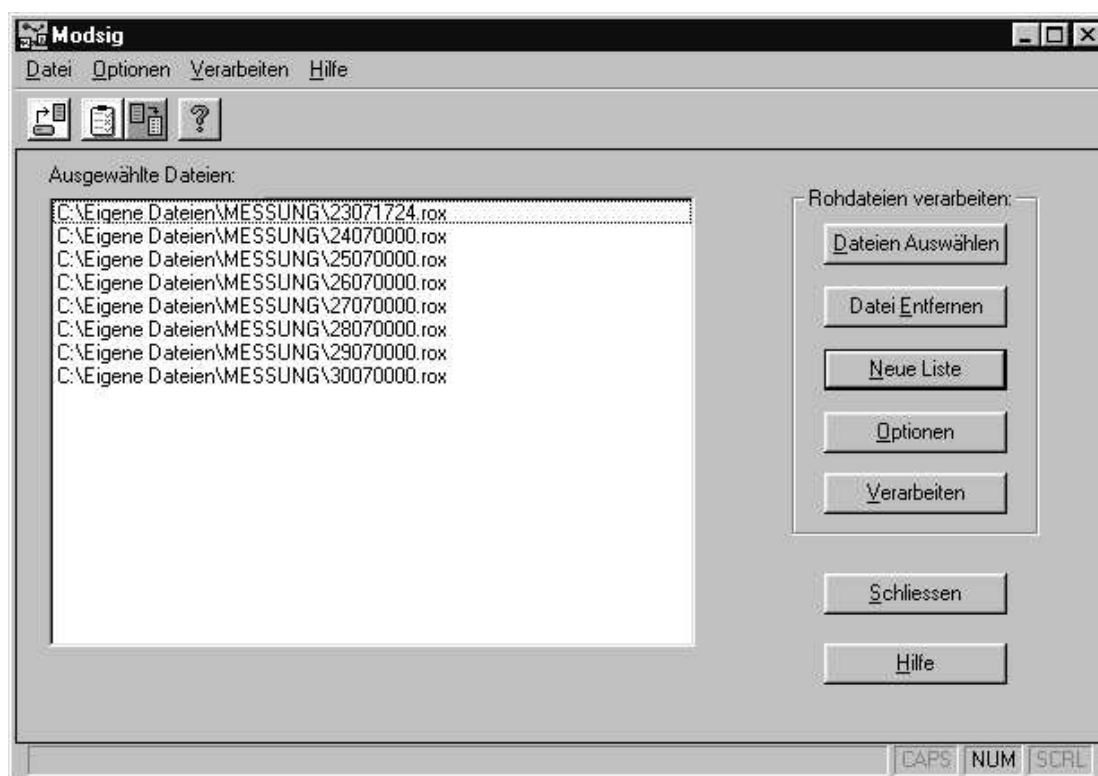


Figure A.2: Screen shot of the main window of `demod.exe`. Files can be selected (or deselected) and options changed by selecting the appropriate buttons.

A.2 Signal demodulation programme: `modsig.exe`

The programme for analysing the data file from the CA and demodulating the signal is written in C/C++ using Borland C/C++ Developer 5.0. It is designed for use under the Microsoft Windows 95 operating system (or higher) and uses the Object Windows Library 5 (OWL5) to provide the necessary Windows functionality.

The C++ extension to C is an object oriented programming (OOP) language and uses objects to represent both data and the windows used for the graphical user interface. Objects are implementations of classes and consist of both data elements and the associated methods to process the data. The programme has a modular design, whereby each of the classes is saved in a separate file. Some classes are used for processing the data, while others are concerned with implementation of the Windows interface. Table A.2 provides a list of the files and the functionality of the associated classes. Figure A.4 shows the classes used in the programme and their functional relationship to one another.

The programme's functions and features are as follows:

- The initial window of the programme contains a main text window and a series

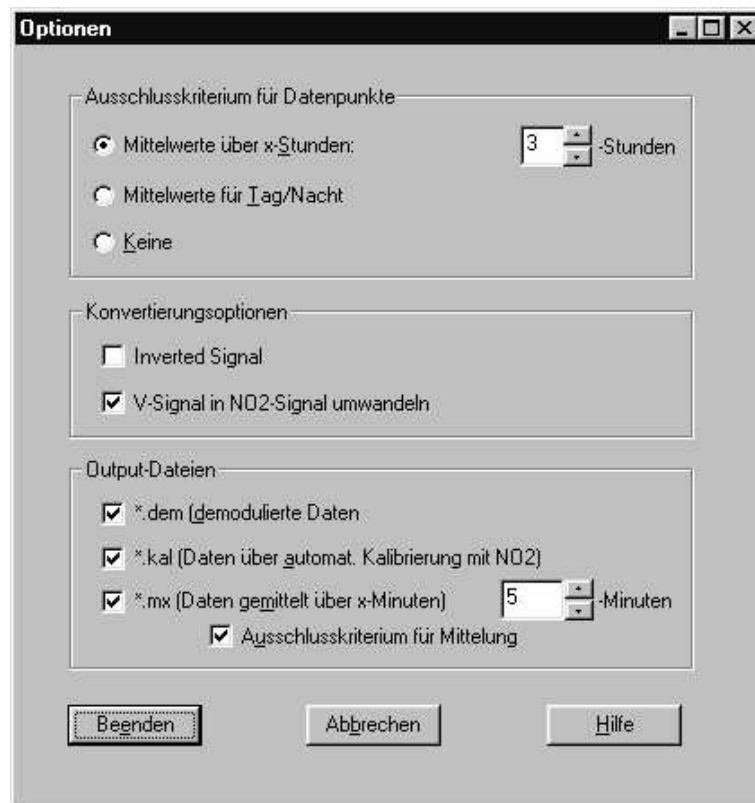


Figure A.3: Screen shot of the configuration window of `demod.exe`. The option for using an average over x hours as a rejection criteria has not yet been implemented.

of buttons allowing files to be added or removed from the list of files to be processed, the configuration options to be changed, and the processing procedure to be started. This window is shown in Figure A.2². The programme can also be ended from this window. If the selected files have not yet been processed, the operator is asked whether or not the programme is to be ended.

- The button labelled “Optionen” allows the programme configuration to be altered. Figure A.3 shows the configuration window. The current settings are shown when the window is initially opened. Options are selected by clicking on the appropriate item³.
- The rejection criterium (Ausschlusskriterium) is used to determine whether a data point is potentially an outlier due to an excessively noisy background signal, and whether or not it should be rejected. The average difference between successive background data points is calculated for the night-time or daytime

²The programme uses German for its text output, so that all screen shots are consequently also in German.

³The option allowing averages over several hours to be used as the basis for the rejection criterium has not yet been fully implemented.

period of interest. This is then used as a reference value for each data point. If the background difference for a given data point exceeds three times the average difference for the relevant time interval, then that data point is rejected.

- The option “inverted Signal” is provided to allow data files for which the inlet was incorrectly connected to be processed properly. In such cases the the background and amplified signals are reversed. This option allows the signal to be correctly demodulated by interpreting the valve settings appropriately.
- The demodulated data can be converted to an NO₂ concentration on the basis of the automated calibration data (option: “V-Signal in NO2-Signal umwandeln”).
- The output files for the processed data can also be selected: the demodulated data as one minute values (*.dem) and/or averaged over a prescribed time interval (*.m x , where x is the number of minutes), and the calibration data (*.kal). If the data is to be averaged over several minutes, then a further rejection criterium can also be selected. In this case, points which lie further than 5σ from the average day or night time concentration are rejected.
- The files to be processed can be selected by clicking the appropriate button from the main window. Multiple files can be selected in the order in which they are to be processed.
- The selected files are processed by clicking the appropriate button or menu item. A window showing the processing status is opened, and the processing procedure can then be started from this window. The file name of the file containing data on the permeation rates of the NO₂ sources is requested first. The calibration data is then interpreted using the permeation rates supplied by this file. The data files are then input sequentially and the calibration data is evaluated. After each stage of the analysis, the file name to be used for the corresponding output file is requested and the output is saved in an ASCII file.
- Data from the automated calibration procedure is marked in the file by the text ‘‘NO2-Eichung’’. When the programme detects this marker while reading data from the file, the following data points are read into an object containing a dynamic data structure for calibration data. This continues until the text marker ‘‘NO2-Eichung zur Ende’’ is encountered. Each data point is then associated with the appropriate NO₂ concentration and a linear fit is passed through the ensemble. The resulting parameters, slope and associated error of the linear fit, intercept and associated error, coefficient of determination (r^2), and its confidence limits are returned to the calling object, and, depending on the selected output options, written in an output file.
- The calibration data is smoothed using a weighted three point running mean before being used to convert the demodulated signal to an NO₂ signal. This is

to remove extreme values which may be due to changes in the NO₂ background during the calibration.

- Data from all the data files to be processed are read into a dynamic memory structure before demodulation. On the basis of the valve settings, the data points are identified as belonging to either background or measurement modes. The background mode points immediately before and after a given measurement mode point are averaged, and then subtracted from the respective data point. The resulting data point represents the demodulated data point. After the entire data set has been demodulated, the rejection criterium can be invoked to determine if any points should be rejected from the data set. The signal is then converted into an NO₂ signal, if required. The slope of the calibration line is used to convert the voltage signal into the equivalent mixing ratio of NO₂.
- The resulting data is then written in text files according to the selected output options.
- Control is returned to the main window after data processing is completed. Other files or configuration settings can then be selected and the procedure can then be repeated.

Table A.1: List of the project, resource and help files required for compiling `modsig.exe`. The project files contain details necessary for the administration of the project. The resource files contain the windows resources necessary for a Windows95 application. The help files contain the text and details necessary for the creation of a Windows help file.

File name	Description
PROJECT FILES	
<code>modsig.ide</code>	project details necessary for administration of the project, for compiling the executable file and for using the Borland Integrated Development Environment
<code>modsig.def</code>	definitions necessary for the Compiler
RESOURCE FILES	
<code>modsgapp.rc</code>	contains details of the resources required for compiling the Windows executable file.
<code>modsgapp.rh</code>	text file containing definitions of parameters necessary for compilation of the resources.
<code>help.cur</code>	help cursor
<code>help.bmp</code>	bitmap for the help button
<code>select.bmp</code>	bitmap for the select button

continued over...

<i>Continuation of Table A.1</i>	
File name	Description
options.bmp	bitmap for the options button
verarb.bmp	bitmap for the button to commence processing
modsig.ico	icon for the Windows application
HELP FILES	
modsig.hpj	main help file for the application. Contains the necessary details for compiling the help file.
mainhelp.rtf	source text for help file
toolbar.rtf	source text for help file
keys.rtf	source text for help file

Table A.2: List of the source text files required for compiling `modsig.exe`. The files contain code for the classes and the functionality of the classes associated with each file is described. The source text is contained in the `*.cpp` files, and declarations in the associated header files with suffix `*.h`.

File name	Class name	Description
modsgapp.cpp	TModsigApp	main application; initiates the setting up of the Windows environment, tool bars and help. Creates a TModsigDlgClient object.
modsgapp.h		

continued over...

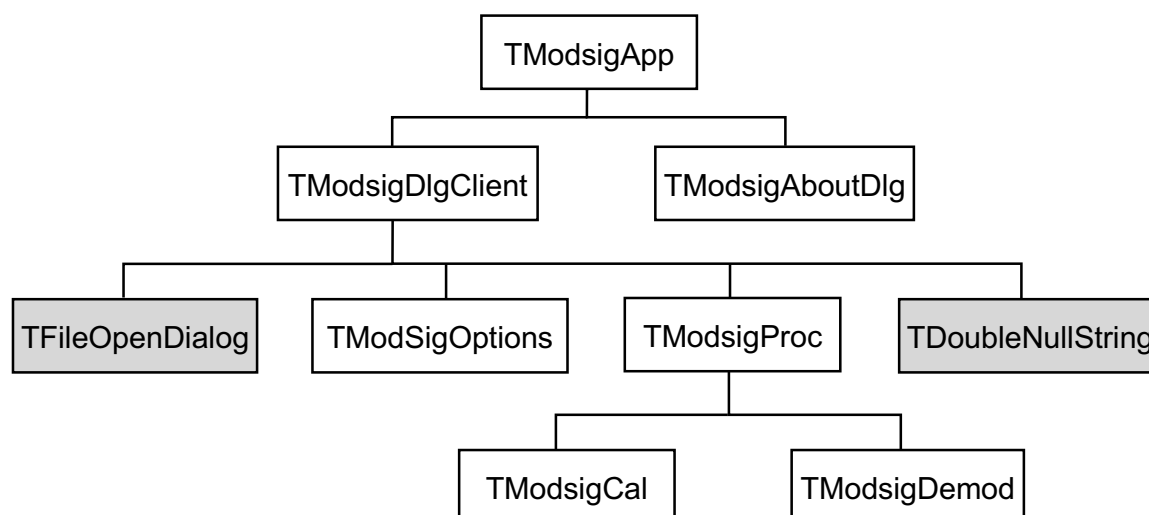


Figure A.4: Main classes used in `demod.exe` and their functional relationships. Additional classes necessary for the windows interface are not portrayed. Auxiliary classes used for inputting file names are shaded.

Continuation of Table A.2

File name	Class name	Description
modsgdlgc.cpp modsgdlgc.h	TModsigDlgClient	constructs and manages the main window (see Figure A.2); responds to commands. Keeps track of the options and the list of files to be processed.
mdsgoptn.cpp mdsgoptn.h	TModSigOptions	constructs and manages the options window (see Figure A.3), including changing the options. The options are passed as flags to the parent object (TModsigDlgClient) on destruction.
mdsgabtd.cpp mdsgabtd.h	TModsigAboutDlg	displays information about the programme. Called by the main TModsigApp object.
modsgprc.cpp modsgprc.h	TModsigProc	processes the file data and displays the progress in a separate window. Reads data from the necessary files and creates the appropriate objects for demodulation of the signal (ModsigDemod or analysis of the calibration data (ModsigCal. Controls the various steps in the demodulation and receives the data from ModsigDemod for output in files. Called by TModsigDlgClient.
modsgdem.cpp modsigdem.h	ModsigDemod	stores the signal data and carries out the processing of the data: demodulation, application of the rejection criteria, and conversion to a NO ₂ signal. Controlled by TModsigProc, to which it passes the processed data for storage. Called by TModsigProc.
modsgcal.cpp modsgcal.h korrel.cpp	ModsigCal	stores and processes the data from the automated calibration process. Data is passed to TModsigProc to allow conversion of the signal to an NO ₂ signal and output of the data in a file. Called by TModsigProc.

continued over...

Continuation of Table A.2

File name	Class name	Description
dzstring.cpp dzstring.h	TDoubleNullString	extracts multiple file names from the string returned by the file open dialogue. Called by TModsigDlgClient.
misc.cpp		text code for miscellaneous functions.
param.cpp		definitions for parameters used in calculations in the programme.

Appendix B

Data for 1998

This appendix presents graphically all meteorological parameters and the mixing ratios of total RO_x, O₃, NO_x, PAN and SO₂ for each of the summer months June to September, 1998, as measured on Kleiner Feldberg. The following table summarises the data sources. The relative humidity data from the HLUG were used in preference to the DWD data due to the closer proximity of the HLUG site to the measurement site for atmospheric components. Comparison of the two data series for RH showed a significant discrepancy between them, whereas for all other parameters the differences between data from the two data sources lay within measurement errors.

Table B.1: List of data sources for meteorological data and atmospheric component measurements. Parameters/components marked with a star were only used to fill gaps in the data series from another data source.

Data Source	Parameters/Components	Comments
DWD	air pressure, temperature, dew point temperature, wind direction and speed, precipitation, visibility	10 min. ave.
HLUG	total sunlight hours temperature*, relative humidity, wind direction*, wind speed*, global radiation, ozone, NO _y , SO ₂ *	Daily total 30 min. ave.
IMG	Actinic Flux (j_{O^1D}), j_{NO_2} , total RO _x , NO, NO ₂	10 min. ave., original data 1 min.
Met. Consult	PAN	One sample is taken every ten minutes.

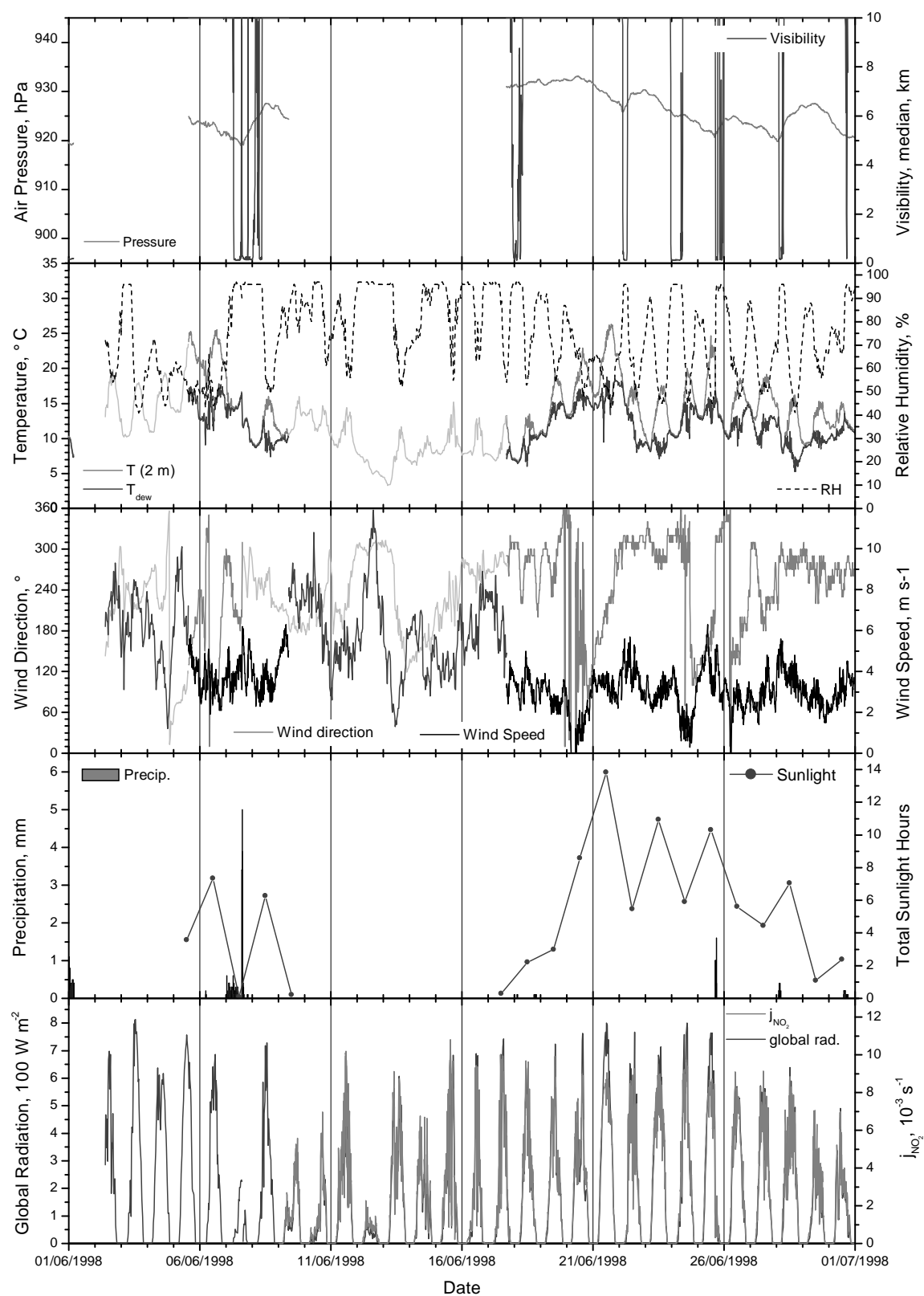


Figure B.1: Meteorological data for June, 1998, at Kleiner Feldberg.

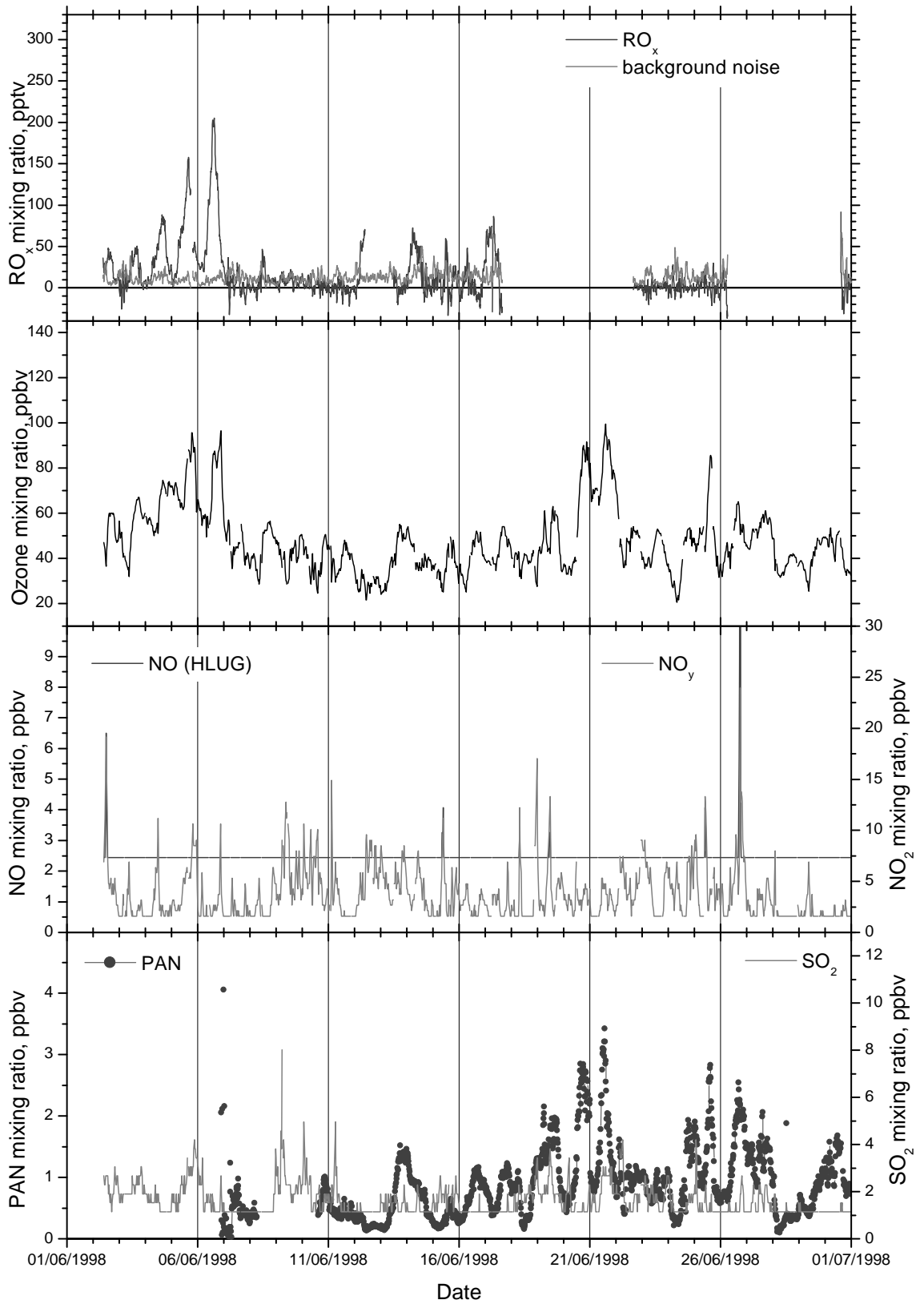


Figure B.2: Mixing ratios for measured components for June, 1998, at Kleiner Feldberg. Ozone, NO_x, and SO₂ data are 30 minute averages from the HLU network.

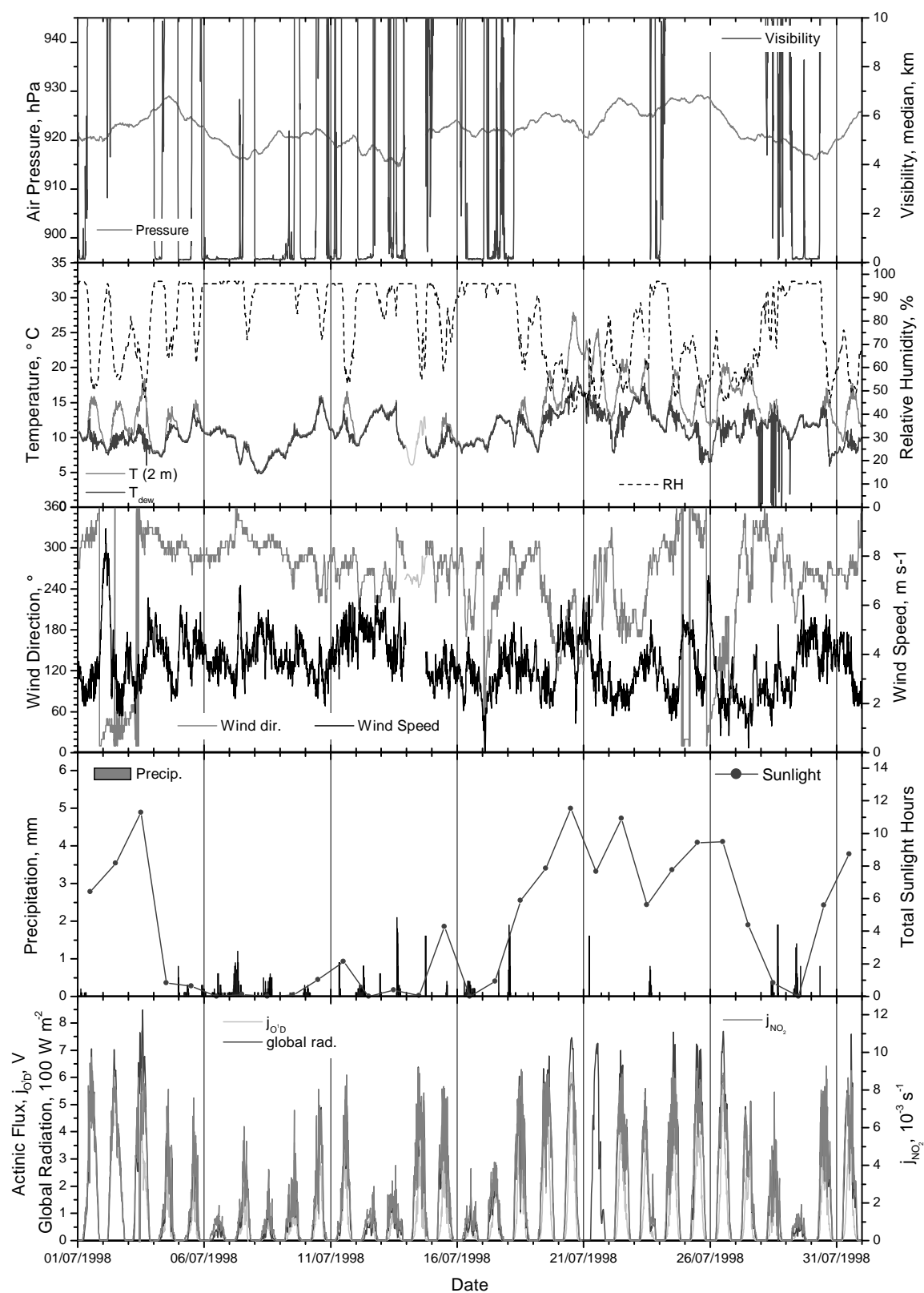


Figure B.3: Meteorological data for July, 1998, at Kleiner Feldberg.

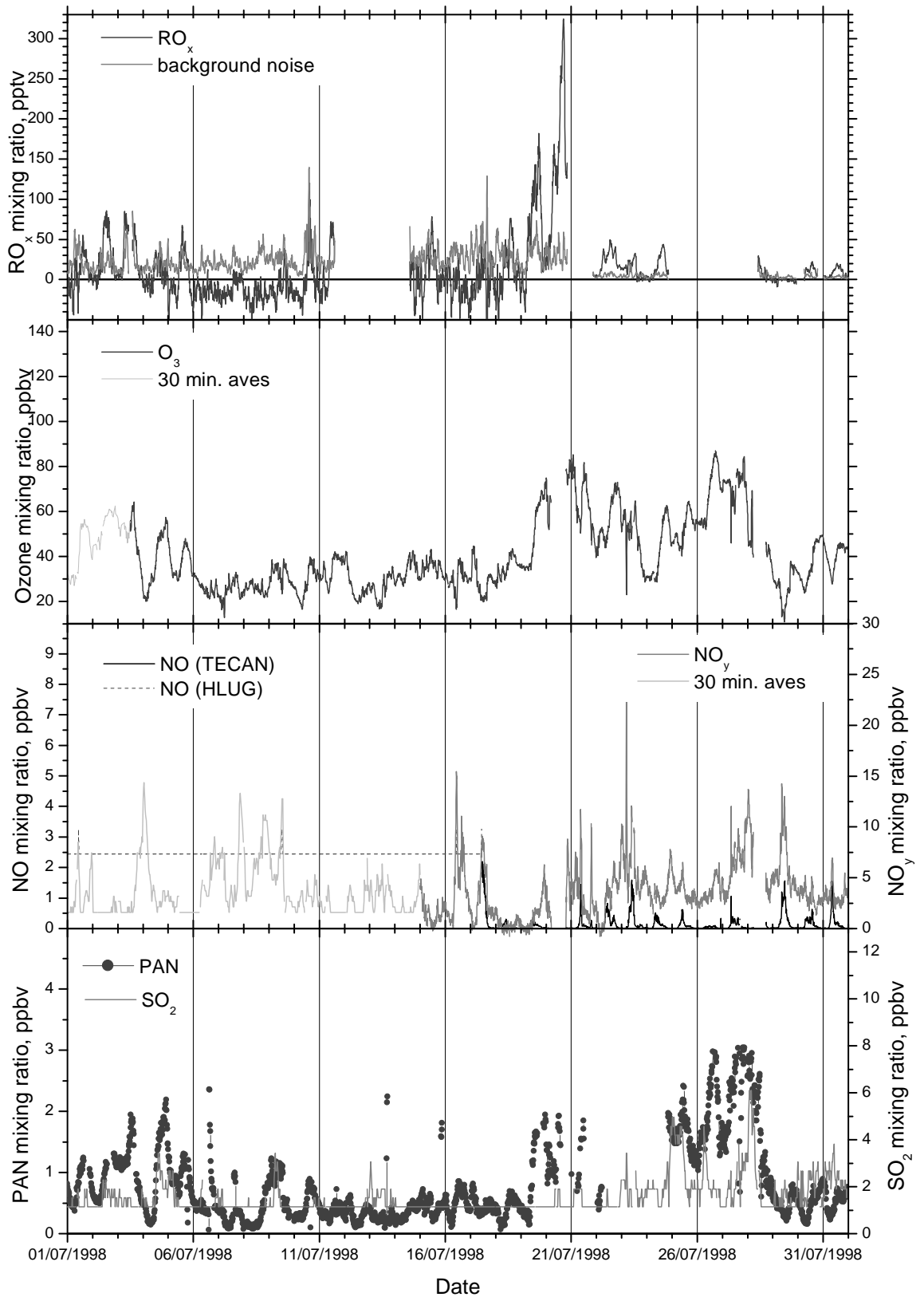


Figure B.4: Mixing ratios for measured components for July, 1998, at Kleiner Feldberg. Ozone (where indicated), NO_x (where indicated or identified as HLUG), and SO₂ data are 30 minute averages from the HLUG network.

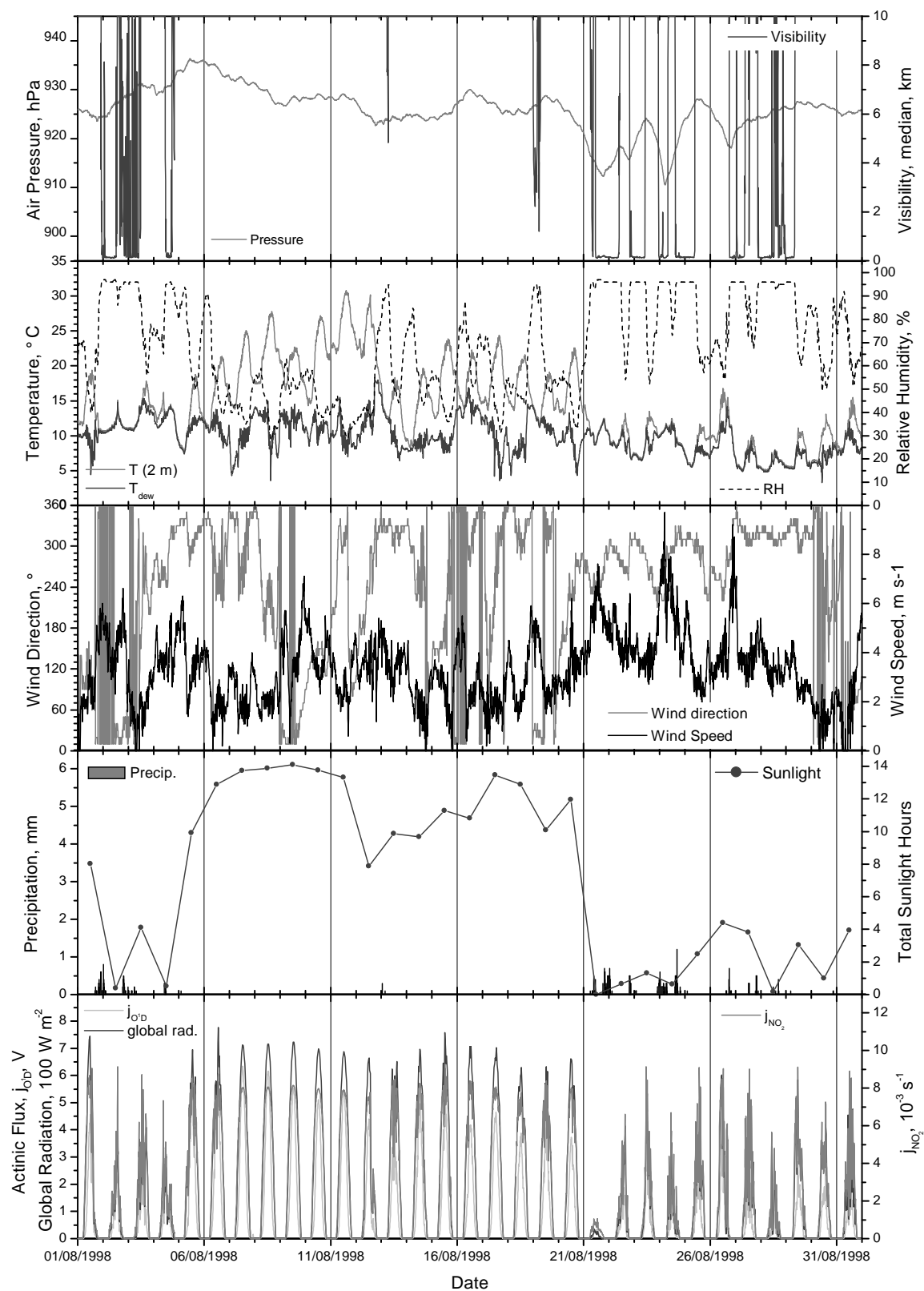


Figure B.5: Meteorological data for August, 1998, at Kleiner Feldberg.

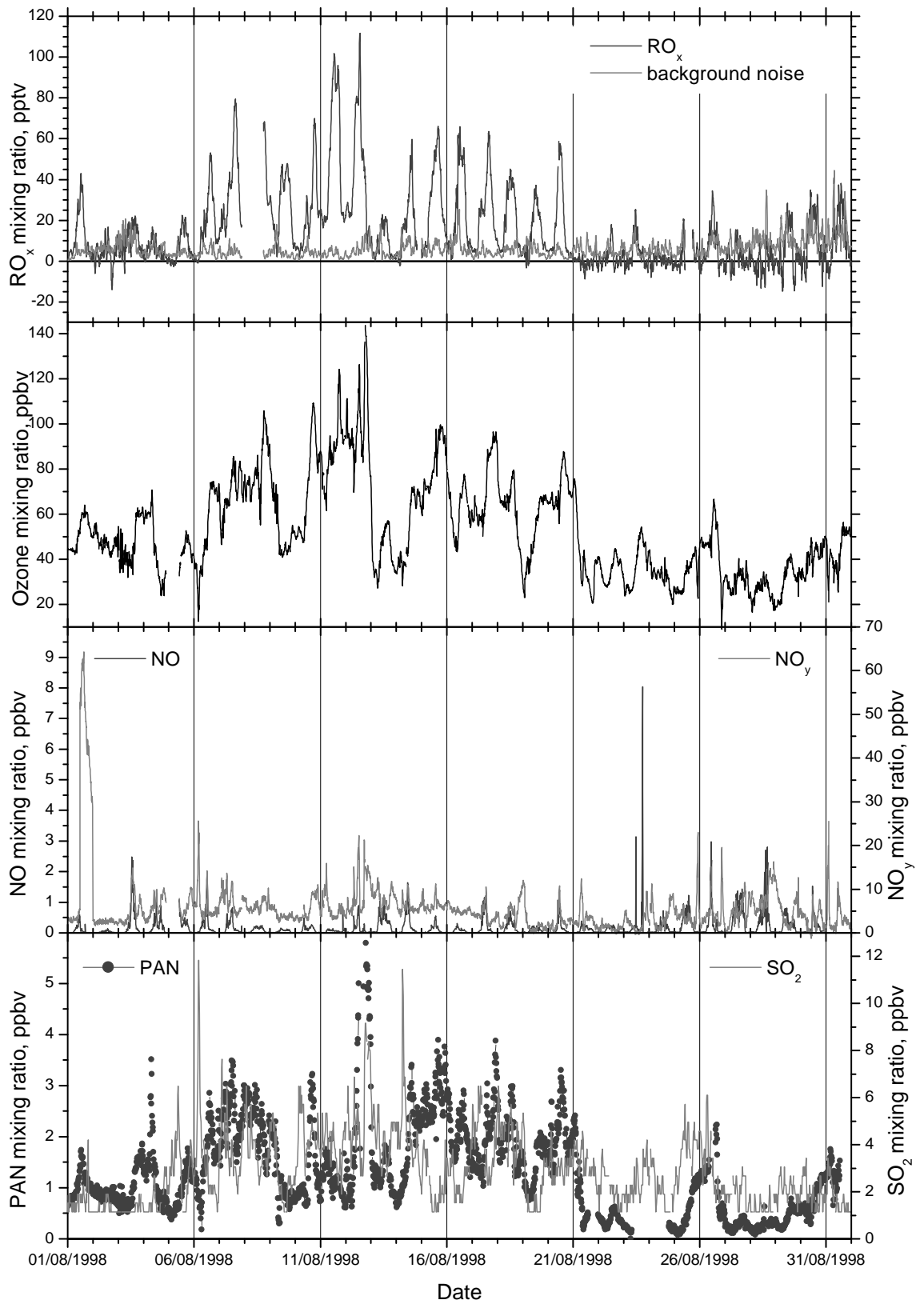


Figure B.6: Mixing ratios for measured components for August, 1998, at Kleiner Feldberg.

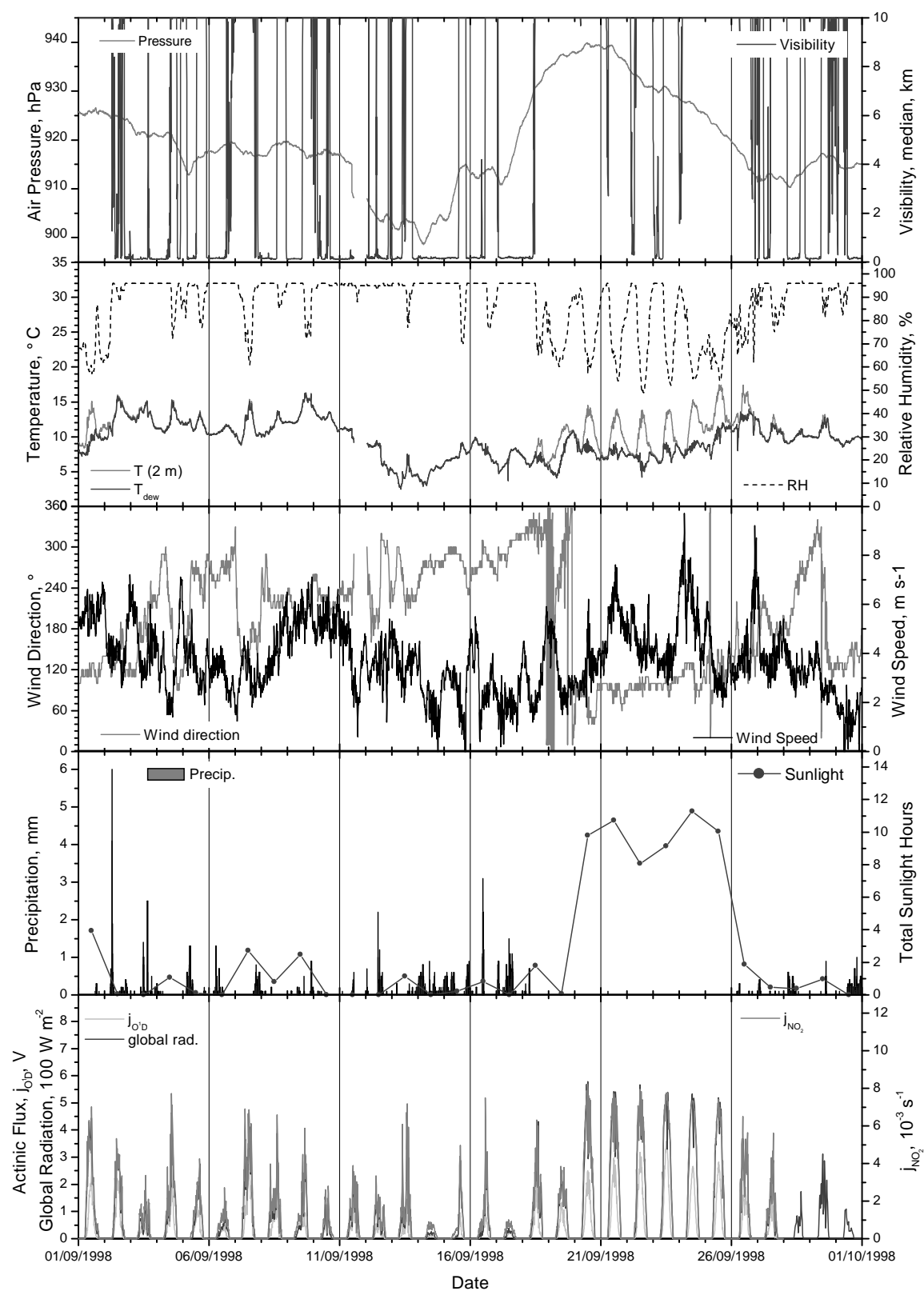


Figure B.7: Meteorological data for September, 1998, at Kleiner Feldberg.

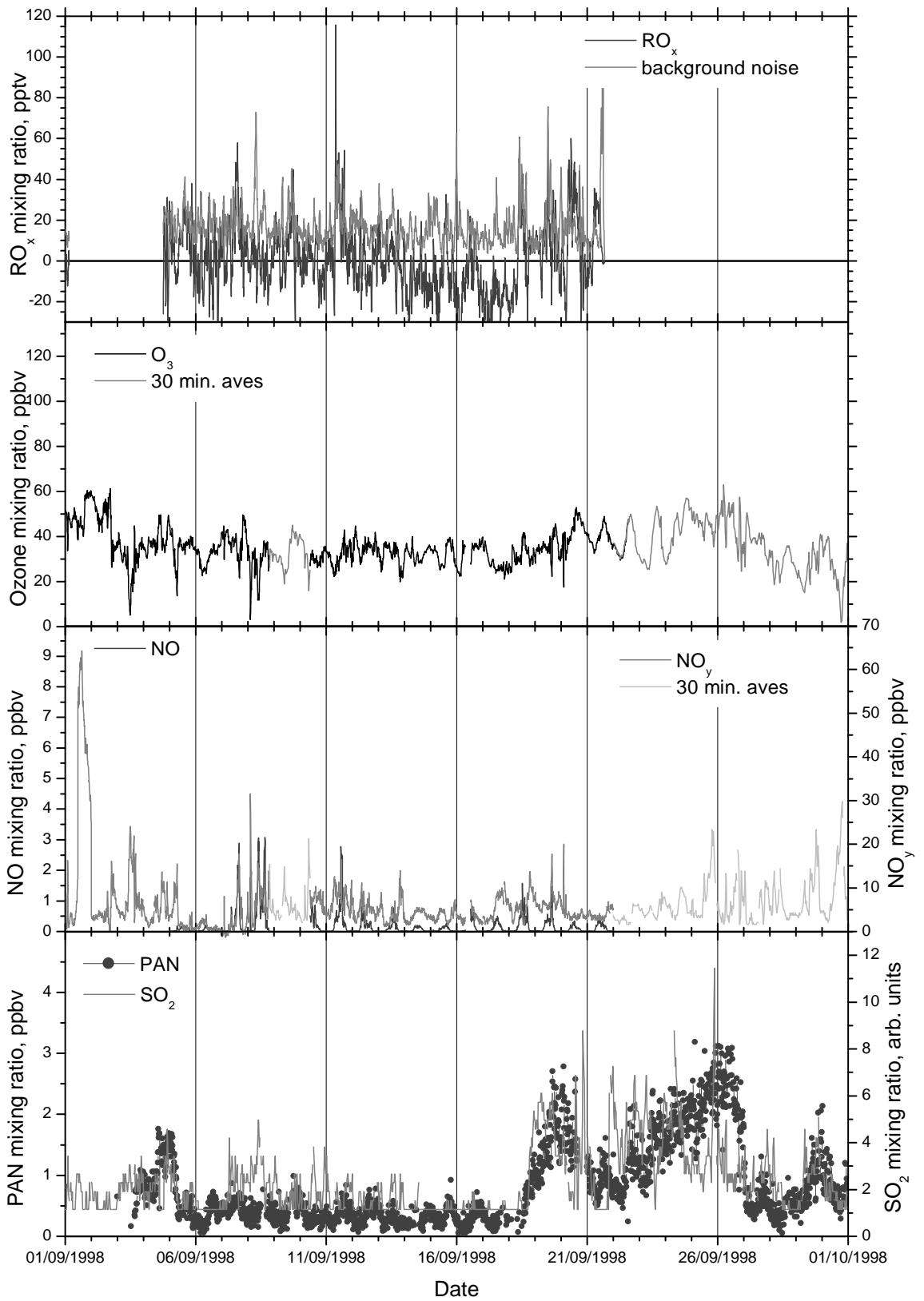


Figure B.8: Mixing ratios for measured components for September, 1998, at Kleiner Feldberg.

Appendix C

Data for 1999

This appendix presents graphically all meteorological parameters and the mixing ratios of total RO_x, O₃, NO_x, PAN and SO₂ for each of the summer months June to September, 1999, as measured on Kleiner Feldberg. The following table summarises the data sources. The relative humidity data from the HLUG were used in preference to the DWD data due to the closer proximity of the HLUG site to the measurement site for atmospheric components. Comparison of the two data series for RH showed a significant discrepancy between them, whereas for all other parameters the differences between data from the two data sources lay within measurement errors.

Table C.1: List of data sources for meteorological data and atmospheric component measurements. Parameters/components marked with a star were only used to fill gaps in the data series from another data source.

Data Source	Parameters/Components	Comments
DWD	air pressure, temperature, dew point temperature, wind direction and speed, precipitation, visibility	10 min. ave.
HLUG	total sunlight hours temperature*, relative humidity, wind direction*, wind speed*, global radiation, ozone, NO _y , SO ₂ *	Daily total 30 min. ave.
IMG	Actinic Flux (j_{O^1D}), j_{NO_2} , total RO _x , NO, NO ₂	10 min. ave., original data 1 min.
Met. Consult	PAN	One sample is taken every ten minutes.

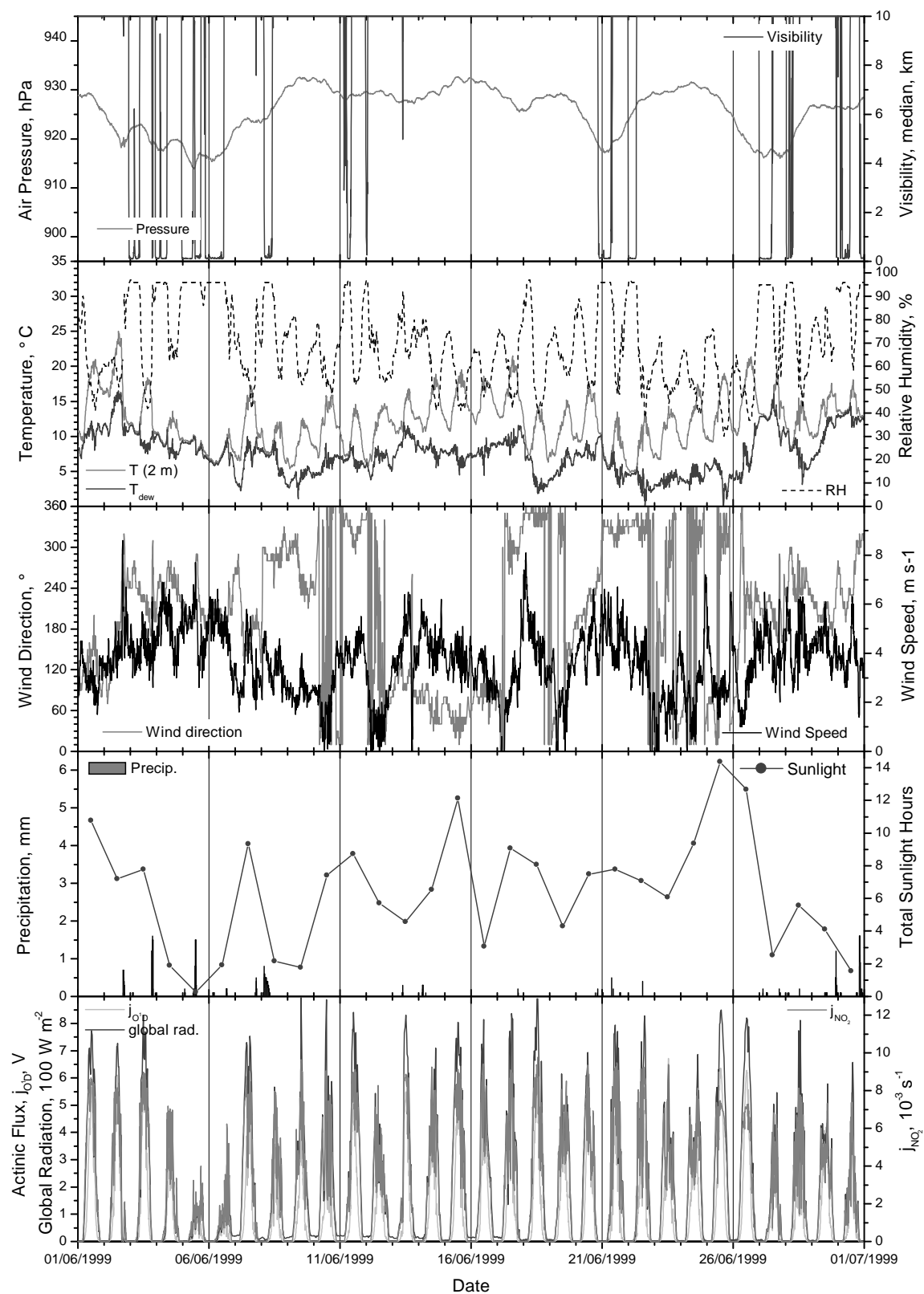


Figure C.1: Meteorological data for June, 1999, at Kleiner Feldberg.

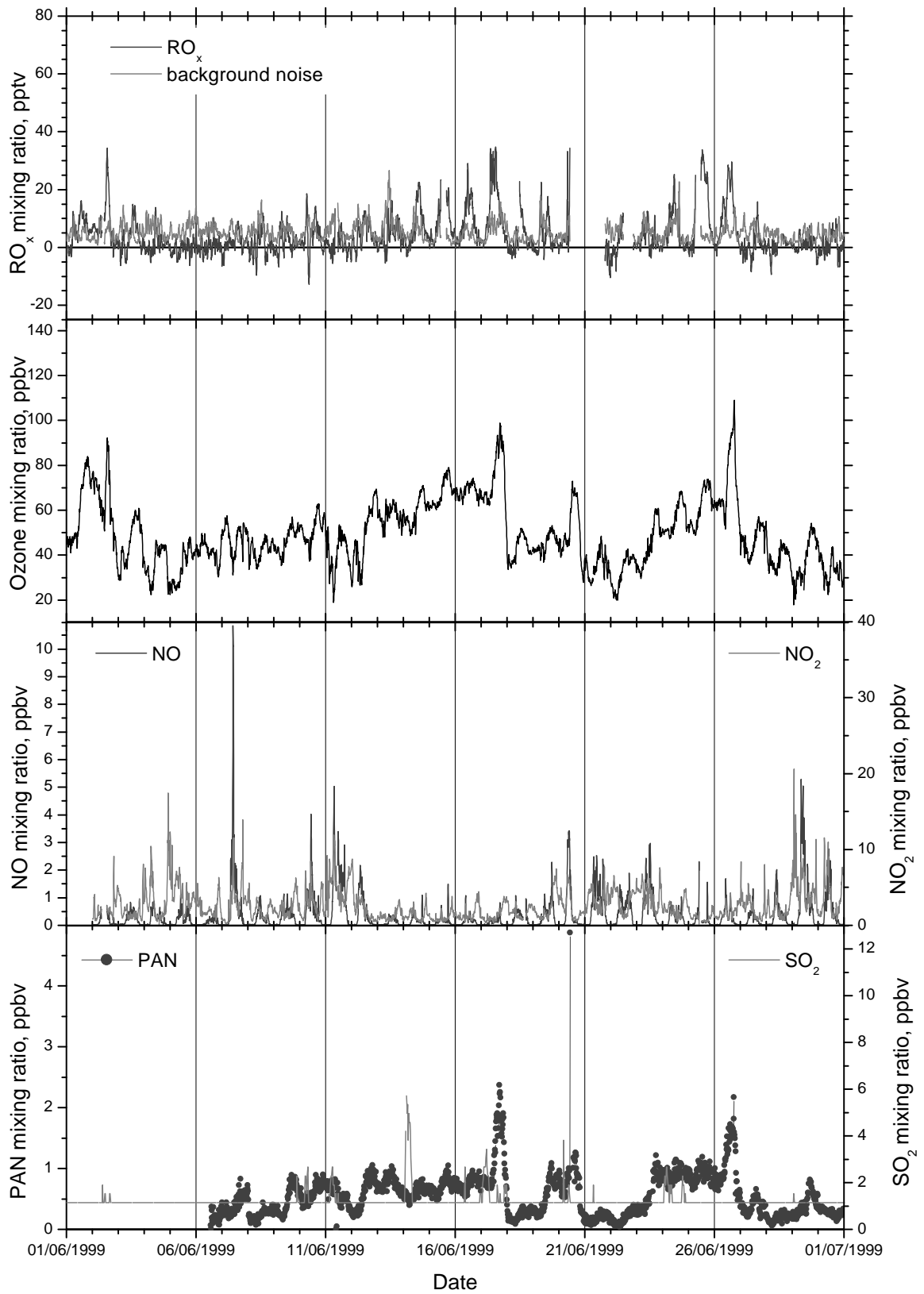


Figure C.2: Mixing ratios for measured components for June, 1999, at Kleiner Feldberg.

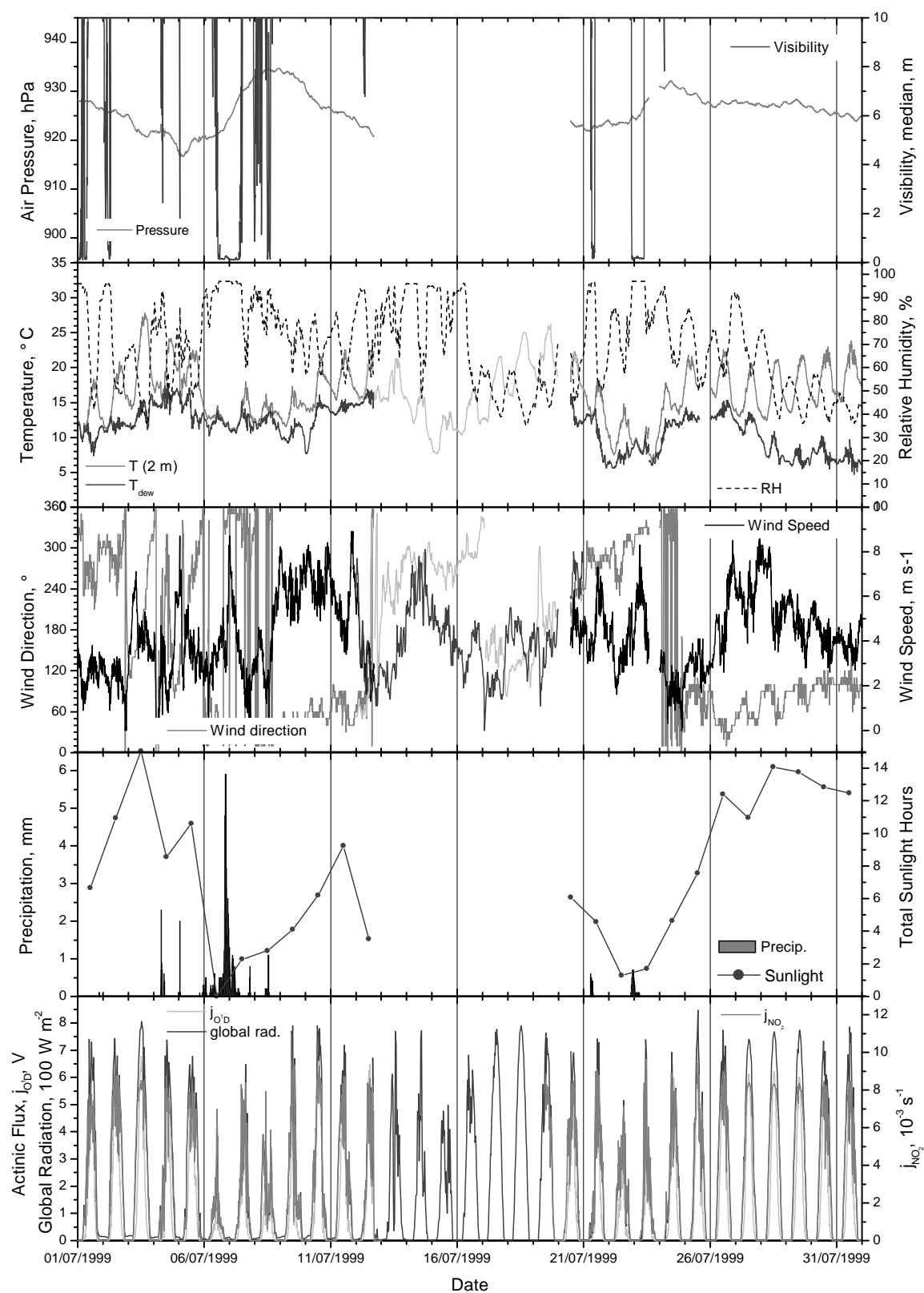


Figure C.3: Meteorological data for July, 1999, at Kleiner Feldberg.

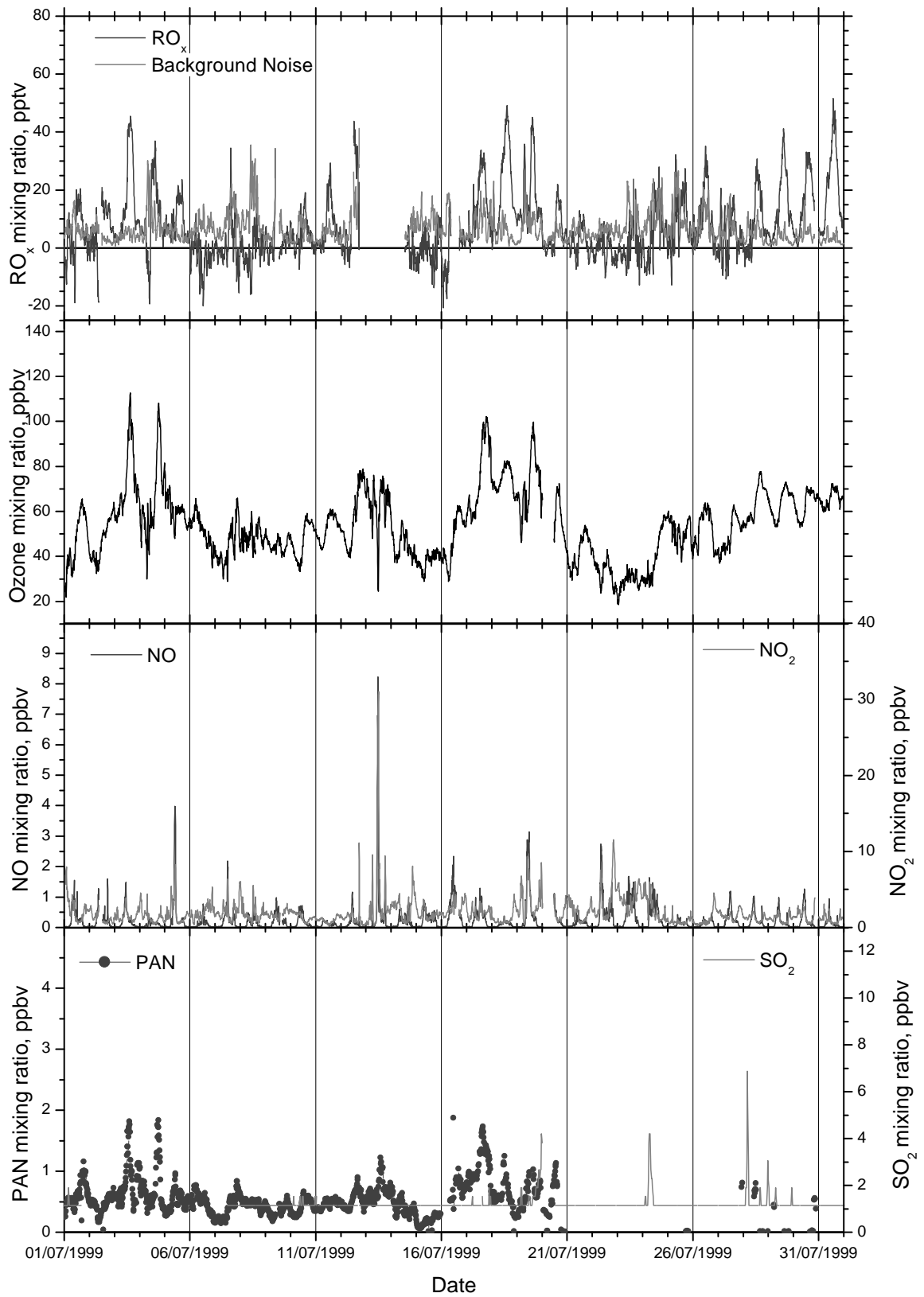


Figure C.4: Mixing ratios for measured components for July, 1999, at Kleiner Feldberg.

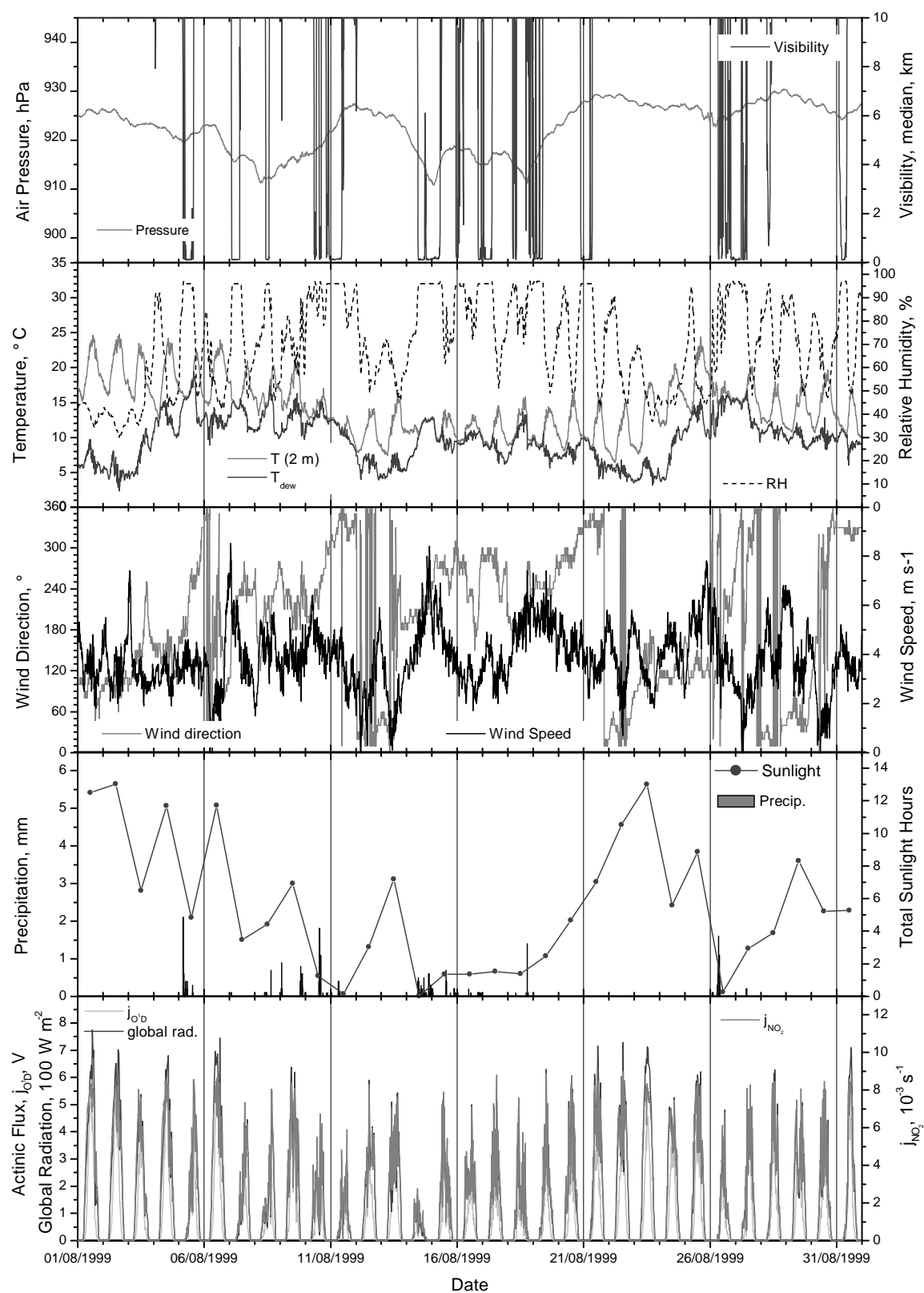


Figure C.5: Meteorological data for August, 1999, at Kleiner Feldberg.

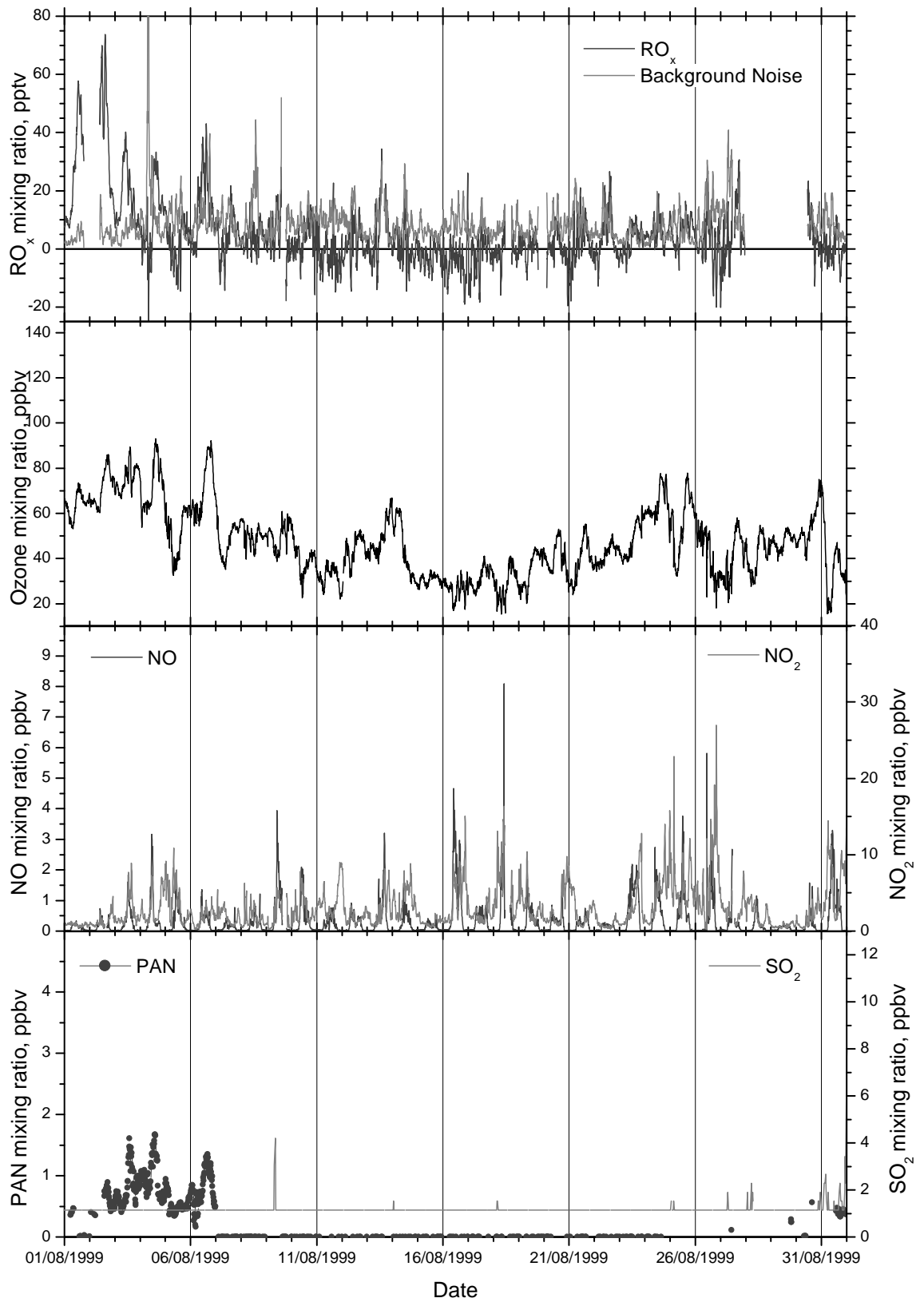


Figure C.6: Mixing ratios for measured components for August, 1999, at Kleiner Feldberg.

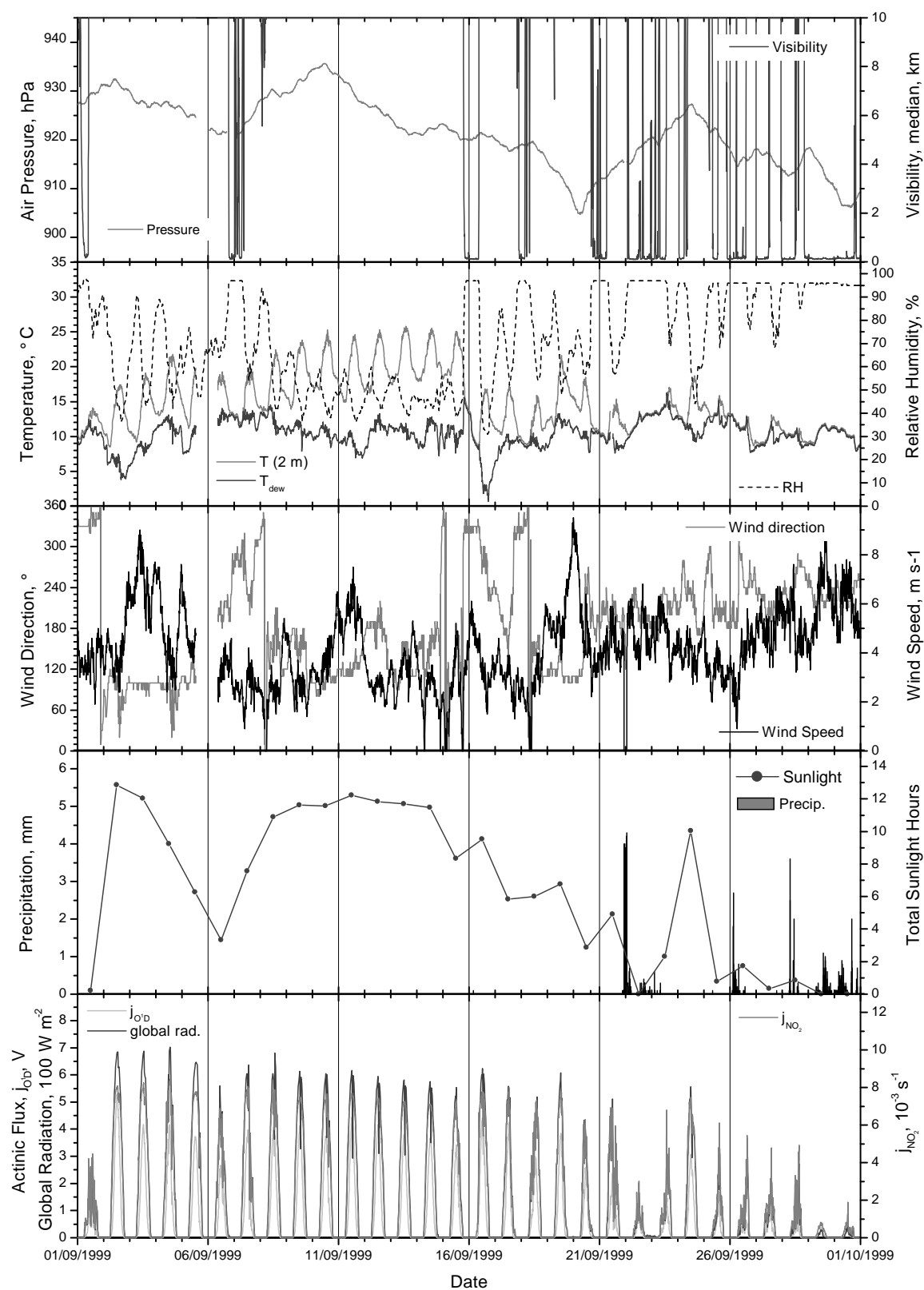


Figure C.7: Meteorological data for September, 1999, at Kleiner Feldberg.

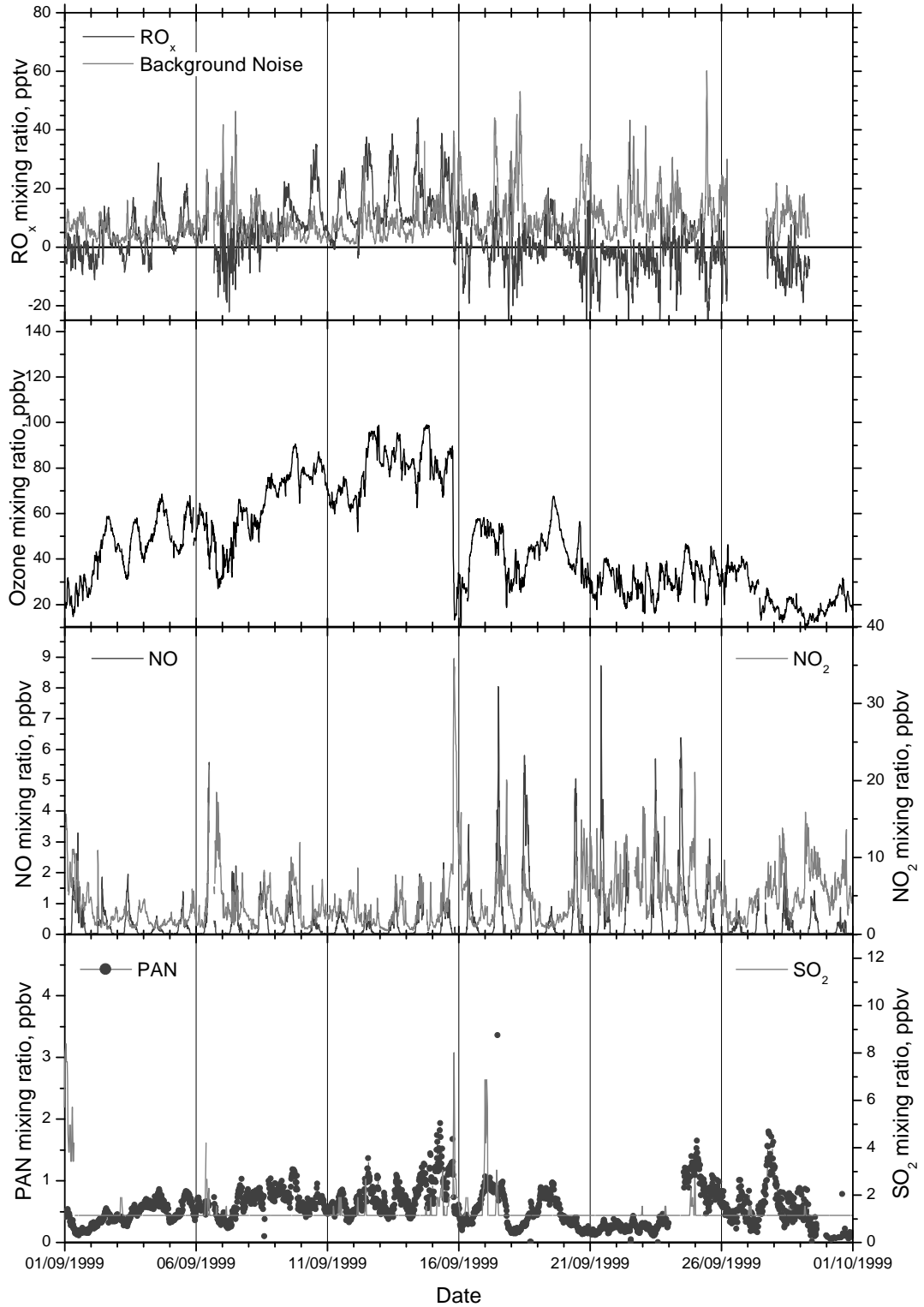


Figure C.8: Mixing ratios for measured components for September, 1999, at Kleiner Feldberg.

Appendix D

Steady State Model

D.1 OH Radical Balance

The reactions and rate coefficients included in the radical balance calculations for OH are shown here in Table D.1. All rate coefficients except those for the measured VOCs are shown in the table. The rate coefficients for the oxidation of NMHCs by OH were selected by *Christian Plass-Dülmer* of MOHp from the NIST tables and are listed in Table D.3. The primary production rate of ozone (denoted $P(OH)$, No. 3 in the table) was calculated using the measured photolysis rate of O_3 , j_{O^1D} . The photolysis rate for H_2O_2 were calculated using the STAR model [*Schwander et al.*, 2001].

Assuming that the OH radical is in steady state, then the rate of change of the OH concentration is nearly zero:

$$\frac{dOH}{dt} \approx 0 = P_{OH} - L_{OH} \quad (D.1)$$

$$\Rightarrow P_{OH} = L_{OH} \quad (D.2)$$

The production and loss rates are then equal to the reaction rates for the reactions listed in Table D.1:

$$\begin{aligned} k_1[HO_2][NO] + k_2[HO_2][O_3] + P(OH) + 2 \cdot j(H_2O_2) = \\ [OH] \left\{ \sum k_{a_i}[NMHC]_i + k_b[CH_4] + k_c[HCHO] + \right. \\ \left. k_d[CO] + k_e[H_2] + k_f[NO_2] + k_g[H_2O_2] \right\} \quad (D.3) \end{aligned}$$

The equation can then be rearranged to solve for the concentration of OH:

$$[OH] = \frac{k_1[HO_2][NO] + k_2[HO_2][O_3] + P(OH) + 2 \cdot j(H_2O_2)}{\sum k_{a_i}[NMHC]_i + k_b[CH_4] + k_c[HCHO] + k_d[CO] + k_e[H_2] + k_f[NO_2] + k_g[H_2O_2]} \quad (D.4)$$

The OH concentration was then calculated for the time of each NMHC measurement. The assumption was made that HO_2 and RO_2 were present in equal quantities. This is

consistent with daytime measurements using MIESR in a number of field campaigns [e.g., *Mihelcic et al.*, 1993, 2001]. This allowed the HO_2 concentration to be obtained from the measured RO_x concentration as the concentration of OH is a factor of 100 less than that of HO_2 , i.e. that

$$[HO_2] = 0.5[RO_2] \quad (D.5)$$

$$= 0.5[RO_x]_{measured} \quad \text{if } [OH] \ll [HO_2] \quad (D.6)$$

The resulting OH concentration is compared with measurements and discussed in section 11.2.

Table D.1: Summary of the reactions and rate coefficients used in the steady state calculation of the OH concentration.

No.	Reaction	k(298) cm ³ molecule ⁻¹ s ⁻¹	Ref.
SOURCES			
1.	$HO_2 + NO \longrightarrow OH + NO_2$	8.3×10^{-12}	[1]
2.	$HO_2 + O_3 \longrightarrow OH + 2.O_2$	2.0×10^{-15}	[1]
3.	$O_3 + h\nu \xrightarrow{H_2O} 2OH + O_2$	measured ^a	
4.	$H_2O_2 + h\nu \longrightarrow 2.OH$	STAR Model	
SINKS			
a.	$OH + NMHC \longrightarrow R + H_2O$	various ^b	
b.	$OH + CH_4 \longrightarrow H_2O + CH_3$	6.4×10^{-15}	[2]
c.	$OH + HCHO \longrightarrow H_2O + HCO$	9.2×10^{-12}	[2]
d.	$OH + CO \longrightarrow CO_2 + H$	2.0×10^{-13}	[2]
e.	$OH + H_2 \longrightarrow H_2O + H$	6.7×10^{-15}	[1]
f.	$OH + NO_2 \xrightarrow{M} HNO_3$	1.2×10^{-11}	[2] ^c
g.	$OH + H_2O_2 \longrightarrow H_2O + HO_2$	1.7×10^{-12}	[1]

^aPrimary production of OH; denoted P(OH)

^bsee Table D.3

^cThe termolecular reaction rate coefficients for this reaction were converted to a bimolecular rate coefficient for conditions of P = 910 hPa and T = 293 K using the recommended Troe expression. The Troe expression must be corrected by replacing the factor 0.6 by the revised factor of $F_c=0.41$ from [1].

References: [1] *Atkinson* [1997a]; [2] *Atkinson et al.* [1999]; [3] *Sander et al.* [2000]

D.2 RO_x radical balance

The reactions and rate coefficients included in the radical balance calculations for RO₂ are shown here in Table D.2. All rate coefficients except those for the measured VOCs are shown in the table. The rate constants for the oxidation of NMHCs by OH were selected by *Christian Plass-Dülmer* of MOHp from the NIST tables and are listed in Table D.3.

For this calculation, it was assumed that HO₂ and RO₂ are present in equal proportions, as above. The procedure is then analogous to that for OH. The sources and sinks of HO₂ are balanced using the reaction rates listed in Table D.2:

$$\begin{aligned}
 [OH] \left\{ \sum k_{a_i} [NMHC]_i + k_b [CH_4] + \right. \\
 \left. k_c [HCHO] + k_d [CO] + k_e [H_2] + k_g [H_2O_2] \right\} = \\
 k_1 [HO_2] [NO] + k_2 [HO_2] [O_3] + k_5 [HO_2]^2 + k_6 [HO_2] [RO_2]
 \end{aligned} \quad (D.7)$$

in which RO₂ is assumed to be entirely CH₃O₂, and [RO₂] is equal to [HO₂], as discussed above. Due to the reactions between the peroxy radicals, this results in a quadratic reaction in HO₂:

$$\begin{aligned}
 (k_5 + k_6) [HO_2]^2 + (k_1 [NO] + k_2 [O_3]) [HO_2] + \\
 [OH] \left\{ \sum k_{a_i} [NMHC]_i + k_b [CH_4] + k_c [HCHO] + \right. \\
 \left. k_d [CO] + k_e [H_2] + k_g [H_2O_2] \right\} = 0 \quad (D.8)
 \end{aligned}$$

This was solved for HO₂ using the standard equation for calculating the roots of a quadratic function:

$$[HO_2] = \frac{-b \pm \sqrt{b^2 - 4ac}}{2a} \quad (D.9)$$

where

$$a = k_5 + k_6$$

$$b = k_1 [NO] + k_2 [O_3]$$

$$c = [OH] \left\{ \sum k_{a_i} [NMHC]_i + k_b [CH_4] + k_c [HCHO] + k_d [CO] + k_e [H_2] + k_g [H_2O_2] \right\}$$

The HO₂ concentration was then calculated using the measured values for the time of each NMHC measurement. The equivalent RO₂ concentration is twice the HO₂ concentration. The resulting RO_x concentration is compared with measurements and discussed in section 11.2.

Table D.2: Summary of the reactions and rate coefficients used in the steady state calculation of the RO_x concentration.

Label	Reaction	$k(298)$ $\text{cm}^3 \text{ molecule}^{-1} \text{ s}^{-1}$	Ref.
SOURCES			
a.	$OH + NMHC \xrightarrow{O_2} RO_2 + H_2O$	various ^a	
b.	$OH + CH_4 \xrightarrow{O_2} CH_3O_2 + H_2O$	6.4×10^{-15}	[2]
c.	$OH + HCHO \longrightarrow H_2O + HCO$	9.2×10^{-12}	[2]
d.	$OH + CO \xrightarrow{O_2} HO_2 + CO_2$	2.0×10^{-13}	[2]
e.	$OH + H_2 \xrightarrow{O_2} HO_2 + H_2O$	6.7×10^{-15}	[1]
g.	$OH + H_2O_2 \longrightarrow H_2O + HO_2$	1.7×10^{-12}	[1]
SINKS			
1.	$HO_2 + NO \longrightarrow OH + NO_2$	8.3×10^{-12}	[1]
2.	$HO_2 + O_3 \longrightarrow OH + 2.O_2$	2.0×10^{-15}	[1]
5.	$HO_2 + HO_2 \longrightarrow H_2O_2 + O_2$	1.6×10^{-12}	[1]
6.	$HO_2 + CH_3O_2 \longrightarrow CH_3OOH + O_2$	5.2×10^{-12}	[2]

^asee Table D.3

References: [1] Atkinson [1997a]; [2] Atkinson et al. [1999]; [3] Sander et al. [2000]

Table D.3: Reaction coefficients for the OH oxidation of the VOCs measured during the measurement campaign at MOHp. Data are from the NIST tables, and were selected by Christian Plass-Dülmer, MOHp.

Substance Name	Formula	Mol. Weight	$k_{OH}(298K)$ $\text{cm}^3 \text{ molecule}^{-1} \text{ s}^{-1}$
ethane	C ₂ H ₆	30.07	2.6×10^{-13}
ethene	C ₂ H ₄	28.05	8.5×10^{-12}
ethyne	C ₂ H ₂	26.04	9.0×10^{-13}
propane	C ₃ H ₈	44.1	1.1×10^{-12}
propene	C ₃ H ₆	42.08	2.6×10^{-11}
propyne	C ₃ H ₄	40.07	5.9×10^{-12}
2-methylpropane	C ₄ H ₁₀	58.12	2.2×10^{-12}
n-butane	C ₄ H ₁₀	58.12	2.4×10^{-12}
trans-2-butene	C ₄ H ₈	56.11	6.4×10^{-11}
1-butene	C ₄ H ₈	56.11	3.1×10^{-11}
2-methylpropene	C ₄ H ₈	56.11	5.1×10^{-11}
cis-2-butene	C ₄ H ₈	56.11	5.6×10^{-11}
1,3-butadiene	C ₄ H ₆	54.09	6.7×10^{-11}
2-methylbutane	C ₅ H ₁₂	72.15	3.7×10^{-12}
n-pentane	C ₅ H ₁₂	72.15	4.0×10^{-12}
cyclopentane	C ₅ H ₁₀	70.14	5.0×10^{-12}
trans-2-pentene	C ₅ H ₁₀	70.14	6.7×10^{-11}
1-pentene	C ₅ H ₁₀	70.14	3.1×10^{-11}
cis-2-pentene	C ₅ H ₁₀	70.14	6.5×10^{-11}
2-methyl-1,3-butadiene	C ₅ H ₈	68.12	1.0×10^{-10}
n-hexane	C ₆ H ₁₄	86.18	5.5×10^{-12}
2-methylpentane	C ₆ H ₁₄	86.18	5.3×10^{-12}
3-methylpentane	C ₆ H ₁₄	86.18	5.4×10^{-12}
2,3-dimethylbutane	C ₆ H ₁₄	86.18	5.8×10^{-12}
methylcyclopentane	C ₆ H ₁₂	84.16	6.8×10^{-12}
cyclohexane	C ₆ H ₁₂	84.16	7.2×10^{-12}
1-hexene	C ₆ H ₁₂	84.16	3.7×10^{-11}
benzene	C ₆ H ₆	78.11	1.2×10^{-12}
2-methylhexane	C ₇ H ₁₆	100.21	5.1×10^{-12}
2,3-dimethylpentane	C ₇ H ₁₆	100.21	6.1×10^{-12}
n-heptane	C ₇ H ₁₆	100.21	7.0×10^{-12}
methylcyclohexane	C ₇ H ₁₄	98.19	1.0×10^{-11}
toluene	C ₇ H ₈	92.14	6.0×10^{-12}
n-octane	C ₈ H ₁₈	114.23	8.7×10^{-12}
3-methylheptane	C ₈ H ₁₈	114.23	8.6×10^{-12}

continued over...

Continuation of Table D.3

Substance Name	Formula	Mol. Weight	$k_{OH}(298K)$ $\text{cm}^3 \text{ molecule}^{-1} \text{ s}^{-1}$
4-methylheptane	C_8H_{18}	114.23	8.6×10^{-12}
ethylbenzene	C_8H_{10}	106.17	7.1×10^{-12}
m,p-xylene	C_8H_{10}	106.17	1.9×10^{-11}
o-xylene	C_8H_{10}	106.17	1.4×10^{-11}
n-nonane	C_9H_{20}	128.26	1.1×10^{-11}
n-propylbenzene	C_9H_{12}	120.2	5.7×10^{-12}
1,3,5-trimethylbenzene	C_9H_{12}	120.2	5.8×10^{-11}
1,2,4-trimethylbenzene	C_9H_{12}	120.2	3.8×10^{-11}
m-ethyltoluene	C_9H_{12}	120.2	1.7×10^{-11}
p-ethyltoluene	C_9H_{12}	120.2	1.1×10^{-11}
α -pinene	$\text{C}_{10}\text{H}_{16}$	136.24	5.4×10^{-11}
β -pinene	$\text{C}_{10}\text{H}_{16}$	136.24	7.9×10^{-11}
camphene	$\text{C}_{10}\text{H}_{16}$	136.24	5.3×10^{-11}
sabinene	$\text{C}_{10}\text{H}_{16}$	136.24	1.2×10^{-10}
myrcene	$\text{C}_{10}\text{H}_{16}$	136.24	2.2×10^{-10}
3-carene	$\text{C}_{10}\text{H}_{16}$	136.24	8.8×10^{-11}
α -terpinene	$\text{C}_{10}\text{H}_{16}$	136.24	2.3×10^{-10}
terpinolene		136.24	2.2×10^{-10}
γ -terpinene	$\text{C}_{10}\text{H}_{16}$	136.24	1.8×10^{-10}
limonene	$\text{C}_{10}\text{H}_{16}$	136.24	1.7×10^{-10}
i-butylbenzene	$\text{C}_{10}\text{H}_{14}$	134.22	8.2×10^{-12}
sec-butylbenzene	$\text{C}_{10}\text{H}_{14}$	134.22	8.2×10^{-12}
p-cymene	$\text{C}_{10}\text{H}_{14}$	134.21	1.5×10^{-11}
1-methyl-3-propylbenzene	$\text{C}_{10}\text{H}_{14}$	134.22	1.47×10^{-11}
1,8-cineol	$\text{C}_{10}\text{H}_{18}\text{O}$	154.24	1.1×10^{-11}
n-undecane	$\text{C}_{11}\text{H}_{24}$	156.31	1.3×10^{-11}
n-dodecane	$\text{C}_{12}\text{H}_{26}$	170.34	1.4×10^{-11}
n-tridecane	$\text{C}_{13}\text{H}_{28}$	184.37	1.6×10^{-11}
tricyclene			5.4×10^{-11}

List of Figures

1.1	Modelled maximum ozone for Halle, Germany	6
2.1	Ozone chemistry in the clean troposphere	18
2.2	Ozone chemistry in the polluted atmosphere	22
2.3	Chemical oxidation cycle leading to ozone production	24
3.1	Sources and sinks of peroxy radicals	28
4.1	Planetary boundary layer	42
4.2	Vertical ozone profiles.	43
6.1	Schematic representation of the peroxy radical chemical amplifier	56
6.2	Chain reaction chemistry in the CA inlet	57
6.3	Measured signal output from the CA for a fine weather period	60
6.4	Schematic representation of the CA modulation cycle	61
6.5	Fractional yield of HO ₂ for a series of RO ₂ radicals	65
6.6	Plot of the effect of water vapour on CL	68
7.1	Schematic representation of the chemical amplifier	72
7.2	Schematic representation of the CA inlet	75
7.3	Schematic representation of the NO ₂ detector	76
7.4	Typical NO ₂ calibration curve showing nonlinearity effect	78
7.5	Example of the demodulation procedure for 6 June, 1998	80
7.6	Schematic representation of the Automated Calibration Unit	83
7.7	Typical data for calibration of the NO ₂ detector	84
7.8	Schematic representation of the HO ₂ radical source	86
7.9	Typical data for calibration of the amplification factor	89
8.1	Sketch map showing the location of Kleiner Feldberg	96
8.2	Topographical map showing the location of the Taunus Observatory	97
8.3	Orography of the Taunus Range	98
8.4	Photo of the container tower	99
8.5	Map showing location of Hohenpeissenberg	100
8.6	Photo of MOHp	101

8.7	Aerial photo of the Taunus Observatory.	108
9.1	Daily average mixing ratios at Kleiner Feldberg, 1998	116
9.2	Daily averages of meteorological parameters at Kleiner Feldberg, 1998	117
9.3	Daily average mixing ratios at Kleiner Feldberg, 1999	118
9.4	Daily averages of meteorological parameters at Kleiner Feldberg, 1999	119
9.5	Diurnal profiles for several trace gases at Kleiner Feldberg	122
9.6	Comparison of the profiles of RO_x and solar radiation	124
9.7	Plot of RO_x vs normalised radiation	125
9.8	Weekly profiles for O_3 , RO_x , NO and ND	128
9.9	Correlation of maximum ozone with various parameters	131
9.10	Correlation of maximum ozone with various components	135
9.11	Plot of r versus time lag for the autocorrelation of ozone	137
9.12	Correlation of average RO_x with various parameters	138
9.13	Correlation of average RO_x with NO and NO_2	140
9.14	Wind rose for 1998 and 1999	141
9.15	Wind roses for several components	143
10.1	Plot of ΔO_3 vs photochemical O_3 production	150
10.2	Plot of ΔO_3 vs photochemical O_3 production, corrected for ΔNO_2 . .	150
10.3	Diurnal profile of the hourly change in the O_3 mixing ratio	152
10.4	Plot of the rate of change of ozone vs the calculated production rate .	153
11.1	Mixing ratios at Hohenpeissenberg, June 2000	159
11.2	Meteorological parameters at Hohenpeissenberg, June 2000	160
11.3	Plots of OH concentration and j_{O^1D}	161
11.4	Mixing ratios of various VOCs at Hohenpeissenberg, June 2000	162
11.5	Plot of RO_x mixing ratio and VOC conversion rate	163
11.6	Block diagram of the chemistry used in the steady state calculations.	164
11.7	Plot of OH concentrations from observation and a steady state model	166
11.8	Plot of the contributions of the various sources and sinks of OH . . .	167
11.9	Plot of RO_x concentrations from observation and a steady state model	169
11.10	Plot of the contributions of the various sources and sinks of RO_x . . .	170
12.1	Average monthly ozone concentrations, Kleiner Feldberg, 1993-99 . . .	174
12.2	Average diurnal ozone profiles for Kleiner Feldberg, 1993-99	176
12.3	Average diurnal profiles for summertime ozone episodes	177
12.4	Ozone concentration vs wind speed; Kleiner Feldberg, 1998	180
12.5	Background ozone concentration vs altitude for stations in Hesse, 1998	182
12.6	Plots of r_t vs distance from Königstein and altitude	185
12.7	Daily profiles of r_d^2 and r_{alt}^2	186
12.8	Daily profiles of r_d^2 and r_{alt}^2 during summer.	188
12.9	Daily profiles of the characteristic distance	190
12.10	Distribution of the r_t for the whole year	192

12.11	Summertime distribution of r_t	193
12.12	Summertime distribution of r_t for the change in ozone concentration between 08:00 and 16:00 CET.	194
A.1	Configuration screen of <code>rox.exe</code>	212
A.2	Main window for <code>demod.exe</code>	214
A.3	Configuration window for <code>demod.exe</code>	215
A.4	Classes used in <code>demod.exe</code>	218
B.1	Meteorological data for June, 1998	222
B.2	Mixing ratios for measured components for June, 1998	223
B.3	Meteorological data for July, 1998	224
B.4	Mixing ratios for measured components for July, 1998	225
B.5	Meteorological data for August, 1998	226
B.6	Mixing ratios for measured components for August, 1998	227
B.7	Meteorological data for September, 1998	228
B.8	Mixing ratios for measured components for September, 1998	229
C.1	Meteorological data for June, 1999	232
C.2	Mixing ratios for measured components for June, 1999	233
C.3	Meteorological data for July, 1999	234
C.4	Mixing ratios for measured components for July, 1999	235
C.5	Meteorological data for August, 1999	236
C.6	Mixing ratios for measured components for August, 1999	237
C.7	Meteorological data for September, 1999	238
C.8	Mixing ratios for measured components for September, 1999	239

List of Tables

7.1	Main characteristics of the peroxy radical chemical amplifier	73
7.2	List of NO ₂ permeation tubes	82
7.3	Estimated uncertainties in s and CL, and instrumental uncertainty	91
8.1	Climate data for Kleiner Feldberg	98
8.2	Summary of instruments at Kleiner Feldberg	102
8.3	Summary of instrumentation at Hohenpeissenberg	103
8.4	Summary of the principle meteorological parameters	109
9.1	Correlations between ozone and various parameters	132
9.2	Correlations of various radiation parameters with temperature and ozone	133
9.3	Correlations between ΔO_3 and various parameters	134
9.4	Correlations between RO _x and various parameters	139
10.1	Multiple linear progression for predicting the O ₃ maximum	154
10.2	Improvement of simple forecast of the daily maximum O ₃ mixing ratio by inclusion of morning RO _x measurements	156
A.1	List of project files	217
A.2	List of source text files	218
B.1	List of data sources	221
C.1	List of data sources	231
D.1	Reactions and rate coefficients used for calculating OH	242
D.2	Reactions and rate coefficients used for calculating RO _x	244
D.3	Reaction coefficients for the OH oxidation of VOCs	245

List of abbreviations

ACU	Automated Calibration Unit
ADC	Analog Digital Converter
AOT40	Accumulated exposure to Ozone above a Threshold mixing ratio of 40 ppbv
ASCII	American Standard Code for Information Interchange
asl	above sea level
CA	Chemical Amplifier
CIMS	chemical ionisation mass spectrometry
CL	chain length (= amplification factor)
CO	carbon monoxide
DWD	Deutscher Wetterdienst (German Weather Service)
FID	Flame ionisation detector
FFT	Fast Fourier Transform
GC	gas chromatograph
HLUG	Hessische Landesamt für Umwelt und Geologie (Bureau for the Environment and Geology of the State of Hesse)
HO ₂	hydro peroxy radical
HONO	nitrous acid
HNO ₃	nitric acid
HO ₂ NO ₂	pernitrous acid
HO _x	odd hydrogen oxides (= OH + HO ₂)
IMG	Institut für Meteorologie und Geophysik (Institute for Meteorology and Geophysics)
IMR-MS	Ion-Molecule Reaction Mass Spectrometry
LIF-FAGE	Laser Induced Fluorescence - Fluorescence Assay by Gas Expansion
MFC	Mass Flow Controller
MIESR	Matrix Isolation - Electron Spin Resonance

MOHp	Meteorological Observatory Hohenpeissenberg
MOR	maximum ozone reactivity
N_2O_5	dinitrogen pentoxide
NO	nitrous oxide
NO ₂	nitric oxide
NO _x	nitrogen oxides (=NO+NO ₂)
NO ₃	nitrate radical
NMHC	non methane hydrocarbons
NMOC	non methane organic compounds
O ₂	molecular oxygen
O ₃	ozone
OH	hydroxy radical
OOP	object Oriented Programming
OWL	Object Windows Library
PA	peroxy acetyl (radicals)
PAN	peroxyacetyl nitrate
PBL	planetary boundary layer
PMT	Photomultiplier
ppbv	parts per billion by volume, nmol mol ⁻¹
ppmv	parts per million by volume, μmol mol ⁻¹
PPN	peroxy propionyl nitrate
pptv	parts per trillion by volume, pmol mol ⁻¹
PRICE	Peroxy Radical Intercomparison Experiment
PSSD	photostationary steady state deviation
RACM	Regional Atmospheric Chemistry Model
RH	relative humidity
RO	organic alkoxy radicals
RO _x	total peroxy radicals (RO _x =OH+HO ₂ +RO ₂ +RO)
RO ₂	organic peroxy radicals
slpm	standard litre per minute
smlpm	standard millilitre per minute
SNR	signal-to-noise ratio
STE	stratospheric-tropospheric exchange
STP	standard temperature and pressure (273 K, 1013 hPa)
TO	Taunus Observatory
VOC	volatile organic compounds

Bibliography

- Alfassi, Z. B. (Editor). *Peroxyl radicals*. John Wiley and Sons Ltd, New York, 1997.
- Altshuller, A. P. and A. S. Lefohn. Background ozone in the planetary boundary layer over the United States. *J. Air Waste Management Assoc.*, 46:134–141, 1996.
- Angeletti, G. and G. Restelli (Editors). *Physico-chemical behaviour of atmospheric pollutants*. Directorate-General for Science, Research and Development, European Commission, Luxembourg, 1994. Report EUR 15609/1 EN.
- Arakaki, T. and B. C. Faust. Sources, sinks and mechanisms of hydroxyl radical (OH) photoproduction and consumption in authentic acidic continental cloudwaters from Whiteface Mountain, New York: the role of the Fe(r) (r=II,III) photochemical cycle. *J. Geophys. Res.*, 103:3487–3504, 1998.
- Ashbourn, S. F. M., M. E. Jenkin, and K. C. Clemitshaw. Laboratory studies of the response of a peroxy radical chemical amplifier to HO₂ and a series of organic peroxy radicals. *J. Atmos. Chem.*, 29(3):233–266, March 1998.
- Atkinson, R. Gas-phase tropospheric chemistry of organic compounds: A review. *Atm. Environ.*, 24A(1):1–41, January 1990.
- Atkinson, R. Atmospheric reactions of alkoxy and beta-hydroxyalkoxy radicals. *Int. J. Chem. Kin.*, 29(2):99–111, February 1997a.
- Atkinson, R. Gas-phase tropospheric chemistry of volatile organic compounds: 1. alkanes and alkenes. *J. Phys. Chem. Ref. Data*, 26(2):215–290, 1997b.
- Atkinson, R. Gas-phase degradation of organic compounds in the troposphere. *Pure Appl. Chem.*, 70(7):1327–1334, Jul 1998.
- Atkinson, R. Atmospheric chemistry of VOCs and NO_x. *Atm. Environ.*, 34(12-14):2063–2101, 2000.
- Atkinson, R., D. L. Baulch, R. A. Cox, R. F. Hampson, Jr., J. A. Kerr, M. J. Rossi, and J. Troe. Evaluated kinetic and photochemical data for atmospheric chemistry, organic species: Supplement VII. *J. Phys. Chem. Ref. Data*, 28(2):191–393, 1999.

- Beck, J. P. and P. Grennfelt. Distribution of ozone over Europe. In P. M. Borrell, P. Borrell, T. Cvitas, and W. Seiler (editors), *Photooxidants, Precursors and Products: Proceedings of EUROTRAC '92*, pages 43–58. SPB Academic Publishing bv, The Hague, 1993. ISBN 90-5103-082-7.
- Beck, J. P. and P. Grennfelt. Estimate of ozone production and destruction over Northwestern Europe. *Atm. Environ.*, 28(1):129–140, January 1994.
- Becker, K. H., W. Fricke, J. Löbel, and U. Schurath. In R. Guderian (editor), *Pollution by Photochemical Oxidants*, pages 3–125. Springer Verlag, Berlin, 1985.
- Beekman, M., G. Ancellet, S. Blonsky, D. de Muer, A. Ebel, H. Elbern, J. Hendricks, J. Kowol, C. Mancier, R. Sladkovic, H. G. J. Smit, P. Smeth, T. Trickl, and P. van Haver. Regional and global tropopause fold occurrence and related ozone flux across the tropopause. *J. Atmos. Chem.*, 28(1-3):29–44, November 1997.
- Behmann, T., M. Weißenmayer, and J. P. Burrows. Peroxy radicals in the night-time oxidation chemistry. In *Angeletti and Restelli* [1994], pages 259–264. Report EUR 15609/1 EN.
- Beilke, S. Langzeitentwicklung der Ozonbelastung im globalen, nationalen, und regionalen Massstab. In *VDI* [2000], pages 55–81. Band 32.
- Beine, H. J., D. A. Jaffe, J. A. Herring, J. A. Kelley, T. Krognes, and F. Stordal. High-latitude springtime photochemistry 1. NO_x , PAN and ozone relationships. *J. Atmos. Chem.*, 27(2):127–153, June 1997.
- Benning, L. and A. Wahner. Measurements of atmospheric formaldehyde (HCHO) and acetaldehyde (CH_3CHO) during POPCORN 1994 using 2,4-DNPH coated silica cartridges. *J. Atmos. Chem.*, 31:105–117, 1998.
- Berresheim, H., F. L. Eisele, D. J. Tanner, L. McInnes, D. C. Ramsey-Bell, and D. S. Covert. Atmospheric sulfur chemistry and cloud condensation nucleus (CCN) over the northeastern Pacific Coast. *J. Geophys. Res.*, 98(D7):12,701–12,711, July 1993.
- Berresheim, H., T. Elste, C. Plass-Dülmer, F. L. Eisele, and D. Tanner. Chemical ionization mass spectrometer for long-term measurements of atmospheric OH and H_2SO_4 . *Int. J. Mass Spectrom.*, 202:91 – 103, 2000.
- Biesenthal, T. A., Q. Wu, P. B. Shepson, H. A. Wiebe, K. G. Anlauf, and G. I. MacKay. A study of relationships between isoprene, its oxidation products and ozone in the Lower Fraser Valley, BC. *Atm. Environ.*, 31(14):2049–2058, July 1997.
- Borrell, P. M., P. Borrell, T. Cvitas, K. Kelly, and W. Seiler (Editors). *Proceedings of EUROTRAC '96*. Computational Mechanics Publications, Southampton, 1996.

- Borrell, P. M., P. Borrell, T. Cvitas, and W. Seiler (Editors). *Transport and Transformation of Pollutants in the Troposphere: Proceedings of EUROTRAC '94*. SPB Academic Publishing bv, The Hague, 1994. ISBN 90-5103-095-9.
- Cantrell, C. Tropospheric peroxy radical measurements. In *IAMAS* [2001], page 114.
- Cantrell, C. A., J. A. Lind, R. E. Shetter, J. G. Calvert, P. D. Goldan, W. Kuster, F. C. Fehsenfeld, S. A. Montzka, D. D. Parrish, E. J. Williams, M. P. Buhr, H. H. Westberg, G. Allwine, and R. Martin. Peroxy radicals in the ROSE experiment: Measurement and theory. *J. Geophys. Res.*, 97(D18):20,671–20,686, Dec 1992.
- Cantrell, C. A., R. E. Shetter, and J. Calvert. Peroxy radical chemistry during FIELD-VOC 1993 in Brittany, France. *Atm. Environ.*, 30(23):3947–3957, December 1996a.
- Cantrell, C. A., R. E. Shetter, and J. G. Calvert. Dual-inlet chemical amplifier for atmospheric peroxy radical measurements. *Anal. Chem.*, 68(23):4194–4199, December 1996b.
- Cantrell, C. A., R. E. Shetter, J. G. Calvert, D. D. Parrish, F. C. Fehsenfeld, P. D. Goldan, W. Kuster, E. J. Williams, H. H. Westberg, G. Allwine, and R. Martin. Peroxy radicals as measured in ROSE and estimated from photostationary state deviations. *J. Geophys. Res.*, 98(D10):18,355–18,366, October 1993a.
- Cantrell, C. A., R. E. Shetter, T. M. Gilpin, and J. G. Calvert. Peroxy radicals measured during Mauna Loa Observatory Photochemistry Experiment 2 - The data and first analysis. *J. Geophys. Res.*, 101(D9):14,643–14,652, June 1996c.
- Cantrell, C. A., R. E. Shetter, T. M. Gilpin, J. G. Calvert, F. L. Eisele, and D. J. Tanner. Peroxy radical concentrations measured and calculated from trace gas measurements in the Mauna Loa Observatory Photochemistry Experiment. *J. Geophys. Res.*, 101(D9):14,653–14,664, June 1996d.
- Cantrell, C. A., R. E. Shetter, J. A. Lind, A. H. McDaniel, J. G. Calvert, D. D. Parrish, F. C. Fehsenfeld, M. P. Buhr, and M. Trainer. An improved chemical amplifier for peroxy radical measurements. *J. Geophys. Res.*, 98(D2):2897–2909, February 1993b.
- Cantrell, C. A. and D. H. Stedman. A possible technique for the measurement of atmospheric peroxy radicals. *Geophys. Res. Lett.*, 9:846–849, 1982.
- Cantrell, C. A., D. H. Stedman, and G. J. Wendel. Measurement of atmospheric peroxy radicals by chemical amplification. *Anal. Chem.*, 56(8):1496–1502, 1984.
- Cantrell, C. A., A. Zimmer, and G. S. Tyndall. Absorption cross sections for water vapour from 183 to 193 nm. *Geophys. Res. Lett.*, 24(17):2195–2198, September 1997.

- Carpenter, L. J., K. C. Clemitshaw, R. A. Burgess, S. A. Penkett, J. N. Cape, and G. C. McFadyen. Investigation and evaluation of the NO_x/O_3 photochemical steady state. *Atm. Environ.*, 32(19):3353–3365, October 1998.
- Carpenter, L. J., P. S. Monks, B. J. Brady, S. A. Penkett, I. E. Galbally, and C. P. M. Meyer. A study of peroxy radicals and ozone photochemistry at coastal sites in the Northern and Southern Hemispheres. *J. Geophys. Res.*, 102(D21):25,417–25,427, November 1997.
- Carslaw, N., L. J. Carpenter, J. M. C. Plane, B. J. Allan, R. A. Burgess, K. C. Clemitshaw, H. Coe, and S. A. Penkett. Simultaneous observations of nitrate and peroxy radicals in the marine boundary layer. *J. Geophys. Res.*, 102(D15):18,917–18,933, August 1997.
- Clemitshaw, K. C., L. J. Carpenter, S. A. Penkett, and M. E. Jenkin. A calibrated peroxy radical chemical amplifier for ground-based tropospheric measurements. *J. Geophys. Res.*, 102(D21):25,405–25,416, November 1997.
- Creasey, D. J., D. E. Heard, and J. D. Lee. Absorption cross-section measurements of water vapour and oxygen at 185 nm. Implications for the calibration of field instruments to measure OH, HO_2 and RO_2 radicals. *Geophys. Res. Lett.*, 27(11):1651–1654, June 2000.
- DeMore, W. B., D. M. Golden, R. F. Hampson, C. J. Howard, M. J. Kurylo, M. J. Molina, A. R. Ravishankara, and S. P. Sander. Chemical kinetics and photochemical data for use in stratospheric modeling, evaluation number 11. JPL Publication 94-26, Jet Propulsion Laboratory, Pasadena, California, 1994.
- Dentener, F. J., G. R. Carmichael, Y. Zhang, J. Lelieveld, and P. J. Crutzen. Role of mineral aerosol as a reactive surface in the global troposphere. *J. Geophys. Res.*, 101:22,869–22,889, 1996.
- Derwent, R. G., M. E. Jenkin, and S. M. Saunders. Photochemical ozone creation potentials for a large number of reactive hydrocarbons under European conditions. *Atm. Environ.*, 30(2):181–199, January 1996.
- Derwent, R. G., P. G. Simmonds, S. Seuring, and C. Dimmer. Observation and interpretation of the seasonal cycles in the surface concentrations of ozone and carbon monoxide at Mace Head, Ireland from 1990 to 1994. *Atm. Environ.*, 32(2):145–157, January 1998.
- Deutscher Wetterdienst. Witterungsreport Express. Technical report, Deutscher Wetterdienst, 1999.
- Eisele, F. L. and D. J. Tanner. Ion-assisted tropospheric OH measurements. *J. Geophys. Res.*, 96:9001–9010, 1991.

- Eisele, F. L. and D. J. Tanner. Measurement of the gas-phase concentration of H_2SO_4 and MSA and estimates of H_2SO_4 production and loss. *J. Geophys. Res.*, 98:9001–9010, 1993.
- European Commission. Ozone position paper. Final version, Office for Official Publications of the European Communities, Luxembourg, 1999.
- Finlayson-Pitts, B. J. and J. N. Pitts, Jr. *Atmospheric Chemistry: Fundamentals and Experimental Techniques*. John Wiley & Sons, Inc., New York, 1986.
- Fricke, W. *Die Bildung und Verteilung von anthropogenem Ozon in der unteren Troposphäre*. Dissertation, Fachbereich Geowissenschaften der Johann Wolfgang Goethe-Universität, Frankfurt am Main, December 1980.
- Fricke, W. Charakteristika der räumlich-zeitlichen Ozonverteilung in der Atmosphäre. In *VDI [2000]*, pages 35–53. Band 32.
- Geiß, H. and A. Volz-Thomas. Lokale und regionale Ozonproduktion: Chemie und Transport. Bericht des Forschungszentrums Jülich Jül-2764, Forschungszentrum Jülich, Jülich, December 1992.
- Geyer, A., B. Alicke, D. Mihelcic, J. Stutz, and U. Platt. Comparison of tropospheric NO_3 radical measurements by differential optical absorption spectroscopy and matrix isolation electron spin resonance. *J. Geophys. Res.*, 104(D21):26,097–26,105, November 1999.
- Gilge, S., D. Kley, A. Volz-Thomas, and H. Geiß. Messungen von Wasserstoffperoxid und organischen Hydroperoxiden am Schauinsland im Schwarzwald. Bericht des Forschungszentrums Jülich Jül-2998, ISSN 0944-2952, Institut für Chemie und Dynamik der Geosphäre 2, Forschungszentrum Jülich, Jülich, December 1994.
- Goldan, P. D., W. C. Kuster, and F. C. Fehsenfeld. Nonmethane hydrocarbon measurements during the Tropospheric OH Photochemistry Experiment. *J. Geophys. Res.*, 102(D5):6315–6324, March 20 1997.
- Grosch, S. and R. Schmitt. Entwicklung eines Verfahrens zur Vorhersage von Sommersmog unter Verwendung von Immissionsmessungen. Final report, Meteorologie Consult GmbH, Glashütten, January 1994.
- Guicherit, R. Ozone on an urban and regional scale - with special reference to the situation in the Netherlands. In I. Isaksen (editor), *Tropospheric Ozone*, pages 49–62. D. Reidel Publishing Company, Dordrecht, 1988.
- Handisides, G. M. *Gesamt-Peroxyradikal-Meßgerät: Handbuch*. Institut für Meteorologie und Geophysik, Frankfurt am Main, Frankfurt am Main, October 1995.

- Handisides, G. M., H. Bingemer, and U. Schmidt. Untersuchung der Bildung und Vorhersage von Photooxidantien am Rande des Belastungsgebietes Rhein-Main. Project annual report, Institut für Meteorologie und Geophysik, Frankfurt am Main, November 1998.
- Handisides, G. M., H. Bingemer, U. Schmidt, and R. Schmitt. Untersuchung der Bildung und Vorhersage von Photooxidantien am Rande des Belastungsgebietes Rhein-Main. Project annual report, Institut für Meteorologie und Geophysik, Frankfurt am Main, November 1999.
- Handisides, G. M., H. Bingemer, U. Schmidt, and R. Schmitt. Untersuchung der Bildung und Vorhersage von Photooxidantien am Rande des Belastungsgebietes Rhein-Main. Abschlussbericht, Universitätsinstitut für Meteorologie und Geophysik, Johann Wolfgang Goethe-Universität, Frankfurt am Main, März 2000.
- Handisides, G. M., H.-W. Georgii, and H. Bingemer. Measurements of peroxy radicals on the Kleiner Feldberg, Germany. In *Borrell et al.* [1996].
- Handisides, G. M., H.-W. Georgii, and H. Bingemer. Messungen der Konzentration von Peroxyradikalen am Taunus-Observatorium: Zusammenhänge zwischen RO_x -Konzentrationen und Ozonbildungsraten. Abschlussbericht zum Werkvertrag Nr. 42320 der Hessische Landesanstalt für Umwelt, Institut für Meteorologie und Geophysik, Frankfurt am Main, November 1996b.
- Hanke, M., J. Ueker, and F. Arnold. Long-term speciated atmospheric measurements of HO_2 and organic peroxy radicals ($\sum\text{RO}_2$) by Chemical Conversion/Ion Molecule Reaction Mass Spectrometry (ROXMAS). In *IAMAS* [2001], page 114.
- Hard, T. M., C. Y. Chan, A. A. Mehrabzadeh, and R. J. O'Brien. Diurnal HO_2 cycles at clean air and urban sites in the troposphere. *J. Geophys. Res.*, 97(D9):9785–9794, June 1992.
- Hard, T. M., R. J. O'Brien, C. Y. Chang, and A. A. Mehrabzadeh. Tropospheric free radical determination by FAGE. *Environm. Sci. Technol.*, 18:768–777, 1984.
- Hastie, D. R., M. Weissenmayer, J. P. Burrows, and G. W. Harris. Calibrated chemical amplifier for atmospheric RO_x measurements. *Anal. Chem.*, 63(18):2048–2057, 1991.
- Hebestreit, K., J. Stutz, D. Rosen, V. Matveev, M. Peleg, M. Luria, and U. Platt. First DOAS measurements of tropospheric BrO in mid latitudes. *Science*, 283:55–57, 1999.
- Heitlinger, M. *Untersuchungen zur Messung von Peroxiradikalen mittels chemischer Verstärkung*. Dissertation, Bergische Universität-Gesamthochschule Wuppertal, Fachbereich Naturwissenschaften II, Juli 1997.

- Heitlinger, M., A. Volz-Thomas, D. Mihelcic, P. Müsgen, J. P. Burrows, M. D. A. Hernández, D. Stöbener, D. Perner, T. Arnold, R. Seuwen, K. C. Clemitshaw, S. A. Penkett, G. Laverdet, K. El-Boudali, S. Teton, J. Hjorth, O. Poulida, D. Hastie, M. C. Arias, P. Borrell, and P. M. Borrell. Peroxy Radical Inter-Comparison Exercise II. In *Larsen et al.* [1997].
- Hessisches Landesvermessungsamt. Blatt l 5716. 1995.
- Hidy, G. M. Ozone process insights from field experiments Part I: Overview. *Atm. Environ.*, 34:2001–2022, 2000.
- HMUEB/HMJFG. Problem Ozon: Information zur Ozonbelastung am Boden während der Sommermonate. July 1993.
- Hofzumahaus, A., T. Brauers, U. Aschmutat, U. Brandenburger, H.-P. Dorn, M. Hausmann, M. Heßling, F. Holland, C. Plass-Dülmer, M. Sedlacek, M. Weber, and D. H. Ehhalt. Reply to comment by *Lanzendorf et al.* [1997]. *Geophys. Res. Lett.*, 24(23):3039–3040, December 1997.
- Höller, H., U. Finke, H. Huntrieser, M. Hagen, and C. Feigl. Lightning-produced NO_x (LINOX): Experimental design and case study results. *J. Geophys. Res.*, 104(D11):13,911–13,922, June 1999.
- Holton, J. R., P. H. Haynes, M. E. McIntyre, A. R. Douglass, R. B. Hood, and L. Pfister. Stratosphere-troposphere exchange. *Rev. Geophys.*, 33:403–439, 1995.
- Höppe, P., G. Rabe, J. Lindner, and G. Praml. Einfluss erhöhter Ozonkonzentrationen auf die Lungenfunktion ausgewählter Bevölkerungsgruppen - Schlussbericht über die Münchner Ozonstudie. Abschlussbericht 149, Bayerisches Staatsministerium für Landesentwicklung und Umweltfragen, München, January 2000.
- Hudson, R. D. and L. J. Kieffer. Absorption cross sections of stratospheric molecules. In *The Natural Stratosphere of 1974*, CIAP Monograph I, pages 5,156–5,194. CIAP, 1975.
- IAMAS. *Abstracts: 8th Scientific Assembly of International Association of Meteorology and Atmospheric Sciences*. IAMAS, Innsbruck, Austria, 10-18 July 2001.
- Jacob, D. J. Heterogeneous chemistry and tropospheric ozone. *Atm. Environ.*, 34(12-14):2131–2159, 2000.
- Jenkin, M. E. and K. C. Clemitshaw. Ozone and other secondary photochemical pollutants: Chemical processes governing their formation in the planetary boundary layer. *Atm. Environ.*, 34(16):2499–2527, 2000.

- Jenkin, M. E., R. G. Derwent, and S. M. Saunders. The calculated fractional response of the chemical amplification technique to peroxy radical populations on a boundary layer trajectory over Europe. In *Larsen et al.* [1997], pages 144–148. EUR 17482 EN.
- Kaminski, U. and S. Gilge. Zum Trend der Hintergrundkonzentration von Ozon. Ozonbulletin des Deutschen Wetterdienstes 75, Deutsches Wetterdienst, June 2000a.
URL http://www.dwd.de/research/mohp/hp2/ozo/oz_start.htm
- Kaminski, U. and S. Gilge. Zum Trend der Hintergrundkonzentration von Ozon an einer städtischen Station (Hamburg-Sasel) und einer ländlichen Bergstation (Hohenpeißenberg). In *VDI* [2000], pages 337–342. Band 32.
- Kanaya, Y., Y. Sadanaga, J. Matsumoto, U. K. Sharma, J. Hirokawa, Y. Kajii, and H. Akimoto. Nighttime observation of the HO₂ radical by an LIF instrument at Oki island, Japan, and its possible origins. *Geophys. Res. Lett.*, 26(14):2179–2182, July 1999.
- Klemm, O., W. R. Stockwell, H. Schlager, and M. Krautstrunk. NO_x or VOC limitation in East German ozone plumes? *J. Atmos. Chem.*, 35(1):1–18, January 2000.
- Konrad, S. *Charakterisierung eines Verfahrens zur Bestimmung der O_x-Konzentrationen in der Atmosphäre.* Diplomarbeit, Bergische Universität-Gesamthochschule Wuppertal, 1997.
- Kraus, A., T. Brauers, D. Brüning, A. Hofzumahauss, F. Rohrer, N. Houben, H.-W. Patz, and A. Volz-Thomas. Ergebnisse des NO₂ Photolysefrequenz Messvergleichs JCOM97: Eine Qualitätssicherungsmassnahme für das BERLIOZ-Experiment im Rahmen des Förderschwerpunktes Troposphärenforschung Leitthema 3 des BMBF. Berichte des Forschungszentrum Jülich GmbH Jül-578, Forschungszentrum Jülich, September 1998.
- Krause, G. H. M. and B. Köllner. Wirkungen auf Bäume und Waldökosysteme. In *VDI* [2000], pages 93–113. Band 32.
- Kunz, H. and P. Speth. Variability of near-ground ozone concentrations during cold front passages - a possible effect of tropopause folding events. *J. Atmos. Chem.*, 28(1-3):77–95, November 1997.
- Lamanna, M. S. and A. H. Goldstein. In situ measurements of C₂-C₁₀ volatile organic compounds above a Sierra Nevada ponderosa pine plantation. *J. Geophys. Res.*, 104(D17):21,247–21,262, September 20 1999.
- Lanzendorf, E. J., T. F. Hanisco, N. M. Donahue, and P. O. Wennberg. Comment on: “The measurement of tropospheric OH radicals by laser-induced fluorescence

- spectroscopy during the POPCORN field campaign” by Hofzumahaus *et al.* and “Intercomparison of tropospheric OH radical measurements by multiple folded long-path laser absorption and laser induced fluorescence” by Brauers *et al.*. *Geophys. Res. Lett.*, 24(23):3037–3038, December 1997.
- Larsen, B., B. Versino, and G. Angeletti (Editors). *The oxidizing capacity of the troposphere: Proceedings of the Seventh European Symposium on Physico-Chemical Behaviour of Atmospheric Pollutants*. European Commission, Brussels, 1997. EUR 17482 EN.
- Leighton, P. A. *Photochemistry of Air Pollution*. Academic Press, San Diego, California, 1961.
- Lesclaux, R. Combination of peroxy radicals in the gas phase. In *Alfassi* [1997], pages 81–112.
- Liang, J. and D. J. Jacob. Effect of aqueous-phase cloud chemistry on tropospheric ozone. *J. Geophys. Res.*, 102:5993–6001, 1997.
- Lightfoot, P. D., R. A. Cox, J. N. Crowley, M. Destriau, G. D. Hayman, M. E. Jenkin, G. K. Moortgat, and F. Zabel. Organic peroxy radicals: Kinetics, spectroscopy, and tropospheric chemistry. *Atm. Environ.*, 26A(10):1805–1961, 1992.
- Lin, C.-Y., D. J. Jacob, J. W. Munger, and A. M. Fiore. Increasing background ozone in surface air over the United States. *Geophys. Res. Lett.*, 27(21):3465–3468, November 2000.
- Luria, M. DOAS measurements of tropospheric bromine oxide over the Dead Sea. Presentation at the 2nd Gentner Symposium on Geoscience: Research Workshop on the Interactions between Chemistry, Physics and Dynamics in the Troposphere, October 1999.
- Maeda, Y. K., K. Aoki, and M. Munemori. Chemiluminescence method for the determination of nitrogen dioxide. *Anal. Chem.*, 52:307–311, 1980.
- Martinez, M., H. Harder, T. Kovacs, P. D. Carlo, A. Fried, W. H. Brune, E. J. Williams, S. R. Hall, R. E. Shetter, and B. Wert. OH and HO₂ variations in urban environments during summer. In *IAMAS* [2001], page 112.
- Mihelcic, D., M. Helten, H. Fark, P. Müsgen, H.-W. Pätz, M. Trainer, D. Kempa, and D. H. Ehhalt. Tropospheric airborne measurements of NO₂ and RO₂ using the technique of matrix isolation and electron spin resonance. In *2nd Symp. Composition of the Nonurban Troposphere, Williamsburg, Virginia, USA*, pages 327–329. 1982.

- Mihelcic, D., D. Klemp, P. Musgen, H. Patz, and A. Volz-Thomas. Simultaneous measurements of peroxy and nitrate radicals at Schauinsland. *J. Atmos. Chem.*, 16(4):313–335, May 1993.
- Mihelcic, D., S. Konrad, H.-W. Pätz, T. Schmitz, A. Volz-Thomas, F. Holland, A. Hofzumahaus, H.-J. K. Bächmann, A. Geyer, and D. Perner. Comparison of measurements of OH, HO₂ and RO₂ radicals during the BERLIOZ campaign. In *IAMAS* [2001], page 113.
- Mihelcic, D., P. Müsgen, and D. H. Ehhalt. An improved method of measuring tropospheric NO₂ and RO₂ by matrix isolation and electron spin resonance. *J. Atmos. Chem.*, 3:341–361, 1985.
- Mihelcic, D. and A. Volz-Thomas. The ratio of organic peroxy to hydroperoxy radicals: Direct measurements by Matrix Isolation/ESR spectroscopy. In *Borrell et al.* [1994], pages 379–383.
- Mihelcic, D., A. Volz-Thomas, H. W. Pätz, and D. Kley. Numerical analysis of ESR spectra from atmospheric samples. *J. Atmos. Chem.*, 11:271–297, 1990.
- Mihele, C. M. and D. R. Hastie. The sensitivity of the radical amplifier to ambient water vapour. *Geophys. Res. Lett.*, 25(11):1911–1913, June 1998.
- Mihele, C. M. and D. R. Hastie. Optimized operation and calibration procedures for radical amplifier-type detectors. *J. Atmos. Ocean Technol.*, 17:788–794, 2000.
- Mihele, C. M., M. Mozurkewich, and D. R. Hastie. Radical loss in a chain reaction of CO and NO in the presence of water: Implications for the radical amplifier and atmospheric chemistry. *Int. J. Chem. Kin.*, 31(2):145–152, February 1999.
- Millàn, M. M., R. Salvador, and E. Mantilla. Tropospheric processes in the Mediterranean Basin relevant to global change. In *Larsen et al.* [1997], pages 406–410. EUR 17482 EN.
- Monks, P. S. A review of the observations and origins of the spring ozone maximum. *Atm. Environ.*, 34(21):3545–3561, July 2000.
- Monks, P. S., L. J. Carpenter, S. A. Penkett, and G. P. Ayers. Night-time peroxy radical chemistry in the remote boundary layer over the Southern Ocean. *Geophys. Res. Lett.*, 23(5):535–538, March 1996.
- Monks, P. S., L. J. Carpenter, S. A. Penkett, G. P. Ayers, R. W. Gillett, I. E. Galbally, and C. P. Meyer. Fundamental ozone photochemistry in the remote marine boundary layer: The SOAPEX experiment, measurement and theory. *Atm. Environ.*, 32(21):3647–3664, November 1998.

- Monks, P. S., G. Salisbury, G. Holland, S. A. Penkett, and G. P. Ayers. A seasonal comparison of ozone photochemistry in the remote marine boundary layer. *Atm. Environ.*, 34(16):2547–2561, 2000.
- Montzka, S. A., M. Trainer, W. M. Angevine, and F. C. Fehsenfeld. Measurements of 3-methyl furan, methyl vinyl ketone, and methylacrolein at a rural forested site in the southeastern United States. *J. Geophys. Res.*, 100(D6):11,393–11,401, June 20 1995.
- Moussiopoulos, N. Air pollution modelling in Southern Europe. In *Borrell et al.* [1994], pages 48–55.
- NIV. Holy Bible: New International Version. 1978. © New York International Bible Society, used by permission.
- Novelli, P. C., P. M. Lang, K. A. Masarie, D. F. Hurst, R. Meyers, and J. W. Elkins. Molecular hydrogen in the troposphere: Global distribution and budget. *J. Geophys. Res.*, 104(D23):30,427–30,444, December 20 1999.
- O'Brien, J. M., P. B. Shepson, Q. Wu, T. Biesenthal, J. W. Bottenheim, H. A. Wiebe, K. G. Anlauf, and P. Brickell. Production and distribution of organic nitrates and their relationship to carbonyl compounds in an urban environment. *Atm. Environ.*, 31(14):2059–2069, 1997.
- Pankow, J. F. Partitioning of semi-volatile organic compounds to the air/water interface. *Atm. Environ.*, 31(6):927–929, 1997.
- Parrish, D. D. and F. C. Fehsenfeld. Methods for gas-phase measurements of ozone, ozone precursors and aerosol precursors. *Atm. Environ.*, 34:1921–1957, 2000.
- Penkett, S. A., N. J. Blake, P. Lightman, A. R. W. Marsh, P. Anwyl, and G. Butcher. The seasonal variation of nonmethane hydrocarbons in the free troposphere over the North Atlantic Ocean - Possible evidence for extensive reaction of hydrocarbons with the nitrate radical. *J. Geophys. Res.*, 98(D2):2865–2885, Feb 1993.
- Penkett, S. A., K. C. Clemitshaw, N. H. Savage, R. A. Burgess, L. M. Cardenas, L. J. Carpenter, G. G. McFadyen, and J. N. Cape. Studies of oxidant production at the Weybourne Atmospheric Observatory in summer and winter conditions. *J. Atmos. Chem.*, 33(2):111–128, June 1999.
- Penkett, S. A., P. S. Monks, L. J. Carpenter, K. C. Clemitshaw, G. P. Ayers, R. W. Gillett, I. E. Galbally, and C. P. Meyer. Relationships between ozone photolysis rates and peroxy radical concentrations in clean air over the Southern Ocean. *J. Geophys. Res.*, 102(D11):12,805–12,817, June 1997.

- Plass-Dülmer, C., T. Brauers, and J. Rudolph. POPCORN: A field study of photochemistry in North-Eastern Germany. *J. Atmos. Chem.*, 31(1-2):5–31, October 1998.
- PORG. Ozone in the United Kingdom. Fourth Report of the Photochemical Oxidants Review Group, Department of the Environment, Transport and the Regions, 1997.
- Rapp, J. Konzeption, Problematik und Ergebnisse klimatologischer Trendanalysen für Europa und Deutschland. Bericht des Deutschen Wetterdienstes 212, Deutsche Wetterdienst, Offenbach am Main, 2000.
- Rapp, J. and C.-D. Schönwiese. *Atlas der Niederschlags- und Temperaturtrends in Deutschland 1891-1990*, volume 5 of *Frankfurter Geowissenschaftliche Arbeiten Serie B - Meteorologie und Geophysik*. Frankfurt am Main, 1996. 2. korrigierte Auflage.
- Reichert, L. *Untersuchung des Wassereffektes eines Peroxyradikal-Detektors*. Diplomarbeit, Institut für Umweltphysik, Universität Bremen, Bremen, April 2000.
- Reiner, T., M. Hanke, and F. Arnold. Atmospheric peroxy radical measurements by Ion Molecule Reaction-Mass Spectrometry: A novel analytical method using amplifying chemical conversion to sulfuric acid. *J. Geophys. Res.*, 102(D1):1311–1326, January 1997.
- Reiner, T., M. Hanke, and F. Arnold. Aircraft-borne measurements of peroxy radicals in the middle troposphere. *Geophys. Res. Lett.*, 25(1):47–50, January 1998.
- Reiner, T., M. Hanke, F. Arnold, H. Ziereis, H. Schlager, and W. Junkerman. Aircraft-borne measurements of peroxy radicals by chemical conversion/ion molecule reaction mass spectrometry: Calibration, diagnostics, and results. *J. Geophys. Res.*, 104(D15):18,647–18,659, August 1999.
- Roberts, J. M., S. B. Bertman, D. D. Parrish, F. C. Fehsenfeld, B. T. Jobson, and H. Niki. Measurement of alkyl nitrates at Chebogue Point, Nova Scotia during the 1993 North Atlantic Regional Experiment (NARE) intensive. *J. Geophys. Res.*, 103(D11):13,569–13,580, June 1998.
- Rüb, A. *Messung der jahreszeitlichen Variabilität des aktinischen Flusses im UV-B-Spektralbereich - Interpretation mit einem einfachen Strahlungsflußmodell*. Diplomarbeit, Fachbereich Geowissenschaft der Johann Wolfgang Goethe-Universität, Frankfurt am Main, April 1999.
- Sander, S. P., R. R. Friedl, W. B. DeMore, A. R. Ravishankara, D. M. Golden, C. E. Kolb, M. J. Kurylo, R. F. Hampson, R. E. Huie, M. J. Molina, and G. K. Moortgat. Chemical kinetics and photochemical data for use in stratospheric modeling, evaluation number 13; supplement to evaluation 12: Update of key reactions. JPL Publication 00-3, Jet Propulsion Laboratory, Pasadena, California, March 2000.

- Scheel, H. E., H. Areskoug, H. Geiss, B. Gomiscek, K. Granby, L. Haszpra, L. Klasinc, D. Kley, T. Laurila, A. Lindskog, M. Roemer, R. Schmitt, P. Simmonds, S. Solberg, and G. Toupance. On the spatial distribution and seasonal variation of lower-troposphere ozone over Europe. *J. Atmos. Chem.*, 28(1-3):11–28, November 1997.
- Schönwiese, C.-D. *Praktische Statistik*. Gebrüder Borntraeger, Berlin/Stuttgart, 2 edition, 1992.
- Schönwiese, C.-D., J. Malcher, and C. Hartmann. Globale Statistik langer Temperatur- und Niederschlagsreihen. Berichte des Instituts für Meteorologie und Geophysik der Universität Frankfurt/Main 65, Institut für Meteorologie und Geophysik, Johann Wolfgang Goethe-Universität, Frankfurt am Main, 1986.
- Schönwiese, C.-D. and J. Rapp. *Climate Trend Atlas of Europe, based on Observations 1891 to 1990*. Kluwer Academic Publishers, Dordrecht, 1997. ISBN 0-7923-4483-9.
- Schultz, M., M. Heitlinger, D. Mihelcic, and A. Volz-Thomas. Calibration source for peroxy radicals with built-in actinometry using H₂O and O₂ photolysis at 185 nm. *J. Geophys. Res.*, 100(D9):18,811–18,816, September 1995.
- Schwander, H., P. Koepke, A. Ruggaber, T. Nakajima, A. Kaifel, and A. Oppenrieder. STARSci 2.1: System for Transfer of Atmospheric Radiation. 2001.
URL <http://www.meteo.physik.uni-muenchen.de/strahlung/uvrad/Star/STARinfo.htm>
- Sehmel, G. A. Particle and gas dry deposition: A review. *Atm. Environ.*, 14:983–1011, 1980.
- Seinfeld, J. H. and S. N. Pandis. *Atmospheric Chemistry and Physics*. John Wiley & Sons, Inc., New York, 1998. ISBN 0-471-17816-0.
- Shepson, P. B., K. G. Anlauf, J. W. Bottenheim, H. A. Wiebe, N. Gao, K. Muthuramu, and G. I. MacKay. Alkyl nitrates and their contribution to reactive nitrogen at a rural site in Ontario. *Atm. Environ.*, 27A(5):749–757, 1992.
- Stull, R. B. *An Introduction to Boundary Layer Meteorology*. Atmospheric Sciences Library. Kluwer Academic Publishers, Dordrecht, 1988. ISBN 90-277-2769-4.
- Tanner, D. J., A. Jefferson, and F. L. Eisele. Selected ion chemical ionization mass spectrometric measurement of OH. *J. Geophys. Res.*, D102:6415–6425, 1997.
- Tyndall, G. S., R. A. Cox, C. Granier, R. Lesclaux, G. K. Moortgat, M. J. Pilling, A. R. Ravishankara, and T. J. Wallington. The atmospheric chemistry of small organic peroxy radicals. *J. Geophys. Res.*, 106(D11):12,157–12,182, June 2001.

- Umweltbundesamt. Jahresbericht 1999 aus dem Messnetz des Umweltbundesamtes. Jahresbericht, Umweltbundesamt, Fachgebiet II 6.5, Berlin, December 2000.
URL <http://www.umweltbundesamt.de>
- VDI. *Troposphärisches Ozon: Eine kritische Bestandsaufnahme über Ursache, Wirkung und Abhilfemaßnahmen*. Kommission Reinhaltung der Luft im VDI und DIN Normenausschuss, Düsseldorf, February 2000. Band 32.
- Vermeil, C., M. Cottin, and J. Masanet. Vacuum UV photochemistry of light and heavy water vapours. pages 69–76. Taylor and Francis, Bristol, Pa., 1967.
- Volz, A. and D. Kley. Evaluation of the Montsouris series of ozone measurements made in the nineteenth century. *Nature*, 332:240–242, 1988.
- Volz-Thomas, A., H.-W. Pätz, B. Alicke, A. Geyer, A. Hofzumahaus, F. Holland, S. Konrad, D. Mihelcic, D. Perner, T. Klüpfel, and T. Schmitz. Comparison of radical and trace gas measurements made during BERLIOZ at Pabstthum using different techniques. In *IAMAS* [2001], page 116.
- Volz-Thomas, A. et al. Peroxy Radical Intercomparison Exercise: A TOR/OCTA experiment at Schauinsland 1994. In *Borrell et al.* [1996].
- Volz-Thomas, A. et al. Peroxy Radical Inter Comparison Exercise. A formal comparison of methods for ambient measurements of peroxy radicals. Bericht des Forschungszentrums Jülich Jül-3597, Forschungszentrum Jülich, Jülich, 1999.
- Wallington, T. J., P. Dagaut, and M. J. Kurylo. Ultraviolet absorption cross sections and reaction kinetics and mechanisms for peroxy radicals in the gas phase. *Chem. Rev.*, 92:667–710, 1992.
- Wallington, T. J., O. J. Nielsen, and K. Sehested. Reactions of organic peroxy radicals in the gas phase. In *Alfassi* [1997], pages 113–172.
- Wang, Y., D. J. Jacob, and J. A. Logan. Global simulation of tropospheric O₃-NO_x-hydrocarbon chemistry: 3. Origin of tropospheric ozone and effects of nonmethane hydrocarbons. *J. Geophys. Res.*, 103(D9):10,757–10,767, May 1998.
- Washida, N., Y. Mori, and I. Tanaka. Quantum yield of ozone formation from photolysis of the oxygen molecule at 1849 and 1931 Å. *J. Phys. Chem.*, 54:1119–1122, 1971.
- Weigel, H.-J. and J. Bender. Wirkungen von Ozon auf landwirtschaftliche Pflanzen und Wildpflanzenarten. In *VDI* [2000], pages 115–135. Band 32.
- Weingartner, H. Korrelation und Information. *Meteorologische Rundschau*, 28:1–8, 1985.

- Weißmayer, M. *Peroxyradikalmessungen in der bodennahen Grenzschicht über dem Atlantik: Aufbau und Betrieb eines Chemischen Verstärkers und ein Vergleich der Meßergebnisse mit Simulationsrechnungen und Modellvorstellungen*. Dissertation, Fachbereich Chemie und Pharmazie der Johannes Gutenberg-Universität, Mainz, 1994.
- Weißmayer, M. and J. P. Burrows. Peroxy radical measurements in the boundary layer above the Atlantic Ocean. In *Angeletti and Restelli* [1994], pages 575–581. Report EUR 15609/1 EN.
- Weißmayer, M., M. D. A. Hernández, T. Behmann, J. Burkett, D. Schwöppe, D. Stöbener, and J. P. Burrows. Der Einfluß der Peroxyradikalkonzentration auf die Höhe der Ozonproduktion. Abschluß-Bericht zum Vorhaben FV 058 des Bremer Senators für Umweltschutz und Stadtentwicklung in Bremen, Institut für Umweltphysik, Universität Bremen, Bremen, December 1995.
- Wendel, G. J., D. H. Stedman, C. A. Cantrell, and L. Damrauer. Luminol-based nitrogen dioxide detector. *Anal. Chem.*, 55:937–940, 1983.
- Wesely, M. L. Turbulent transport of ozone to surfaces common in the eastern half of the United States. In S. E. Schwartz (editor), *Trace Atmospheric Constituents: Properties, Transformations and Fates*, pages 345–370. John Wiley, New York, 1983.
- Wesely, M. L. Parameterization of surface resistances to gaseous dry deposition in regional-scale numerical models. *Atm. Environ.*, 23:1293–1304, 1989. Cited in *Wesely and Hicks* [2000].
- Wesely, M. L. and B. B. Hicks. A review of the current status of knowledge on dry deposition. *Atm. Environ.*, 34(12-14):2261–2282, 2000.
- Wetter, T. *Eine Untersuchung zur Charakterisierung der zeitlichen Variabilität der luftchemischen Bedingungen am Taunus-Observatorium: Messungen des CO- und H₂-Mischungsverhältnisses im Winter 1996/97*. Diplomarbeit, Fachbereich Geowissenschaften der Johann Wolfgang Goethe-Universität, Frankfurt am Main, April 1998.
- Wobrock, W., D. Schell, R. Maser, W. Jaeschke, H.-W. Georgii, W. Wiprecht, B. G. Arends, J. J. Mols, G. Kos, S. Fuzzi, M. C. Facchini, G. Orsi, A. Berner, I. Solly, C. Kruisz, I. B. Svenningsson, A. Wiedensohler, H. Hanssin, J. A. Ogren, K. J. Noone, A. Hallberg, S. Pahl, T. Schneider, P. Winkler, W. Winiwarter, R. N. Colville, T. W. Choularton, A. I. Flossmann, and S. Borrmann. The Kleiner Feldberg Cloud Experiment 1990. *J. Atmos. Chem.*, 19:3–35, 1994.
- Yoshino, K., J. R. Esmond, W. H. Parkinson, K. Ito, and T. Matsui. Absorption cross-section measurements of water vapour in the wavelength region 120 to 188 nm. *Chem. Phys*, 211:387–391, 1996.

- Zanis, P., P. S. Monks, E. Schuepbach, and S. A. Penkett. On the relationship of $\text{HO}_2 + \text{RO}_2$ with $j(\text{O}^1\text{D})$ during the Free Tropospheric Experiment (FREETEX '96) at the Jungfraujoch Observatory (3580 m above sea level) in the Swiss Alps. *J. Geophys. Res.*, 104(D21):26,913–26,925, November 1999.
- Zenker, T., H. Fischer, C. Nikitas, U. Parchatka, G. Harris, D. Mihelcic, P. Musgen, H. Patz, M. Schultz, A. Volz-Thomas, R. Schmitt, T. Behmann, M. Weissenmayer, and J. Burrows. Intercomparison of NO , NO_2 , NO_y , O_3 , and RO_x measurements during the Oxidizing Capacity of the Tropospheric Atmosphere (OCTA) campaign 1993 at Izaña. *J. Geophys. Res.*, 103(D11):13,615–13,634, June 1998.

Acknowledgements

It is almost a truism to say that this dissertation would never have come into being without the help and encouragement of a large number of people, but it is nevertheless true, and for that reason I would like to express my gratitude to all those who have helped me to get this far in many different ways.

Firstly, I would like to firstly thank my “Doktorvater” Prof. Dr. H.-W. Georgii for taking me on as a doctoral student and for providing the interesting research topic. I greatly appreciate the fact that he was prepared to take me on even though he was preparing to retire. He has continued to follow the progress of my work ever since.

My heartfelt thanks also go to Dr Heinz Bingemer, who has provided much practical assistance and many useful discussions over the course of the project. He has also graciously put up with my attempts at German reports and turned them into readable efforts. This project would not have been possible without his help.

Prof. Dr. U. Schmidt has supported this project in diverse ways since coming to the Institute. I greatly appreciate his continued support and his practical advice and the cooperative atmosphere he has provided here.

For the greater part of this project, I have had the pleasure of sharing an office with Xu Xiaobin (徐晓斌) and I have benefitted greatly from our discussions (in various languages). I have learnt a lot and hope our paths will cross again.

The Hessische Landesamt für Umwelt und Geologie (formerly the Hessische Landesanstalt für Umwelt) funded the research project, and have also provided data from their measurement network. Mr S. Baltrusch, helped coordinate our cooperative activities and was my main contact person. Dr S. Jacobi of the HLUG has also helped numerous times by calibrating our O₃ and SO₂ analysers.

Prof. John P. Burrows and the Peroxy Radical Work Group at the Institute for Environmental Physics, University of Bremen, have also been very helpful. Michael Weißenmayer and Thomas Behmann provided considerable help and advice during the initial phase of building the chemical amplifier. “Lola” Maria Andres-Hernandez and Dirk Stöbener have helped provide suggestions and information over their own CA development work.

Dr R. Schmitt of Meteorologie Consult GmbH helped with PAN, TECAN and radiation measurements at Kleiner Feldberg. Many helpful discussions were also held while testing equipment on the roof platform or rebuilding the TECAN calibration unit.

Grateful thanks also to the mechanical workshop under Robert Röder. He has also put up with my rather non-concrete wishes, and built what I wanted, rather than what I asked for. Werner Haunold of the Zentrum für Umweltforschung provided the design for the permeation ovens, as well as sundry other help and equipment. Ralph Strobl has provided assistance with the design of the electronics and by dealing with computer and network problems. I have also appreciated his at times rapid repair of lightning-damaged computers. Vera Fischer helped with the design and constructions of the signal processing unit for the CA. Dieter Vogler helped look after the instrumentation at Kleiner Feldberg, and Johannes Wolf helped greatly by airing the containers to prevent overheating during high summer.

Thanks also go to the work group led by Prof. Harald Berresheim at Hohenpeissenberg. It has been a pleasure working with Christian Plass-Dülmer during the measurement campaign and data analysis; thanks for the hospitality.

Andreas Rüb and Thomas Wetter also helped operate some of the instrumentation at Kleiner Feldberg. Fruitful discussions with Thomas, Melanie Müller, Ulrich Bundke and other “real” meteorologists have also been greatly appreciated. Discussions with Anja Werner were a great help in helping me understand “significance levels”, congruence and other statistical niceties. The stratospheric work group of Oliver Riediger, Martin Strunk, Michael Volk, Andreas Engel, Hans-Peter Haase, Katja Ivanova, and others have also provided numerous ideas for instrumental and analytical techniques, as well as the loan of tools and fittings. Oli in particular has been a great help with programming questions, and helping to lighten the atmosphere. Bettina Schaefer also was the source of much creative discussion during the initial stages of the project.

Numerous other colleagues from the Institut für Meteorologie und Geophysik have also provided assistance and useful discussions, and I wish to thank you all warmly. It has been a pleasure being able to work in such a friendly atmosphere.

A very special thanks goes to Ana, my wife, for her patience and encouragement. I know you have put up with a lot, and I am grateful that you didn’t give up on me. Samuel and Rebekah have also kept life interesting, thanks for putting up with daddy spending so much time at work.

My parents, Maurice and Margaret, have also supported my endeavours, and have diligently proofread parts of the manuscript.

I am also grateful to the large number of other friends who encouraged me during my work. Thanks especially to Bernd und Gabi B., Bernd Ö. and others from Christliches Zentrum Nordweststadt.

Lastly, but most importantly, I wish to thank God for his persistence and help throughout this project.

Oberursel, Hesse
August 8, 2001

Graeme M. Handisides

Curriculum Vitae

Personal Details

Full Name	Graeme Maurice Handisides
Date of Birth	8 December 1962
Place of Birth	Mangakino, New Zealand
Nationality	New Zealand
Marital Status	Married, with two children
Native Language	English
Other languages	German, fluent Chinese, fluent (Certificate of Proficiency in Chinese as a Foreign Language)

Academic Record

1967-1974	Vauxhall Primary School, Devonport, New Zealand
1974-1975	Belmont Intermediate School, Belmont, New Zealand
1976-1980	Takapuna Grammar School, Takapuna, New Zealand
1981-1983	Undergraduate Student at University of Auckland, New Zealand
May, 1984	Bachelor of Science in Physics
1984-1986	Graduate Student at University of Auckland, New Zealand
May, 1986	Master of Science (Honours), Thesis Title: "Drop Size Measurement using Optical Scattering Techniques"
1986-1989	Foreign Language Department, Xiamen University, China
1992-1993	German Language Study in Frankfurt am Main, Germany
1993	Diploma in Teaching English as a Foreign Language
1994-present	Doctoral Student in the Institute for Meteorology and Geophysics, Johann Wolfgang Goethe University, Frankfurt am Main, Germany

Employment Record

1989-1990	English Teacher in the Physics Department, Dalian Railway Institute, China
1990-1992	English Teacher at Liaoning Teachers University, China
1994-present	Research Assistant at Institute for Meteorology and Geophysics, J. W. Goethe University, Frankfurt am Main, Germany

